Neutral Particle Integral Transport in Inertial Confinement Fusion Systems Using Time Dependent Integral Transport Methods

K.R. Olson

December 1999

UWFDM-1117

FUSION TECHNOLOGY INSTITUTE

UNIVERSITY OF WISCONSIN

MADISON WISCONSIN

Neutral Particle Integral Transport
in
Inertial Confinement of Fusion Systems
Using
Time Dependent Integral Transport Methods

K. R. Olson

A dissertation submitted in partial fulfillment of the requirements for the degree of

Doctor of Philosophy

Nuclear Engineering and Engineering Physics

at the

University of Wisconsin - Madison

1999

Abstract

Time-dependent radiative transport is important in inertial confinement of fusion targets. The target must be illuminated with as symmetric a source as possible to ensure an isentropic compression. Once the fusion event begins, energy is taken away from the burn via radiation transport. This process represents a large percentage of the total energy loss. Similarly, neutron transport is important to calculate accurately as it influences neutronic heating and the time-dependent neutron spectrum. Both radiative and neutronic transport are valuable as a diagnostic tools.

Four time-dependent finite media benchmarks were calculated using the time-dependent integral method. The four benchmarks that were produced are: homogeneous Cartesian with uniform source, homogeneous Cartesian with localized source, homogeneous spherical with localized source, and heterogeneous Cartesian with localized source. The benchmarks were calculated using the subtraction of singularity method, solving for the uncollided flux analytically and numerically solving for the collided flux. Time-dependent, heterogeneous, integral kernels were derived for point, line, and planar geometries. These kernels are newly developed to the field of radiative integral transport.

The Time-Dependent Bubble Integral Transport (TBIT) method was introduced. The technique follows the causality of the particles exactly without the need to save the complete history of the problem. The method was benchmarked against the four finite media, time-dependent benchmarks. In Cartesian coordinates, the TBIT method produced errors of no more than 1.6in three-dimensional spherical coordinates of 6.5

The TBIT method was applied to two problems typical to Inertial Confinement of Fusion devices. A three-dimensional spherical capsule illumination was simulated for a two, four, and six laser entrance hole spherical hohlraum. As the surface area of the laser entrance hole gets larger, the capsule illumination becomes more non-uniform. The

TBIT method predicted that the greater the number of laser entrance holes, for equal surface areas, the more uniform the capsule illumination. The second application was for a neutron time of flight diagnostic found on experimental ICF devices. The simulation showed that scattering effects from the walls would shift the detected spectrum only a small amount.

Acknowledgments

The author would like to thank several people for their help and encouragement without which this dissertation would be impossible.

I would like to express my love and devotion to my beautiful wife Tiffany who has stood by me throughout this research.

I would like to thank my parents for passing on to me the love of learning and their faith in my abilities. The trip from kindergarten to graduate school has been a long one, but they have been with me every step of the way.

I would like to thank Rogue Squadron at Robotech Research for their help in relieving stress. The group trips off the SS. Valley Forge were highlights of my weekends.

I am grateful to Dennis Bruggink for his help on the creation of the diagrams in this dissertation.

I would like to thank Dan Heit for his consulting help and the use of his computer to run cases when the "crunch" came.

Last but not least, the author would like to show his appreciation to my advisor Professor Douglass Henderson. Without his initial work in integral transport and his patience in me when I "lost" his papers this entire dissertation would be impossible.

Contents

List of Tables

List of Figures

Chapter 1

Introduction

Fusion has several distinct advantages over traditional forms of energy production. First, the elements used in fusion are plentiful and easily obtained. Second, fusion waste products are typically light stable rather than heavy radioactive nuclei. Finally, the fusion reaction produces copious amounts of energy. One of the most promising fusion reactions for energy production is the DT reaction, as shown in Eqn. 1.1.

$$D + T \rightarrow \alpha\ (3.5\,MeV) + n\ (14.1\,MeV)\,. \tag{1.1}$$

Although fusion has several distinct advantages for energy production, there is a considerable price to pay. The ions that fuse together are positively charged. As a result, their initial kinetic energy must be high enough to overcome their mutual Coulombic repulsion. Typically the reactants must be heated to some 100 million degrees, or 10 keV, before thermonuclear fusion can occur. Several methods have been used to initiate fusion. One such approach controls the fusion process through the use of inertial confinement

To begin the inertial confinement fusion (ICF) process, sufficient energy must be transported to compress the target to 1,000 times the density of water [2]. This transport can occur in one of two ways. The target can either be directly illuminated with laser or ion beams, whereby the lasers or ions travel straight from their source and strike the target, or the target can be indirectly illuminated. For this second method, the lasers or ions strike a cylindrically shaped high-Z material, called a hohlraum. The areas on the hohlraum where the beams strike heat up and produce X-rays, which then proceed to illuminate the target. Figure 1.1 shows an ICF hohlraum and DT containing fuel capsule

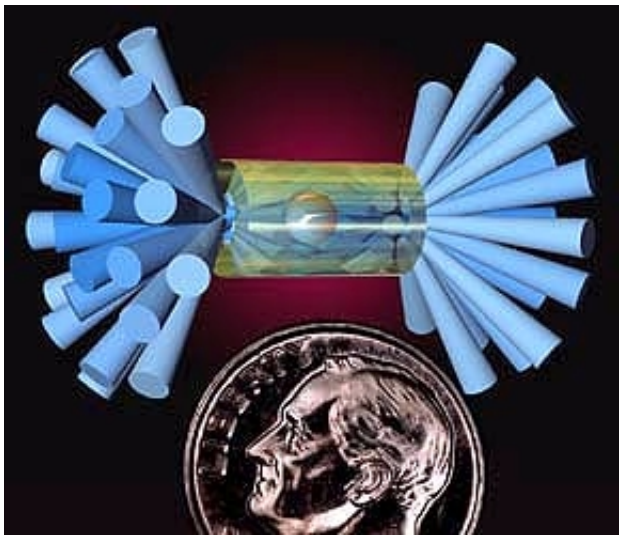

Figure 1.1: ICF Hohlraum and Capsule (Courtesy of LLNL)

next to a dime for size comparison. In either case, direct or indirect drive, the goal is to illuminate the capsule with as uniform a source as possible.

The implosion of the target begins when the energy beams strike and ablate off the outer portions of the capsule driving a shock wave inward. Once the shock wave converges at the center of the pellet, a small central region achieves the pressures and densities necessary for thermonuclear fusion. This region then ignites, thereby creating a thermonuclear spark which heats up adjacent cooler layers causing the fusion reaction to propagate outward.

The key to an efficient burn is the propagation of the reaction from the central region of the target. The outer layers must remain cool while they are being compressed so that the compression is as isentropic as possible. In this way only a small central volume is given the thermal energy needed to initiate thermonuclear fusion. The outer regions are then compressed and heated by a self sustained reaction that was initiated by the central

spark, lowering the initial energy requirement by a factor of ten [3].

An ideal isentropic compression of the outer layers of the target is difficult to obtain. Alpha particles produced in the burn have relatively short mean free paths. As a result, they deposit their energy in areas adjacent to the thermonuclear burn, lowering the energy requirement by allowing the outer layers to be compressed while still being relatively cold.

However, the 14.1 MeV neutrons that are produced in the fusion process have much longer mean free paths. In DT targets, the fuel pellet is compressed to an areal density, ρR, between 3 to 6 g/cm^2 [4]. The mean free path of DT neutrons multiplied by the density of the DT target is roughly 5 g/cm^2 [5]. Thus, neutrons can interact with the background plasma and deposit a fraction of their substantial 14.1 MeV kinetic energy.

In general, the performance potential of ICF targets is limited by: entropy changes, fluid instabilities, asymmetries, poor absorption, and poor implosion efficiencies. An optimum target design incorporates methods by which each of these are controlled [6].

1.1 Time-Dependent Radiative Transport

Radiation transport plays a critical role throughout the entire ICF process. To begin the implosion, the target must be illuminated with a symmetric source of radiation. The energy is transported into the target which ablates off the outer surface and drives a shock wave in towards the center. If any part of this calculation is modeled incorrectly, a non-uniform implosion could occur, which would degrade the target's performance.

Once the shock wave converges into the center of the target, a small spark region is formed and thermonuclear fusion can occur. The plasma created in the implosion process emits and reabsorbs X-rays. During the thermonuclear burn, the energy contained within the radiation field is roughly the same order of magnitude as the thermal energy contained within the plasma [7]. When the energy in the radiation field is comparable to the energy

found within the plasma, the radiation and material time-dependency must be advanced simultaneously [8].

The hot plasma in the center of the target will lose energy via radiation transport to the outer regions of the target. In many target designs a high-Z material surrounds the capsule to prevent radiation loss. Nevertheless, this radiation loss represents a large portion of the total energy of the system and must be calculated correctly in order to model the thermonuclear burn of the system [9].

Radiation transport from the target capsule provides valuable diagnostic information. Spatial and temporal measurements of the radiation field are the primary source of information for the implosion and subsequent burn.

1.2 Time-Dependent Neutron Transport

Neutronic heating is detrimental to the ideal isentropic compression. Unlike the charged alpha particles, neutrons deposit their energy throughout the interior of the pellet, which heats up the outer layers before they are compressed. Calculations considering the transport of neutrons show that neutronic heating is an important process in the burn phase of reactor grade ICF pellets. Simulations show that if neutron heating is neglected, the fuel gain of DT pellets is overestimated [10, 11]. The simulated target was a DT pellet compressed to an areal density of $\rho R = 4.3$ g/cm^2 [4, 12]. The rate of neutron energy deposition is calculated using the following KERMA-factor method:

$$P_{n,i}(\vec{r},t) = \sum_{j\neq e}\int n_j(\vec{r},t)K_j(E)\phi_n(\vec{r},E,t)dE \tag{1.2}$$

$$P_{n,e}(\vec{r},t) = 0, \tag{1.3}$$

where: $P_{n,(i,e)}$ is the volumetric heating rate for ions or electrons, $K_j(E)$ is the total neutron KERMA factor of species j, n_j at the current number density [12], and $\phi_n(\vec{r},E,t)$ is the scalar flux. These calculations showed that without the inclusion of neutronic

heating the gain of reactor grade pellets, at $\rho R = 6$ g/cm^2, is overestimated by roughly 15%. This overestimation becomes even greater with increasing values of ρR.

Neutrons deposit some of their kinetic energy into the plasma causing the pellet to disassemble and terminate the thermonuclear burn sooner than if neutronic heating is neglected. The expansion of the pellet then broadens the energy spectrum of neutrons leaving the target.

Time-dependent and steady-state calculations for the neutron spectrum emanating from a target have been compared [4]. In both cases the energy distribution peaks around 14.1 MeV, which is the uncollided kinetic energy of neutrons freely escaping the capsule. However, in the time-dependent analysis neutrons can have energies greater than 14.1 MeV if they are emitted in the same direction as the expanding medium. The average energy of neutrons leaving an expanding target is approximately 10 MeV; whereas, the average energy of neutrons leaving a steady state capsule is only 9 MeV. When the target is compressed to an areal density of 6 g/cm^2, roughly 60% of the kinetic energy is carried away by escaping neutrons [4].

A reliable neutron spectrum is essential for the calculation of the tritium breeding ratio and the design of ICF reactor blankets. Therefore in order to obtain the most reliable results, a time-dependent calculation must be performed. Many different attempts have been made to couple neutron transport to the hydrodynamics of the ICF target. They range from simple analytical steady-state collisional methods, to moderately complex diffusion based calculations, and finally to large scale time-dependent discrete ordinate and P_l codes [10, 13, 14, 15].

1.3 Introduction to Research

The question then becomes, how much time-dependent transport is enough? A possible solution would be to combine the target hydrodynamics with a time-dependent discrete ordinates code such as TIMEX [16]. However, this coupling would increase the already substantial run-time for target simulations. On the other hand in order to optimize computer run-time, a simple representation for radiative transport may be included. However, incorrect modeling of the radiation transport can predict vastly differing results than those obtained experimentally.

The following research was to develop time-dependent integral transport methods such that they can be used in Inertial Confinement of Fusion systems. Chapter 2 will review some of the other methods by which radiative transport can be implemented in ICF systems.

As there are no finite-media benchmark calculations for time-dependent neutral particle transport, a sizable amount of work was devoted to producing benchmark quality time-dependent results. Chapter 3 will describe how these results were obtained and present four one-dimensional, time-dependent, finite media benchmarking cases.

Chapter 4 will introduce the Time-Dependent Bubble Integral Transport (TBIT) method and describe in depth the intricacies of the numerical method. The TBIT method is compared against the time-dependent benchmarks in Chapter 5.

Chapter 6 will detail two relevant ICF applications using the TBIT method. The first application is a presentation of a three-dimensional radiative transport simulation of the illumination of a DT capsule within a spherical hohlraum. The second application will be devoted to the calculation of the time-dependent energy spectrum for a neutron time-of-flight diagnostic. Chapter 7 will give conclusions from the current work and point to areas that need to researched further.

Chapter 2

Literature Review

The neutral particle transport equation is a version of the Boltzmann equation used in the kinetic theory of gases. This equation describes the transport of particles as a function of space, $\vec{r}$, directional travel, $\hat{\Omega}$, energy, E, and time, t. The neutral particle transport equation is:

$$\left[\frac{1}{v}\frac{\partial}{\partial t} + \hat{\Omega}\cdot\vec{\nabla} + \Sigma\left(\vec{r},E,t\right)\right]\psi\left(\vec{r},\hat{\Omega},E,t\right) = \\ + \int dE' \int d\Omega' \Sigma_s\left(\vec{r},E'\rightarrow E,\hat{\Omega}'\rightarrow\Omega,t\right)\psi\left(\vec{r},\hat{\Omega}',E',t\right) + q_{ex}\left(\vec{r},E,\hat{\Omega},t\right), \quad (2.1)$$

where: $\psi\left(\vec{r},\hat{\Omega},E,t\right)$ is the time-dependent angular flux, $\Sigma\left(\vec{r},E,t\right)$ is the total macroscopic cross section for particles with energy of E, $\Sigma_s\left(\vec{r},E'\rightarrow E,\hat{\Omega}'\rightarrow\hat{\Omega},t\right)$ is the double differential macroscopic scattering cross section, and $\mathrm{q}_{ex}\left(\vec{r},\Omega,E,t\right)$ is the source term which can include the addition of particles resulting from fission or fusion.

Solving Eqn. 2.1 directly is an almost impossible feat to perform analytically and difficult to achieve numerically. In general, Eqn. 2.1 has been simplified by some of the following assumptions: time-independence, isotropic scattering, homogeneous materials, or monoenergetic particles. Numerical calculations can then proceed without being burdened by the full fledged transport equation, and analytical solutions can be found for simple one-dimensional infinite or semi-infinite problems [17, 18].

There is a substantial amount of work in the field of neutral particle transport. Therefore, this literature search will be limited to those methods which can, and have, been used in time-dependent radiative transport in ICF targets.

2.1 Multiple Collision Method

The multiple collisional method has been applied to time-dependent neutron transport problems [19, 20, 21, 22]. Specifically, B.D. Ganapol has used multiple collision techniques to obtain solutions for infinite and semi-infinite problems in 1-D Cartesian coordinates. These results were then compared to calculations predicted from P_1 and diffusion theory calculations [23, 24, 25, 26, 27]. The angular and scalar flux using the multiple collisional method are given by:

$$\psi(x,\nu,t) = \sum_{n=0}^{\infty} \psi_n(x,\nu,t) \tag{2.2}$$

$$\phi(x,t) = \sum_{n=0}^{\infty} \phi_n(x,t). \tag{2.3}$$

Assuming that the external source only feeds into the uncollided flux, then the uncollided flux and subsequent collided fluxes are given by:

$$\begin{aligned}
\left(\frac{1}{v}\frac{\partial}{\partial t} + \hat{\Omega}\cdot\vec{\nabla} + \Sigma(\vec{r})\right)\psi_0\left(\vec{r},\hat{\Omega},t\right) &= S\left(\vec{r},\hat{\Omega},t\right) \\
\left(\frac{1}{v}\frac{\partial}{\partial t} + \hat{\Omega}\cdot\vec{\nabla} + \Sigma(\vec{r})\right)\psi_1\left(\vec{r},\hat{\Omega},t\right) &= \int_{4\pi}\Sigma_s\left(\vec{r},\hat{\Omega}'\to\hat{\Omega}\right)\psi_0\left(\vec{r},\hat{\Omega}',t\right)d\hat{\Omega}' \\
&\vdots \quad\quad \vdots \\
\left(\frac{1}{v}\frac{\partial}{\partial t} + \hat{\Omega}\cdot\vec{\nabla} + \Sigma(\vec{r})\right)\psi_n\left(\vec{r},\hat{\Omega},t\right) &= \int_{4\pi}\Sigma_s\left(\vec{r},\hat{\Omega}'\to\hat{\Omega}\right)\psi_{n-1}\left(\vec{r},\hat{\Omega}',t\right)d\hat{\Omega}',
\end{aligned} \tag{2.4}$$

where the source term for the n^{th} collided flux is all the neutrons in the $n-1^{th}$ collided flux which have suffered a additional collision.

The multiple collisional method was applied to finite slabs [22]. Time-dependent analytical solutions to the second collided flux for a delta function source in time and up to the first collided flux for a step function with a pulse width of Δt were derived. The calculations involved in obtaining these solutions are incredibly detailed and difficult

to derive. However, they give valuable insight in the time-dependent properties of the system in question.

Heterogeneous systems can be calculated using multiple collisional method [28, 29]. For heterogeneous cases, the volume of interest is divided into cells that are small enough that the material within each cell is homogeneous and at most one mean free path length in width [30]. The system is divided into small components to ensure that the flat flux approximation is valid within each unit cell.

2.2 Flux Expansion by Legendre Polynomials

In multiple collision theory, the scalar and angular fluxes were broken into collided components. Each collided component was solved using numerical integration and recursion schemes. However, solutions could be derived from the multiple collisional method by expanding the the scalar and angular fluxes in terms of Legendre polynomials. This approach could incorporate anisotropic scattering by expanding the cross sections in terms of Legendre polynomials providing the means to write a fast, efficient, time-dependent code to benchmark problems.

The monoenergetic transport equation in one-dimensional Cartesian coordinates with anisotropic scattering and a delta function source in time and space is:

$$\left(\frac{1}{v}\frac{\partial}{\partial t}+\mu\frac{\partial}{\partial x}+\Sigma\left(x,t\right)\right)\phi\left(x,\mu,t\right)=\int_{-1}^{1}\Sigma_{s}\left(x,\mu^{'}\rightarrow\mu,t\right)\phi\left(x,\mu^{'},t\right)d\mu^{'}+Q\left(\mu\right)\delta\left(x\right)\delta\left(t\right). \tag{2.5}$$

Equation 2.5 has been shown to be expressible in the following convergent series [31]:

$$\phi\left(x,t\right)=\frac{e^{-t}}{t}\sum_{n=0}^{\infty}\frac{ct^{n}}{n!}\psi_{n}\left(\eta\right)H\left(1-\left|\eta\right|\right), \tag{2.6}$$

where: η=x/vt, H is the Heaviside function, and $\psi_{n}\left(\eta\right)$ is the reduced collided scalar flux given by:

$$\psi_{n}\left(\eta\right)=\int_{-1}^{1}F_{n}\left(\mu,\eta\right)d\mu. \tag{2.7}$$

F_n obeys the following differential recursion relation (called the reduced collision equations) [25]:

$$\left[(\mu-\eta)\frac{\partial}{\partial t}+n-1\right]F_n(\mu,\eta)= \\ n\sum_{l=0}^{L}\frac{2l+1}{2}\omega_l P_l(\mu)\int_{-1}^{1}P_l(\mu')\,F_{n-1}(\mu',\eta)\,d\mu'. \tag{2.8}$$

ψ_n can be expanded in terms of η and Legendre polynomials as:

$$\psi_n(\eta)=\sum_{k=0}^{\infty}\frac{2k+1}{2}f_{n,k}^0 P_k(\eta), \tag{2.9}$$

with the expansion coefficients given by:

$$f_{n,k}^0\equiv\int_{-1}^{1}P_k(\eta)\,\psi_n(\eta)\,d\eta. \tag{2.10}$$

Using these expansions, Equation 2.6 simplifies to:

$$\begin{aligned}\phi(x,t) &= \frac{e^{-t}}{t}\sum_{n=0}^{n_s-1}\frac{(ct)^n}{n!}\psi(\eta) \\ &\quad+\sum_{k=0}^{\infty}\frac{2k+1}{2}f_k(t)\,P_k(\eta),\end{aligned} \tag{2.11}$$

where:

$$f_k(t)=\frac{e^{-t}}{t}\sum_{n=n_s}^{\infty}\frac{(ct)^n}{n!}f_{n,k}^0. \tag{2.12}$$

The infinite planar geometry P_1 equations have received considerable interest. Figure 2.1 shows the comparison between the time-dependent results for the neutron density within an infinite medium of carbon containing a delta function source in time and space against those predicted from the multiple collisional theory, P_1 equations, and diffusion theory [32]. The multiple collisional theory was carried out until its solution had converged below some predetermined tolerance. This converged multiple collisional solution, for the purposes of this comparison, was considered to be exact.

These results show that the time-dependent diffusion theory was a better approximation to the "exact" solution than the P_1 equation. This conclusion is somewhat puzzling

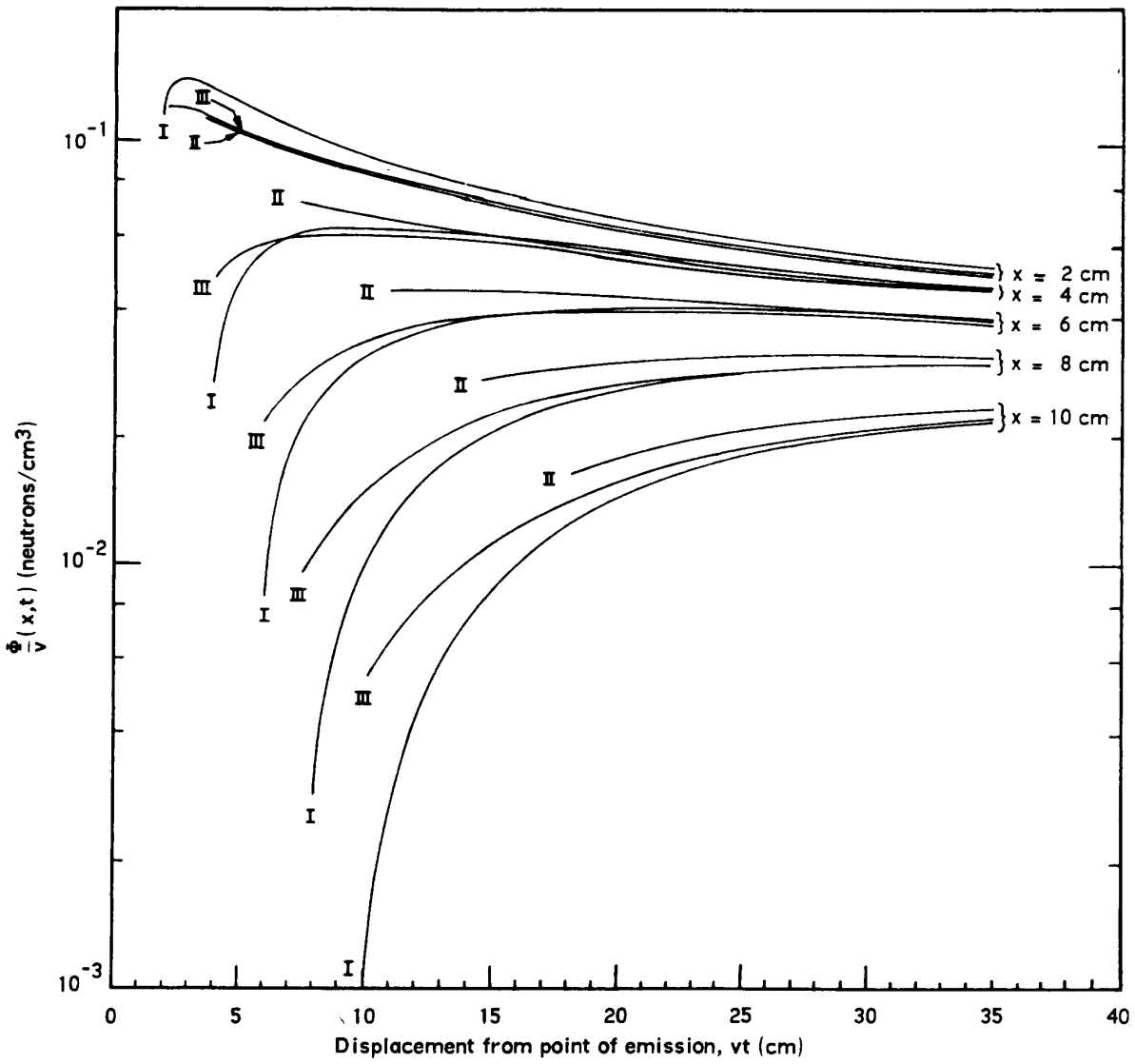

Figure 2.1: Comparison of Time-Dependent calculations in carbon using: (I) Multiple collisional method, (II) P1 approximation, (III) diffusion approximation

as diffusion approximations can not model any type of wave behavior. Although, this system should possess a wave of neutrons that stream out from the delta function source in the center of the infinite medium. In addition, the further away particles travel from the source, the better the approximation diffusion theory becomes. This result is predictable because as the neutrons travel further away from the source and as time increases, the number of collisions that neutrons undergo also increases and approaches the infinite number of collisions assumed by diffusion theory.

Higher order expansions to the time-dependent P_n equations have only been calculated numerically. Ganapol has reconstructed the time-dependent neutron flux from its moments in the one velocity approximation. This method can treat anisotropic scattering, but is only applicable to infinite medium problems. LASNEX, a two-dimensional hydrodynamics code has a P_n transport model for one-dimensional simulation studies [33].

2.3 Diffusion Based Calculations

There are many different methods to solve radiation transport within ICF targets. Perhaps none are simpler to implement than a numerical scheme based on diffusion theory. In general, hydrodynamics codes already require an inordinate amount of run-time and the addition of extremely accurate transport methods was thought to provide little benefit for the increased amount of work. Thus, diffusion based calculations have become the method of choice for coupling with hydrodynamic codes. The LASNEX code, in addition to having a P_n transport model, contains a diffusion based radiation transport package [34, 35].

There are several problems that arise with the use of diffusion based calculations. The time-dependent material temperature and photon diffusion equations can either be coupled in an explicit or implicit fashion. With the explicit coupling, an independent

diffusion equation is obtained for each energy group. Thus, the radiative transport can be solved easily and quickly. However, explicit solutions are only stable for sufficiently small time-steps [36]. Unconditional stability is achieved when using an implicit scheme. However, the group diffusion equations are no longer independent because there is now a common source term for each energy group that makes transport within a group dependent on all the other groups [36]. The resulting set of implicit equations are solved iteratively.

A second disadvantage with the use of diffusion theory is that diffusion approximation is most accurate in materials where particles undergo many collisions and the mean free path is small compared to the medium. If the material is optically thin, a calculation using transport theory is more appropriate. Time-dependent radiation transport calculations for high-Z materials using diffusion base techniques produce results that compare favorably to experimental results. However, diffusion calculations for low-Z materials, such as plastic, predict incorrect behaviors [7]. A high-Z material scatters X-rays to a much greater extent than a low-Z material. The greater the number of scattering events, the more applicable diffusion theory becomes and hence better results are obtained.

2.3.1 Radiation Diffusion on an Eulerian Mesh

The time-dependent, frequency-integrated radiation diffusion equation is [37]:

$$\frac{1}{c}\frac{\partial E}{\partial t} = \vec{\nabla} \cdot \left(D\vec{\nabla}E\right) - \kappa_p \rho E + \kappa_p \rho \theta, \tag{2.13}$$

where: $E{=}aT_R^4$ is the radiation energy density, T_R is the radiation temperature, c is the speed of light, t is the time, $D{=}\ 1/3\kappa_R\rho$ is the radiation diffusion coefficient, κ_R is the frequency integrated Planckian opacity, ρ is the mass density, $\theta{=}aT^4$, and T is the material temperature. The first term on the right hand side is the divergence of radiation as it is transported through the material. The last two terms represent the absorption

and blackbody emission of radiation, respectively.

Under equilibrium conditions, the material temperature is equal to the radiation temperature. This is the one temperature approximation (T). There are many types of representations for the two-temperature (2T) non-equilibrium radiation diffusion equation. One such approximation assumes that the materials are grey (no frequency dependence), then the simplest formulation is to use two temperatures, $T_{radiation}$ and T, for the two Planckian opacities [37]. Likewise, a three-temperature scheme (3T) would include temperatures for ions, electrons, and radiation.

The radiation energy density was assumed to be constant throughout the interior of each cell. The Eulerian cells are then fixed throughout the simulation. However as will be discussed later in this section, the cells can be adapted to the hydrodynamic evolution of the problem.

For this particular example of a diffusion based calculation on an Eulerian mesh, cylindrical geometry was used, Figure 2.2. The average energy in a cell was defined as [37]:

$$E_{i,j} = \frac{\int_{i,j} E\left(r,z\right)}{V_{i,j}}. \tag{2.14}$$

The volume averaged absorption term for each cell is [37]:

$$\left(\kappa_p \rho\right)_{j,k} E_{j,k} = \frac{\int_{j,k} \kappa_P \rho E dV}{V}_{j,k}. \tag{2.15}$$

The volume integral of the divergence term becomes a surface integral:

$$\frac{1}{V_{j,k}} \int_{j,k} \vec{\nabla} \cdot \left(D\vec{\nabla}E\right) dV = \frac{1}{V_{j,k}} \oint_{j,k} \hat{n} \cdot \left(D\vec{\nabla}E\right) dS = \frac{1}{V_{j,k}} \sum_{s=1}^{4} \left(AD\hat{n} \cdot \vec{\nabla}E\right)_s, \tag{2.16}$$

where: $\hat{n}$ is the outward normal on each of the four faces and A is its area. The current across each boundary is assumed to be continuous. Under these assumptions, the energy density in each cell, defined as a volume integrated finite-differenced form, becomes:

$$\frac{V_{j,k}}{c}\frac{\partial E_{j,k}}{\partial t} = d_{j+1/2,k}\left(E_{j+1,k} - E_{j,k}\right) - d_{j-1/2,k}\left(E_{j,k} - Ej-1,k\right) + d_{j,k+1/2}\left(E_{j,k+1} - E_{j,k}\right)$$

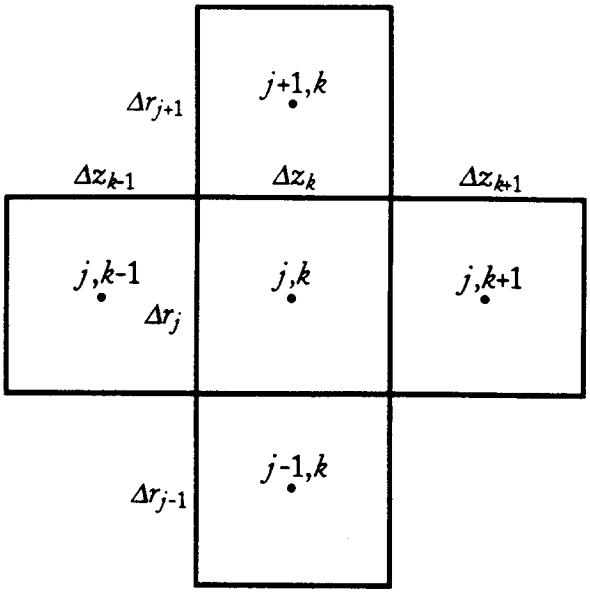

Figure 2.2: The rz coordinate system with j, k indexing scheme

$$-d_{j,k-1/2}\left(E_{j,k}-E_{j,k-1}\right)-V_{j,k}\left(\kappa\rho\right)_{j,k}+V_{j,k}\left(\kappa\rho\right)_{j,k}\theta_{j,k}, \tag{2.17}$$

where: $d_{j,k\pm1/2}$ are the scaled diffusion coefficients that are defined such that the current across each boundary is continuous, and E is the volume averaged energy in their respective cell [37].

There are several different types of adaptive mesh refinements (AMR) used for Eulerian coordinates. One approach is to use patches where the mesh is much finer than in the surrounding regions. With such a method the patches are coupled to the rest of the mesh through boundary conditions [38, 39].

An alternative approach, would be to refine the spatial cells by a constant factor of 1/2 between each level. Then, rather than use boundary conditions to match the cells, the finite difference equations are modified to explicitly couple the cells that have different sizes, see Figure 2.3. The current condition still holds, however, in this case the rightward incoming current into the j^{th}, k^{th} cell must be equal to the combination of the

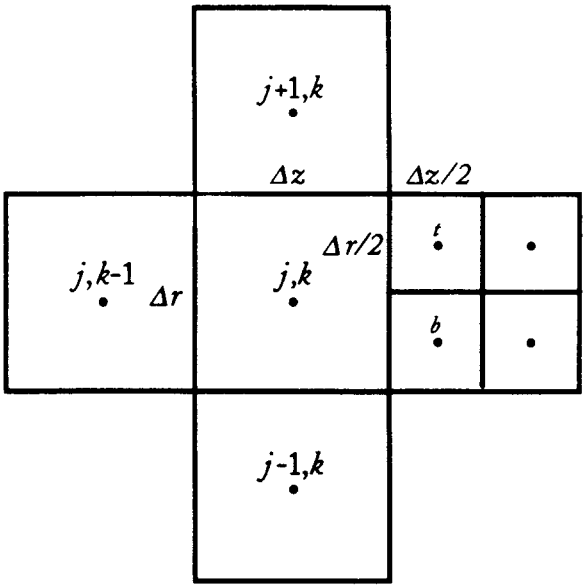

Figure 2.3: Mesh cell with a refined cell on only one side

leftward outgoing currents from the two adjacent cells.

2.3.2 Radiation Diffusion on Lagrangian Mesh

The radiative diffusion equation can be modified for use on Lagrangian meshes. These meshes follow the hydrodynamic evolution of the plasma, and as such are no longer static. A rewritten form of the diffusion equation that can be used on Lagrangian meshes, as opposed to Eqn. 2.13, is:

$$\frac{1}{v}\frac{\partial \phi}{\partial t} + \vec{\nabla} \cdot \vec{J} + \Sigma_a \phi = S, \tag{2.18}$$

where: t is the time variable, v is the particle speed, ϕ is the particle flux, $\vec{J}$ is the particle current, Σ_a is the macroscopic absorption cross section, and Q is the source function.

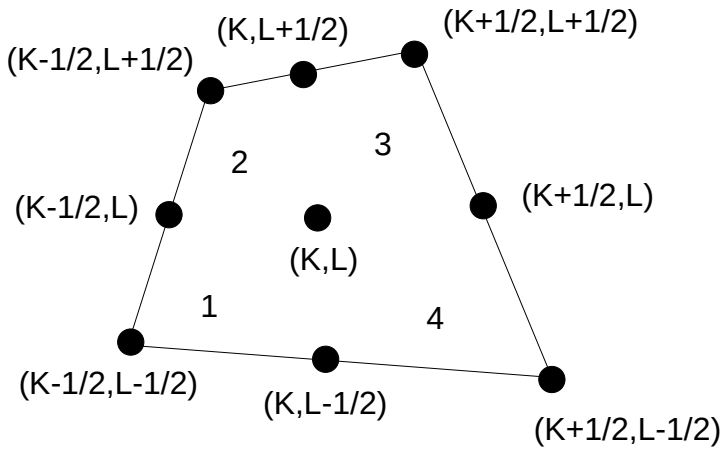

Figure 2.4: Generalized Cell for Lagrangian Coordinates

Assuming Fick's Law of Diffusion, the particle current is related to the particle flux by:

$$\vec{J} = -D\vec{\nabla}\phi, \tag{2.19}$$

where D is the diffusion coefficient.

In two-dimensional coordinates, the unit cells are quadrilateral. During each time-step the material within the cell is homogeneous, although the bordering cells can be of differing material. A generalized example for a unit cell in modified Lagrangian coordinates is given in Figure 2.4.

The particle flux is defined at the center of each cell. A diffusion coefficient and current is defined at each of the cell's four boundaries. Equation 2.18, is then differenced implicitly in time and integrated over the cell volume, as shown in Figure 2.4. The resulting finite-differenced expression for energy conservation within each cell is [40]:

$$\begin{aligned}\frac{1}{v}\frac{\phi_{k,l}^{n+1}-\phi_{k,l}^{n}}{\Delta t}V_{k,l} + \vec{J}_{k+1/2,l}^{n+1}\cdot\vec{A}_{k+1/2,l} - \vec{J}_{k-1/2,l}^{n+1}\cdot\vec{A}_{k-1/2,l} \\ -\vec{J}_{k,l+1/2}^{n+1}\cdot\vec{A}_{k,l+1/2} - \vec{J}_{k,l-1/2}^{n+1}\cdot\vec{A}_{k,l-1/2} + \sigma_{a,k,l}\phi_{k,l}^{n+1}V_{k,l} = Q_{k,l}V_{k,l},\end{aligned} \tag{2.20}$$

where: n denotes the time index, Δt is the time step, $A_{k+1/2,l}$ is the vector outwardly-

directed from cell (k,l) and normal to the edge at $(k+1/2,l)$ with a magnitude equal to the area associated with that cell edge, $A_{k,l+1/2}$ denotes a vector outwardly directly from cell (k,l) and normal to the edge at $(k,l+1/2)$ with a magnitude equal to the area associated with that cell edge, and $V_{k,l}$ denotes the cell volume. As presented in Section 2.3.1, the current across each of the boundaries is conserved. Once the current across each of the boundaries and the cell centered flux is calculated, the hydrodynamics calculations can then proceed. The hydrodymanic calculations will distort the boundaries of each individual cell; however using this technique, the unit cells must be quadrilaterals.

2.3.3 Flux-Limited Diffusion Theory

Unfortunately, the standard diffusion equation is not a very good approximation for the transport of particles through optically thin materials. As a result several "fix-up" methods have been proposed to adjust the diffusion equation such that it produces better results. One such method is based on the principle of flux limiting.

Standard diffusion theory makes the assumption that Fick's Law of Diffusion is valid, Eqn. 2.19. This law simply relates the particle current to the gradient of the particle flux. However, in certain cases in which $|\phi/\nabla\phi| < \lambda_{mfp}$ the solution to the diffusion equation can produce results in which the current is larger than the product of the particle's speed and flux. An ad hoc flux limiter is introduced by rewriting Fick's law as [41, 42, 43]:

$$\vec{J} = -\frac{1}{\Sigma_{tr}\left[3+\frac{|\vec{\nabla}\phi|}{\Sigma_{tr}\phi}\right]}\vec{\nabla}\phi. \tag{2.21}$$

If the mean free path of the particles is short, then in the limit $\vec{\nabla}\phi \to 0$, Eqn. 2.21 converges back into Fick's Law. If on the other had the mean free path is long, $\vec{\nabla}\phi \to \inf$, then the diffusion coefficient converges into the free-streaming limit.

The advantage of the flux-limited diffusion theory is that it uses existing diffusion based methods and with little modification produce more consistent results [43]. However,

the choice for the new diffusion coefficient, Eqn. 2.21, is completely arbitrary. This particular form of the diffusion coefficient was chosen because in the limit of long and short mean free paths its behavior was consistent.

2.4 TIMEX - Time-Dependent Discrete Ordinates

TIMEX, is a time-dependent one-dimensional discrete ordinates radiation transport code which uses finite element methods for the spatial discretization and Legendre polynomial expansions of the scattering function in order to solve the Boltzmann transport equation with anisotropic scattering, Eqn. 2.22 [44, 45, 46, 47, 48]. Discrete ordinates codes solve the transport equation along predetermined directions. These directions are then integrated using highly accurate quadrature sets, preferably Gaussian.

TIMEX has been successfully integrated into several hydrodynamics codes. G. Velarde has modified TIMEX to include the addition of Lagrangian coordinates by modifying the standard Boltzmann equation with a divergence term which will take into account the hydrodynamic evolution of the spatial mesh [49]. This modified transport equation is:

$$\left[\frac{1}{v}\frac{\partial}{\partial t}+\vec{\nabla}\cdot\left(\hat{\Omega}-\frac{\vec{u}}{v}\right)+\Sigma\left(\vec{r},E,t\right)\right]\psi\left(\vec{r},\hat{\Omega},E,t\right)=q_{ex}\left(\vec{r},\hat{\Omega},E,t\right)$$
$$+\int dE'\int d\Omega'\Sigma_s\left(\vec{r},E'\rightarrow E,\hat{\Omega}'\cdot\Omega\right)\psi\left(\vec{r},\hat{\Omega}',E',t\right)+S\left(\vec{r},E,\hat{\Omega},t\right). \quad (2.22)$$

Radiation energy deposition for both neutrons and prompt gamma rays is calculated using KERMA-factors (Kinetic Energy Release in MAterials) [50]. KERMA-factors assume that the energy deposition for the particles occurs locally, at the spot where the original interaction between the high energy photon/neutron occurs. The ions are then transported through the plasma depositing their energy before slowing down.

The hydrodynamics code MEDUSA-KA-TIMEX has been developed by B. Goel and W. Hoebel to include time-dependent high energy neutronic effects in ICF targets [10].

Unlike the previous method, the transport in MEDUSA-KA-TIMEX does not occur in Lagrangian coordinates but in Eulerian. This is because the divergence term is negligible for these higher energy neutrons. The resulting calculation for a time-dependent neutron spectrum emanating from a DT target is similar to those presented by [4].

The use of discrete ordinates is not always the best solution method. Kornreich compared the accuracy of the ONEDANT discrete ordinates code to results obtained using the F_n method for the thickness of critical slabs [51]. The F_n method uses the Placzek lemma to establish a system of singular integral equations and constraints [52]. The F_n method has been shown to yield concise and accurate results for problems with semi-finite and finite slabs [53]. Although these results are for steady state calculations, they showed that the F_n method converged to the same accuracy as the discrete ordinates method using only half the number of spatial mesh cells.

2.5 Integral Transport Methods

Although the use of discrete ordinate or Monte Carlo codes is widespread in solving problems with neutron transport, there are cases for which direct numerical solutions of the integral form of the Boltzmann Equation becomes attractive. The resulting integral equations are weakly singular in nature [54].

2.5.1 Manipulation of the Angular Flux

Munier manipulated the time-dependent radiative transfer equation for one-dimensional Cartesian coordinates without scattering. He then transformed this equation into an integral equation in terms of the angular flux. [55]. The one-dimensional Cartesian neutral particle transport equation without scattering is:

$$\frac{1}{c}\frac{\partial I}{\partial t} + \mu\frac{\partial I}{\partial x} = K\left(t, x, \nu, \mu\right)\left[B\left(t, x, \nu, \mu\right) - I\right], \tag{2.23}$$

where: I is the photon intensity, $K\left(t,x,\nu,\mu,\right)$ is the photon opacity, and $B\left(t,x,\nu,\mu,\right)$ is the photon emission rate. Equation 2.23 is solved for the following arbitrary boundary condition:

$$I\left(t,x_{lim},\nu,\mu\right)=f\left(t,\nu,\mu\right), \tag{2.24}$$

and initial conditions:

$$I\left(t=0,x,\nu,\mu\right)=g\left(t,\nu,\mu\right). \tag{2.25}$$

For a homogeneous slab with a uniform source, $B\left(t,x\right)=B=constant$ and $K\left(t,x\right)=constant$. The system of characteristics for this system is:

$$c\frac{dt}{1}=\frac{dx}{\mu}=\frac{d\mu}{0}=\frac{d\nu}{0}=\frac{dI}{K\left(B-I\right)}. \tag{2.26}$$

From which the following is obtained:

$$\gamma=ct-\frac{x}{\mu}, \tag{2.27}$$

where γ is the time-characteristic for the system and a constant of integration for the homogeneous slab. Munier derived characteristics containing I [55]. This was done by coalescing the second and the fifth terms of Eqn. 2.23 to find:

$$\left(I-B\right)\exp\left(Kx/\mu\right)=\Phi_0=constant, \tag{2.28}$$

or by combining the first and the fifth:

$$\left(I-B\right)\exp\left(Kct\right)=\Psi_0=constant. \tag{2.29}$$

From these equations, two expressions for the general solution of the transport solution in a homogeneous medium are derived:

$$I\left(t,x,\mu\right)=B+\Phi_0\left(\gamma,\mu\right)\exp\left(-Kx/\mu\right), \tag{2.30}$$

and

$$I\left(t,x,\mu\right)=B+\Psi_0\left(\gamma,\mu\right)\exp\left(-Kct\right), \tag{2.31}$$

where:

$$\Phi(\gamma,\mu) = \Psi(\gamma,\mu)\exp\left[-K\left(ct - x/\mu\right)\right] = \Psi(\gamma,\mu)\exp\left(-K\gamma\right). \tag{2.32}$$

Munier then showed that the general time-dependent solution for radiation transport in a homogeneous slab with an isotropic source is:

$$\begin{aligned} I(t,x,\mu) = {} & B + H(l-ct)\left[g(-\gamma\mu,\mu) - B\right]\exp\left(-Kct\right) \\ & + H(ct-l)\left(f\left[\left(\gamma + x_{lim}/\mu\right)/c,\mu\right] - B\right)\exp\left[-K\left(x - x_{lim}\right)/\mu\right]. \end{aligned} \tag{2.33}$$

Equation 2.33 possesses several distinct components which affect the angular flux. The first term is simply the isotropic uniform source distributed throughout the interior of the slab. The second term is the propagation along the characteristics between the difference in the source terms for the initial conditions and the uniform emission. This portion of the solution is attenuated exponentially in time. The final component of the solution is propagated along the directions of the characteristics with a magnitude equal to the difference between the source and boundary conditions for the slab and attenuated by the optical depth. The first and the third term of Eqn. 2.33 are just the steady state solution for the same homogeneous system [55]. The method used to derive Eqn. 2.33 can be used to calculate the angular flux in an purely absorptive heterogeneous medium.

This integral method does have its limitations. The derivation of Eqn. 2.33 used the assumption that the material was purely absorptive. Therefore, these type of formulations would be of use for photon transport where the ratio of scattering to absorption is small. However, for neutron transport, where this ratio can be quite large, this method would have limited use.

2.5.2 Manipulation of Scalar Flux

Time-dependent integral transport kernels for a homogeneous medium in the three standard orthogonal coordinate systems were derived by Henderson and Maynard [56]. Ad-

ditional integral transport kernels in heterogeneous media were later derived by Olson and Henderson [57]. This method is unlike that presented in Section 2.5.1 in two ways. First, the integral equations are formulated in terms of the scalar and not the angular flux. Second, the method is derived for use in either a scattering or non-scattering media.

Analytical solutions for the first collided flux within slab and spherical geometry for an infinite medium were solved and compared to existing analytical solutions derived by other means [56]. A formalism for numerical solutions was later provided by Olson and Henderson [58]. The time-dependent transport equation for monoenergetic particles in a homogeneous medium with an arbitrary isotropic source is:

$$\left(\frac{1}{v}\frac{\partial}{\partial t} + \hat{\Omega}\cdot\vec{\nabla} + \Sigma\right)\psi\left(\vec{r},\hat{\Omega},t\right) = \frac{Q(\vec{r},t)}{4\pi}\,. \tag{2.34}$$

This differential form of the transport equation can be converted into an integral equation using either the method of characteristics or Laplace transforms [56]. The resulting time-dependent integral equation for the scalar flux is:

$$\Phi(\vec{r},t) = \int_0^t dt' \int_{V'} K(\vec{r},\vec{r}';t,t')\,Q(\vec{r}',t')\,d\vec{r}'\,, \tag{2.35}$$

where: $K(\vec{r},\vec{r}';t,t')$ is the time-dependent kernel and $Q(\vec{r}',t')$ is the time-dependent source. The integration is carried out over the volume of interest V' from time zero until some later time t. The source term includes contributions from both an isotropic scattering flux and an arbitrary isotropic source:

$$Q(\vec{r},t) = \Sigma_s\,\Phi(\vec{r},t) + S(\vec{r},t)\,. \tag{2.36}$$

The homogeneous kernels in the standard coordinate systems have already been derived [56]. For completeness they are provided in Table 2.1. In addition, the generalized heterogeneous point, planar, and two-dimensional Cartesian kernels have been derived [57]. They are presented in Table 2.2 and derived in Appendix A.

Table 2.1: Time-Dependent Integral Transport Kernels in Homogeneous Materials

Geometry	**Time-Dependent Integral Kernels**
Point	$K_{pt}(\vec{r},\vec{r}';t,t') = \dfrac{\exp(-\Sigma\, v[t-t'])}{4\pi\lvert\vec{r}-\vec{r}'\rvert(t-t')}\,\delta\left(t-t'-\dfrac{\lvert\vec{r}-\vec{r}'\rvert}{v}\right)$
Plane	$K_{pl}(x,x';t,t') = \dfrac{\exp(-\Sigma\, v[t-t'])}{2(t-t')}H\left(t-t'-\dfrac{\lvert x-x'\rvert}{v}\right)$
Spherical Shell	$K_{ss}(r,r';t,t') = \dfrac{\exp(-\Sigma\, v[t-t'])}{8\pi rr'(t-t')} \times \left[H\left(t-t'-\dfrac{\lvert r-r'\rvert}{v}\right) - H\left(t-t'-\dfrac{\lvert r+r'\rvert}{v}\right)\right]$
2-D Cartesian	$K_{2D,C}(x,x';y,y';t,t') = \dfrac{\exp(-\Sigma\, v[t-t'])}{2\pi(t-t')\sqrt{(v[t-t'])^2-\lvert x-x'\rvert^2-\lvert y-y'\rvert^2}}\, H\left(t-t'-\dfrac{\sqrt{(\lvert x-x'\rvert^2+\lvert y-y'\rvert^2)}}{v}\right)$

Table 2.2: Time-Dependent Integral Transport Kernels in Heterogeneous Materials

Geometry	**Time-Dependent Integral Kernels**
Point	$K_{pt}(\vec{r},\vec{r}';t,t') = \dfrac{\exp(-\tau(\vec{r},\vec{r}'))}{4\pi\left\|\vec{r}-\vec{r}'\right\|^2}\delta\left(t-t'-\dfrac{\left\|\vec{r}-\vec{r}'\right\|}{v}\right)$
Plane	$K_{pl}(x,x';t,t') = \dfrac{\exp\left(\frac{-\tau(x,x')v(t-t')}{\left\|x-x'\right\|}\right)}{2(t-t')}H\left(t-t'-\dfrac{\left\|x-x'\right\|}{v}\right)$
2-D Cartesian	$K_{2D,C}(x,x';y,y';t,t') = \dfrac{\exp\left(\frac{-\tau(x,x';y,y')v(t-t')}{\sqrt{\left\|x-x'\right\|^2+\left\|y-y'\right\|^2}}\right)}{2\pi(t-t')\sqrt{(v[t-t'])^2-\left\|x-x'\right\|^2-\left\|y-y'\right\|^2]}}$ $H\left(t-t'-\dfrac{\sqrt{\left\|x-x'\right\|^2+\left\|y-y'\right\|^2}}{v}\right)$
	where τ is the optical depth between two points

The Heaviside function, within each of the time-dependent kernels, provides causality information for a particle's motion. A finite amount of time must pass before a particle can affect the flux at a location other than where it was born or scattered.

This method can easily calculate problems in either infinite or finite geometries. In an infinite medium, the integration in the spatial domain would have limits from zero to infinity. In finite problems, the vacuum boundaries are placed as the limits of integration.

An advantage of this method is that the angular flux is handled exactly. Notice that the solution for the scalar flux has no angular dependence. This is because the formulation for the angular flux has already been integrated out. Therefore extremely accurate solutions can be calculated, provided that an accurate numerical quadrature set is used in the numerical formulation for the integrals.

There are several disadvantages with using this type of integral technique. The formulation for the time-dependent scalar flux is in terms of an integration over the temporal domain from $t = 0^+$ until the time of interest, t. Hence, as the time increases the limits of the integration also increase as well as the computational time for each successive generation. Unfortunately, this disadvantage prevents this method from general use in many time-dependent radiative transport codes. Often it is impossible to save material, source, and scalar flux data for all the points previous to the calculational point.

Chapter 3

Generation of Time-Dependent Benchmarks

The importance of time-dependent benchmark solutions can not be understated when developing a new time-dependent method. Any method that has not been adequately benchmarked places into question any results that might be calculated. Unfortunately, very few time-dependent benchmarks exist and those that do are for problems in semi and infinite media.

Finite media, time-dependent benchmarks were developed to adequately benchmark the TBIT method. These benchmarks were calculated using the "standard" integral transport method, as described in Section 2.5.2. All the benchmarks were calculated for finite one-dimensional Cartesian and spherical geometries with homogeneous and heterogeneous media. Chapter 3 describes these benchmarks in more detail.

The chapter is divided into three main sections. Section 3.2 discusses the mathematical theory and numerical evaluation procedure for the solution of the time-dependent integral transport equation. The implementation and evaluation process are illustrated and discussed using the one-dimensional, homogeneous media, planar geometry integral equation as the basis. The integration quadrature sets and the subtraction of singularity method are detailed. Difficulties with the incorporation of the causality constraint inherent in the time-dependent Green's functions are brought to light and the solution for the integration over the domain of interest is presented.

In Section 3.3, time-dependent benchmark solutions are calculated using these standard integral techniques. The calculational procedure as developed by Olson and Henderson consists of the straight forward evaluation of a multi-dimensional integral equation

consisting of a Volterra integral equation in the time domain and Fredholm integral equation in the spatial domain [58]. Standard classical integral evaluation techniques such as the use of Newton-Cotes and Gregory type integration rules, the construction of double and triple composite sets, the use of Romberg integration procedures, and the subtraction of singularity method are all employed in the evaluation of the integrals [54,59-64]. The standard integral method is compared to a benchmark in an infinite Cartesian coordinate system. This was done to show the accuracy of the standard integral method.

Four time-dependent benchmark solutions in finite media using the standard integral transport are generated:

- Uniform Source in Homogeneous One-Dimensional Cartesian Coordinates;
- Localized Source in Homogeneous One-Dimensional Cartesian Coordinates;
- Localized Source in Homogeneous One-Dimensional Spherical Coordinates;
- Localized Source in Heterogeneous One-Dimensional Cartesian Coordinates.

The chapter ends with a discussion of the the inadequacies of time-dependent diffusion theory. Section 3.4 presents concrete examples of time-dependent results calculated using diffusion theory and those calculated using transport.

3.1 Introduction

The importance of accurate time-dependent benchmark solutions can not be underestimated; however, as mentioned earlier a majority of the time-dependent benchmark solutions are presented in infinite and semi-infinite media. Although these are of some interest, real world problems take place in finite media and thus time-dependent benchmark solutions were developed in order to properly benchmark the TBIT method.

Time-dependent finite media benchmark calculations was found using the time-dependent analytical integral techniques first derived by Henderson and Maynard [56] and the numerical techniques by Olson and Henderson [58]. Central to solving the the time-dependent integral equation is the use of first flight (single collision) kernels or Green's functions. Henderson and Maynard derived the homogeneous media scalar flux Green's functions in the three standard orthogonal coordinate systems for the time-dependent single collision kernels using Laplace transforms [56]. Olson and Henderson then derived heterogeneous point, planar, and two-dimensional Cartesian scalar flux kernels using similar methods [58].

The advantage of the integral formulation over the previous methods employed is the straight forward extension to multi-dimensional finite geometries and the use of realistic as well as singular source distributions. Most recently, the one-dimensional planar geometry homogeneous medium time-dependent single collision kernel provided the basis for the development of a one-dimensional planar geometry, time-dependent collision probability method [65].

3.2 Mathematical Theory and Numerical Evaluation Procedure for Integral Transport Methods

The time-dependent transport equation for monoenergetic particles in a homogeneous medium with an arbitrary isotropic source in general coordinates is:

$$\left(\frac{1}{v}\frac{\partial}{\partial t} + \hat{\Omega}\cdot\vec{\nabla} + \Sigma\right)\psi\left(\vec{r},\hat{\Omega},t\right) = \frac{Q(\vec{r},t)}{4\pi}\,. \tag{3.1}$$

Equation 3.1 can be converted into an integral equation using either the method of characteristics or Laplace transform techniques [47, 56]. The resulting time-dependent integral equation for the scalar flux is:

$$\Phi(\vec{r},t) = \int_0^t dt' \int_{V'} K(\vec{r},\vec{r}\,';t,t')\,Q(\vec{r}\,',t')\,d\vec{r}\,'\,, \tag{3.2}$$

where $K(\vec{r},\vec{r}';t,t')$ is the time-dependent kernel and $Q(\vec{r}',t')$ is the time-dependent source. The source term $Q(\vec{r},t)$ includes contributions from both an isotropic scattering flux and an arbitrary isotropic source:

$$Q(\vec{r},t) = \Sigma_s\,\Phi(\vec{r},t) + S(\vec{r},t)\,. \tag{3.3}$$

The integral equation that is solved in Eqn. 3.2 is of the Volterra type in the temporal dimension and of the Fredholm type in the spatial dimension. The integrations are carried out over the volume of interest V' from time zero until some later time t. Straightforward procedures for solving the multi-dimensional integrals are employed in the evaluation of Eqn. 3.2. Solutions for homogeneous media problems in one-dimensional planar and spherical media are considered in this chapter. The time-dependent kernels (Green's functions) for these geometries are presented in Table 2.1 and were previously derived in ref. [56].

An interesting feature to note about these time-dependent scalar flux kernels is the presence of the Heaviside function. This provides causality information for a particle's motion. A source particle traveling at a speed v from a point $\vec{r}$ at a time t' cannot contribute to the scalar flux at a point $\vec{r}$ at a time t unless the following condition is met; $v\,\Delta t = \Delta\vec{r}$, where $\Delta\vec{r} = |\vec{r}-\vec{r'}|$ and $\Delta t = (t-t')$. In other words, a finite amount of time must pass before a particle can affect the flux at a location other than where it was born or scattered. From a computational standpoint, this means that values of the external and scattered source at the position $\vec{r}'$, which have not had time to communicate with the current position $\vec{r}$, are not needed to calculate the flux at the position $\vec{r}$.

Figure 3.1 shows a pictorial representation of how this causality information is practically used for an infinite medium in one-dimensional Cartesian coordinates. The points (x',t'), shown as blackened circles, are within the *triangular region* of communication which extends backwards in time from the point of interest (x,t) and are therefore in-

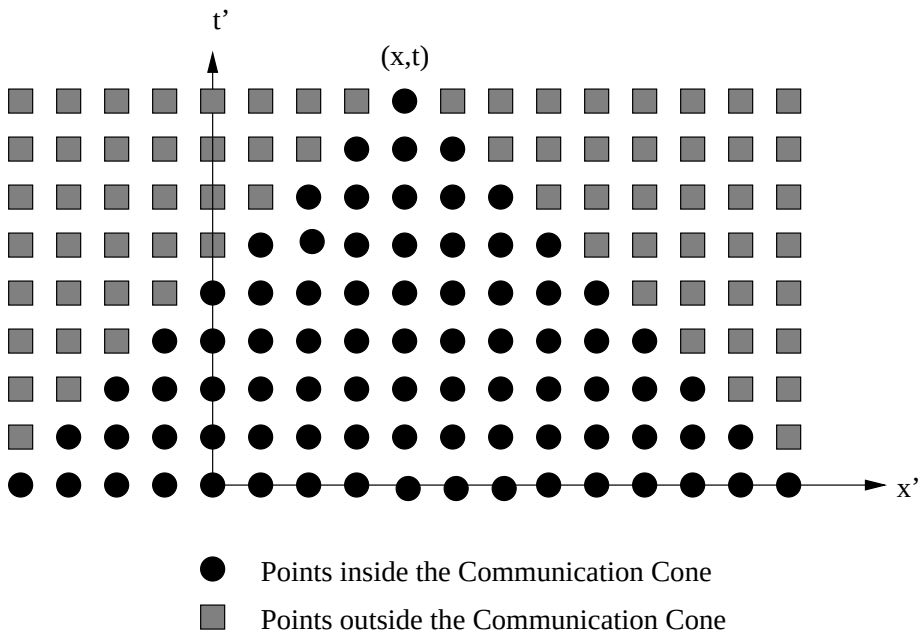

Figure 3.1: Communication in an Infinite Medium

cluded in the numerical evaluation of the integrals. Points outside the triangle have not had time to affect the flux and are excluded. As the medium is infinite, the integration extends over the region defined between the left and right moving wavefronts which are given by the outward most circles on the triangle's base at each time step. As time proceeds during a numerical calculation, the triangle's height and width of the base both increase.

The situation for a finite region in one-dimensional Cartesian geometry is depicted in Figure 3.2. The figure shows a vertical slab topped by a triangular region. The boundaries of the slab are placed as the limits of integration and make up the sides of the slab. At early times, the points (x, t) behave as though they are in an infinite medium (hence the triangular shape) until the wavefront has had time to communicate with the boundaries of the region. As time proceeds in a numerical simulation, the height of the slab region increases. For two-dimensional Cartesian coordinates the region

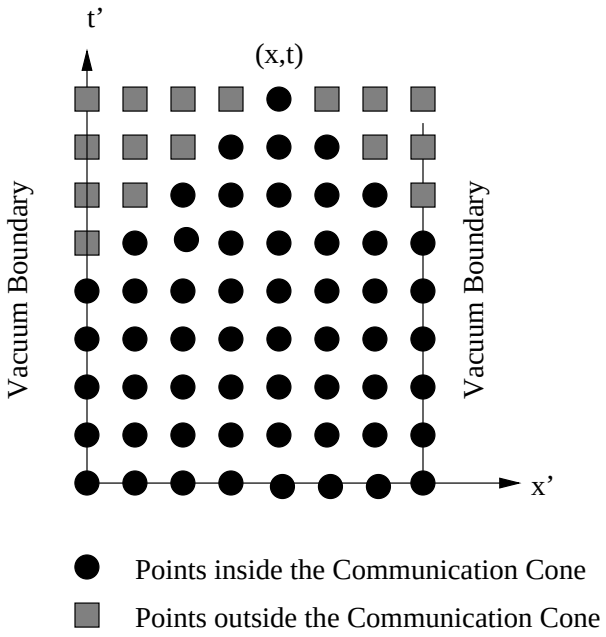

Figure 3.2: Communication in an Finite Medium

of integration is a vertical rectangular parallelepiped topped by an offset rectangular base pyramid. For two-dimensional polar coordinates, the integration region would be a right circular cylinder topped by an offset cone region. Three-dimensional Cartesian regions are characterized by defective spherical integration regions having one or more flat surfaces. Three-dimensional curvilinear coordinates contain defective spherical integration regions with one or more curved surfaces.

The standard approach to solving a Volterra/Fredholm type integral equation is to set up a system of algebraic equations based on the number of quadrature nodes and the composite rules for the solution of multiple integrals. The usual procedure is to solve this system of equations by direct matrix methods. However, as time proceeds the size of the matrix increases and the matrix can become quite large. To avoid this difficulty another approach is taken. Both Volterra and Fredholm integral equations can be solved through the use of successive approximation [62]. Therefore, an iterative scheme is chosen to

solve the 'mixed' Volterra/Fredholm time-dependent integral equation instead of a direct matrix based method. At a given time, t, we iterate the spatial values, x.

In addition to the numerical difficulties posed by the implementation of the causality constraint, the kernels possess a singularity at the temporal point $t = t'$. The singular kernels appearing in the integrals are numerically evaluated by the method of subtraction of singularity [54, 59, 60, 61]. At a given time, t, we iterate the spatial values, x.

The following example illustrates the salient features of the time-dependent integral transport equation, the scalar flux kernels, and the use of the subtraction of singularity method. The time-dependent integral equation, for the scalar flux in general coordinates, is given by Eqn. 3.2. After the substitution of Eqn. 3.3 into Eqn. 3.2, the application of the subtraction of singularity method, and the implementation of the iteration procedure, the following expression with iteration index n is obtained:

$$\begin{aligned}
\Phi^{n+1}(\vec{r},t) &= \Sigma_s \int_0^t dt' \int_{V'} K(\vec{r},\vec{r}',t,t')\{\Phi^n(\vec{r}',t') - \Phi^n(\vec{r},t)\}\, d\vec{r}' \\
&+ \Sigma_s\, \Phi^n(\vec{r},t) \int_0^t dt' \int_{V'} K(\vec{r},\vec{r}',t,t')\, d\vec{r}' \\
&+ \int_0^t dt' \int_{V'} K(\vec{r},\vec{r}',t,t')\, S(\vec{r}',t')\, d\vec{r}' \,. \qquad (3.4)
\end{aligned}$$

The first term now evaluates to zero at the singular point $t^{'} = t$. The first term is the collided component of the scalar flux. When $t^{'} = t$, the Heaviside function only possesses a value when $r = r^{'}$; hence $\Phi^n(\vec{r}',t') = \Phi^n(\vec{r},t)$ and the integrand evaluates to zero.

The third term convolutes the source term with the kernel and represents the uncollided flux distribution in the medium. For simple source function distributions, this term can be evaluated analytically. The second term can either be analytically or numerically integrated. Improved accuracy in the solution of the integral equation is achieved through use of analytical solutions for the second and third terms in Eqn. 3.4. Analytical solutions were derived with the help from the *Mathematica* numerical software package [67]. For example, a finite slab in one-dimensional Cartesian coordinates with width of a and a

uniformly distributed source of strength S_0, the analytical integration of the second and third terms leads to the following expression:

$$\begin{aligned}\Phi^{n+1}(x,t) &= \int_0^t dt' \int_0^a K_{1D,C}(x,x',t,t')\,\Sigma_s\left[\Phi^n(x',t') - \Phi^n(x,t)\right]dx' \\ &+ \frac{S_0 + \Sigma_s\Phi^n(x,t)}{\Sigma}\left(\left[1 - e^{-\Sigma vt}\right]\right. \\ &+ \left[e^{-\Sigma vt} - e^{-\Sigma x} + \Sigma x\left\{E_1\left[\Sigma x\right] - E_1\left[\Sigma vt\right]\right\}\right] H\left[t - \frac{x}{v}\right] \\ &+ \left.\left[e^{-\Sigma vt} - e^{-\Sigma(a-x)} + \Sigma\left(a-x\right)\left\{E_1\left[\Sigma\left(a-x\right)\right] - E_1\left[\Sigma vt\right]\right\}\right] H\left[t - \frac{a-x}{v}\right]\right).\end{aligned} \tag{3.5}$$

As mentioned earlier, the integral equations are solved using an iterative process. This is indicated through the use of the superscripts n in Eqns. 3.4 and 3.6. The scalar flux at any given iteration $(n+1)$ is calculated using the previous iterate for the scalar flux n. To begin the iterative process, a guess for the flux at the current time and position is required, the zeroth iterate $n = 0$. This initial guess can either use the solution from the previous iteration at that point or can obtain a solution by interpolating over the previous values of the scalar flux at the current position. A numerical interpolation scheme which interpolates the scalar flux using up to a 5^{th} order polynomial (six previous points) was implemented to calculate a more accurate guess. In order to calculate the interpolating polynomial, a simple divided difference method was used [66].

The numerical solution was found once the change in the scalar flux from the n^{th} to the $(n+1^{\text{th}})$ iteration is below some predetermined tolerance. Table 3.1 shows the average number of iterations that are required to reduce the change in the scalar flux for several tolerances run with typical one-dimensional Cartesian problems.

The numerical evaluation of Eqn. 3.6 proceeds by subdividing both the spatial and time domains. For simplicity, the geometry of interest is divided into equally spaced subdivisions. Time-steps are chosen such that the monoenergetic particle travels one spatial division during one time step: $\Delta t = \Delta x/v$. The flux at the current time and position is calculated by integrating back over previous values of the flux at all spatial

Table 3.1: Iterations for specific Tolerances

Tolerance	**Iterations**
10^{-2}	2
10^{-4}	4
10^{-6}	7
10^{-8}	9
10^{-10}	11

locations which satisfy the causality constraint. The numerical integration in both the spatial and temporal dimensions is carried out using a 5^{th} order Gregory integration rule whenever possible [62].

In order to use the 5^{th} order Gregory method, a minimum of six initial points are needed. When there are fewer than six points in either the spatial or the temporal direction, a Newton-Cotes integration rule [63, 64] corresponding to the number of available points is used. In the temporal dimension, at the i^{th} time step there are $i + 1$ points. For example, at the first time-step there are two temporal points available and hence the trapezoid integration rule is used. The Romberg extrapolation procedures is employed to obtain benchmark solutions.

3.3 Calculational Results

All the problems analyzed, except for the benchmark problem proposed by Ganapol in Section 3.3.1 and the heterogeneous benchmark, are finite media utilizing the time-dependent, homogeneous kernels displayed in Table 2.1. In Section 3.3.1 the time-dependent integral transport method is compared to a benchmark problem proposed

by B.D. Ganapol [71]. In Sections 3.3.2, 3.3.3, 3.3.4, and 3.3.5 time-dependent benchmark solutions for finite media in one-dimensional Cartesian and spherical geometries are presented. Time-dependent integral calculations are compared to time-dependent diffusion based results in Section 3.4.

In all the homogeneous benchmark solutions, the particles are assumed to have a velocity of 1 cm/s and material properties found in Table 3.2. The only change in the material will be in the scattering cross section. For the infinite media benchmark, the material will be purely scattering $\Sigma_s = 1.0$ cm^{-1}. The finite homogeneous media benchmarks will have a scattering cross section of $\Sigma_s = 0.9$ cm^{-1}.

Table 3.2: Material Properties for Particles in Unit Material

Total Cross Section Σ	1.0 cm^{-1}
Infinite Media Σ_s	1.0 cm^{-1}
Finite Media Σ_s	0.9 cm^{-1}
Isotropic source strength	1.0 n/cm^3-s

For every benchmark case, Romberg integration techniques were used. To begin the process, 20 nodes were distributed uniformly throughout the interior of the problem. The simulation was run and results were obtained. At that point the results were defined as the R(1,1) level for the Romberg integration. The same simulation was run again for each benchmark using twice the number of nodes and thus calculating the $R(2,1), R(3,1), ...R(K,1)$ levels of the Romberg integration scheme until the difference between the k^{th} and the $k+1^{th}$ Romberg integration yielded results with no less than 4 significant figures for all times and spatial positions. This criteria was satisfied in each benchmark case after the 6^{th} level of Romberg integration was computed with 640 spatial

nodes distributed uniformly throughout the interior of the each particular problem.

The benchmark solution was calculated from the R(6,6) level of the Romberg integration technique using the scheme shown in Table 3.3 with the intermediate values calculated using Equation 3.6.

Table 3.3: Romberg Integration

R(1,1)					
R(2,1)	$R(2,2)^{+}$				
R(3,1)	R(3,2)	R(3,3)			
R(4,1)	R(4,2)	R(4,3)	R(4,4)		
$\vdots$	$\vdots$	$\vdots$	$\vdots$	$\ddots$	
R(K,1)	R(K,2)	R(K,3)	R(K,4)	$\cdots$	R(K,K)

$$^{+}R\left(n+1,m+1\right)=R\left(n+1,m\right)+\frac{1}{4^{m}-1}\left[R\left(n+1,m\right)-R\left(n,m\right)\right] \tag{3.6}$$

3.3.1 Infinite Medium Benchmark Comparison

The most active researcher involved in the generation of time-dependent benchmark solutions has been B.D. Ganapol, who in the past has referred to himself as the "4 place theorist" [72]. He has applied the multiple collision method and the so-called reduced collision equations to obtain benchmark solutions to isotropically emitting point, planar and line sources within an infinite medium, to semi-infinite medium problems with mono-directional incoming sources and to multigroup and continuous energy problems for infinite media [71-81].

One of the methods by which the time-dependent integral transport was benchmarked

is against semi-analytical infinite medium results [71]. B.D. Ganapol was able to derive time-dependent semi-analytical results for the scalar flux of particles in semi and infinite media problems. This particular comparison was for a unit source of pulsed particles located at the origin of an infinite medium in one-dimensional planar geometry.

Particles released from the source have a velocity of 1 cm/s. Therefore, a position 'x' cm from the source will only have flux if 'x' seconds have passed for the particles to travel from the source to that position. The medium was purely scattering with a macroscopic interaction cross section of 1.0 cm^{-1}. The pulsed source is defined as:

$$S(x,t) = S_0\,\delta(t)\,\delta(x), \tag{3.7}$$

where $S_0 = 1$. This is a difficult problem to solve as the source is singular emitting neutrons only at $t = 0$ from the origin at $x = 0$.

Insertion of this source distribution into the general time-dependent integral equation, application of the one-dimensional Cartesian coordinate kernel, and analytical evaluation of the source component gives:

$$\begin{aligned}\Phi(x,t) &= \Sigma_s \int_0^t dt' \int_{-\infty}^{\infty} \frac{e^{-\Sigma\, v(t-t')}}{2(t-t')}\, H\left(t - t' - \frac{|x-x'|}{v}\right) \Phi(x',t')\, dx' \\ &\quad + S_0\, \frac{e^{-\Sigma v t}}{2\,t}\, H\left(t - \frac{|x|}{v}\right).\end{aligned} \tag{3.8}$$

The forcing function for the integral equation represents the uncollided flux distribution and the singularity at $t = 0$ is inherited from the original source function. Attempts to solve this equation proved unsatisfactory due to the singularity at $t = 0$. Since the uncollided flux is infinite at $t = 0$, the integration around this point must be performed with high precision to obtain accurate results at later times. To circumvent this problem, the following functional form for $\Phi(x,t)$ is introduced into Eqn. 3.9:

$$\Phi(x,t) = \Psi(x,t)\,\frac{e^{-\Sigma v t}}{t}\,. \tag{3.9}$$

Substitution of this relation into Eqn. 3.9 leads to the following integral equation for $\Psi(x,t)$:

$$\Psi(x,t) = \Sigma_s \int_0^t dt' \int_{-\infty}^{\infty} \frac{\Psi(x',t')t}{2(t-t')\,t'} H\left(t - t' - \frac{|x-x'|}{v}\right) dx' + \frac{S_0}{2} H\left(t - \frac{|x|}{v}\right) . \quad (3.10)$$

The singularities in the integrand at $t' = 0$ and $t' = t$ are handled with the method of subtraction of singularity as mentioned in Section 3.2.

Table 3.4, 3.5, and 3.6 show Ganapol's results [71] compared to the results calculated using the time-dependent integral method. The results are in excellent agreement. The two methods agree to four significant figures throughout the entire simulation. In addition only at four points, as indicated with underscores in the table, do the two methods differ at the 5^{th} significant figure. This comparison shows that highly accurate solutions can be obtained using the time-dependent integral formulation.

Although Table 3.4, Table 3.5 and Table 3.6 show the direct comparisons to Ganapol's analytical method. All the times and positions from $t = 0$ $x = 0$ to $t = 45$ and $x = 45$ were calculated using the numerical method. Ganapol, only published the analytical results for specific times and positions; however, a more complete table of the flux for this particular problem is presented in Appendix C.

Table 3.4: Error Analysis for Integral Method vs. Ganapol's Results - Early Times

Time	x	**Flux Ganapol**	**Flux Integral**
1	1	1.8394E-01	1.8394E-01
1	2	0.0000E+00	0.0000E+00
1	3	0.0000E+00	0.0000E+00
1	4	0.0000E+00	0.0000E+00
1	5	0.0000E+00	0.0000E+00
1	6	0.0000E+00	0.0000E+00
3	1	2.3942E-01	2.3942E-01
3	2	9.3836E-02	9.3835E-02
3	3	8.2978E-03	8.2978E-03
3	4	0.0000E+00	0.0000E+00
3	5	0.0000E+00	0.0000E+00
3	6	0.0000E+00	0.0000E+00
5	1	1.9957E-01	1.9957E-01
5	2	1.2105E-01	1.2105E-01
5	3	4.9595E-02	4.9595E-02
5	4	1.1823E-02	1.1823E-02
5	5	6.7379E-04	6.7379E-04
5	6	0.0000E+00	0.0000E+00

Table 3.5: Error Analysis for Integral Method vs. Ganapol's Results - Middle Times Times

Time	x	**Flux Ganapol**	**Flux Integral**
7	1	1.7347E-01	1.7347E-01
7	2	1.2293E-01	1.2293E-01
7	3	6.8028E-02	6.8028E-02
7	4	2.8447E-02	2.8447E-02
7	5	8.4158E-03	8.4157E-03
7	6	1.5036E-03	1.5036E-03
9	1	1.5528E-01	1.5528E-01
9	2	1.1935E-01	1.1935E-01
9	3	7.6384E-02	7.6384E-02
9	4	4.0186E-02	4.0186E-02
9	5	1.7004E-02	1.7004E-02
9	6	5.5765E-03	5.5764E-03
15	1	1.2269E-01	1.2269E-01
15	2	1.0514E-01	1.0514E-01
15	3	8.1158E-02	8.1159E-02
15	4	5.6305E-02	5.6305E-02
15	5	3.4985E-02	3.4985E-02
15	6	1.9376E-02	1.9376E-02

Table 3.6: Error Analysis for Integral Method vs. Ganapol's Results - Late Times

Time	x	**Flux Ganapol**	**Flux Integral**
25	1	9.6128E-02	9.6128E-02
25	2	8.7720E-02	8.7720E-02
25	3	7.5287E-02	7.5287E-02
25	4	6.0744E-02	6.0744E-02
25	5	4.6042E-02	4.6042E-02
25	6	3.2757E-02	3.2757E-02
35	1	8.1632E-02	8.1632E-02
35	2	7.6491E-02	7.6491E-02
35	3	6.8624E-02	6.8624E-02
35	4	5.8937E-02	5.8937E-02
35	5	4.8445E-02	4.8445E-02
35	6	3.8099E-02	3.8099E-02
45	1	7.2182E-02	7.2182E-02
45	2	6.8630E-02	6.8630E-02
45	3	6.3091E-02	6.3091E-02
45	4	5.6074E-02	5.6074E-02
45	5	4.8177E-02	4.8177E-02
45	6	4.0007E-02	4.0007E-02

3.3.2 Benchmark 1: One-Dimensional Cartesian with Uniform Source

The time-dependent integral transport method produced highly accurate results; therefore, finite media benchmarks were calculated with a degree of confidence. The first of the four benchmarks presented in this chapter was of a uniformly distributed source embedded in a one-dimensional slab. The infinite medium problem simulated the effect of an outgoing wavefront. This problem showed the time-dependent effects that vacuum boundaries have on finite media problems.

Figure 3.3 shows the geometry of the problem. The media for all the homogeneous benchmarks has a scattering cross section of $\Sigma_s = 0.9\ \mathrm{cm}^{-1}$. The other material properties are found in Table 3.2. The slab is 10 mean free paths (mfp) thick. There are no particles within the slab at $t = 0^-$ and the source is turned on at $t = 0^+$. The source remains at a constant strength level of 1.0 n/cm^3-s throughout the entire simulation. Particles released from the source have a velocity of 1 cm/s. For this simple source distribution, the uncollided flux is computed analytically. The integral equation which is numerically solved along with the analytical expressions for the uncollided flux and the integration of the singularity is presented in Equation B.5 of Appendix B.

The results shown in Table 3.7 are qualitative values for the particle flux at discrete points in the slab after: 1.0, 2.5, 5.0, and 10 mean free times (mft) respectively. At these particular times the particles have had enough time to travel exactly 1/10, 1/4, 1/2, 3/4 of the way, and completely across the slab.

Figure 3.4 shows a graphical output for the scalar flux. The scalar flux increases in magnitude for each succeeding step as expected during the early stages of the simulation. Each curve represents an increment of 1/2 of a mean free time (mft), or the amount of time that it takes for particles to travel 1/2 of a mean free path length (mfp).

At the beginning of the simulation the particle flux within the interior of the slab is

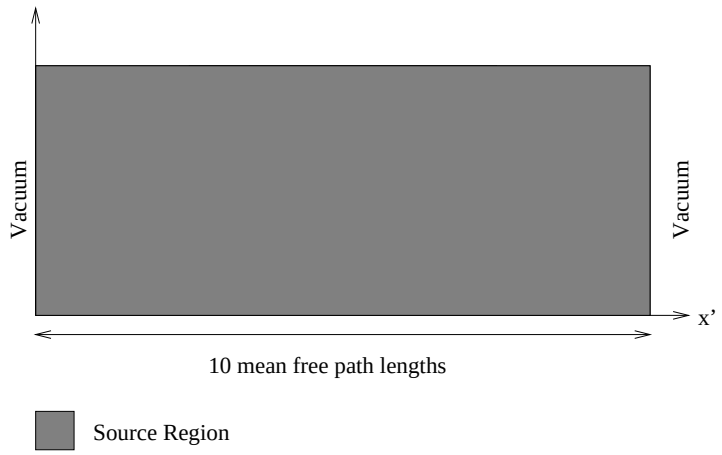

Figure 3.3: Geometry for Uniform Source in 10 mfp Slab

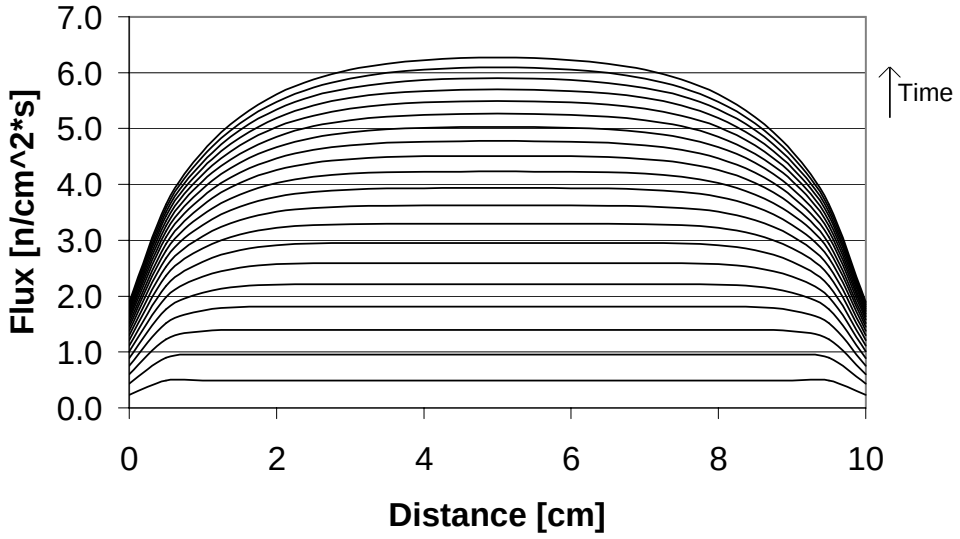

Figure 3.4: Time-Dependent Flux for Uniform Source in 10 mfp Thick Slab

flat. Particles in the interior of the slab require a finite amount of time to communicate with the vacuum boundaries. Initially, these interior points have not felt the leakage depletion wave, which is launched from the boundaries at $t = 0^+$, and therefore behave as though they were in an infinite medium.

These interior points, which have not communicated with the vacuum boundaries, can be benchmarked against the analytical time-dependent infinite medium solution for the scalar flux. The analytical infinite medium time-dependent solution is:

$$\Phi(x,t) = \frac{S_0}{\Sigma_a}\left(1 - e^{-\Sigma_a v t}\right). \tag{3.11}$$

The numerical solution for the points in the interior of the slab differ by no more than $1.44 \times 10^{-7}\%$ from the analytical results presented in Eqn. 3.11. This maximum error occurs at the first time-step of the simulation. This behavior is expected, for as mentioned earlier, the lack of integration nodes in the time domain at early times necessitates the use of lower order integration rules.

As the simulation proceeds, higher order integration rules are used. As a result, by the 10^{th} time step the error has decreased to $2.65 \times 10^{-8}\%$. Eventually enough time passes for particles born in the interior to travel to the edges and escape.

An important check is whether or not the time-dependent results converge to the correct steady-state values. After an extended period of time and with the condition that the source distribution remained at a constant level, the simulation converged to a steady-state flux distribution. The time-dependent kernels converge to their corresponding steady-state functional forms as $t \to \infty$ [56], however this type of calculation showed how well the code converged to the correct steady-state result.

The time-dependent code with twenty spatial nodes, was allowed to run until a converged steady-state result was achieved. The flux was deemed to converged once the maximum change in consecutive time-steps (i^{th} to the $(i+1)^{th}$) was less than $10^{-8}\%$

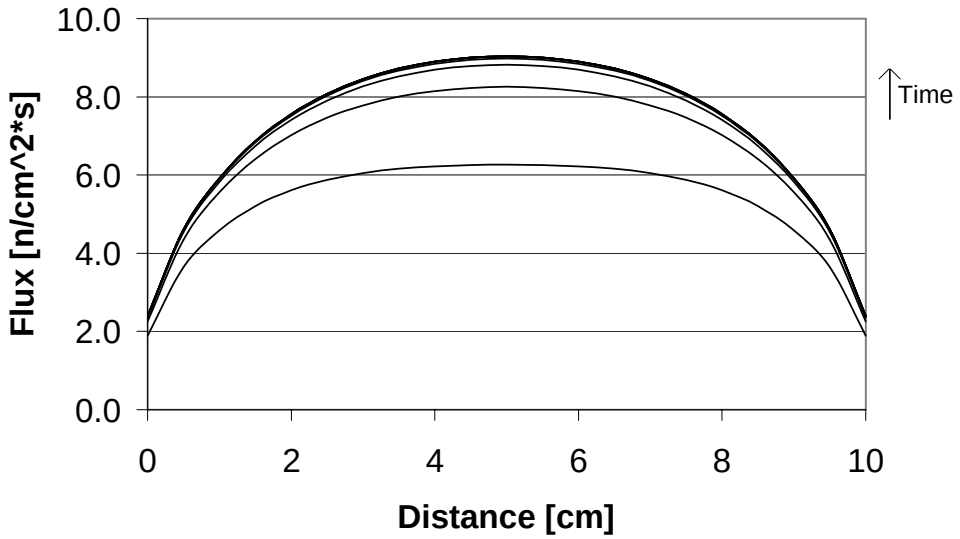

Figure 3.5: Converged Time-Dependent Results for Uniform Source in Slab

for any given spatial node. The convergence criteria was satisfied after 100 mft. The converged result, with 20 nodes distributed in the interior of the slab, was used as the R(1,1) level for the Romberg integration. The number of nodes for the problem was then doubled, until the R(6,1) level of the Romberg integration was completed. At this point, the final results, or the R(6,6) level of the Romberg integration, was calculated using the techniques discussed earlier.

The converged time-dependent calculation was compared to a steady-state result computed using identical source, material conditions, and using the same six level Romberg integration convergence techniques. Figure 3.5 shows the convergence of the time-dependent scalar flux to a steady state result. The figure shows 10 curves with each curve representing 10 mft. The derivation of the steady-state results for the benchmark problems are presented in Appendix D. Each curve corresponds to 10 mft. This corresponds to the amount of time that is necessary for particles to travel completely across the slab.

Table 3.8 shows data from the first benchmark case for 20, 50, 70, and 100 mft. From

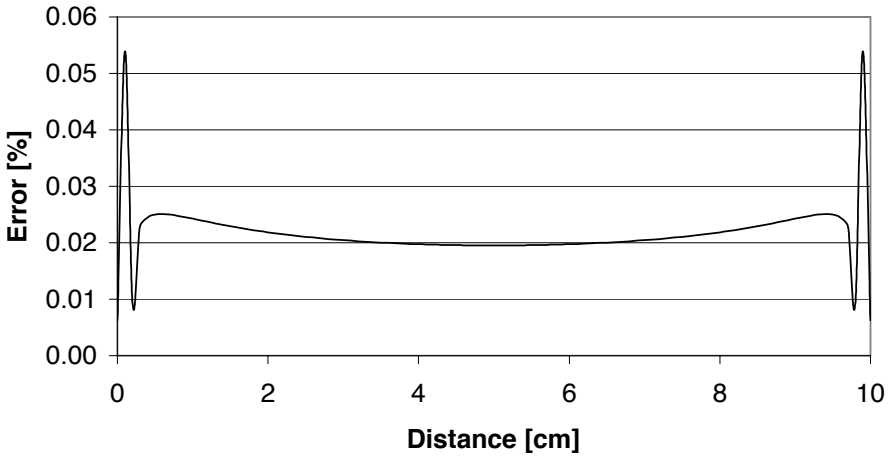

Figure 3.6: Relative Error between the Converged Time-Dependent Calculations and the Steady-State Results

this data it is apparent that the results are converging to a steady-state result.

The relative error between the converged time-dependent calculation and the converged steady-state results are shown in Figure 3.6. The maximum error occurs near the vacuum boundary. The integration is divided up into leftward and rightward traveling particles. Therefore, at one node in from the boundary there are only two integration nodes to calculate the particles that are traveling away from the boundary and a low order trapezoidal scheme is used. However, it should be noticed that the maximum error between the two results is only a miniscule 0.05% and the results are in excellent agreement with each other.

Table 3.7: Benchmark Solutions for Uniform Source in 10 mfp Slab at Early Times

x [cm]	1.0 mft	2.5 mft	5.0 mft	7.5 mft	10.0 mft
0.0	0.430	0.889	1.378	1.684	1.889
0.5	0.898	1.762	2.676	3.255	3.644
1.0	0.952	2.061	3.271	4.054	4.586
1.5	0.952	2.174	3.600	4.548	5.202
2.0	0.952	2.207	3.777	4.855	5.611
2.5	0.952	2.212	3.867	5.041	5.880
3.0	0.952	2.212	3.909	5.151	6.053
3.5	0.952	2.212	3.926	5.213	6.161
4.0	0.952	2.212	3.932	5.245	6.226
4.5	0.952	2.212	3.934	5.261	6.259
5.0	0.952	2.212	3.934	5.265	6.269
5.5	0.952	2.212	3.934	5.261	6.259
6.0	0.952	2.212	3.932	5.245	6.226
6.5	0.952	2.212	3.926	5.213	6.161
7.0	0.952	2.212	3.909	5.151	6.053
7.5	0.952	2.212	3.867	5.041	5.880
8.0	0.952	2.207	3.777	4.855	5.611
8.5	0.952	2.174	3.600	4.548	5.202
9.0	0.952	2.061	3.271	4.054	4.586
9.5	0.898	1.762	2.676	3.255	3.644
10.0	0.430	0.889	1.378	1.684	1.889

Table 3.8: Benchmark Solutions for Uniform Source in 10 mfp Slab at Late Times

x [cm]	20 mft	50 mft	70 mft	100 mft
0.0	2.253	2.386	2.389	2.389
0.5	4.343	4.599	4.604	4.605
1.0	5.551	5.907	5.914	5.915
1.5	6.404	6.850	6.859	6.860
2.0	7.020	7.547	7.557	7.558
2.5	7.465	8.063	8.075	8.076
3.0	7.783	8.440	8.454	8.455
3.5	8.004	8.709	8.723	8.724
4.0	8.149	8.887	8.903	8.904
4.5	8.230	8.990	9.005	9.007
5.0	8.256	9.023	9.039	9.040
5.5	8.230	8.990	9.005	9.007
6.0	8.149	8.887	8.903	8.904
6.5	8.004	8.709	8.723	8.724
7.0	7.783	8.440	8.454	8.455
7.5	7.465	8.063	8.075	8.076
8.0	7.020	7.547	7.557	7.558
8.5	6.404	6.850	6.859	6.860
9.0	5.551	5.907	5.914	5.915
9.5	4.343	4.599	4.604	4.605
10.0	2.253	2.386	2.389	2.389

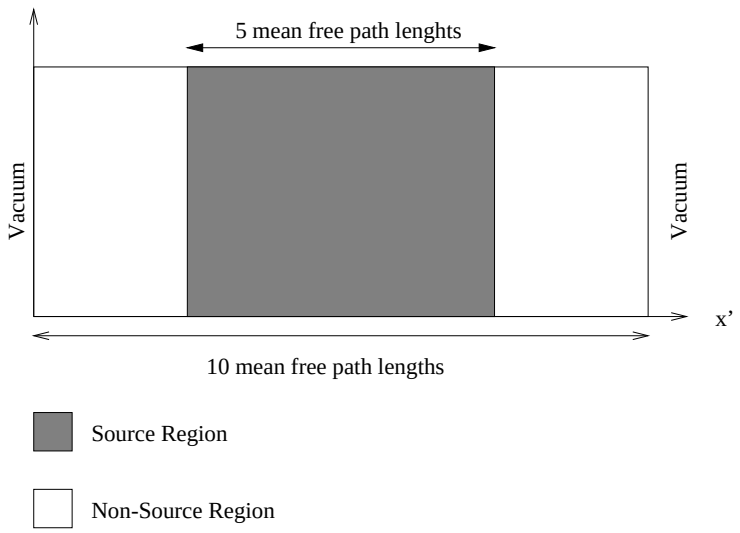

Figure 3.7: Geometry for Localized Source in 10 mfp Thick Slab

3.3.3 Benchmark 2: One-Dimensional Cartesian with Localized Source

The second benchmark case is very similar to that presented in Section 3.3.2. The only difference between the two is that this case has a localized source distributed in the center one-half (or inner 5 mfp) of the slab. The source strength remains 1.0 n/cm^3-s throughout the entire simulation. The integral equation, which is numerically solved along with the analytical expressions for the uncollided flux and the integration of the singularity, is presented in Equation B.6 of Appendix B.

The geometry of the problem is shown in Figure 3.7. The material properties are given in Table 3.2. Vacuum boundary conditions exist on either side of the slab. There are no particles within the slab at $t = 0^-$ and the source is turned on at $t = 0^+$. The source stays on and remains at a constant level throughout the simulation.

The results shown in Table 3.9 are qualitative values for the particle flux at discrete points in the slab after: 1.0, 2.5, 5.0, 7.5, and 10.0 mean free times. At these particular times the particles have had enough time to travel: 1/10, 1/4, 1/2, 3/4 of the way, and completely across the slab.

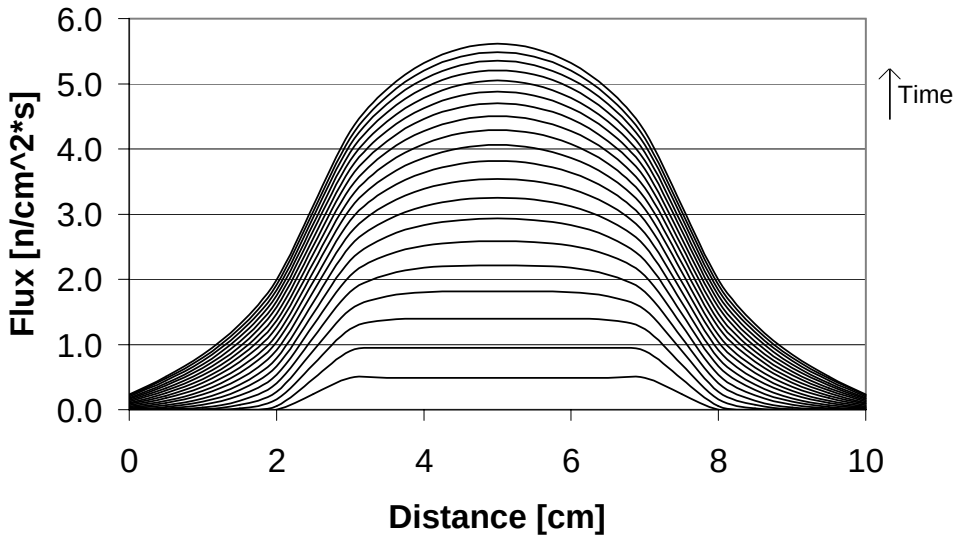

Figure 3.8: Time-Dependent Flux for Particles with Localized Source

Table 3.9 shows that at early times there is zero particle flux in the outer portions of the slab. This shows the built in causality of the time-dependent kernels. There physically has not been enough time for particles born in the central source region to travel into the outer non-source portions of the slab. As a result, the particle flux is zero until later times when particles can physically reach those areas.

For reasons mentioned in Section 3.3.2, at early times particles in the interior of the slab have not felt the leakage effects from either the vacuum boundary nor the effects from the source/non-source boundary. Therefore, initially these interior points behave as though they are in an infinite medium. However, as time progresses, these interior points feel the edge effects first from the source/non-source boundary, because of its proximity to these inner points, and eventually from the vacuum boundary.

Figure 3.8 shows a graphical output for the scalar flux. Each curve represents an increment of 1/2 mft, or the amount of time that it takes for particles to travel 1/2 of a mfp. As expected, the particle flux builds up and is greatest in the central source region and decreases in the non-source region as particles are lost either through absorption or

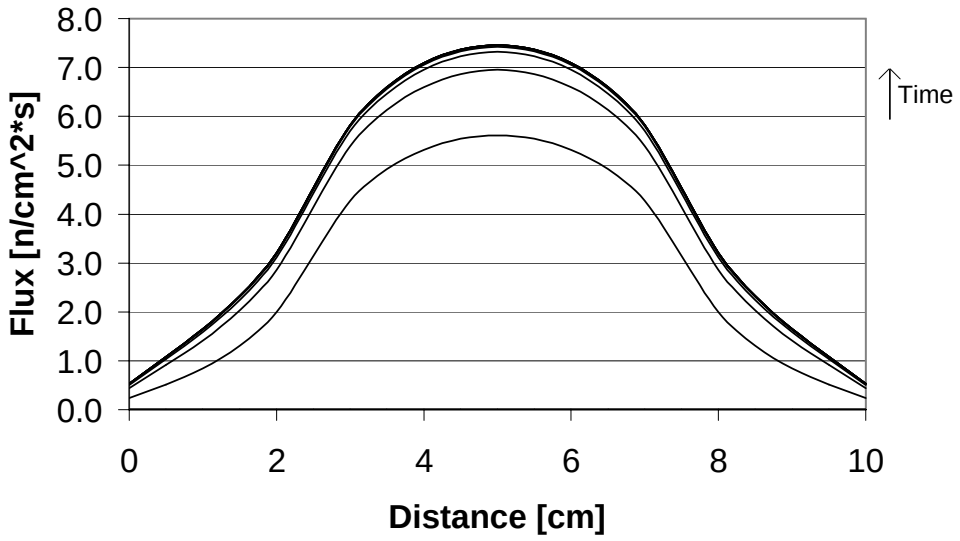

Figure 3.9: Converged Time-Dependent Results for Localized Source

leakage from the boundary.

Upon closer examination of Figure 3.8, one notices slight "bumps" on either side of the source region. These "bumps" are artifacts from the graphics program used to plot the data. The curves are actually polynomial fits of the finite data points used in the calculation. The interpolation polynomial tends to experience a Gibbs effect near boundaries where the scalar flux under goes a large change. Thus, in reality, instead of a "bump" there should be a straight line throughout the center of the source region for those two curves at early times.

The time-dependent code was run until a converged steady-state result was achieved and then compared to a steady-state result computed using identical source and material conditions. The convergence criteria was identical to that presented in Section 3.3.2. Figure 3.9 shows the convergence of the time-dependent scalar flux to a steady state result. Each curve corresponds to an increment of 10 mft. The flux builds up until a steady level is attained.

Table 3.10 shows data from the second benchmark case for 20, 50, 70, and 100 mft.

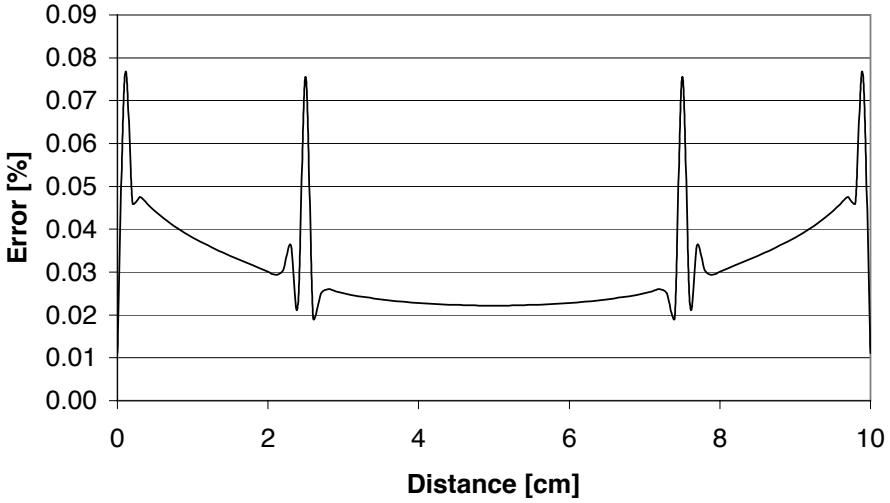

Figure 3.10: Relative Error between the Converged Time-Dependent Calculations and the Steady-State results

From this data it is apparent that the results are converging to a steady-state result.

The relative error between the converged time-dependent calculation and the converged steady-state results are shown in Figure 3.10. The maximum error for the localized source in Cartesian coordinates occurs at the vacuum boundary and the boundary between the source and non-source region. As mentioned earlier, these maximum errors are the result of the quadrature set and how the integration is performed. The maximum error was relatively small peaking at 0.075%. This shows that the converged time-dependent and steady-state results are in excellent agreement.

Table 3.9: Benchmark Solutions for Localized Source in 10 mfp Slab at Early Times

x [cm]	1.0 mft	2.5 mft	5.0 mft	7.5 mft	10.0 mft
0.0	0.000	0.000	0.051	0.144	0.235
0.5	0.000	0.005	0.138	0.333	0.511
1.0	0.000	0.036	0.290	0.586	0.845
1.5	0.000	0.140	0.562	0.972	1.313
2.0	0.052	0.405	1.035	1.571	1.993
2.5	0.476	1.106	1.968	2.634	3.137
3.0	0.899	1.807	2.900	3.692	4.270
3.5	0.952	2.071	3.371	4.275	4.917
4.0	0.952	2.175	3.636	4.628	5.320
4.5	0.952	2.207	3.771	4.819	5.542
5.0	0.952	2.212	3.812	4.880	5.613
5.5	0.952	2.207	3.771	4.819	5.542
6.0	0.952	2.175	3.636	4.628	5.320
6.5	0.952	2.071	3.371	4.275	4.917
7.0	0.899	1.807	2.900	3.692	4.270
7.5	0.476	1.106	1.968	2.634	3.137
8.0	0.052	0.405	1.035	1.571	1.993
8.5	0.000	0.140	0.562	0.972	1.313
9.0	0.000	0.036	0.290	0.586	0.845
9.5	0.000	0.005	0.138	0.333	0.511
10.0	0.000	0.000	0.051	0.144	0.235

Table 3.10: Benchmark Solutions for Localized Source in 10 mfp Slab at Late Times

x [cm]	20 mft	50 mft	70 mft	100 mft
0.0	0.443	0.528	0.530	0.530
0.5	0.917	1.081	1.085	1.085
1.0	1.415	1.644	1.649	1.649
1.5	2.038	2.325	2.331	2.332
2.0	2.863	3.204	3.211	3.212
2.5	4.139	4.525	4.533	4.534
3.0	5.386	5.812	5.821	5.821
3.5	6.128	6.585	6.594	6.595
4.0	6.601	7.081	7.091	7.092
4.5	6.867	7.360	7.371	7.371
5.0	6.953	7.451	7.461	7.462
5.5	6.867	7.360	7.371	7.371
6.0	6.601	7.081	7.091	7.092
6.5	6.128	6.585	6.594	6.595
7.0	5.386	5.812	5.821	5.821
7.5	4.139	4.525	4.533	4.534
8.0	2.863	3.204	3.211	3.212
8.5	2.038	2.325	2.331	2.332
9.0	1.415	1.644	1.649	1.649
9.5	0.917	1.081	1.085	1.085
10.0	0.443	0.528	0.530	0.530

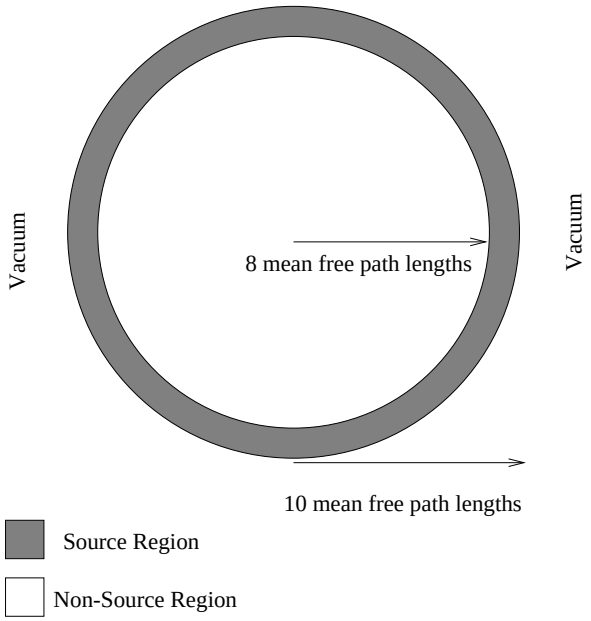

Figure 3.11: Geometry for Localized Source in 10 mfp Sphere

3.3.4 Benchmark 3: One-Dimensional Sphere with Localized Source

The third benchmark problem is a calculation of a one-dimensional homogeneous sphere with a localized source distributed in the outer 2 cm of the sphere. The source strength remains 1.0 n/cm^3-s throughout the entire simulation. The integral equation, which is numerically solved, along with the analytical expressions for the uncollided flux and the integration of the singularity is presented in Equation B.7 of Appendix B.

The geometry of the problem is shown in Figure 3.11. A vacuum boundary surrounds the sphere. There are no particles within the sphere at $t = 0^-$ and the source is turned on at $t = 0^+$. The source stays on and remains at a constant level throughout the simulation.

As with the previous benchmarks, this problem was run using Romberg Integration techniques and convergence criteria presented in Section 3.3.2.

The results shown in Table 3.11 are qualitative values for the particle flux at discrete

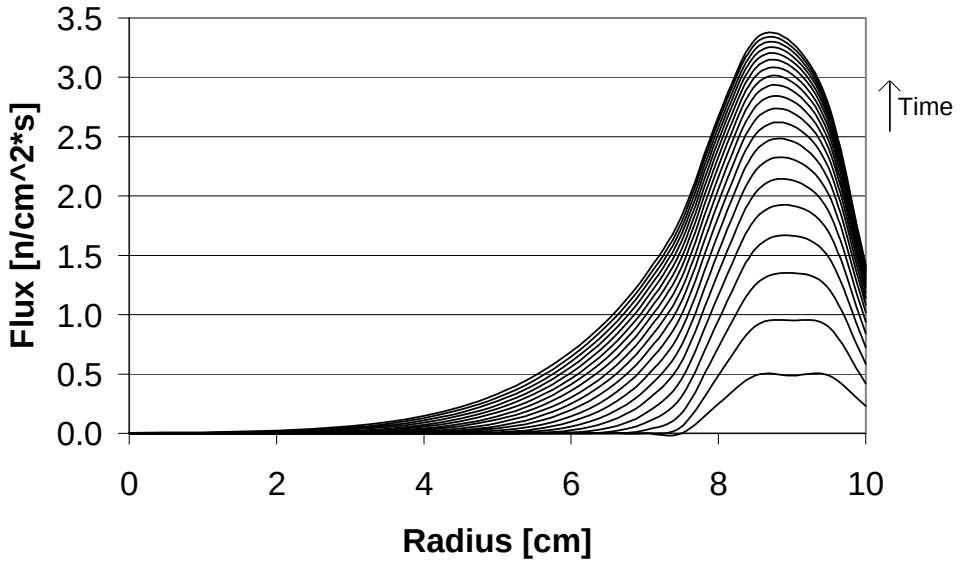

Figure 3.12: Time-Dependent Flux for Particles in Localized Source Sphere

points in the sphere after: 1.0, 2.5, 5.0, 7.5, and 10.0 mean free times respectively. At these particular times the particles have had enough time to travel 1/10, 1/4, 1/2, 3/4 of the way, and finally completely across the sphere.

The results given in Table 3.11 show that it takes a finite amount of time for particles to travel from the outer source region into the inner non-source region. Points in the interior are not populated with particles at early times because they are too distant at that particular time to feel the influence of the outer source region.

Figure 3.12 shows the build up of the scalar flux over time. Every line of output represents an increment of 1/2 mft. As expected, the particle flux is greatest in the outer source region and decreases in the non-source region as particles are lost either through absorption or leakage from the boundary conditions.

The slight "dip" that appears in Figure 3.12 on either side of the source region at early times, is caused because of the polynomial fit that the graphical routine uses to fit the data points. All the data points across the source region have identical values, until the depletion wave from the source/non-source or vacuum boundary arrives.

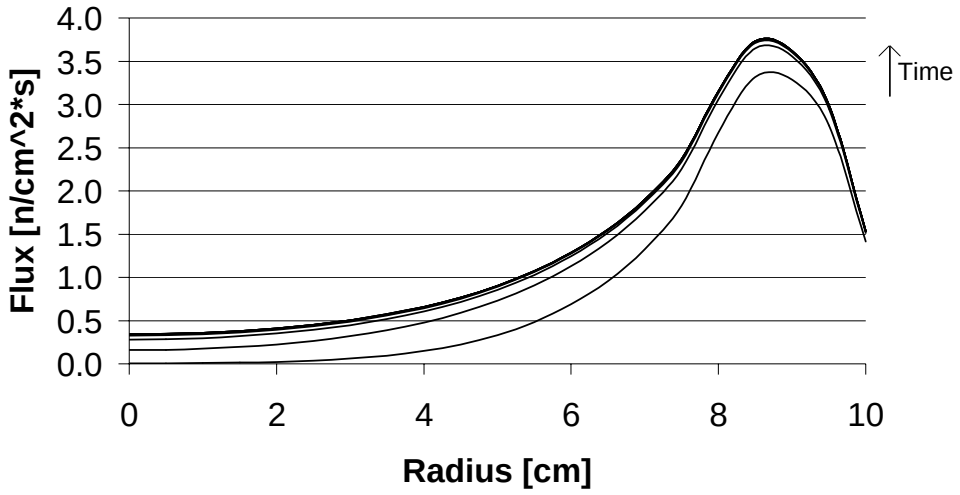

Figure 3.13: Converged Time-Dependent Results for Localized Source in Sphere

The time-dependent code was run until a converged steady state result was achieved. The convergence criteria was identical that that presented in Section 3.3.2. The converged time-dependent calculation was compared to a steady state result computed using identical source and material conditions. As for the previous cases, Figure 3.13 shows the convergence of the time-dependent scalar flux to a steady state result. Each line of output corresponds to 10 mean free times.

Table 3.12 shows data from the third benchmark case for 20, 50, 70, and 100 mft. The data clearly shows that the problem is converging towards a steady-state solution.

The relative error between the converged time-dependent calculation and the converged steady-state results are shown in Figure 3.14. The two areas of highest error are at the vacuum boundary and the source/non-source interface region. Again, the higher errors at these two locations are a result of the quadrature set used to integrate across the source region. In the portions of the slab, be that in the source or non-source regions, that are away from these discontinuities the error is only a fraction of the peaks. The maximum error is only 0.12%.

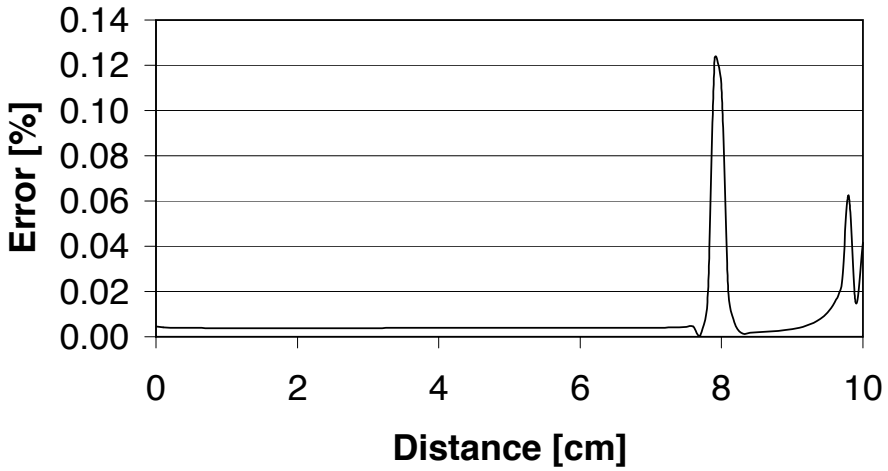

Figure 3.14: Relative Error between the Converged Time-Dependent Calculations and the Steady-State results for a Localized Source in Spherical Coordinates

Table 3.11: Benchmark Solutions for Localized Source in 10 mfp Sphere at Early Times

x [cm]	1.0 mft	2.5 mft	5.0 mft	7.5 mft	10.0 mft
0.0	0.000	0.000	0.000	0.000	0.005
0.5	0.000	0.000	0.000	0.000	0.006
1.0	0.000	0.000	0.000	0.000	0.008
1.5	0.000	0.000	0.000	0.001	0.014
2.0	0.000	0.000	0.000	0.002	0.022
2.5	0.000	0.000	0.000	0.006	0.037
3.0	0.000	0.000	0.000	0.013	0.060
3.5	0.000	0.000	0.001	0.028	0.095
4.0	0.000	0.000	0.004	0.056	0.148
4.5	0.000	0.000	0.014	0.102	0.225
5.0	0.000	0.000	0.040	0.176	0.333
5.5	0.000	0.000	0.094	0.291	0.483
6.0	0.000	0.007	0.196	0.461	0.686
6.5	0.000	0.046	0.373	0.707	0.960
7.0	0.000	0.167	0.660	1.055	1.327
7.5	0.057	0.456	1.113	1.552	1.830
8.0	0.489	1.164	1.948	2.401	2.671
8.5	0.903	1.805	2.639	3.074	3.319
9.0	0.952	1.920	2.705	3.084	3.288
9.5	0.894	1.691	2.320	2.608	2.759
10.0	0.420	0.842	1.186	1.339	1.417

Table 3.12: Benchmark Solutions for Localized Source in 10 mfp Sphere at Late Times

x [cm]	20 mft	50 mft	70 mft	100 mft
0.0	0.159	0.339	0.343	0.344
0.5	0.162	0.342	0.347	0.347
1.0	0.174	0.354	0.359	0.359
1.5	0.194	0.375	0.379	0.380
2.0	0.224	0.405	0.409	0.410
2.5	0.265	0.446	0.450	0.451
3.0	0.319	0.500	0.504	0.504
3.5	0.389	0.568	0.572	0.572
4.0	0.478	0.655	0.658	0.659
4.5	0.590	0.763	0.766	0.767
5.0	0.731	0.899	0.902	0.902
5.5	0.908	1.068	1.071	1.071
6.0	1.130	1.281	1.284	1.284
6.5	1.411	1.551	1.553	1.553
7.0	1.771	1.898	1.900	1.900
7.5	2.251	2.364	2.366	2.366
8.0	3.055	3.151	3.152	3.153
8.5	3.650	3.729	3.730	3.730
9.0	3.554	3.615	3.616	3.616
9.5	2.949	2.991	2.992	2.992
10.0	1.514	1.535	1.536	1.536

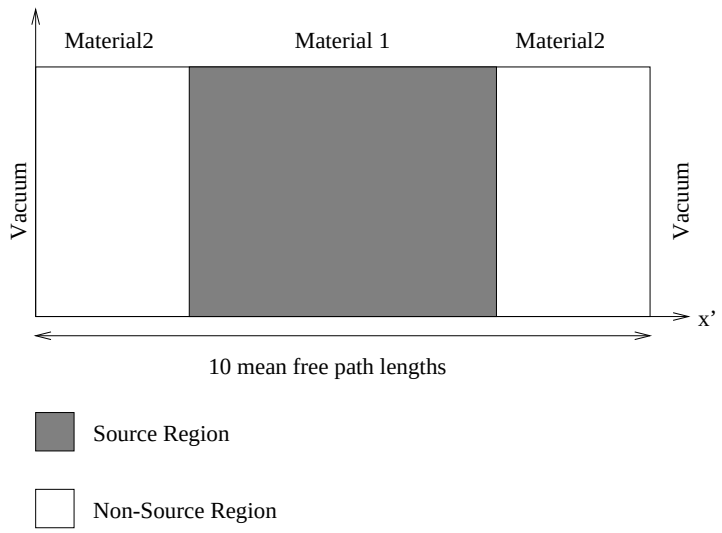

Figure 3.15: Geometry for Localized Source in 10 mfp Slab

3.3.5 Benchmark 4: Heterogeneous Cartesian Benchmark

The final benchmark problem is a simulation of a one-dimensional heterogeneous slab with a localized source confined in the inner 1/2 of the slab, or totally within the central material. Figure 3.15 shows the geometry for this problem. A vacuum boundary surrounds the slab on either side. There are no particles within the heterogeneous slab at $t = 0^-$ and the source is turned on at $t = 0^+$. The source strength remains 1.0 n/cm^3-s throughout the entire simulation. The integral equation, which is numerically solved along with the analytical expressions for the uncollided flux and the integration of the singularity, is presented in Equation B.12 of Appendix B. The one-dimensional geometry, as described in Figure 3.15, was run using Romberg Integration techniques and convergence criteria presented in Section 3.3.2. The slab is heterogeneous with two differing types of materials. The material properties for both regions are given in Table 3.13

The results shown in Table 3.14 are qualitative values for the particle flux at discrete points in the slab after: 1.0, 2.5, 5.0, 7.5, and 10.0 mean free times respectively. At these particular times the particles have had enough time to travel 1/10, 1/4, 1/2, 3/4 of the

Table 3.13: Material Properties for Particles in Heterogeneous Benchmark

	Material 1	Material 2
Σ	2.0 cm^{-1}	1.0 cm^{-1}
Σ_s	1.5 cm^{-1}	0.9 cm^{-1}
S_o	1.0 n/cm^3-s	0 n/cm^3-s

way, and finally completely across the slab.

The results given in Table 3.14 show that it takes a finite amount of time for particles to travel from the inner source region into the outer non-source region. Points in the interior of the slab which have no values for the scalar flux at early times, are locations that are too distant at that particular time to feel the influence of the outer source region.

Figure 3.16 shows the build up of the scalar flux over time. Every curve represents an increment of 1/2 mft. As expected, the particle flux is greatest in the inner source region and decreases in the non-source region as particles are lost either through absorption or leakage from the boundary. As mentioned in the previous section, the small "bumps" that appear on either side of the source region at early times are artifacts from the interpolating polynomial used to plot the data.

A point of difference between this benchmark problem and that presented for the localized problem in a homogeneous material, is the rate at which they reach a steady-state solution. Because this problem has a material in the center with a higher total cross section, fewer particles are able to communicate directly across the central source region. Therefore, particles that travel long distances across the slab are not as important when calculating the scalar flux. Thus the heterogeneous case, for the material conditions given, reaches a steady-state solution faster than the homogeneous localized case. If

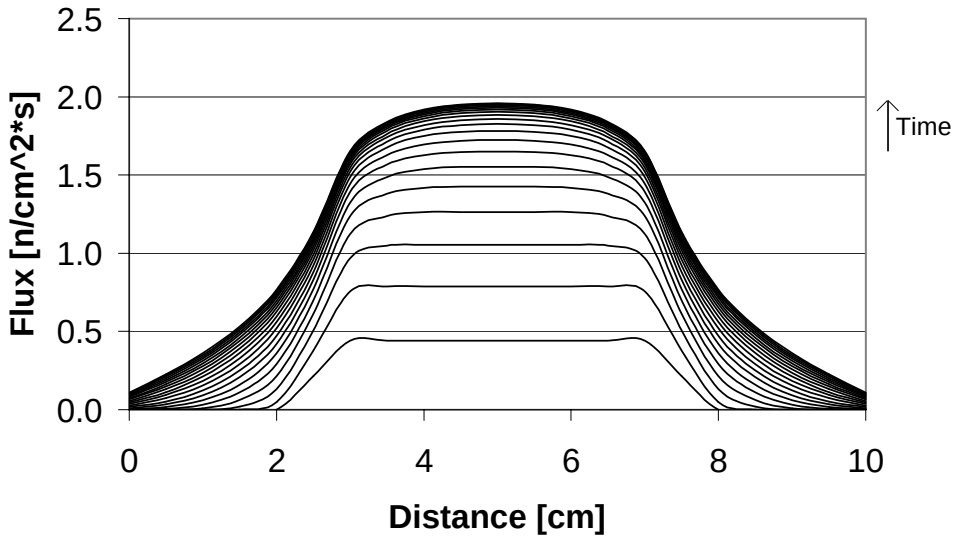

Figure 3.16: Time-Dependent Flux for Particles in Heterogeneous Slab

the central material was composed of a material with a smaller total cross section, the heterogeneous case would take longer to reach a steady-state solution.

The time-dependent code was run until a converged steady-state result was achieved, and the convergence criteria was identical to that presented in Section 3.3. The converged time-dependent calculation was compared to a steady-state result computed using identical source and material conditions. Figure 3.17 shows the convergence of the time-dependent scalar flux to a steady-state result. Each curve corresponds to 10 mean free times. There are 10 curves shown on Figure 3.17, corresponding to 100 mft, however because the solution reaches a steady-state solution very quickly only two of these curves are evident.

Table 3.15 shows data from the fourth benchmark case for 20, 50, 70, and 100 mft. As mentioned previously, the heterogeneous case reaches a steady-state solution much more quickly than the previous cases.

Figure 3.18 shows the percent error between the converged time-dependent results to the Romberg integrated steady-state results. The error for this particular case is

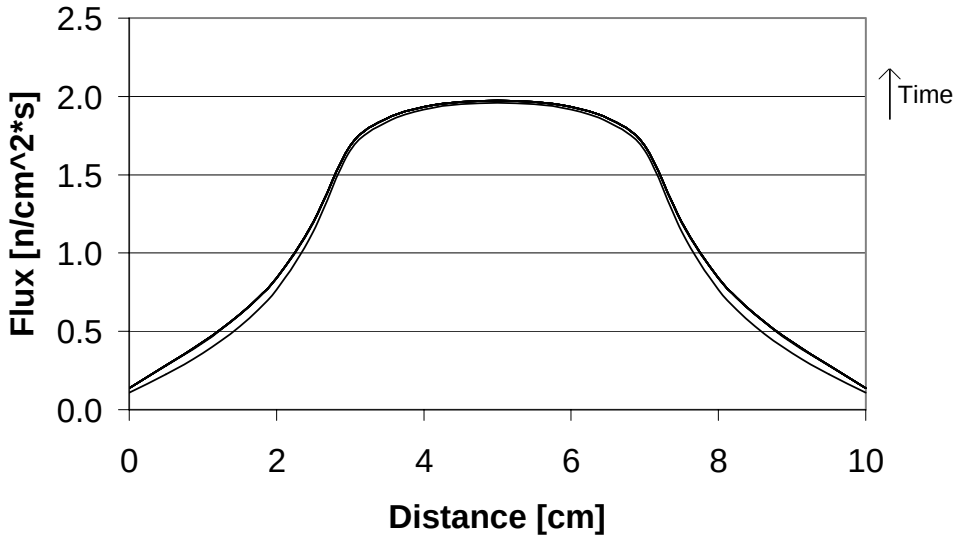

Figure 3.17: Converged Time-Dependent Results for Heterogeneous Slab

greater than that presented for the earlier benchmark case. This error can be explained because the heterogeneous benchmark and the steady-state are not identical. This slight difference is due to the different methods by which the steady-state method and the time-dependent method define material boundaries. For the time-dependent method used in the benchmark, the nodes lay immediately on the material discontinuity. Whereas for the steady-state method, the material is defined on the node and thus material discontinuities change at $dx/2$. Therefore, as the number of nodes $\rightarrow \infty$ the error goes to zero. However, for these benchmark cases 640 nodes were uniformly scattered over the 10 mfp (10 cm). Thus there is a difference of: $0.5 * dx = 5/640$ or 0.0078125 cm between the two methods. As expected, the highest error occurs at the material source interface conditions and at the vacuum boundary conditions. In the portions of the slab were there is a source the error is quite low. However, at the interface the error peaks at -0.8%.

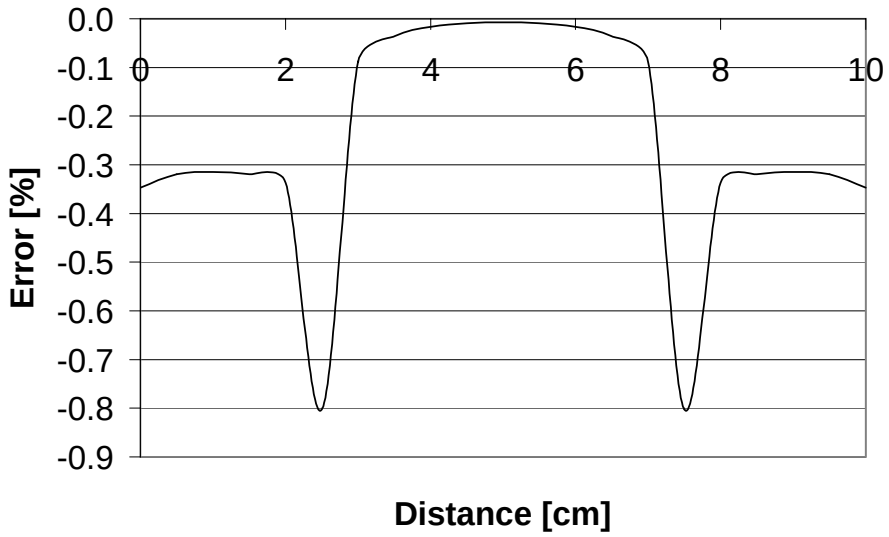

Figure 3.18: Relative Error between the Converged Time-Dependent Calculations and the Steady-State results for Localized Source in Spherical Coordinates

Table 3.14: Benchmark Solutions for 10 mfp Heterogeneous Slab at Early Times

x [cm]	1.0 mft	2.5 mft	5.0 mft	7.5 mft	10.0 mft
0.0	0.000	0.000	0.036	0.080	0.107
0.5	0.000	0.004	0.094	0.177	0.227
1.0	0.000	0.031	0.183	0.296	0.360
1.5	0.000	0.111	0.330	0.462	0.533
2.0	0.048	0.292	0.560	0.697	0.768
2.5	0.379	0.698	0.960	1.080	1.138
3.0	0.755	1.237	1.520	1.614	1.652
3.5	0.787	1.380	1.712	1.806	1.837
4.0	0.787	1.419	1.789	1.888	1.917
4.5	0.787	1.426	1.818	1.922	1.951
5.0	0.787	1.427	1.826	1.931	1.960
5.5	0.787	1.426	1.818	1.922	1.951
6.0	0.787	1.419	1.789	1.888	1.917
6.5	0.787	1.380	1.712	1.806	1.837
7.0	0.755	1.237	1.520	1.614	1.652
7.5	0.379	0.698	0.960	1.080	1.138
8.0	0.048	0.292	0.560	0.697	0.768
8.5	0.000	0.111	0.330	0.462	0.533
9.0	0.000	0.031	0.183	0.296	0.360
9.5	0.000	0.004	0.094	0.177	0.227
10.0	0.000	0.000	0.036	0.080	0.107

Table 3.15: Benchmark Solutions for 10 mfp Heterogeneous Slab at Late Times

Distance	20 mft	50 mft	70 mft	100 mft
0.0	0.136	0.138	0.138	0.138
0.5	0.280	0.284	0.284	0.284
1.0	0.426	0.431	0.431	0.431
1.5	0.605	0.610	0.610	0.610
2.0	0.837	0.842	0.842	0.842
2.5	1.194	1.198	1.198	1.198
3.0	1.684	1.686	1.686	1.686
3.5	1.859	1.860	1.860	1.860
4.0	1.934	1.935	1.935	1.935
4.5	1.965	1.965	1.965	1.965
5.0	1.973	1.974	1.974	1.974
5.5	1.965	1.965	1.965	1.965
6.0	1.934	1.935	1.935	1.935
6.5	1.859	1.860	1.860	1.860
7.0	1.684	1.686	1.686	1.686
7.5	1.194	1.198	1.198	1.198
8.0	0.837	0.842	0.842	0.842
8.5	0.605	0.610	0.610	0.610
9.0	0.426	0.431	0.431	0.431
9.5	0.280	0.284	0.284	0.284
10.0	0.136	0.138	0.138	0.138

3.4 Benchmark Comparison with Diffusion Theory

In this section, time-dependent transport results are compared to similarly posed diffusion results using integral methods. This illustrates the differences between both schemes. Diffusion theory is known to be accurate in the center of large highly diffusive media; however, it produces less accurate results in highly absorptive media and near vacuum boundaries. Two examples will be simulated showing the differences between time-dependent transport and time-dependent diffusion theory varying only the source distributions. Both examples are simulated in Cartesian geometry with a slab of 40 cm in thickness (over 15 mfp). The first case simulated a uniform thermal neutron source and the second simulate a localized source in the inner 1/2 of the slab. For both cases, there are no neutrons in the slab at $t = 0^-$ and the source is turned on at $t = 0^+$ and remains on. The material properties of thermal neutrons in carbon are given in Table 3.16 [90]:

Table 3.16: Material Properties for Thermal Neutrons in Carbon

Σ	0.38532 cm^{-1}
Σ_s	0.385 cm^{-1}
S_0	1.0 $\text{n/cm}^3\text{-s}$

The time-dependent diffusion equation in one-dimensional Cartesian coordinates is:

$$\frac{1}{v}\frac{d\phi}{dt} - D\frac{d^2\phi}{dx^2} + \Sigma_a\phi\left(x,t\right) = S\left(x,t\right). \tag{3.12}$$

Eqn. 3.12 can be converted into an integral equation using Laplace transforms [56]. The resulting time-dependent integral diffusion equation is of the same form as Eqn. 3.2 with the only difference coming in the functional form of the kernel. The time-dependent

one-dimensional kernel was generated using extrapolated boundary conditions and presented in Table 3.17. The kernel was deemed to have converged once the difference from the n to the $(n+1)$ term was less than $10^{-8}\%$.

Table 3.17: One-Dimensional Cartesian Time-Dependent Diffusion Kernels

$x > x'$	$K_{1D,C}(x,x';t,t') = \frac{\sqrt{v}\exp(-\Sigma_a\, v[t-t'])}{2\sqrt{\pi D[t-t']}} \times$ $\sum_{n=1}^{\infty}\left[\exp\left(-\frac{\kappa_a^2}{4[t-t']}\right)+\exp\left(-\frac{\kappa_b^2}{4[t-t']}\right)+\exp\left(-\frac{\kappa_c^2}{4[t-t']}\right)+\exp\left(-\frac{\kappa_d^2}{4[t-t']}\right)\right]$ $\kappa_a = \frac{-x+x'+4a(n+1)}{\sqrt{vD}}$ $\quad$ $\kappa_b = \frac{x-x'+4an}{\sqrt{vD}}$ $\kappa_c = \frac{x+x'+4an+2a}{\sqrt{vD}}$ $\quad$ $\kappa_d = \frac{-x-x'+4an+2a}{\sqrt{vD}}$
$x < x'$	$K_{1D,C}(x,x';t,t') = \frac{\sqrt{v}\exp(-\Sigma_a\, v[t-t'])}{2\sqrt{\pi D[t-t']}} \times$ $\sum_{n=1}^{\infty}\left[\exp\left(-\frac{\zeta_a^2}{4[t-t']}\right)+\exp\left(-\frac{\zeta_b^2}{4[t-t']}\right)+\exp\left(-\frac{\zeta_c^2}{4[t-t']}\right)+\exp\left(-\frac{\zeta_d^2}{4[t-t']}\right)\right]$ $\zeta_a = \frac{-x+x'+4an}{\sqrt{vD}}$ $\quad$ $\zeta_b = \frac{x-x'+4a(n+1)}{\sqrt{vD}}$ $\zeta_c = \frac{x+x'+4an+2a}{\sqrt{vD}}$ $\quad$ $\zeta_d = \frac{-x-x'+4an+2a}{\sqrt{vD}}$

For the first comparison, a uniform unit source (1 n/cm^3-s) is distributed throughout the interior of a carbon slab. The slab had a width of 40 cm. A larger slab width was used for these particular cases because in order for diffusion theory to be sufficiently accurate the slab must be "many" mean free path lengths in width. The results of the comparison are shown in Figure 3.19.

As shown the two methods compare favorably for the initial time-steps. However, after approximately 100 microseconds the two solutions begin to show slight differences

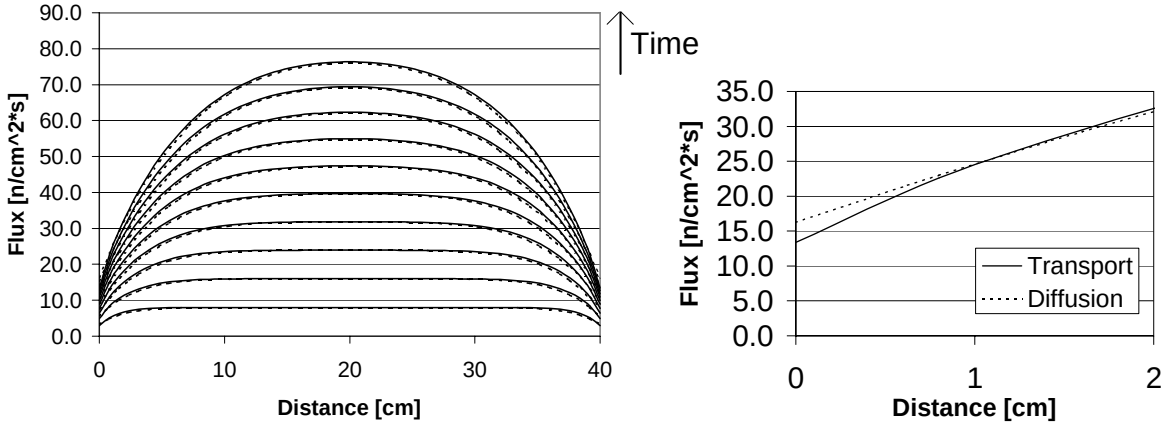

Figure 3.19: Diffusion vs. Transport for Uniform in Carbon (Blowup at Right Boundary after 365.8 μ sec)

near the boundaries. The diffusion based calculation overestimates the scalar flux close to the boundary. This is expected as diffusion based calculations are known to model the scalar flux incorrectly near vacuum boundaries. As time continues to progress, the two methods begin to differ near the center of the slab, with the transport solution calculating slightly higher ($\sim 0.5\%$) scalar fluxes. As expected, the time-dependent diffusion theory and transport theory agree to within a fraction of a percent over the vast majority of the slab.

The next comparison shows the inadequacies of diffusion based methods in modeling time-dependent problems. The material is again a 40 cm slab of carbon; however, in this case the source is confined to the inner 20 cm of the slab.

Figure 3.20 shows the results of the comparison. After 10 mean free times, the first curve on Figure 3.20, the diffusion based solution differs by a maximum of 1% over the interior of the source region. As time progresses, the agreement between the diffusion based and transport results becomes progressively less. After 100 mean free times, the

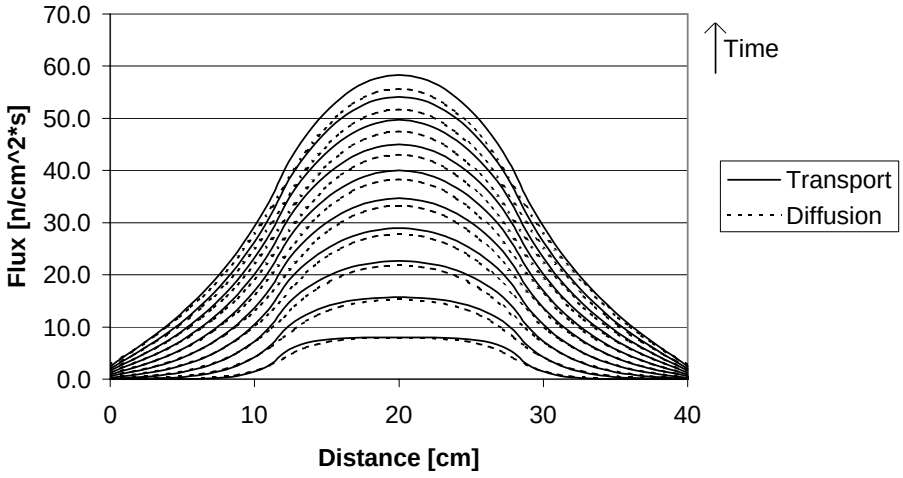

Figure 3.20: Diffusion vs. Transport for Localized Source in Carbon

upper curve on Figure 3.20, diffusion theory predicts a scalar flux 7% lower than transport theory in the source region.

Figure 3.21 shows the region just adjacent to the source region 7.5 microseconds after the source is turned on. The predictions of the two methods are shown on the figure. The transport solution kernel has causality information built into the kernel. This means that after only 7.5 microseconds there has not been enough time for neutrons to travel any further than 1 cm away from the inner source region. The transport solution agrees with this causality information and Figure 3.21 shows this characteristic. The diffusion based method predicts a scalar flux in portions of the slab for which there has not been enough time for neutrons to populate. This is shown in the figure as values for the flux further than 1 cm away from the inner source region.

In summary, diffusion theory and transport theory compare favorably in regimes for which diffusion theory holds true, uniform source and highly scattering regions. However, for geometries in which there is an obvious causality effect, such as a localized source regions and a few mean free path lengths away from boundaries for localized source

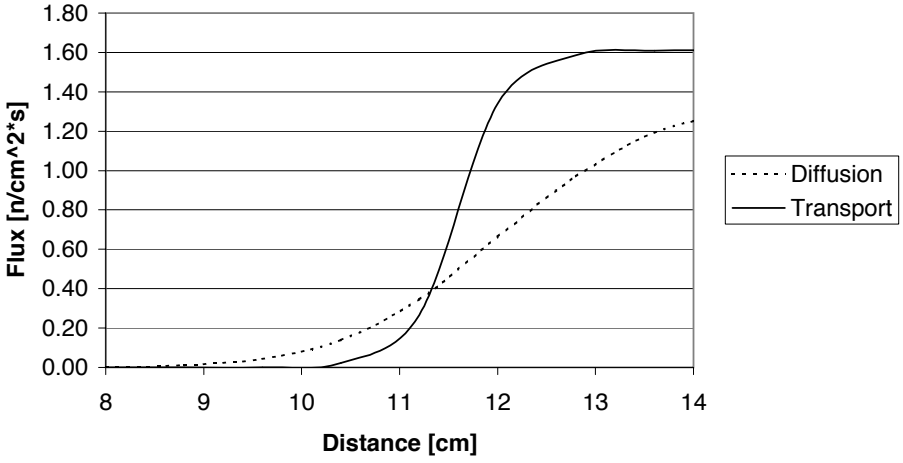

Figure 3.21: Diffusion vs. Transport for Localized Source in Carbon at 7 μs

regions, diffusion theory models the scalar flux incorrectly because of its assumption of infinite propagation speed and low degree of particle field anisotropy.

Chapter 4

TBIT Theory and Implementation

When developing a time-dependent radiative transport method for general use it should be: accurate, fast and ideally, only require that data need to be saved from the previous time-step to calculate the current time-step. The "standard integral method", as discussed in the previous chapter, is very accurate; however, it suffers inadequacies in the later two requirements.

The most important disadvantage for the "standard" integral method is the requirement that all the information up until the time-step of interest t must be kept. Therefore, the amount of information that must be kept scales with the number of nodes in each dimension multiplied by the number of temporal time-steps. For simple one-dimensional calculations this is not much of a problem; however, for three-dimensional problems with hundreds of nodes in each dimension, array sizes become increasingly large. Even if the memory requirements were not a problem, some codes do not save the spatial, material, and source conditions for time-steps in the distant past which would be necessary to calculate the scalar flux using the "standard" method.

In addition to the memory requirements, the computational time increases with every time-step. In order to solve the integral equations presented in Table 2.1 and 2.2, calculations at the n^{th} time-step must integrate all the way back to the first time-step. Although in practice integration back 10 mfp is adequate. Problems solved using the "standard" integral method scale to the cubed root of the number of spatial nodes for one-dimensional problems. Doubling the number of nodes results in eight times the amount of CPU time necessary for completion.

The purpose of this research is to produce an integral method that retains the accuracy of the "standard method"; yet, does not suffer the penalty of having to save all the information in the problem at every calculational time-step. For one-dimensional geometries, a time-step method would scale as the square of the number of spatial nodes. This would save a great amount of time over the "standard" method which scales as the cube of the number of nodes. This new time-dependent radiative transport method, or the Time-Dependent Bubble Integral Transport (TBIT) Method, will be required to calculate the angular flux instead of the scalar flux that is necessary for the "standard" method.

Chapter 4 is divided into several sections. Section 4.1 will present the derivation of the angular form of the time-dependent integral equation. In Section 4.2 the Time-Dependent Bubble Integral Transport (TBIT) method will be derived and the numerical method will be discussed. This chapter will conclude with a description of the code in Section 4.3

4.1 Derivation of Integral Transport Equation

The neutral particle transport equation is a version of the Boltzmann equation used in the kinetic theory of gases. This equation describes the transport of particles as a function of space, $\vec{r}$, directional travel, $\hat{\Omega}$, energy, E, and time, t. The Boltzmann equation is:

$$\left[\frac{1}{v}\frac{\partial}{\partial t} + \hat{\Omega}\cdot\vec{\nabla} + \Sigma\left(\vec{r},E,t\right)\right]\psi\left(\vec{r},\hat{\Omega},E,t\right) = Q_{ex}\left(\vec{r},E,\hat{\Omega},t\right), \tag{4.1}$$

where: $\psi\left(\vec{r},\hat{\Omega},E,t\right)$ is the time-dependent angular flux, $\Sigma\left(\vec{r},E,t\right)$ is the total macroscopic cross section for particles with energy of E, $\Sigma_s\left(\vec{r},E'\rightarrow E,\hat{\Omega}'\rightarrow\hat{\Omega},t\right)$ is the macroscopic scattering cross section, and $Q_{ex}\left(\vec{r},\Omega,E,t\right)$ is the source term which includes the addition of particles from any arbitrary source. The source term can include the addition of particles that are created from fission, fusion, up-scattering down-scattering, or any

other physical process that results in the addition of particles into the energy group of interest.

In Cartesian coordinates, the first two derivative terms in Equation 4.1, $\frac{\partial}{\partial t}$ and $\hat{\Omega}\cdot\vec{\nabla}$, are:

$$\left(\frac{1}{v}\frac{\partial}{\partial t}+\Omega_x\frac{\partial}{\partial x}+\Omega_y\frac{\partial}{\partial y}+\Omega_z\frac{\partial}{\partial z}\right)\psi\left(\vec{r},\hat{\Omega},E,t\right). \tag{4.2}$$

The total derivative, using the method of characteristics, is written as:

$$\frac{d\psi}{ds}=\frac{\partial\psi}{\partial t}\frac{dt}{ds}+\frac{\partial\psi}{\partial x}\frac{dx}{ds}+\frac{\partial\psi}{\partial y}\frac{dy}{ds}+\frac{\partial\psi}{\partial z}\frac{dz}{ds}. \tag{4.3}$$

Identifying each term from Equation 4.2 and 4.3 the corresponding solutions for each term in the total derivative is:

$$\begin{aligned}
\frac{dt}{ds}&=\frac{1}{v} \quad \text{with solutions} \quad && t=t_0+\frac{s}{v}\\
\frac{dx}{ds}&=\Omega_x && x=x_0+s\Omega_x\\
\frac{dx}{ds}&=\Omega_y && y=y_0+s\Omega_y\\
\frac{dx}{ds}&=\Omega_z && z=z_0+s\Omega_z,
\end{aligned} \tag{4.4}$$

where x_0, y_0, and z_0 are arbitrary constants of integration. Equation 4.1 can be rewritten as:

$$\frac{d}{ds}\psi\left(\vec{r_0}+s\hat{\Omega},\hat{\Omega},E,t_0+\frac{s}{v}\right)+\Sigma\psi=Q\left(\vec{r_0}+s\hat{\Omega},\hat{\Omega},E,t_0+\frac{s}{v}\right). \tag{4.5}$$

Equation 4.5 is just a first order equation which can be integrated and solved by using the proper integration factor. The following solution is obtained:

$$\begin{aligned}
&\frac{d}{ds}\left[\psi\left(\vec{r_0}+s\hat{\Omega},\hat{\Omega},E,t_0+\frac{s}{v}\right)\exp\left[\int^s\Sigma\left(\vec{r_0}+s'\vec{\Omega},E\right)ds'\right]\right]=\\
&\qquad\exp\left[\int^s\Sigma\left(\vec{r_0}+s'\vec{\Omega},E\right)ds'\right]Q\left(\vec{r_0}+s\hat{\Omega},\hat{\Omega},E,t_0+\frac{s}{v}\right).
\end{aligned} \tag{4.6}$$

This equation can be solved as the following:

$$\begin{aligned}
&\psi\left(\vec{r_0}+s\hat{\Omega},\hat{\Omega},E,t_0+\frac{s}{v}\right)=\\
&\qquad\int_{-\infty}^s\exp\left[\int_{s'}^s-\Sigma\left(\vec{r_0}+s'\hat{\Omega},E\right)ds''\right]\left[Q\left(\vec{r_0}+s\hat{\Omega},\hat{\Omega},E,t_0+\frac{s}{v}\right)\right]ds'
\end{aligned} \tag{4.7}$$

In arriving at Equation 4.7, an assumption was made that there were no particles in the system at early times. Therefore, the second term that results from the evaluation of the lower limit from Equation 4.6 is identical to zero or:

$$\psi\left(\vec{r_0}+s\hat{\Omega},\hat{\Omega},E,t_0+\frac{s}{v}\right)\rightarrow 0\ as\ s\rightarrow-\infty. \tag{4.8}$$

Equation 4.7 is simplified by the following:

$$\vec{r_0}+s\hat{\Omega}=\vec{r}\,\text{and}\,t_0+\frac{s}{v}=t, \tag{4.9}$$

and changing the integration so that it runs from 0 to ∞ instead of from 0 to s' in the two integrals. The final version of the time-dependent angular integral equation is:

$$\psi\left(\vec{r_0}+s\hat{\Omega},\hat{\Omega},E,t_0+\frac{s}{v}\right)=\int_0^{\infty}\left[e^{-\tau\left(\vec{r}-s'\hat{\Omega},E,t\right)}Q\left(\vec{r_0}+s\hat{\Omega},\hat{\Omega},E,t_0+\frac{s}{v}\right)\right]ds', \tag{4.10}$$

where the optical distance between two points x and s' is just:

$$\tau\left(\vec{r},\hat{\Omega},E,t\right)=\int_0^{s'}\Sigma\left(\vec{r}-s''\hat{\Omega},E,t\right). \tag{4.11}$$

The integration over s' need not be from 0 until ∞, as would be the case if the calculational point is within an infinite media. However if the calculational point is within a finite media, then the path of integration need only proceed along $\vec{r}=s\hat{\Omega}$ until the path of integration intersects with the vacuum boundary. If there is an external source condition at the vacuum boundary, then an additional source term is added. With these previous conditions and assuming that the boundary B is located such that all the initial uncollided source particles have traveled out of the system, then the following is obtained:

$$\begin{aligned}\psi\left(\vec{r_0}+s\hat{\Omega},\hat{\Omega},E,t_0+\frac{s}{v}\right)=&\\ \int_0^{B}\left[e^{-\tau\left(\vec{r}-s'\hat{\Omega},E,t\right)}Q\left(\vec{r_0}+s\hat{\Omega},\hat{\Omega},E,t_0+\frac{s}{v}\right)\right]ds&\\ +\psi_{boundary}\left(\vec{r_0}+B\hat{\Omega},\hat{\Omega},E,t_0+\frac{B}{v}\right)e^{-\tau\left(\vec{r}-s'\hat{\Omega},E,t\right)}.&\end{aligned} \tag{4.12}$$

4.2 Derivation of the Time-Dependent Bubble Integral Transport Method

Equation 4.13 can be transformed into an integral equation in terms of the scalar flux as described in Chapter 2. However, as mentioned earlier, integral equations of this form produce integrals that must be integrated over temporal limits of 0 to the current time of interest t. Although this method produces highly accurate results, which was used in Chapter 3 to produced time-dependent finite media benchmarks, the temporal integration constraint proves extremely disadvantageous.

Therefore, an alternative integral method must be developed with the constraint that it must only need to save information from the previous time time-step. The Time-Dependent Bubble Integral Transport (TBIT) Method will use the angular flux instead of the scalar flux. The derivation starts with Equation 4.6

$$\frac{d}{ds}\left[\psi\left(\vec{r_0}+s\hat{\Omega},\hat{\Omega},E,t_0+\frac{s}{v}\right)\exp\left[\int^{s}\Sigma\left(\vec{r_0}+s^{'}\vec{\Omega},E\right)ds'\right]\right]= \exp\left[\int^{s}\Sigma\left(\vec{r_0}+s^{'}\vec{\Omega},E\right)ds'\right]Q\left(\vec{r_0}+s\hat{\Omega},\hat{\Omega},E,t_0+\frac{s}{v}\right). \tag{4.13}$$

However unlike the general method where one integrates back along the characteristic path from $s=0$ to ∞, the TBIT method only integrates from $s=0$ back one time-step. This time-step is defined as $\Delta x = v_g \Delta t$. Where, v_g is the velocity of the particles in the g^{th} energy group and Δx is the spacing between spatial nodes. Normally, this condition determines the duration of the time-step as the other two variables are predetermined. Thus, the time-step for the g^{th} energy group will have a duration in proportion to the other energy groups based on the square root of the velocities of the two groups in question. The following is arrived at:

$$\psi\left(\vec{r},\hat{\Omega},E,t\right)=\int_0^{\Delta x}\left[e^{-\tau\left(\vec{r}-s\hat{\Omega},E,t\right)}Q\left(\vec{r_0}+s\hat{\Omega},\hat{\Omega},E,t_0+\frac{s}{v}\right)\right]ds' +\psi\left(\vec{r}-\Delta x\hat{\Omega},\hat{\Omega},E,t-\Delta t\right)e^{-\tau\left(\vec{r},\hat{\Omega},E,t\right)}. \tag{4.14}$$

The assumption is made that all the scattering in the system is isotropic in the center

of mass coordinate system (ie no scattering angles are preferred), then expanding the source term into its constituent components of its collided and uncollided sources, the following is arrived at:

$$\psi\left(\vec{r},\hat{\Omega},E,t\right) = \int_0^{\Delta x} e^{-\tau\left(\vec{r}-s\hat{\Omega},E,t\right)}\left[\Sigma_s\left(\vec{r},\hat{\Omega},E,t\right)\Phi\left(\vec{r},\hat{\Omega},E,t\right)+S_o\left(\vec{r},\hat{\Omega},E,t\right)\right]ds' + \psi_{boundary}\left(\vec{r}-\Delta x\hat{\Omega},\hat{\Omega},E,t-\Delta t\right)e^{-\tau\left(\vec{r}-s\hat{\Omega},E,t\right)}. \quad (4.15)$$

Perhaps it is best to understand Equation 4.15 through a visual representation. Figure 4.1 shows Equation 4.15 from a visual standpoint. The TBIT method calculates

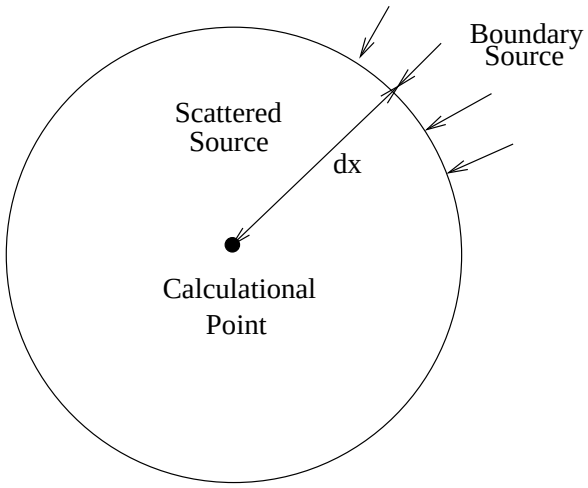

Figure 4.1: Graphical representation of TBIT Method

the time-dependent scalar flux at a particular point by drawing a sphere of radius one Δx around the calculational point. Thus, only particles that scatter during the current time-step into the calculational angle, or particles that are on the boundary of the sphere during the previous time-step will influence the angular flux at the current time-step. The scattered component is calculated by integrating along the line of sight until the boundary of the 'sphere' or material/vacuum boundary is met. The boundary component is

calculated through simple exponential attenuation along the line of sight.

4.3 Numerical Implementation of Time-Dependent Bubble Method

In a simplistic manner, the scalar flux could be calculated by solving Eqn. 4.15 along specific angular directions and then integrating these directions in order to solve for the scalar flux. After each time-step, the boundary source term is updated and the calculation can proceed with only the information from the previous time-step needed.

However, there are several complications that must be addressed. The first problem is how exactly to determine the incoming boundary source such that every zone is guaranteed to affect the scalar flux at any calculational point. Once this is determined, a second question is how to integrate the scattered source, when none of the points used in the integration is guaranteed to rest on a point for which the scattered source is known exactly. A third problem is how to calculate the constantly changing streaming angles as particles travel through spherical coordinates. A final difficulty presents itself when trying to calculate the down-scattered flux. Each of these issues will be discussed in the remainder of this chapter.

4.3.1 Determination of Angular Source Term

The first problem that arises when determining a workable method by which the time-dependent flux can be calculated using the TBIT method, is the determination of the boundary source term. From a naive standpoint, the value of the boundary term could be taken at the point where the angular direction intersects with the sphere at one dx.

Figure 4.2 shows this simple case. The angular flux is calculated in the direction μ. Once the value for the boundary flux is determined, then its influence on the angular flux at the current time and position is calculated through simple exponential decay.

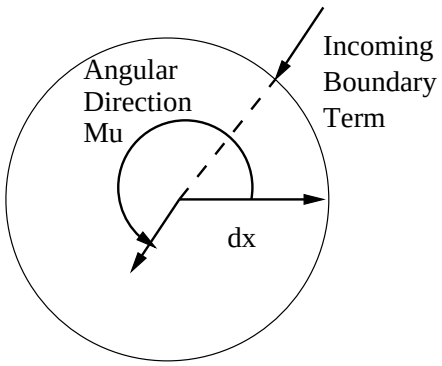

Figure 4.2: Simplistic Calculation for the Boundary Source Term

In Cartesian coordinates, the angular directions can be easily distributed such that the distributions guarantees that every spatial node will influence the angular flux to some extent. Taking the angular directions back into time will insure that they will intersect with every calculational node.

Unfortunately, in spherical coordinates this is not the case. Although the TBIT method only integrates back one time-step, or a distance of dx, boundary source terms are communicated across the problem from one boundary to the next. Thus they are "effectively" integrated along a specific angular direction from the calculational point. However because of the spherical coordinates and the resultant streaming of the particles across the geometry, it is possible that particular regions of the sphere could be missed as a result. Figure 4.3 shows this behavior for one-dimensional spherical coordinates.

Any time-dependent, time-step integral method used must integrate along discrete angular directions, i.e. the number of angular directions must be less than infinity. As such, integrating along specific characteristics in spherical coordinates, there is the possibility of missing specific regions entirely.

Figure 4.3 shows the calculation along specific characteristics for a time late enough

that the point in question can communicate all across the sphere. As shown in the figure there are two regions that are missed entirely in the integration along these lines. In calculating the total scalar flux correctly, contributions from every region that can contribute directly with the calculational point must be included in the integration. There are several proposed methods to fix this error:

- Increase the number of spatial directions
- Increase the number of integration nodes along the spatial direction
- Vary the spatial directions of the nodes such that at least one spatial direction is guaranteed to intersect with each node
- Integrate the source contribution on surfaces rather than along spatial lines

All of the proposed fixes would add complexity to the algorithm. The first two solutions, increasing the number of spatial directions or increasing the number of integration nodes, do not guarantee that contributions from each spatial subdivision contribute to the scalar flux at the calculational point.

The third solution, although it will guarantee that every characteristic will intersect every zonal region, forces any numerical calculation to recalculate at every time-step the angular directions. In addition, it is possible that there will be as many angular directions as there are regions in the problem. This will add considerable calculational overhead to the problem.

Only the last method, integrate the source contribution on the surfaces rather than along spatial lines, guarantees that every spatial region will be included in the calculation while providing that the angular directions are constant for every spatial position. Figure 4.4 shows how this integration will be performed in practice. Instead of calculating the boundary source from a single discrete angle (left side of the figure), the boundary source

term will be the result of an integration along the curved boundary between the lower and upper midpoints of the angular directions.

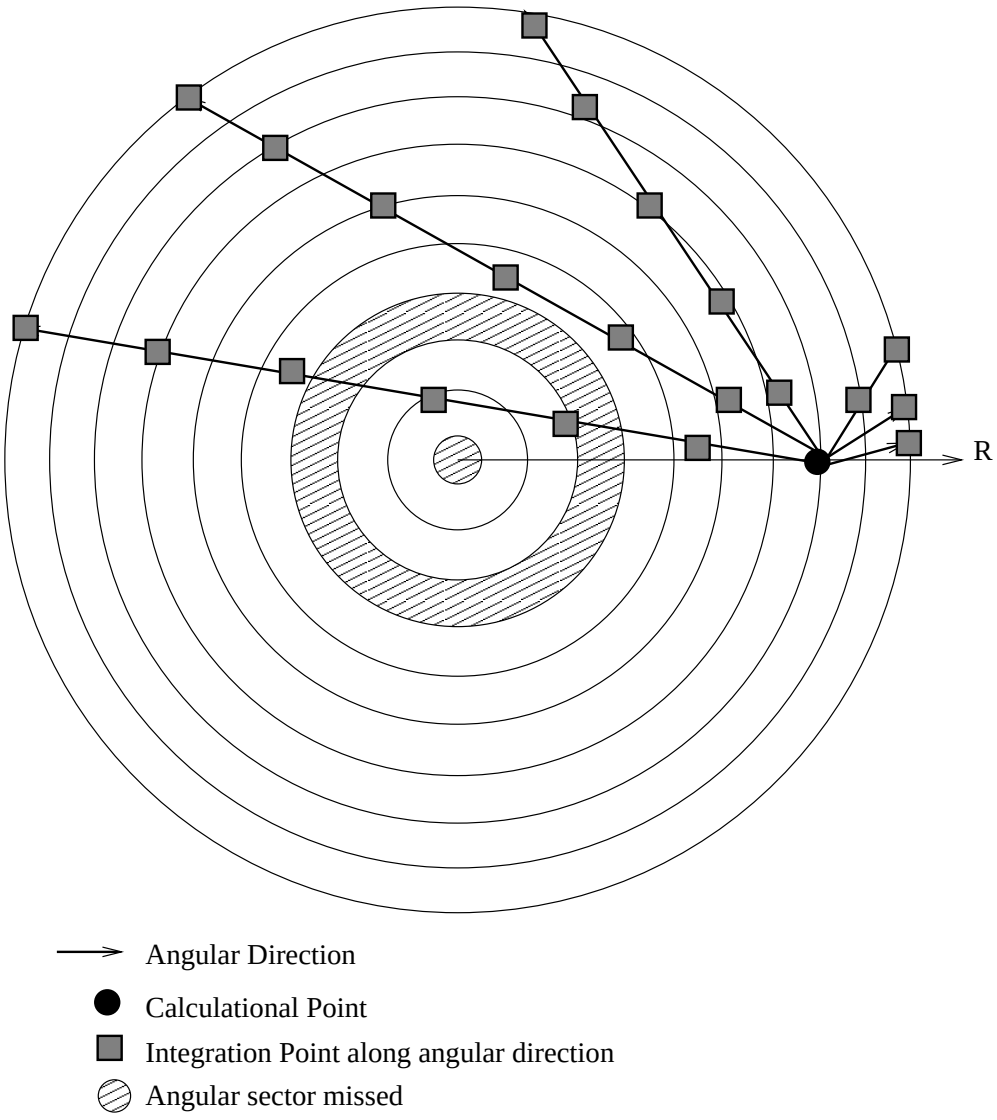

Figure 4.3: Error cause by Direct Application of Equation 4.15

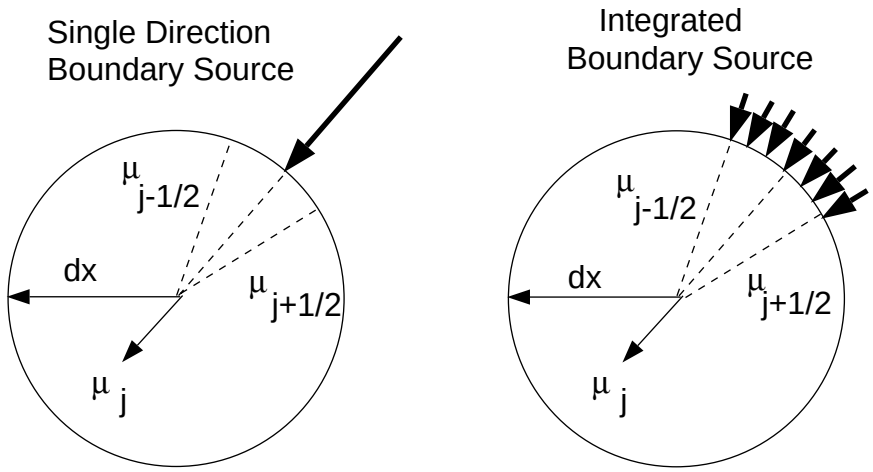

Figure 4.4: Integration along the Surface for the Boundary Source Term

4.3.2 Integration of the Scattered and Boundary Flux

Now that the surface term is handled in a more correct fashion, additional difficulties are added in determining the angular flux. Figure 4.5 shows the calculation of the angular flux in a particular direction μ_j in one-dimensional Cartesian geometry.

For this particular example, the surface integration is performed along the circular boundary using five distinct points. All of these points are boundary source terms saved from the previous time-step. These boundary values necessary for the integration of the source term neither lay on integer values for the spatial grid, $i-1$, i, or $i+1$, nor on the angular grid, j. Only angular and spatial positions that lay on integer values were calculated in the previous time-step. Similarly, this is a problem when calculating the scattered flux. In order to obtain values for these positions several methods were proposed and tested:

1. linear approximation in space and angle
2. linear approximation and/or cubic spline approximation in space and Legrende polynomial expansion in angle
3. cubic spline approximation in space and angle

Through testing, the cubic spline approximations appeared to converge to the time-dependent benchmarks (presented in Chapter 3) in a more accurate fashion than either of the previous two methods. Therefore, for the TBIT method cubic splines were used to interpolate data in both space and angle when the calculational nodes lay off known data points.

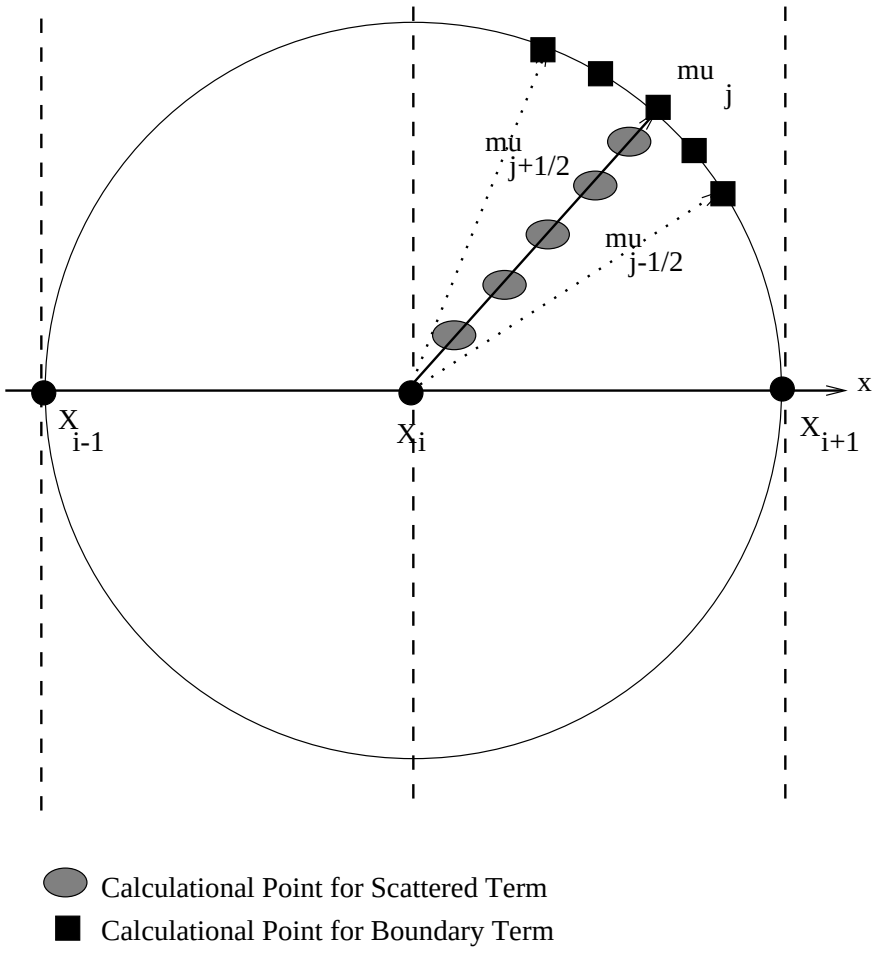

Figure 4.5: Integration of the Scattered and Boundary Flux

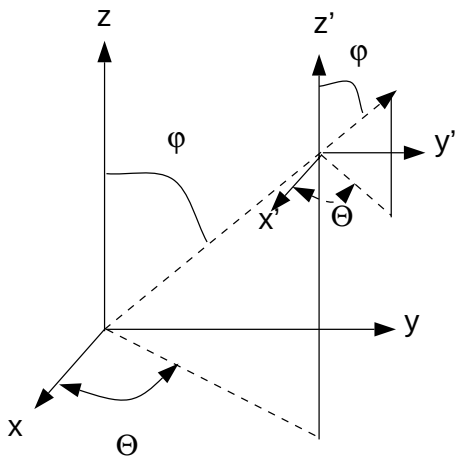

Figure 4.6: Constant Streaming Directions in Cartesian Coordinates

4.3.3 Streaming in Spherical Coordinates

In Cartesian coordinates, the streaming angles of particles as they cross the geometry remains constant. Particles in Cartesian coordinates that are emitted with angular directions θ and ϕ always travel with those angular directions throughout the entire slab. This is shown in Figure 4.6.

Unlike Cartesian geometries, the streaming angles in spherical coordinates change as the particle travels through the material. Thus as the TBIT code integrates back along the particles path, the streaming angles change with the angular positions of the particle. This occurs even though the integration is carried out over only one time-step. Geometric relationships must be derived to allow the TBIT code to calculate the streaming angles for any arbitrary angular position.

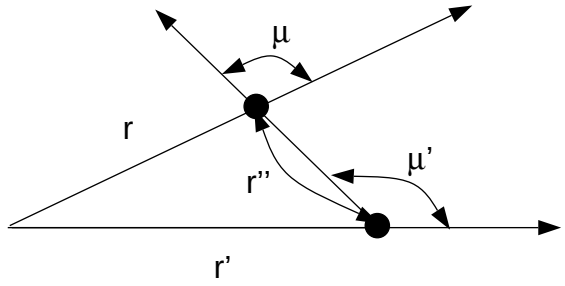

Figure 4.7: Streaming Directions in 1-D Spherical Coordinates

4.3.3.1 Streaming in One Dimensional Spherical Coordinates

In one-dimensional spherical coordinates, the particle flux only depends on the radial position r. Likewise, the only streaming direction that TBIT must recalculate is μ, which can range from 0 to π. Figure 4.7 shows a pictorial representation of calculational variables in one-dimensional spherical coordinates. The new radial position is therefore:

$$r' = \sqrt{r^2 + r''^2 + 2rr'' \cos \mu}. \tag{4.16}$$

The the new streaming direction μ' is:

$$\mu' = \pi + d\theta - \mu. \tag{4.17}$$

4.3.3.2 Streaming in Two-Dimensional Spherical Coordinates

In two-dimensional spherical coordinates, the particle flux depends on the radial position r and the polar angle θ. Like the one-dimensional case, only a single streaming variable μ is needed; however, unlike the one-dimensional case μ runs from 0 to 2π. Figure 4.8 shows a pictorial representation of calculational variables in two-dimensional spherical coordinates. The new radial position is therefore:

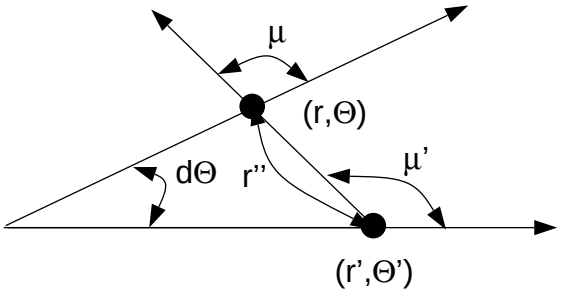

Figure 4.8: Streaming Directions in 2-D Spherical Coordinates

$$r' = \sqrt{r^2 + r''^2 + 2rr'' \cos\mu}. \tag{4.18}$$

The angle dθ is:

$$d\theta = cos^{-1}\left(\frac{r'^2 + r^2 - r''^2}{2r'r}\right). \tag{4.19}$$

Therefore the new angular position of the point is:

$$\theta^{'} = \theta + d\theta. \tag{4.20}$$

The new streaming direction μ' is calculated as:

$$\mu' = \pi + d\theta - \mu. \tag{4.21}$$

4.3.3.3 Streaming in Three-Dimensional Spherical Coordinates

The calculation of the streaming directions in three-dimensional coordinates is considerably more difficult than the relatively easy transformations in one and two dimensions. The basic methodology used will be to transform the coordinates of the calculational point (r, θ, ϕ) into Cartesian coordinates (x, y, z). This coordinate system will be rotated using the directional streaming angles and the streaming point will be calculated in Cartesian coordinates and then transferred back into spherical coordinates $(r'\,\theta', \phi')$.

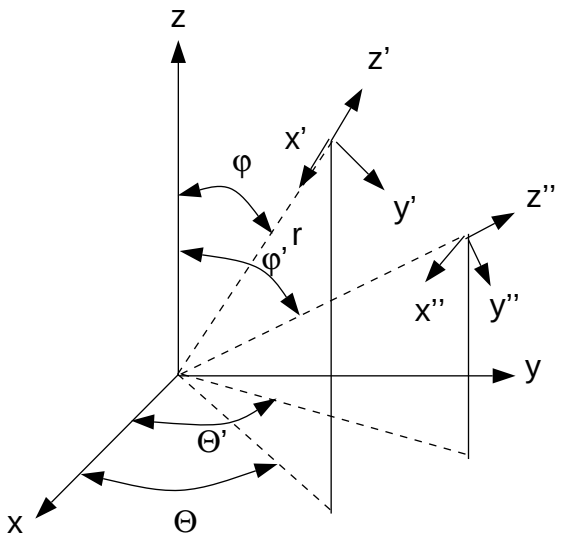

Figure 4.9: Streaming Directions in 3-D Spherical Coordinates

Fortunately, calculating the streaming angles at the new point is not as difficult and can be done easily without any coordinate transformations. Figure 4.9 shows a pictorial representation of calculational variables in one-dimensional spherical coordinates.

The calculational point (r, θ, ϕ) is first transformed into Cartesian coordinates through the well known coordinate transformation:

$$\begin{aligned} x = &\quad rcos\,(\theta)\,sin\,(\phi) \\ y = &\quad rsin\,(\theta)\,sin\,(\phi) \\ z = &\quad\quad r\,cos\,(\phi). \end{aligned} \tag{4.22}$$

The coordinate system is translated such that the origin of the Cartesian coordinate system is centered on the calculational point. The streaming point is calculated in the

shifted Cartesian coordinates as:

$$\begin{aligned} x'_{streaming} &= r cos\,(\mu)\, sin\,(\eta) \\ y'_{streaming} &= r sin\,(\mu)\, sin\,(\eta) \\ z'_{streaming} &= r cos\,(\eta)\,. \end{aligned} \tag{4.23}$$

where: μ and η are the streaming angles from the original calculational point measured as the polar and azimuthal angles respectively.

The streaming Cartesian coordinates (x'_{stream},y'_{stream}, z'_{stream}) are translated to the calculational Cartesian coordinates through the following:

$$\begin{pmatrix} x_{stream} \\ y_{stream} \\ z_{stream} \end{pmatrix} = \begin{pmatrix} cos\,(\theta)\, cos\,(\phi) & -sin\,(\theta) & cos\,(\theta)\, sin\,(\phi) \\ sin\,(\theta)\, cos\,(\phi) & cos\,(\theta) & sin\,(\theta)\, sin\,(\phi) \\ -sin\,(\phi) & 0 & cos\,(\phi) \end{pmatrix} \begin{pmatrix} x'_{stream} \\ y'_{stream} \\ z'_{stream} \end{pmatrix}. \tag{4.24}$$

Once the coordinates are transformed, it is simple to recalculate the streaming positions in the original spherical coordinate system by translating the coordinates back to the original origin and then transforming the Cartesian coordinate system back into the original spherical coordinate system.

In a similar fashion to the one and two dimensional cases, the directional angles at the new coordinates can be found. The directional angles μ and η are calculated by the following and shown in Figure 4.10:

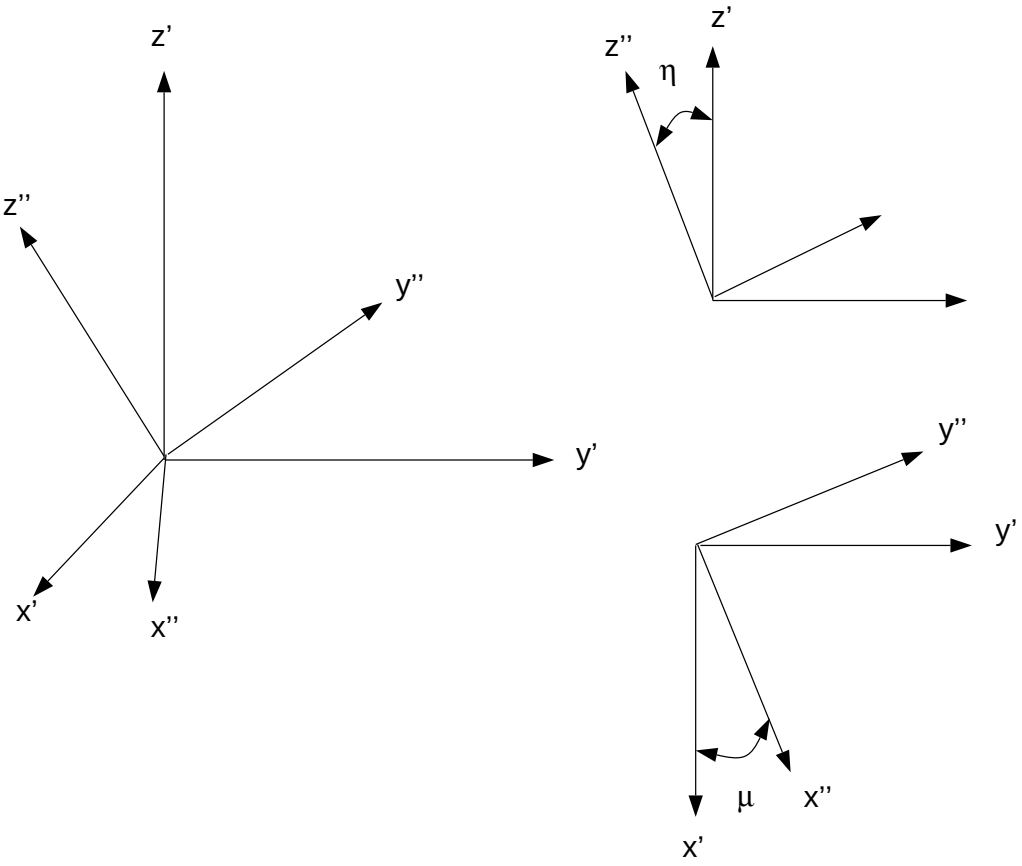

Figure 4.10: Directional Angle μ and η

Table 4.1: Directional angle μ

$\mu < \pi$	$\pi - cos^{-1}\left(\frac{r'^2 + r''^2 - r^2}{2r'r''}\right)$
$\mu >= \pi$	$\pi + cos^{-1}\left(\frac{r'^2 + r''^2 - r^2}{2r'r''}\right)$

Table 4.2: Directional angle η

$\eta < 0.5\pi$	$-0.5\pi + cos^{-1}\left(\frac{r'^2 + r''^2 - r^2}{2r'r''}\right)$
$\eta >= 0.5\pi$	$1.5\pi - cos^{-1}\left(\frac{r'^2 + r''^2 - r^2}{2r'r''}\right)$

4.3.4 Down-scattering with TBIT

Transporting down-scattered photons with the TBIT method is fairly simple. The upper energy groups are determined, and the lower energy groups are then calculated from the down-scattered component and the uncollided source term for that particular frequency group. Furthermore, because all the lower energy groups travel at the same speed, the time-steps and spatial steps are equal.

Difficulties arise when dealing with neutronic transport because the lower energy groups travel at slower velocities than the higher energy groups. This places restraints on energy groups the time-dependent code can use. All energy groups used in the direct calculations must have integer multiples of the highest energy group. Thus, if the next lower energy group has twice the time-step of the higher energy group, the lower energy group must have one-fourth the energy, assuming a non-relativistic particle ($E = \frac{1}{2}mv^2$).

However, if the energy groups need to be closer than multiples of one-fourth the energy of each other, then the TBIT method calculates the higher energy group throughout the simulation. The down-scattered flux is then written to an output file along with the spatial and temporal time-steps for the point in the simulation where the particles appear as lower energy particles. Once the lower energy is calculated and the time-step is reached where the down-scattered particles appear, the down-scattered source is read into the TBIT method as uncollided particles in the lower energy group. This second method will be used when simulating the time-of-flight neutron diagnostics ICF devices as simulated in Section 6.2.

4.4 Description of the TBIT Code

The numerical development for the Time-Dependent Bubble Method was written using C++. Figure 4.11 shows how the TBIT code is organized. The remainder of Chapter 4

will describe in brief, each of the major components of the TBIT code

The *Initialize* routine, takes the data input and reads it into TBIT. The input file is described more in depth in Appendix F; however in brief, in the first couple of lines the user must enter the number of dimensions and the geometry type. The initialization routine reads data based off the type of problem which was inputed.

The subroutine *InitArray* handles the dynamic declaration of all the arrays for the problem. Typical array sizes can range over several orders of magnitude. The angular flux array for a simple one-dimensional problem with 20 nodes in the spatial variable and 16 angular directions has only 640 double precision elements or 5.1k. However, for large three dimensional problems with 80 nodes in each direction and 64 nodes in the polar angle and 32 in the azimuthal the number of elements is 2.1×10^9 or 16.8 gigabytes of memory.

The *Source* routine handles the uncollided source for each energy group. As mentioned previously, the down-scattered flux can either be calculated directly from the code or read in from an input file. If the down-scattered flux is less than 1/2 of the energy of the current group and an input file must be read, the source routine also reads in this down-scattered flux. The uncollided source distribution for each energy group must be entered into the code before each run.

The *Gauleg* subroutine is used if the spatial integration in the radial direction will be done using a Gauss-Quadrature set. Typical problems show little difference between uniform spacing in the radial direction and the non-uniform spacing necessary for Gauss-Quadrature sets. As such, this routine is only used if the user determines that the particular problem converges better using Gauss Quadrature. If the user does not specify the integration, then Newton-Cotes type rules are used. The quadrature sets for Newton-Cotes type rules are initialized in the *Initialize* routine.

The *Calculation* subroutines calculates the angular flux for each time-step. Each

subroutine is slightly different because of geometry and dimensional differences in the calculation. Each of the six geometries which can be calculated have the five major subroutines that are shown in lower portion of Figure 4.11. The *Bubble* subroutine calculates the scattered component of the angular flux. This is the angular component which scatters within one Δx of the calculational point. The uncollided component of the angular flux, particles which have not suffered a collision since they were born, are calculated in the *Line* subroutine. The Boundary routine calculates the portion of the angular flux which is the result of scattered particles that have suffered a collision outside of one Δx. The particles which are down-scattered from higher energy groups and are born as source particles in the current energy group are calculated in the *DownScattered* subroutine. Finally, the spatial and angular interpolation is handled in the *Spline* subroutine. However, the interpolation itself does not have to be performed using cubic splines. The flux can be expanded using a wide variety of methods such as a simple linear method or expansion based on Legrende polynomials. However, in each of the cases the interpolation or expansion technique must be modified in the *Spline* routines.

The *Output* subroutine formats the output for the particular problem. Depending on the requirements for output, each particular case of output can be formatted to meet the requirements for the particular user. Currently, the output is formatted for use in Microsoft Excel (used for the graphs) and Tecplot (used for multi-dimensional graphs and movies).

Finally, the *VoidArray* subroutines will dynamically reclaim all the memory that was allocated. This is extremely important because the memory requirements for some problems are extremely high. As such, once the problem has been completed, freeing up memory for other applications is a necessity.

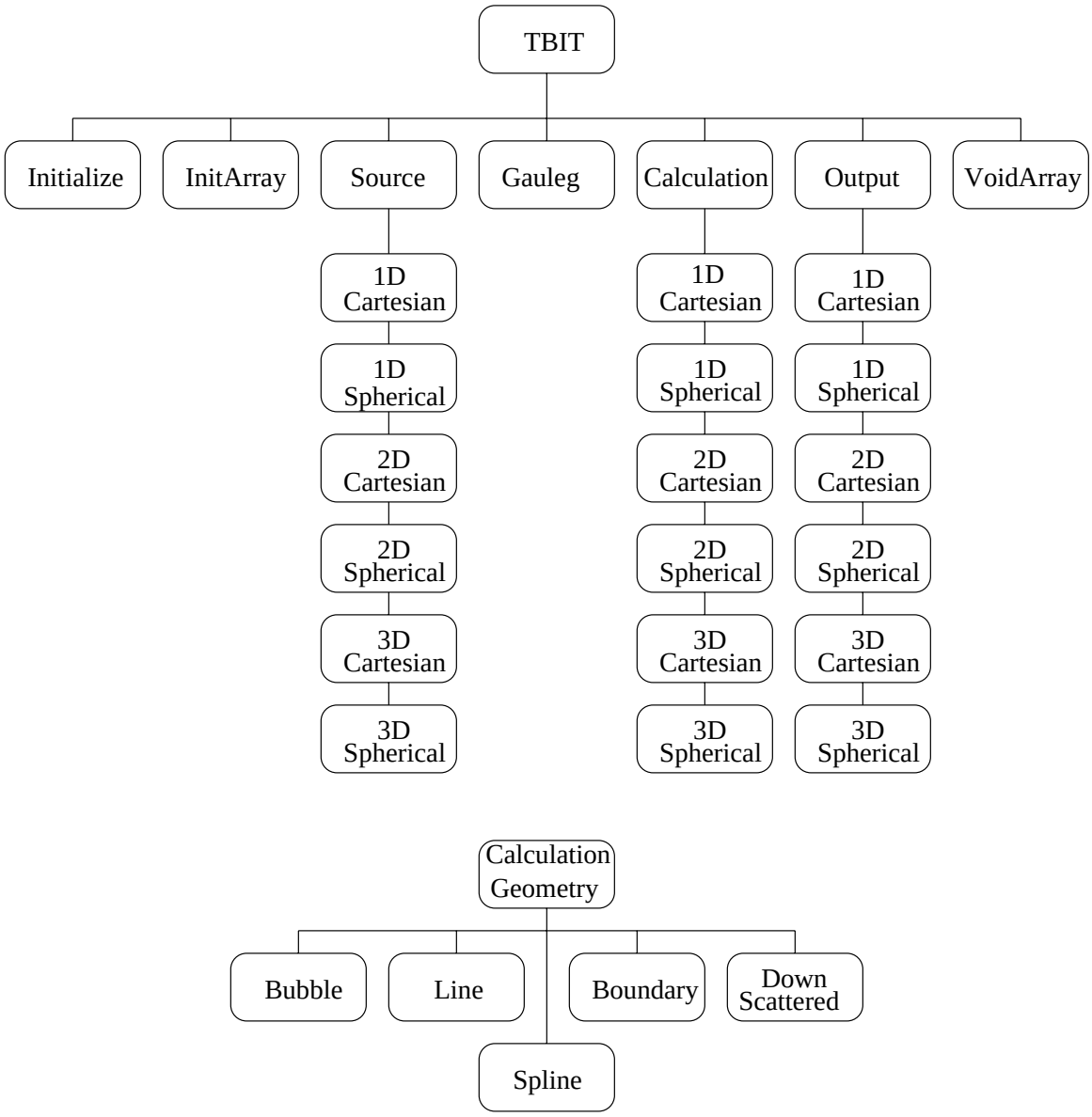

Figure 4.11: Numerical Implementation of TBIT Method

Chapter 5

TBIT Validation

Chapter 3 presented four finite media time-dependent benchmarks. In Chapter 5, the TBIT method will be validated using these benchmarks. In Section 5.1 one-dimensional problems using the TBIT method will be compared to the benchmarks in Chapter 3. In Sections 5.2 and 5.3 two and three dimensional problems in spherical coordinates will be validated.

The TBIT method will be compared to a particle balance in Section 5.4. This comparison will show how well the TBIT method conserves particles in addition to producing results that benchmark favorably. The particle check will be accomplished by using the conservation equation to measure the balance of particles (loses and gains) over each node using the heterogeneous benchmark problem (benchmark number 4) for reference.

Section 5.5 will present a new heterogeneous two-dimensional Cartesian finite media benchmark. Although the TBIT method produces results that are within a fraction of a percent of the "true" value and are not as accurate as those results presented in Chapter 3, this two-dimensional benchmark is of valuable use for future researchers in validating their time-dependent methods.

5.1 One-Dimensional TBIT comparisons to finite benchmarks

The TBIT method was compared to all four of the one-dimensional benchmark cases presented in Section 3.3. For each comparison, the TBIT method was benchmarked using the same Romberg integration techniques as presented in Chapter 3. This means that six levels of calculations were used in determining the final converged result that

was then compared to the benchmarks. Sixty-four discrete directions in the polar angle, spanning from $\pi >= \theta >= 0$, were used for all of the one-dimensional TBIT calculations.

5.1.1 Benchmark Homogeneous Cartesian with Uniform Source

The TBIT method was compared to the one-dimensional homogeneous benchmark with a uniform source. The geometry for this benchmark was given previously in Figure 3.3.

Figure 5.1 shows the percent error between the TBIT method and the first benchmark case from zero until ten mean free times. Each curve represents the passage of one-half of a mft. As shown in the figure, the error is highest near the edges for the first couple of time-steps peaking at -1.2%. The error in the center of the slab is much lower, peaking at approximately 0.20%. Table 5.1 shows the numerical error between the TBIT method and the benchmark after 1.0, 2.5, 5.0, 7.5, and 10.0 mft have past.

As time passes, the absolute value for the error on the vacuum boundary decreases while the error in the center of the slab slightly increases. This shows that the TBIT method is converging towards the correct steady-state value.

Furthermore, the error is slightly asymmetric. For the standard integral method, given enough time all the points within the slab contribute directly to the integration of the scalar flux at a particular point and time. However, not all the points in the TBIT method contribute directly to the angular flux at a discrete point and direction. Some boundary points are calculated using interpolation procedures discussed in the previous chapter. Small differences in the calculation of the cubic splines for the boundary and scattered sources result in the slight asymmetry evident from the figure.

Figure 5.2 shows the percent error for the TBIT method verses the first benchmark case from 10 until 100 mft. Each curve represents a time-step of 10 mft. Again, as for the early time-steps, the maximum error occurs near the vacuum boundaries. The absolute value of the error in the center of the slab continues to increase until it reaches

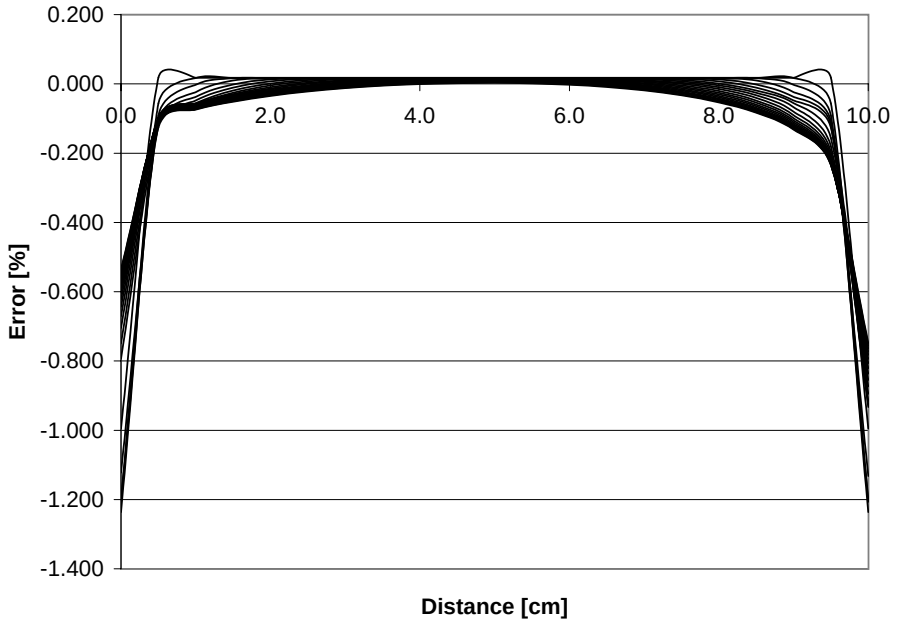

Figure 5.1: TBIT Method vs Cartesian Homogeneous Uniform Benchmark at Early Times

a steady-state value.

Table 5.2 shows the numerical error between the TBIT method and the benchmark after 20, 50, 70 and 100 mft have past. This table shows that the TBIT method has converged to within 0.56% of the benchmark solutions. As evident from the data, the error converges between the benchmark data and the TBIT results. Hence, the TBIT method also converges to the correct values.

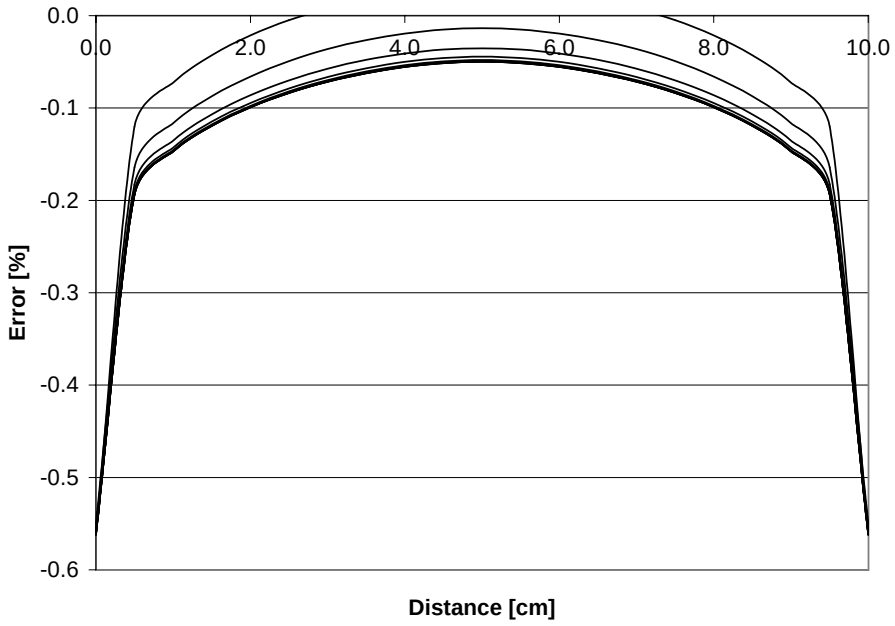

Figure 5.2: Error for TBIT Method vs Cartesian Homogeneous Uniform Benchmark at Late Times

Table 5.1: TBIT vs Cartesian Homogeneous Uniform Benchmark at Early Times

Distance [cm]	1.0 mft [Error %]	2.5 mft [Error %]	5.0 mft [Error %]	7.5 mft [Error %]	10.0 mft [Error %]
0.0	-1.201	-1.123	-0.643	-0.568	-0.536
0.5	-0.056	-0.118	-0.097	-0.104	-0.113
1.0	0.017	-0.038	-0.057	-0.065	-0.074
1.5	0.017	-0.002	-0.032	-0.042	-0.051
2.0	0.017	0.013	-0.013	-0.025	-0.035
2.5	0.017	0.015	0.000	-0.013	-0.022
3.0	0.017	0.015	0.008	-0.004	-0.012
3.5	0.017	0.015	0.011	0.003	-0.005
4.0	0.017	0.015	0.013	0.007	-0.001
4.5	0.017	0.015	0.013	0.009	0.002
5.0	0.017	0.015	0.013	0.010	0.003
5.5	0.017	0.015	0.013	0.009	0.002
6.0	0.017	0.015	0.013	0.007	-0.001
6.5	0.017	0.015	0.011	0.003	-0.005
7.0	0.017	0.015	0.008	-0.004	-0.012
7.5	0.017	0.015	0.000	-0.013	-0.022
8.0	0.017	0.013	-0.013	-0.025	-0.035
8.5	0.017	-0.002	-0.032	-0.042	-0.051
9.0	0.017	-0.038	-0.057	-0.065	-0.074
9.5	-0.056	-0.118	-0.097	-0.104	-0.113
10.0	-1.201	-1.123	-0.643	-0.568	-0.536

Table 5.2: TBIT vs Cartesian Homogeneous Uniform Benchmark at Late Times

Distance [cm]	20 mft [Error %]	50 mft [Error %]	70 mft [Error %]	100 mft [Error %]
0.0	-0.550	-0.561	-0.561	-0.562
0.5	-0.164	-0.192	-0.192	-0.194
1.0	-0.116	-0.146	-0.146	-0.147
1.5	-0.087	-0.118	-0.118	-0.119
2.0	-0.066	-0.098	-0.098	-0.099
2.5	-0.049	-0.082	-0.082	-0.084
3.0	-0.036	-0.070	-0.070	-0.072
3.5	-0.026	-0.060	-0.060	-0.062
4.0	-0.019	-0.054	-0.054	-0.055
4.5	-0.015	-0.049	-0.049	-0.051
5.0	-0.014	-0.048	-0.048	-0.050
5.5	-0.015	-0.049	-0.049	-0.051
6.0	-0.019	-0.054	-0.054	-0.055
6.5	-0.026	-0.060	-0.060	-0.062
7.0	-0.036	-0.070	-0.070	-0.072
7.5	-0.049	-0.082	-0.082	-0.084
8.0	-0.066	-0.098	-0.098	-0.099
8.5	-0.087	-0.118	-0.118	-0.119
9.0	-0.116	-0.146	-0.146	-0.147
9.5	-0.164	-0.192	-0.192	-0.194
10.0	-0.550	-0.561	-0.561	-0.562

5.1.2 Benchmark Homogeneous Cartesian with Localized Source

The one dimensional homogeneous benchmark with a localized source in Cartesian coordinates was compared against the results obtained from the TBIT method. The geometry for this benchmark was shown previously in Figure 3.7.

Figure 5.3 shows the percent error for the TBIT method verses the second benchmark case from zero until 10 mean free times. Each curve represents the passage of 0.5 mft. As shown in Figure 5.3, the maximum error occurs at the wave front as it moves out from the central source region. The maximum error peaks at roughly 1.0% roughly 1.5 mfp from the vacuum boundary. After this point, the error on the wave front decreases as it approaches the vacuum boundary. After the wave front passes out of the material, the maximum error continually decreases, from 6 mft until 10 mft. At 10 mft, the maximum error over the entire slab is less than 0.2%.

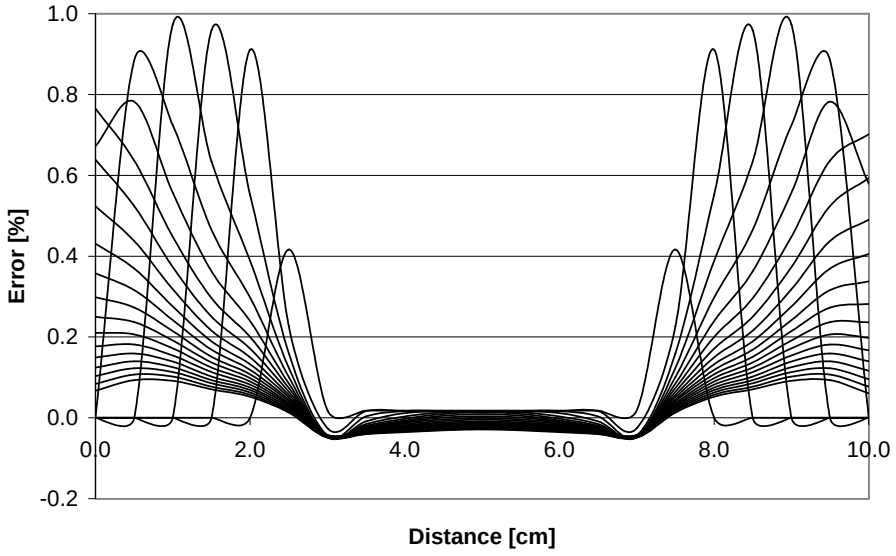

Figure 5.3: Error for TBIT Method vs Cartesian Homogeneous Localized Benchmark at Early Times

Table 5.3 shows the numerical error between the TBIT method and the benchmark at fix distances after 1.0, 2.5, 5.0, 7.5, and 10.0 mean free times.

Figure 5.4 shows the percent error for the TBIT method verses the second benchmark case from 10 until 100 mean free times. Each line represents a time-step of 10 mft. As with the first benchmark, the maximum error occurs at the vacuum boundary condition with the TBIT method converging on a steady-state solution. However, in this case there is a localized maximum error that occurs near the source boundary. The absolute value for the error is increasing over the simulation until a steady-state solution is achieved after approximately 50 mft. At that point the error converges.

As mentioned and explained in the previous section, the error over the slab is slightly asymmetric. This is evident from the figure as the error on the right side of the slab is slightly higher that that on the left.

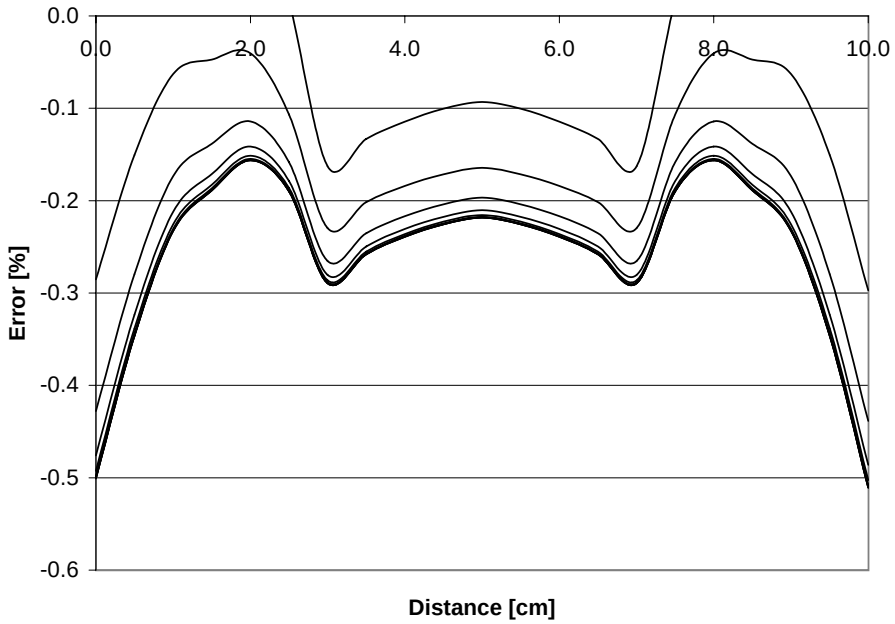

Figure 5.4: Error for TBIT Method vs Cartesian Homogeneous Localized Benchmark at Late Times

Table 5.4 shows the numerical error between the TBIT method and the benchmark after 20, 50, 70 and 100 mean free times have past. This table shows that the TBIT method has converged to within 0.50% of the correct steady-state value as given by the second benchmark.

Table 5.3: TBIT vs Cartesian Homogeneous Localized Benchmark at Early Times

Distance [cm]	1.0 mft [Error %]	2.5 mft [Error %]	5.0 mft [Error %]	7.5 mft [Error %]	10.0 mft [Error %]
0.0	0.000	0.000	0.431	0.177	0.067
0.5	0.000	0.884	0.369	0.182	0.093
1.0	0.000	0.724	0.275	0.154	0.092
1.5	0.000	0.465	0.189	0.113	0.071
2.0	0.911	0.298	0.133	0.082	0.052
2.5	0.227	0.101	0.051	0.029	0.013
3.0	-0.026	-0.048	-0.043	-0.045	-0.049
3.5	0.017	-0.015	-0.026	-0.034	-0.041
4.0	0.017	0.003	-0.015	-0.027	-0.035
4.5	0.017	0.014	-0.008	-0.022	-0.031
5.0	0.017	0.016	-0.005	-0.020	-0.029
5.5	0.017	0.014	-0.008	-0.022	-0.031
6.0	0.017	0.003	-0.015	-0.027	-0.035
6.5	0.017	-0.015	-0.026	-0.034	-0.041
7.0	-0.026	-0.048	-0.043	-0.045	-0.049
7.5	0.227	0.101	0.051	0.029	0.013
8.0	0.911	0.298	0.133	0.082	0.052
8.5	0.000	0.465	0.189	0.113	0.071
9.0	0.000	0.724	0.275	0.154	0.092
9.5	0.000	0.884	0.369	0.182	0.093
10.0	0.000	0.000	0.431	0.177	0.067

Table 5.4: TBIT vs Cartesian Homogeneous Localized Benchmark at Late Times

Distance [cm]	20 mft [Error %]	50 mft [Error %]	70 mft [Error %]	100 mft [Error %]
0.0	-0.285	-0.493	-0.500	-0.501
0.5	-0.151	-0.338	-0.346	-0.346
1.0	-0.063	-0.226	-0.232	-0.232
1.5	-0.047	-0.183	-0.188	-0.189
2.0	-0.040	-0.151	-0.156	-0.156
2.5	-0.107	-0.186	-0.190	-0.190
3.0	-0.230	-0.286	-0.289	-0.289
3.5	-0.202	-0.255	-0.258	-0.258
4.0	-0.184	-0.236	-0.239	-0.239
4.5	-0.172	-0.223	-0.225	-0.226
5.0	-0.164	-0.216	-0.218	-0.218
5.5	-0.172	-0.223	-0.225	-0.226
6.0	-0.184	-0.236	-0.239	-0.239
6.5	-0.202	-0.255	-0.258	-0.258
7.0	-0.230	-0.286	-0.289	-0.289
7.5	-0.107	-0.186	-0.190	-0.190
8.0	-0.040	-0.151	-0.156	-0.156
8.5	-0.047	-0.183	-0.188	-0.189
9.0	-0.063	-0.226	-0.232	-0.232
9.5	-0.151	-0.338	-0.346	-0.346
10.0	-0.285	-0.493	-0.500	-0.501

5.1.3 Benchmark Homogeneous Spherical with Localized Source

The one-dimensional homogeneous benchmark with a localized source in spherical coordinates was compared against the results obtained from the TBIT method. The geometry for this benchmark is shown in Figure 3.11.

Figure 5.5 shows the percent error for the TBIT method verses the homogeneous spherical benchmark from zero until ten mean free times. Each curve represents one-half of a mean free time of output. As shown in the figure, the error is highest on the inward launched particle wave as it travels from the outer source region into the non-source interior. The error, however, remains less than 2.0% for the first 10 mft. The maximum error occurs 1.5 mfp from the center of the sphere. After the inward launched wave has passed this point, the maximum error decreases through the remainder of the simulation. As for the previous two cases, the TBIT method predicts values for the flux in the source region slightly less than the benchmark results.

Table 5.5 shows the numerical error between the TBIT method and the benchmark at fixed distances after 1.0, 2.5, 5.0, 7.5, and 10.0 mean free times have past.

Figure 5.6 shows the percent error for the TBIT method verses the localized spherical benchmark for times between 10 and 100 mft. Each curve represents a time-step of 10 mft. As expected from the previous comparisons, the error peaks near the vacuum boundary.

In addition, in this particular case the error also peaks nearest to the center of the sphere. The closer particles get to the center of the sphere, the greater the change in their streaming angles. As with the previous cases, the TBIT method converged to the correct steady-state solution. However, for this spherical case the agreement is to within 1.5%.

Table 5.6 shows the numerical error between the TBIT method and the benchmark

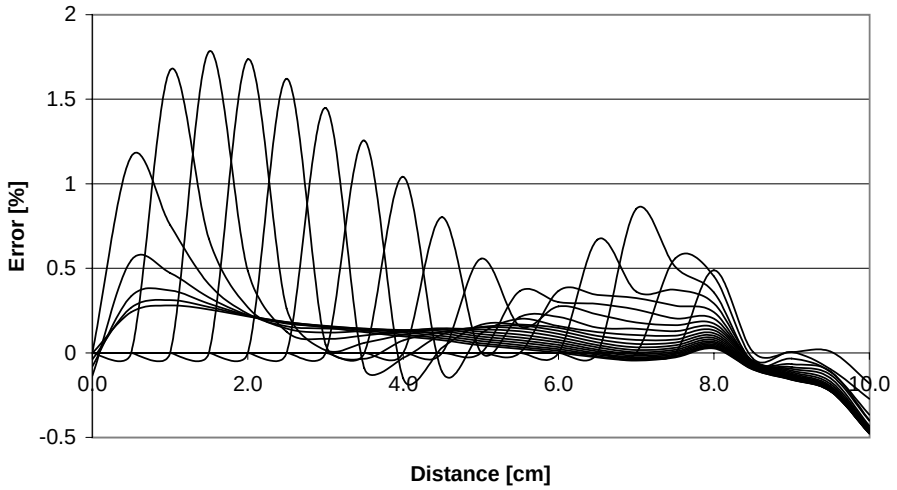

Figure 5.5: Error for TBIT Method vs Spherical Homogeneous Localized Benchmark at Early Times

after 20, 50, 70 and 100 mean free times have past.

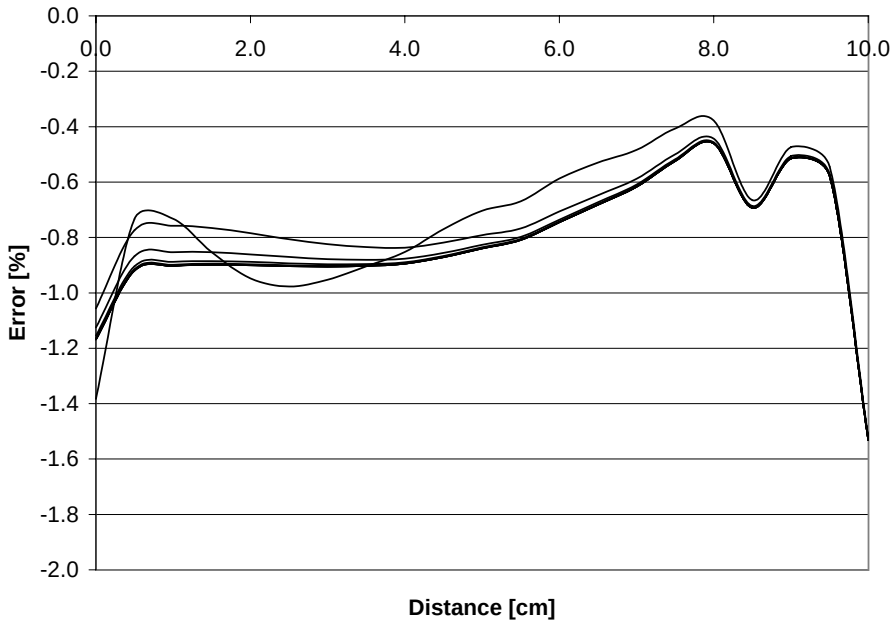

Figure 5.6: Error for TBIT Method vs Spherical Homogeneous Localized Benchmark at Late Times

Table 5.5: TBIT vs Spherical Homogeneous Localized Benchmark at Early Times

Distance [cm]	1.0 mft [Error %]	2.5 mft [Error %]	5.0 mft [Error %]	7.5 mft [Error %]	10.0 mft [Error %]
0.0	0.000	0.000	0.000	0.000	-0.001
0.5	0.000	0.000	0.000	0.000	0.240
1.0	0.000	0.000	0.000	1.671	0.280
1.5	0.000	0.000	0.000	0.676	0.256
2.0	0.000	0.000	0.000	0.269	0.215
2.5	0.000	0.000	0.000	0.144	0.179
3.0	0.000	0.000	0.000	0.120	0.150
3.5	0.000	0.000	1.255	0.130	0.123
4.0	0.000	0.000	-0.151	0.134	0.097
4.5	0.000	0.000	0.031	0.138	0.075
5.0	0.000	0.000	0.166	0.111	0.045
5.5	0.000	0.000	0.168	0.091	0.023
6.0	0.000	0.366	0.147	0.061	0.001
6.5	0.000	0.343	0.100	0.020	-0.028
7.0	0.000	0.323	0.076	-0.007	-0.045
7.5	0.559	0.279	0.079	0.008	-0.028
8.0	0.453	0.240	0.116	0.057	0.026
8.5	-0.034	-0.054	-0.060	-0.085	-0.099
9.0	0.005	-0.084	-0.129	-0.150	-0.160
9.5	-0.097	-0.130	-0.205	-0.222	-0.229
10.0	-0.272	-0.402	-0.460	-0.473	-0.478

Table 5.6: TBIT vs Spherical Homogeneous Localized Benchmark at Late Times

Distance [cm]	20 mft [Error %]	50 mft [Error %]	70 mft [Error %]	100 mft [Error %]
0.0	-1.057	-1.164	-1.168	-1.168
0.5	-0.774	-0.915	-0.919	-0.919
1.0	-0.758	-0.898	-0.902	-0.902
1.5	-0.766	-0.895	-0.898	-0.898
2.0	-0.785	-0.897	-0.899	-0.900
2.5	-0.807	-0.901	-0.903	-0.903
3.0	-0.824	-0.903	-0.905	-0.905
3.5	-0.835	-0.901	-0.902	-0.903
4.0	-0.837	-0.893	-0.894	-0.895
4.5	-0.818	-0.870	-0.871	-0.871
5.0	-0.791	-0.838	-0.839	-0.839
5.5	-0.767	-0.808	-0.810	-0.809
6.0	-0.706	-0.744	-0.745	-0.745
6.5	-0.647	-0.682	-0.682	-0.681
7.0	-0.588	-0.616	-0.617	-0.616
7.5	-0.500	-0.523	-0.524	-0.524
8.0	-0.443	-0.460	-0.460	-0.460
8.5	-0.687	-0.693	-0.693	-0.693
9.0	-0.506	-0.515	-0.515	-0.515
9.5	-0.572	-0.578	-0.579	-0.579
10.0	-1.530	-1.531	-1.531	-1.532

5.1.4 Benchmark Heterogeneous Cartesian with Localized Source

The one-dimensional heterogeneous benchmark with a localized source in Cartesian coordinates was compared against the results obtained from the TBIT method. The geometry for this benchmark was shown in Figure 3.15.

Figure 5.7 shows the percent error for the TBIT method verses the fourth, and final, benchmark case from zero until 10 mean free times. Each curve represents one half of a mean free time of output. As with the localized homogeneous case, the maximum error occurs on the wave boundary as it travels away from the source region. For the time period up until the wave hits the boundary, the TBIT method errors on the positive side. After that point, the error slowly decreases until by the 10 mft the TBIT method errors completely on the negative side from the benchmark case.

Unlike the homogeneous case, the material discontinuity has an effect on the error. This is evident as the TBIT method predicts slightly lower results in the area immediately to either side of the material boundary after the particle wave has passed outside the material (after 5 mft).

From Figure 5.7 a relatively large error, as compared to the global errors in this problem, is noticed at the material/source interface conditions. This error can be explained because the heterogeneous benchmark and the TBIT simulation are not exactly identical. This slight difference is due to the different methods by which the TBIT method and the standard method define material boundaries. For the standard method used in the benchmark, the nodes lay immediately on the material discontinuity. Whereas for the TBIT method, the material is defined on the node and thus material discontinuities change at $dx/2$. Therefore, as the number of nodes $\rightarrow \infty$ the error goes to zero. However for this benchmark case, 640 nodes were uniformly scattered over the 10 mfp (10 cm) of the slab. Thus, there is a difference of: $0.5 \times dx = 5/640$ or 0.0078125 cm between the

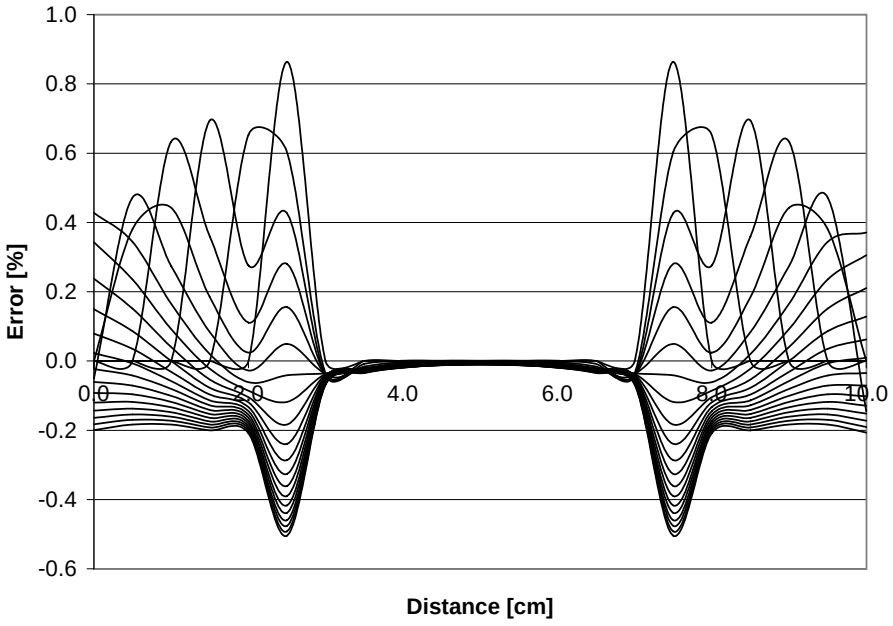

Figure 5.7: Error for TBIT Method vs Cartesian Heterogeneous Localized Benchmark at Early Times

two.

Table 5.7 shows the numerical error between the TBIT method and the benchmark at fix distances and after 1.0, 2.5, 5.0, 7.5, and 10.0 mean free times. As mentioned previously and shown in the table, the TBIT method produces results that are slightly asymmetric across the slab.

Figure 5.8 shows the percent error for the TBIT method verses the heterogeneous benchmark case from 10 until 100 mean free times. Each curve represents a time-step of 10 mft. As with all of the previous benchmarks, the maximum error occurs at the vacuum boundary. In addition the error also peaks near the material discontinuity; however, the reason for this error was explained earlier. In addition, a steady state-solution is achieved as evident from the convergence of the error solutions.

Table 5.8 shows the numerical error between the TBIT method and the benchmark

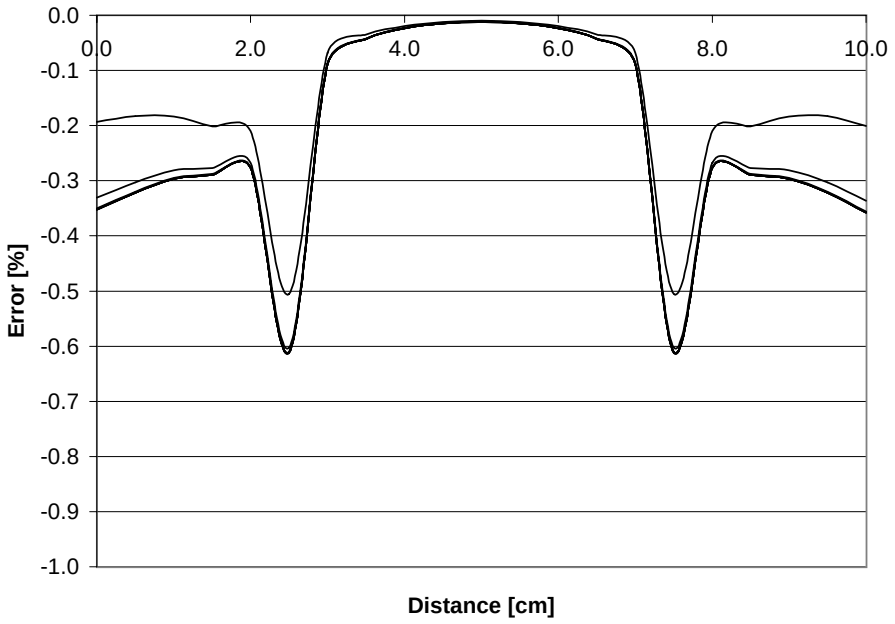

Figure 5.8: Error for TBIT Method vs Cartesian Heterogeneous Localized Benchmark at Late Times

after 20, 50, 70 and 100 mean free times have past. This table shows that the TBIT method has converged to within 0.350% of the correct steady-state value.

From these one-dimensional benchmarks, several conclusions can be made. First, the TBIT method errors the greatest near vacuum and/or source boundary conditions. In addition, the TBIT method produces results that can be slightly asymmetric. As mentioned in Section 5.1.1, within each bubble the scattered and boundary source terms can converge to slightly differing results because of the interpolation routines used.

A second observation is that on the outward particle wave, the TBIT method always errors on the positive side. The reason for this behavior, is that particles on the wave can only be emitted in very specific angular sectors. For example, in order to travel 5 mfp from the emission location after 10 mean free times, particles have to be emitted from $-\pi/4$ to $\pi/4$. However, because the TBIT method uses finite directions, it includes

all particles between $-\pi/4 - \epsilon$ to $\pi/4 + \epsilon$ to make absolutely sure that all particles are included. This causes the TBIT method to overestimate the flux by some small amount inversely proportional to the number of angular directions used.

The final global observation that can be made, is that for all the cases, the steady-state TBIT calculation converge to a solution that is a fraction of a percent less than the 'true' solution as defined by the benchmark problem. This indicates the that TBIT method is to some small extent losing particles. This issue will be addressed in Section 5.4 when a particle balance will be applied to the one-dimensional heterogeneous benchmark using the TBIT method.

Table 5.7: TBIT vs Cartesian Heterogeneous Localized Benchmark at Early Times

Distance [cm]	1.0 mft [Error %]	2.5 mft [Error %]	5.0 mft [Error %]	7.5 mft [Error %]	10.0 mft [Error %]
0.0	0.000	0.000	0.149	-0.093	-0.200
0.5	0.000	0.381	0.086	-0.097	-0.183
1.0	0.000	0.442	0.000	-0.118	-0.183
1.5	0.000	0.184	-0.078	-0.153	-0.200
2.0	0.653	0.024	-0.120	-0.173	-0.208
2.5	0.603	0.156	-0.239	-0.417	-0.504
3.0	-0.036	-0.038	-0.043	-0.057	-0.068
3.5	0.000	-0.021	-0.025	-0.030	-0.035
4.0	0.000	-0.006	-0.014	-0.017	-0.019
4.5	0.000	0.000	-0.007	-0.010	-0.012
5.0	0.000	0.000	-0.005	-0.009	-0.010
5.5	0.000	0.000	-0.007	-0.010	-0.012
6.0	0.000	-0.006	-0.014	-0.017	-0.019
6.5	0.000	-0.021	-0.025	-0.030	-0.035
7.0	-0.036	-0.038	-0.043	-0.057	-0.068
7.5	0.603	0.156	-0.239	-0.417	-0.504
8.0	0.653	0.024	-0.120	-0.173	-0.208
8.5	0.000	0.184	-0.078	-0.153	-0.200
9.0	0.000	0.442	0.000	-0.118	-0.183
9.5	0.000	0.381	0.086	-0.097	-0.183
10.0	0.000	0.000	0.149	-0.093	-0.207

Table 5.8: TBIT vs Cartesian Heterogeneous Localized Benchmark at Late Times

Distance [cm]	20 mft [Error %]	50 mft [Error %]	70 mft [Error %]	100 mft [Error %]
0.0	-0.331	-0.352	-0.352	-0.352
0.5	-0.303	-0.322	-0.322	-0.322
1.0	-0.281	-0.297	-0.297	-0.297
1.5	-0.277	-0.289	-0.289	-0.289
2.0	-0.267	-0.276	-0.276	-0.276
2.5	-0.603	-0.612	-0.611	-0.611
3.0	-0.087	-0.089	-0.089	-0.089
3.5	-0.042	-0.043	-0.043	-0.043
4.0	-0.023	-0.023	-0.023	-0.023
4.5	-0.014	-0.015	-0.015	-0.015
5.0	-0.012	-0.012	-0.012	-0.012
5.5	-0.014	-0.015	-0.015	-0.015
6.0	-0.023	-0.023	-0.023	-0.023
6.5	-0.042	-0.043	-0.043	-0.043
7.0	-0.087	-0.089	-0.089	-0.089
7.5	-0.603	-0.612	-0.611	-0.611
8.0	-0.087	-0.089	-0.089	-0.089
8.5	-0.277	-0.289	-0.289	-0.289
9.0	-0.281	-0.297	-0.297	-0.297
9.5	-0.303	-0.322	-0.322	-0.322
10.0	-0.331	-0.352	-0.352	-0.352

5.2 Two-Dimensional Spherical TBIT comparisons to Benchmarks

A two-dimensional spherical calculation was compared to the finite media spherical localized benchmark (number 3). Whereas, a two-dimensional Cartesian problem can not be formulated in such a way that the one-dimensional Cartesian benchmarks are valid, a two-dimensional spherical problem is easily compared to the one-dimensional benchmark. The two-dimensional formulation of the one-dimensional spherical benchmark was shown in Figure 3.11.

Figure 5.9 shows the percent error for the TBIT method verses the third benchmark case from zero until 10 mean free times. On the figure each curve represents one half of a mean free time of output. As shown in the figure, the error is highest on the inward launched particle wave as it travels from the source region into the non-source interior. This behavior is identical to that shown for the one-dimensional spherical case. However, the error in the two-dimensional spherical case reaches a maximum of 4.0% for the first 10 mft.

Table 5.9 shows the numerical error between the TBIT method and the benchmark at fixed distances and at 1.0, 2.5, 5.0, 7.5, and 10.0 mean free times.

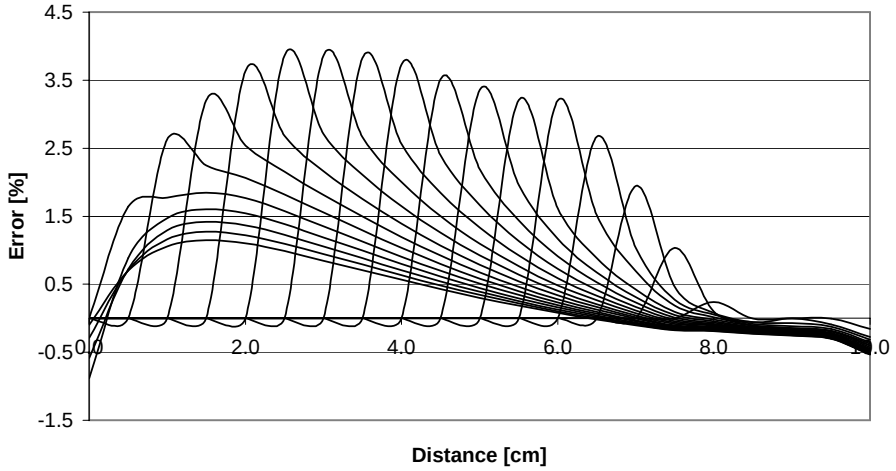

Figure 5.9: Two-Dimensional TBIT comparison to Spherical Homogeneous Cartesian Localized Benchmark

Table 5.9: Two-Dimensional TBIT comparison to Spherical Benchmark

Distance [cm]	1.0 mft [Error %]	2.5 mft [Error %]	5.0 mft [Error %]	7.5 mft [Error %]	10.0 mft [Error %]
0.0	0.000	0.000	0.000	0.000	-0.097
0.5	0.000	0.000	0.000	0.000	0.701
1.0	0.000	0.000	0.000	2.630	1.057
1.5	0.000	0.000	0.000	2.249	1.147
2.0	0.000	0.000	0.000	2.064	1.100
2.5	0.000	0.000	0.000	1.822	0.987
3.0	0.000	0.000	0.000	1.554	0.847
3.5	0.000	0.000	3.829	1.294	0.707
4.0	0.000	0.000	2.565	1.036	0.566
4.5	0.000	0.000	1.844	0.800	0.430
5.0	0.000	0.000	1.334	0.583	0.301
5.5	0.000	0.000	0.926	0.397	0.185
6.0	0.000	3.201	0.589	0.233	0.078
6.5	0.000	1.515	0.331	0.093	-0.016
7.0	0.000	0.692	0.117	-0.029	-0.103
7.5	1.033	0.188	-0.046	-0.131	-0.179
8.0	0.103	0.016	-0.098	-0.156	-0.191
8.5	-0.055	-0.107	-0.161	-0.202	-0.227
9.0	-0.003	-0.148	-0.194	-0.232	-0.254
9.5	-0.094	-0.190	-0.239	-0.278	-0.299
10.0	-0.277	-0.402	-0.462	-0.511	-0.535

The error plots between the one and two dimensional spherical cases are striking. Both figures have similar features: negative error in the source region, error peaking on inward particle wave and decreasing once the wave reaches the center of the sphere. The only major difference between the two is that for the two-dimensional case, the inward error peaks at 3.0 mfp instead of 1.5 for the one-dimensional case.

5.3 Three-Dimensional TBIT comparisons to finite benchmarks

In a similar fashion to the calculations in Section 5.2, benchmark comparisons can be made with a three-dimensional spherical problem. However, unlike all of the other TBIT benchmark validation cases, six levels of Romberg integration were not used. For this particular case only three levels are used. This was not because of any problem with the algorithm, but was caused by the limitations placed by the computer hardware used in the numerical evaluation. The TBIT method stores all the values for the current and the previous value of the angular flux as double precision values. Thus, if there are 20 nodes in the radial direction, 20 in the θ, 10 in the ϕ, 20 in the μ, and 10 in the η. This amounts to 1.6 million entries for all the angular values for the current and the previous time-step, or 25 megabytes of ram. The sixth level of the Romberg integration would produce memory requirements 64 times this or over 1 gigabyte of addressable memory just for the angular flux. In order to produce run-times that did not require a substantial amount of hard-disk swapping three Romberg integration levels were used.

Figure 5.10 shows the percent error for the three-dimensional spherical TBIT method verses the first benchmark case from zero until 10 mft. Each curve represents one-half of a mean free time of output. As with all the comparisons, the highest error occurs on the wave front as it is launched inwards. For the three-dimensional case, the maximum error occurs once the wave is 1 mft from the center of the slab, and peaks at nearly 7.0%.

Comparing the one, two and three dimensional spherical TBIT benchmarks show that with each additional dimension the maximum error increases. However, as mentioned previously, the three-dimensional case was not run to the same level of Romberg convergence criteria as the one and two dimensional cases.

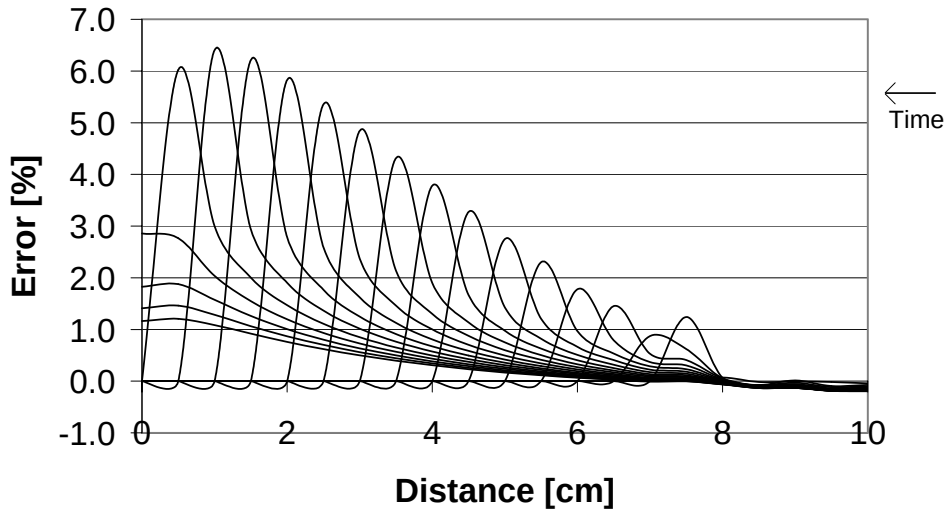

Figure 5.10: Three-Dimensional TBIT comparison to Spherical Homogeneous Cartesian Localized Benchmark

Table 5.10 shows the numerical error between the TBIT method and the benchmark at fix distances and at 1.0, 2.5, 5.0, 7.5, and 10.0 mean free times.

Table 5.10: Three-Dimensional TBIT comparison to Spherical Benchmark

Distance [cm]	1.0 mft [Error %]	2.5 mft [Error %]	5.0 mft [Error %]	7.5 mft [Error %]	10.0 mft [Error %]
0.0	0.000	0.000	0.000	0.000	1.161
0.5	0.000	0.000	0.000	0.000	1.204
1.0	0.000	0.000	0.000	6.400	1.083
1.5	0.000	0.000	0.000	2.940	0.919
2.0	0.000	0.000	0.000	1.901	0.760
2.5	0.000	0.000	0.000	1.367	0.620
3.0	0.000	0.000	0.000	1.015	0.499
3.5	0.000	0.000	4.313	0.764	0.396
4.0	0.000	0.000	1.898	0.574	0.307
4.5	0.000	0.000	1.138	0.427	0.231
5.0	0.000	0.000	0.751	0.309	0.167
5.5	0.000	0.000	0.502	0.216	0.112
6.0	0.000	1.777	0.327	0.139	0.065
6.5	0.000	0.789	0.207	0.081	0.027
7.0	0.000	0.368	0.109	0.028	-0.009
7.5	1.241	0.306	0.092	0.026	-0.005
8.0	0.064	0.038	-0.020	-0.049	-0.063
8.5	-0.074	-0.093	-0.115	-0.126	-0.132
9.0	0.015	-0.074	-0.111	-0.124	-0.131
9.5	-0.096	-0.150	-0.176	-0.184	-0.188
10.0	-0.072	-0.127	-0.173	-0.188	-0.194

5.4 TBIT comparisons to balance of particles

In an effort to make the TBIT method as accurate as possible, comparisons were made against the conservation equation. This was done to ensure that a particle balance around each nodal region was maintained, or more simply put the time rate of change for the number of particles in a specific region plus the number that leak out or are absorbed must equal the number of particles created in that particular region.

The conservation equation is obtained through the following simple derivation. The single speed Boltzmann equation can be written as:

$$\left[\frac{1}{v}\frac{\partial}{\partial t} + \hat{\Omega}\cdot\vec{\nabla} + \Sigma\left(\vec{r},E,t\right)\right]\psi\left(\vec{r},\hat{\Omega},E,t\right) = q\left(\vec{r},\hat{\Omega},Et\right). \tag{5.1}$$

Integrating Equation 5.1 over all angles one obtains:

$$\begin{aligned}\frac{1}{v}\frac{1}{\partial t}\int d\Omega\,\psi\left(\vec{r},\hat{\Omega},E,t\right) + \vec{\nabla}\cdot\int d\Omega\,\psi\left(\vec{r},\hat{\Omega},E,t\right)\\ \Sigma\left(\vec{r},E,t\right)\int d\Omega\,\psi\left(\vec{r},\hat{\Omega},E,t\right) = \int d\Omega\,q\left(\vec{r},\hat{\Omega},E,t\right).\end{aligned} \tag{5.2}$$

Using the standard definitions for the scalar flux and current and defining:

$$Q\left(\vec{r},E,t\right) = \int d\Omega q\left(\vec{r},\hat{\Omega},E,t\right), \tag{5.3}$$

one obtains the standard form for the balance or conservation equation as:

$$\frac{1}{v}\frac{\partial}{\partial t}\Phi\left(\vec{r},E,t\right) + \vec{\nabla}\cdot\vec{J}\left(\vec{r},E,t\right) + \Sigma\left(\vec{r},E,t\right)\Phi\left(\vec{r},E,t\right) = Q\left(\vec{r},E,t\right). \tag{5.4}$$

Implementing a simple numerical scheme to numerically difference Equation 5.4 and bringing the source term to the left hand side one arrives at the following:

$$\frac{\Phi_i^{n+1}-\Phi_i^n}{\Delta x} + \frac{\Sigma_a}{2}\left(\Phi_i^{n+1}-\Phi_i^n\right) + \frac{\left(J_{i+1}^{n+1}+J_{i+1}^n-J_{i-1}^{n+1}-J_{i-1}^n\right)}{4\Delta x\Sigma_a} + \frac{1}{2}\left(Q_i^{n+1}+Q_i^n\right) = 0 \tag{5.5}$$

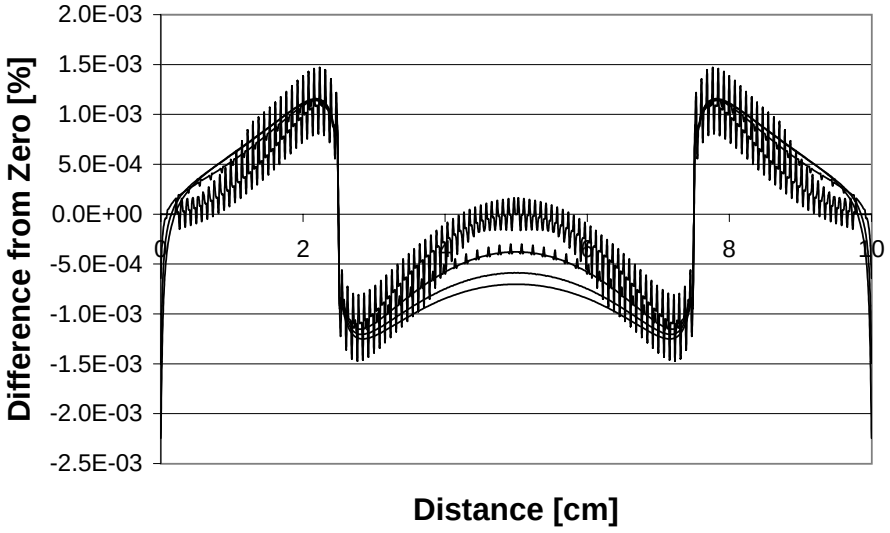

Figure 5.11: Particle Balance for the TBIT Method

where: n is the time index, i is the spatial index, and recalling that Δx is defined as $v\Delta t$. The particle current is defined at each cell as:

$$\vec{J} \equiv \int d\Omega \hat{\Omega} \psi \left(\vec{r}, \hat{\Omega}, E, t \right). \tag{5.6}$$

Equation 5.5 was implemented in the TBIT code as a check for the one-dimensional benchmarks described earlier in the chapter. At every spatial node for every time-step a simple check was performed to make sure that the particle balance was correct. Figure 5.11 shows the deviation from zero for the right hand side of Equation 5.5.

The results presented in this section are for the one-dimensional heterogeneous benchmark with 640 nodes distributed throughout the interior of the slab. The same heterogeneous materials used in the earlier benchmark were used for this balance calculation, Table 3.13. Four different curves are shown on the figure. These curves correspond to the particle balance after: 2.5, 5.0, 7.5, and 10.0 mft. Hence, at the last output particles have traveled completely across the slab. The curve shown with the high frequency response is

the balance at 2.5 mft. As shown in the figure, the balance at 2.5 mft balances particles almost exactly in the center of the slab. As time progresses, the balance in the center source region errors on the negative side.

As shown in Figure 5.11 a majority of nodes conserve particles to within 1 part in 10^5. Points close to the vacuum boundary conserve particles to within 1.5 parts in 10^5. As expected, in those regions that are source driven (central region) differ from zero by a negative amount. This is because the external source term Q dominates and contributes a negative quantity to Equation 5.5. Likewise, the regions that are dominated by streaming deviate from zero by a positive amount.

Table 5.11 shows the numerical deviation from zero. If the number of particles are conserved, both sides of Equation 5.5 are identical to zero. If the balance of particles is increasing, then a numerical evaluation of Equation 5.5 will be negative, and, similarly, if the balance is decreasing a numerical evaluation of Equation 5.5 will result in a positive value.

Table 5.11: Balance of Particles for TBIT Method

Distance [cm]	2.5 mft [Error %]	5.0 mft [Error %]	7.5 mft [Error %]	10.0 mft [Error %]
0.0	0.000E+00	-6.427E-04	-1.494E-03	-2.247E-03
0.5	-9.346E-05	3.035E-04	3.377E-04	3.226E-04
1.0	3.001E-04	5.289E-04	5.954E-04	6.020E-04
1.5	5.908E-04	8.060E-04	8.570E-04	8.608E-04
2.0	1.383E-03	1.088E-03	1.113E-03	1.104E-03
2.5	-2.245E-06	-2.572E-06	-2.200E-05	-5.261E-05
3.0	-1.387E-03	-1.096E-03	-1.168E-03	-1.223E-03
3.5	-5.953E-04	-8.257E-04	-9.441E-04	-1.022E-03
4.0	-3.049E-04	-5.989E-04	-7.489E-04	-8.457E-04
4.5	9.012E-05	-4.293E-04	-6.269E-04	-7.382E-04
5.0	-2.472E-06	-3.784E-04	-5.883E-04	-7.025E-04
5.5	9.012E-05	-4.293E-04	-6.269E-04	-7.382E-04
6.0	-3.049E-04	-5.989E-04	-7.489E-04	-8.457E-04
6.5	-5.953E-04	-8.257E-04	-9.441E-04	-1.022E-03
7.0	-1.387E-03	-1.096E-03	-1.168E-03	-1.223E-03
7.5	-2.245E-06	-2.572E-06	-2.200E-05	-5.261E-05
8.0	1.383E-03	1.088E-03	1.113E-03	1.104E-03
8.5	5.908E-04	8.060E-04	8.570E-04	8.608E-04
9.0	3.001E-04	5.289E-04	5.954E-04	6.020E-04
9.5	-9.346E-05	3.035E-04	3.377E-04	3.226E-04
10.0	0.000E+00	-6.427E-04	-1.494E-03	-2.247E-03

5.5 TBIT calculation of a Two-Dimensional Finite Heterogeneous Media Benchmark

The previous sections demonstrated that the TBIT technique produced results that were within a fraction of a percent, for Cartesian geometries, and within a few percent, for spherical geometries, to the time-dependent finite media benchmarks. The higher error in spherical geometries is due, in most part, to the added difficulties in calculating the streaming angles when particles traverse the geometry. However, all the previous comparisons with TBIT have been against one-dimensional benchmarks. This restriction was placed because of the complications involved with analytically solving for the uncollided flux and integrating the kernel in more than one dimension. In an effort to supply a benchmark in two-dimensions that should be within 1% of the actual value, a two-dimensional TBIT benchmark problem was run.

The geometry of the problem is shown in Figure 5.12 and the material properties are given in Table 3.13. The inner source region is a square with inner dimensions that run from 2.25 to 7.75 cm.

As with the previous benchmark cases, six levels of Romberg integration were run and a converged result was calculated. The scalar flux at selected points at 1.0, 2.5, 5.0, 7.5, and 10.0 mft are given in Tables 5.12, 5.13, 5.14, 5.15, and 5.16.

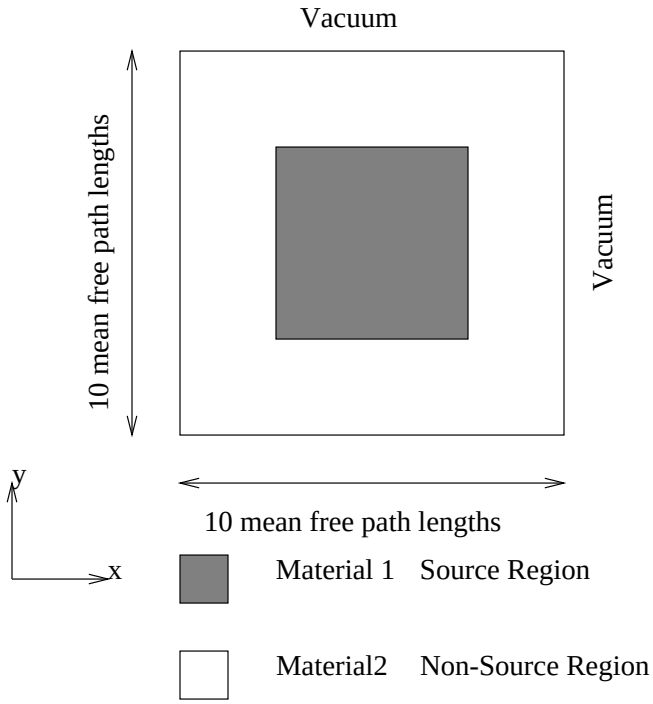

Figure 5.12: Geometry for Two-Dimensional Heterogeneous Benchmark

Table 5.12: Particle Flux at 1.0 mft for Two-Dimensional Heterogeneous Benchmark

x/y [cm]	0.0	1.0	2.0	3.0	4.0	5.0
0.0	0.00E+00	0.00E+00	0.00E+00	0.000E+00	0.00E+00	0.00E+00
1.0	0.00E+00	0.00E+00	0.00E+00	0.00E+00	0.000E+00	0.00E+00
2.0	0.00E+00	0.00E+00	0.00E+00	0.00E+00	0.000E+00	0.00E+00
3.0	0.00E+00	0.00E+00	0.00E+00	4.42E-01	4.42E-01	4.42E-01
4.0	0.00E+00	0.00E+00	0.00E+00	4.42E-01	4.42E-01	4.42E-01
5.0	0.00E+00	0.00E+00	0.00E+00	4.42E-01	4.42E-01	4.42E-01

Table 5.13: Particle Flux at 2.5 mft for Two-Dimensional Heterogeneous Benchmark

x/y [cm]	0.0	1.0	2.0	3.0	4.0	5.0
0.0	0.00E+00	0.00E+00	0.00E+00	0.00E+00	0.00E+00	0.00E+00
1.0	0.00E+00	2.232E-03	1.94E-02	4.82E-02	6.51E-02	6.71E-02
2.0	0.00E+00	1.937E-02	1.07E-01	2.63E-01	3.45E-01	3.58E-01
3.0	0.00E+00	4.82E-02	2.63E-01	9.81E-01	1.16E+00	1.17E+00
4.0	0.00E+00	6.51E-02	3.45E-01	1.16E+00	1.38E+00	1.41E+00
5.0	0.00E+00	6.71E-02	3.58E-01	1.17E+00	1.41E+00	1.43E+00

Table 5.14: Particle Flux at 5.0 mft for Two-Dimensional Heterogeneous Benchmark

x/y [cm]	0.0	1.0	2.0	3.0	4.0	5.0
0.0	3.46E-03	1.27E-02	2.78E-02	4.62E-02	6.08E-02	6.61E-02
1.0	1.27E-02	4.69E-02	1.02E-01	1.72E-01	2.25E-01	2.43E-01
2.0	2.78E-02	1.02E-01	2.37E-01	4.35E-01	5.63E-01	5.96E-01
3.0	4.62E-02	1.72E-01	4.35E-01	1.16E+00	1.39E+00	1.43E+00
4.0	6.08E-02	2.25E-01	5.63E-01	1.39E+00	1.68E+00	1.73E+00
5.0	6.61E-02	2.43E-01	5.96E-01	1.43E+00	1.73E+00	1.78E+00

Table 5.15: Particle Flux at 7.5 mft for Two-Dimensional Heterogeneous Benchmark

x/y [cm]	0.0	1.0	2.0	3.0	4.0	5.0
0.0	0.00E+00	0.00E+00	0.00E+00	0.00E+00	0.00E+00	0.00E+00
1.0	0.00E+00	2.23E-03	1.94E-02	4.82E-02	6.51E-02	6.71E-02
2.0	0.000E+00	1.94E-02	1.07E-01	2.63E-01	3.45E-01	3.58E-01
3.0	0.00E+00	4.82E-02	2.63E-01	9.81E-01	1.16E+00	1.17E+00
4.0	0.00E+00	6.51E-02	3.45E-01	1.16E+00	1.38E+00	1.41E+00
5.0	0.00E+00	6.71E-02	3.58E-01	1.17E+00	1.41E+00	1.43E+00

Table 5.16: Particle Flux at 10.0 mft for Two-Dimensional Heterogeneous Benchmark

x/y [cm]	0.0	1.0	2.0	3.0	4.0	5.0
0.0	1.74E-02	4.15E-02	6.85E-02	9.59E-02	1.16E-01	1.24E-01
1.0	4.15E-02	1.11E-01	1.91E-01	2.77E-01	3.40E-01	3.62E-01
2.0	6.85E-02	1.91E-01	3.52E-01	5.59E-01	6.95E-01	7.32E-01
3.0	9.59E-02	2.77E-01	5.59E-01	1.26E+00	1.48E+00	1.53E+00
4.0	1.16E-01	3.40E-01	6.95E-01	1.48E+00	1.77E+00	1.82E+00
5.0	1.24E-01	3.62E-01	7.32E-01	1.53E+00	1.82E+00	1.88E+00

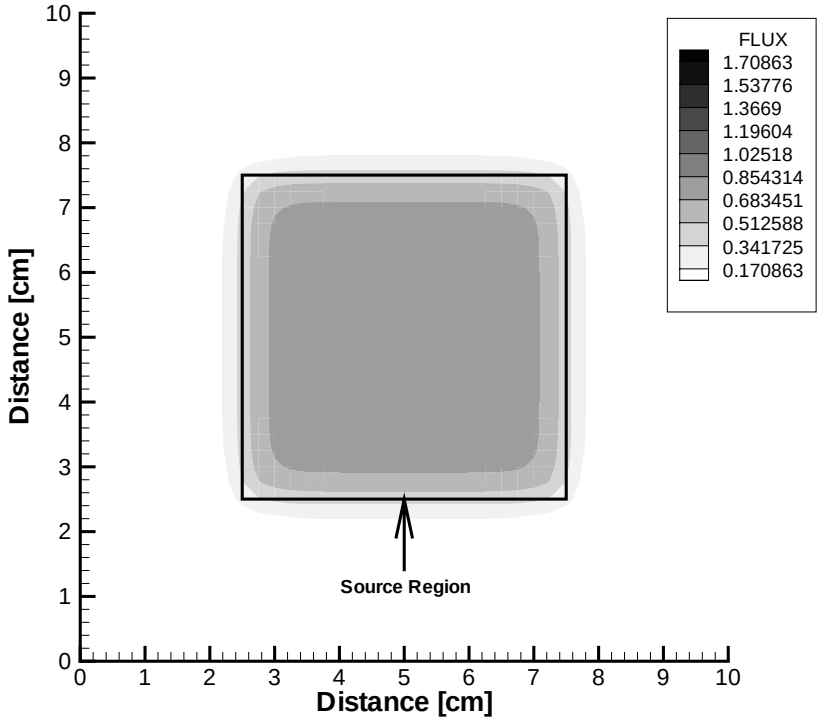

Figure 5.13: Particle Flux at 1.0 mft for Two-Dimensional Heterogeneous Benchmark

Similarly, graphical outputs at 1.0, 2.5, 5.0, 7.5, and 10.0 mft are shown in Figures 5.13, 5.14, 5.15, 5.16, 5.17. At early times, particles have made few collisions, and, therefore, a majority of the particles entering the outer non-source region are uncollided. The flux contours verify this by emulating the inner square source region. Although the magnitude of the uncollided flux decreases as time progresses and making it difficult to discertain from the figures, the sharp edges that result from the uncollided flux progress outwards until they reach the material boundary. At this point, all the points within the geometry can communicate with the inner source region.

As time progresses, particles are able to travel further away from the source region while undergoing multiple collisions. The flux contours at these later times show that the further one travels from the inner source region the more circular they become.

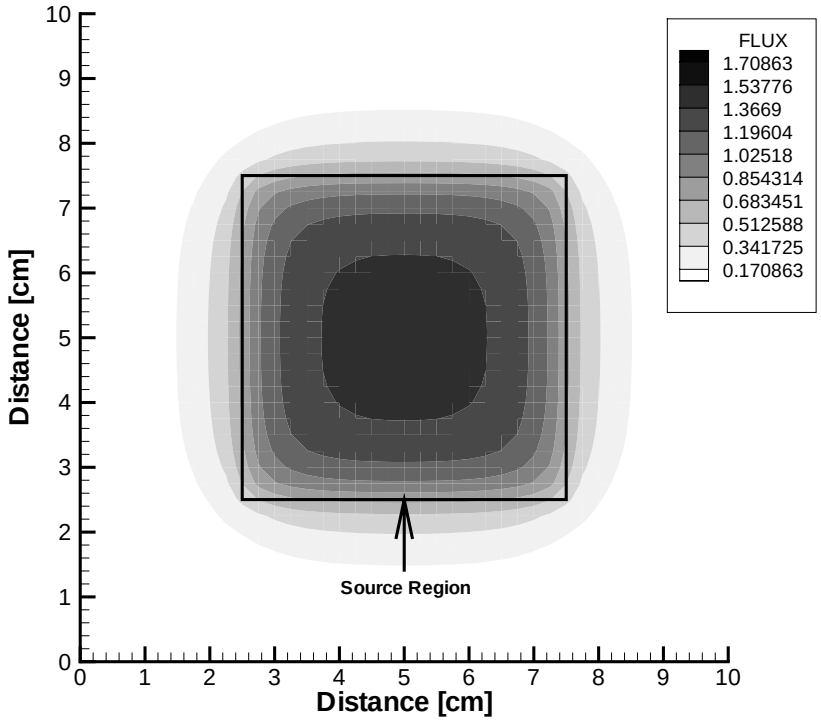

Figure 5.14: Particle Flux at 2.5 mft for Two-Dimensional Heterogeneous Benchmark

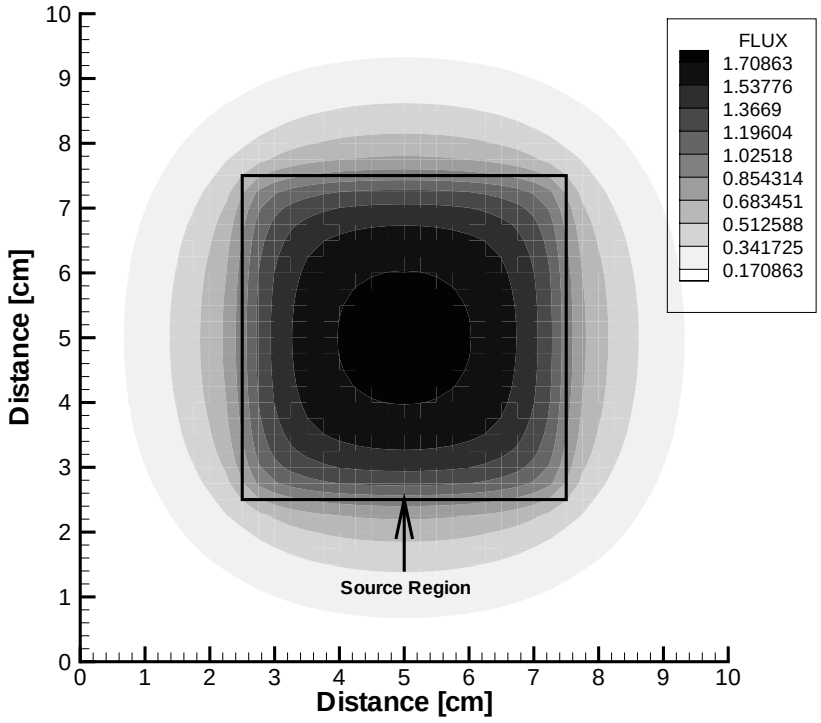

Figure 5.15: Particle Flux at 5.0 mft for Two-Dimensional Heterogeneous Benchmark

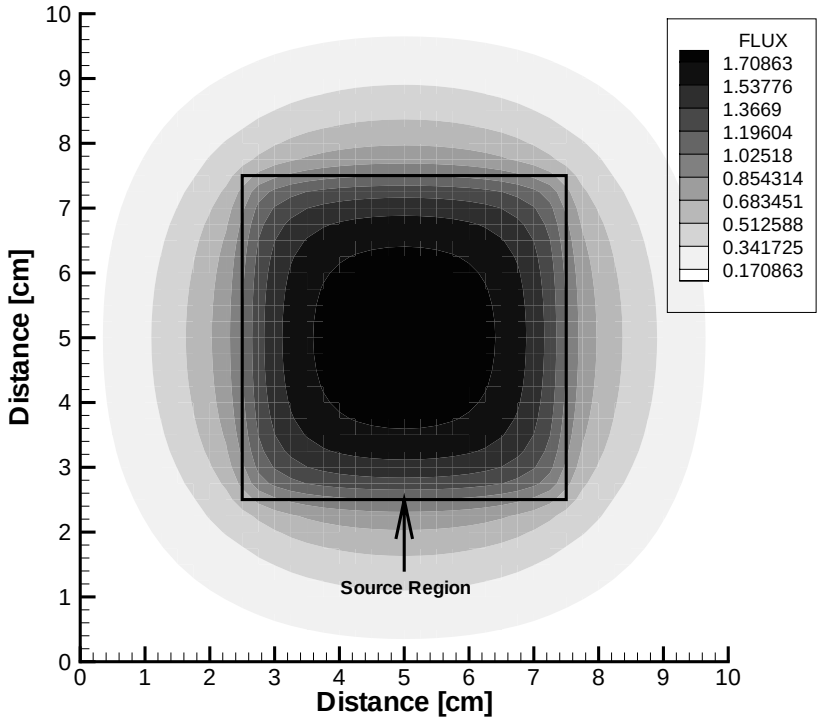

Figure 5.16: Particle Flux at 7.5 mft for Two-Dimensional Heterogeneous Benchmark

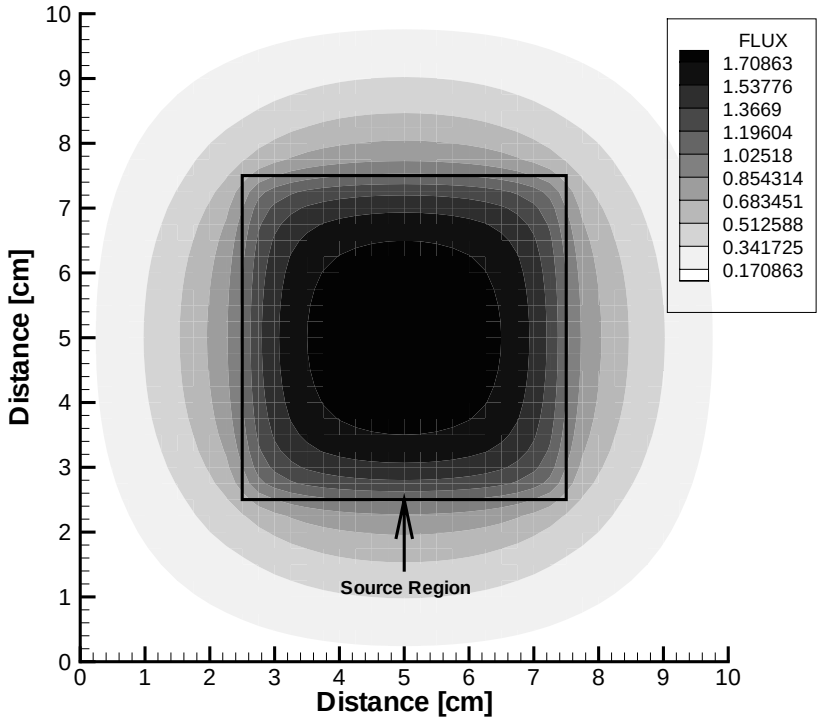

Figure 5.17: Particle Flux at 10.0 mft for Two-Dimensional Heterogeneous Benchmark

Chapter 6

TBIT Applications to ICF Problems

In the previous two chapters, the Time-Dependent Bubble Integral Transport Method (TBIT) was introduced and developed. The TBIT method was benchmarked against a series of finite media time-dependent benchmarks. In Chapter 6, the TBIT method will be used to simulate two problems pertaining to radiative transport in ICF targets.

The first application will calculate three dimensional radiative transport in a spherical hohlraum. This is done to investigate the effect that the placement and size of the laser entrance holes have on the non-uniformity of the illumination on the capsule.

The second application will be that of neutron transport down a tube that measures the energy spectrum based on the time of flight from the fusion event to the detector. This will show how scattering events in the tube affect the perceived energy spectrum by scattering into lower energy groups and increasing the distance over which neutrons must travel.

6.1 3-D radiation transport on Spherical Hohlraum

As mentioned in Chapter 1, one of the routes to high gain targets and ignition is through the use of thin wall cylindrical hohlraums composed of a high Z material, usually gold, that surrounds a DT target suspended in the center. Laser energy enters through two laser entrance holes (LEH) on either side of the cylinder and proceed to heat up the high Z material of the hohlraum resulting in the production of X-rays. The X-rays then irradiate the capsule as well as other portions of the hohlraum not directly heated by the laser energy. These "secondary" zones then proceed to emit X-rays of their own. Under

ideal circumstances, the capsule is illuminated as uniformly as possible. For a capsule to properly compress and initiate fusion, the non-uniformity of the X-ray illumination must be on the order of $\sim 1\%$ [92]

In general, a cylindrical hohlraum has a length that is greater than its diameter. This type of geometry is needed to balance the lack of a X-ray source at the LEH with the large source caused by the lasers striking the hohlraum and the resultant X-ray emission.

An alternate design would be to make the hohlraum spherical instead of cylindrical and aim the lasers into the hohlraum such that they illuminate the area beyond the LEH. In contrast to cylindrical hohlraums, where beam phasing is needed to ensure a uniform illumination, spherical hohlraums can use identical temporal beam histories thereby producing more symmetrical capsule illuminations [93]. There are several disadvantages to using spherical hohlraums [93]:

1. Beam placement for spherical hohlraums may be incompatible with cylindrical hohlraum designs.

2. The hydrodynamics and radiative transport is more difficult to model in three-dimensional spherical coordinates.

3. There may be greater radiative losses because of the added number of LEH.

When designing spherical hohlraums several considerations must be made when determining the area of the LEH as compared to the total area of the hohlraum. Ideally, the lasers should convert all of their energy into X-rays in the interior of the hohlraum. Obviously, total conversion is impossible; however, the LEH must be large enough such that the lasers enter into the hohlraum unimpeded by the plasma ablating off near the LEH.

On the other hand, an ideal design should also allow all of the X-ray energy to be transported into the capsule. This means that the LEH be as small as possible to avoid

X-ray losses. These two design considerations are in direct conflict with one another. When balancing these two criteria, the overriding consideration must be the uniformity of the capsule illumination.

Provided in Table 6.1 and shown in Figure 6.1 are the proposed dimensions for a spherical hohlraum on the NIF [93].

Table 6.1: Proposed Spherical Hohlraum Design for NIF

Case Radius	R_c (mm)	4.55
Hole Radius	R_h (mm)	1.14
Capsule Radius	R_{cap} (mm)	1.13
R_{cap}/R_c		0.25
Case Area	A_c (mm^2)	243.8
Total Hole Area	A_h (mm^2)	16.33
A_h/A_c		0.067

The proposed spherical hohlraum for the NIF has four holes placed at the vertices of a tetrahedron, or known as a "tetrahedral hohlraum. Although there have been different proposed angles for the LEH on the NIF tetrahedral hohlraum, the calculations will proceed using LEH that are uniformly distributed over the surface of the hohlraum at 60 degree angles from each other.

The TBIT method is used to investigate the uniformity of the capsule illumination for three different spherical hohlraums designs: two LEH holes at either pole on the hohlraum, the NIF tetrahedral hohlraum, and a six hole design with two LEHs on either pole and four uniformly distributed LEHs on the equator. The total surface area will be the same for all three designs.

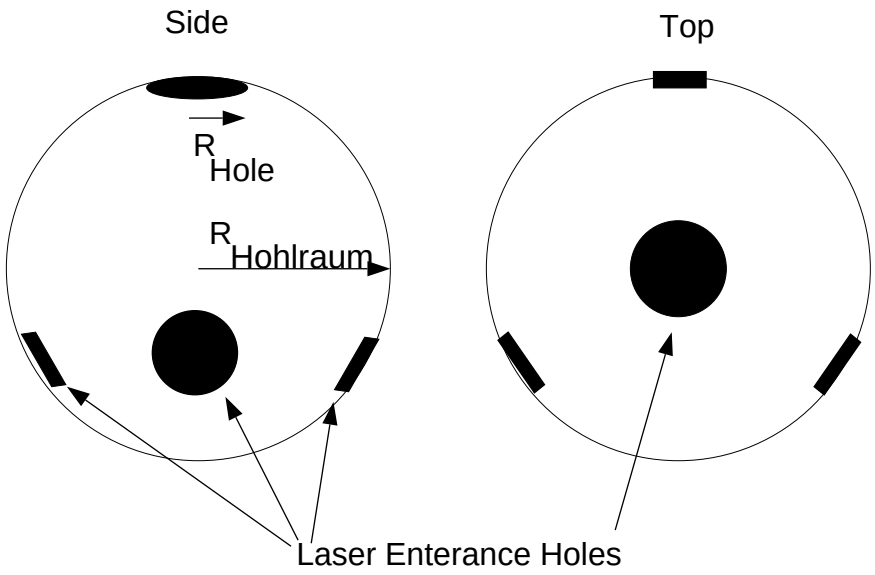

Figure 6.1: Proposed NIF Spherical Hohlraum

The figure of merit when determining the uniformity of the capsule illumination is the area of the LEH verses the total area of the hohlraum. For each of the three geometry types, three different LEH surface areas will be run. The first will have a LEH surface area of 50% that of the NIF design, the second equal to the NIF design, and the final 200% that of the NIF. The code will then calculate the capsule illumination for each of the three geometry types and for each of the three LEH surface areas.

Several complications arise when using the TBIT method. First, the LEH, not positioned at either pole of the spherical hohlraum, can not be modeled as circular using the currently implemented TBIT method. The coordinate system for the code is defined at the center of the capsule and the material boundaries on the hohlraum can only change at discrete values for the azimuthal and polar angles. As a result, the area of these LEH are "arcs" on the hohlraum with areas of $A_{LEH} = \rho^2 d\theta d\phi$. These LEH holes have the same area as those at the poles with the only difference coming in the shape of the hole. The TBIT method was run using the numerical parameters shown in Table 6.2.

Several simplifying assumptions are made. First the capsule is assumed to be com-

Table 6.2: Numerical Parameters for TBIT method

Nodes in Radial Direction	20
dr (mm)	0.2275
dt (picosecond)	0.758
Nodes in Polar Direction	40
Nodes in Azimuthal Direction	20

pletely black. This means that any incident X-ray flux will be absorbed and not transported through the capsule. This need not necessarily be the case. Real opacities could be used for the DT target; however, as the TBIT method is not coupled to a hydrodynamics code and the opacities and geometry for the problem are fixed, radiation would just travel through the capsule and affect the illumination on the other side. The present calculations are to determine the capsule illumination as a result of the X-ray flux incident on the capsule, and any "from the rear" illumination would distort the results.

Second, because the material changes on discrete nodes, the capsule in the simulation is slightly larger than the NIF target given in Table 6.2. For this particular problem there are 20 nodes scattered uniformly in the interior of the hohlraum, dr=0.2275 mm. The capsule in the interior is completely black to all radiation and is composed of the inner 5 nodes, or 1.14 mm.

Only a signal frequency will be transported for the purpose of this simulation. This will allow the determination of the effect that the LEH size and placement has on the uniformity of the capsule illumination.

A uniform, isotropic, unit source will be distributed over each LEH. All of the outgoing photons from the LEH are pointed towards the hohlraum. Once the photon flux intersects

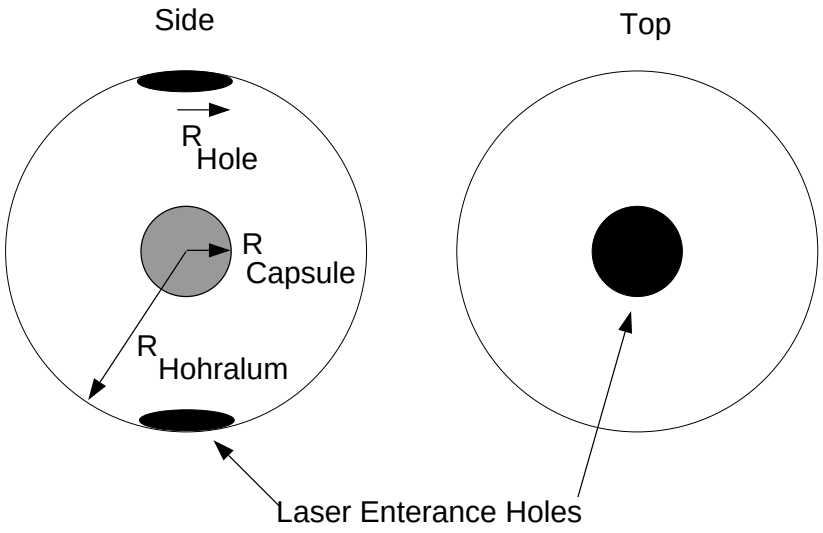

Figure 6.2: Two Laser Entrance Hole Spherical Hohlraum

with the hohlraum, 80% of the incoming intensity will be isotropically remitted as X-rays at the next time-step.

6.1.1 Two Laser Entrance Holes

The first simulation is of a spherical hohlraum with identical dimensions to that of the NIF hohlraum given in Table 6.1, including the total surface area of the LEH. The simulated two LEH hohlraum is shown in Figure 6.2.

Figure 6.3 shows the capsule illumination at 27.32 picoseconds. Figure 6.4 shows the capsule mapped onto a two-dimensional plane. At this early time, X-rays have just enough time to travel from the LEH to the hohlraum and then to the capsule. The effect of the LEH is noticeable from both pictures as a large "cool"area located on either pole of the capsule. The middle of the capsule has the highest illumination, because it is the only area that can be illuminated by both of the LEH.

Figures 6.5 and 6.6 show the capsule illumination at 59.19 picoseconds. At this later time, X-rays can travel approximately twice across the diameter of the hohlraum. The

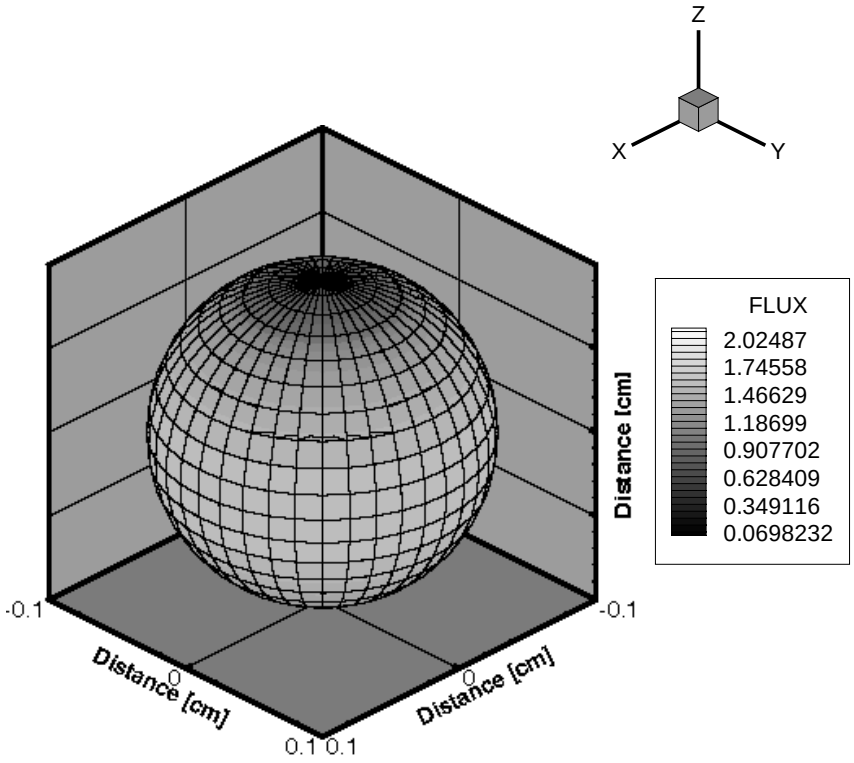

Figure 6.3: Two LEH Capsule at 27.32 picoseconds

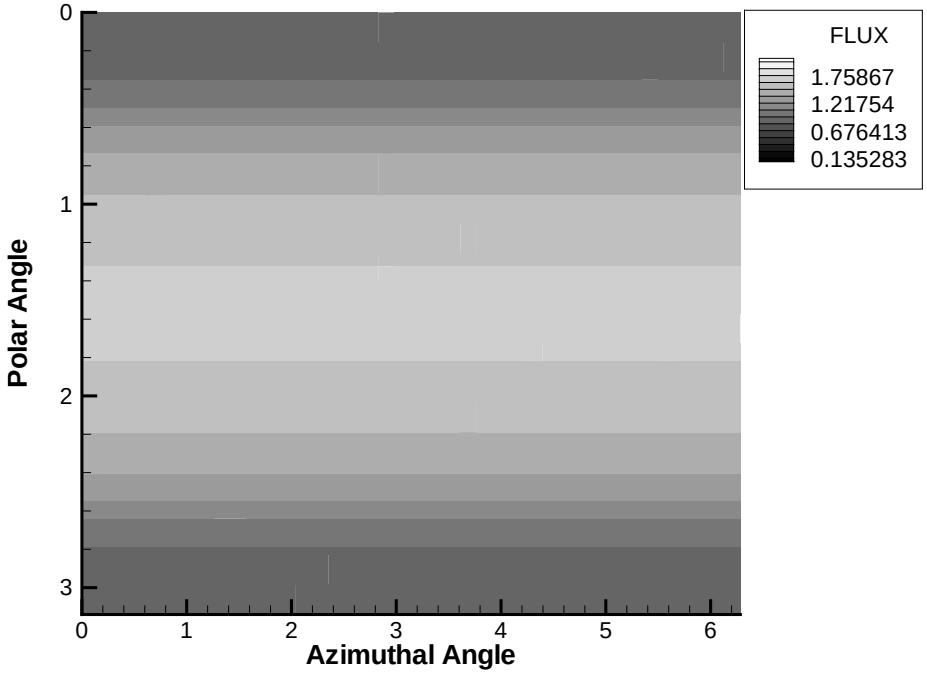

Figure 6.4: Two LEH Capsule at 27.32 picoseconds

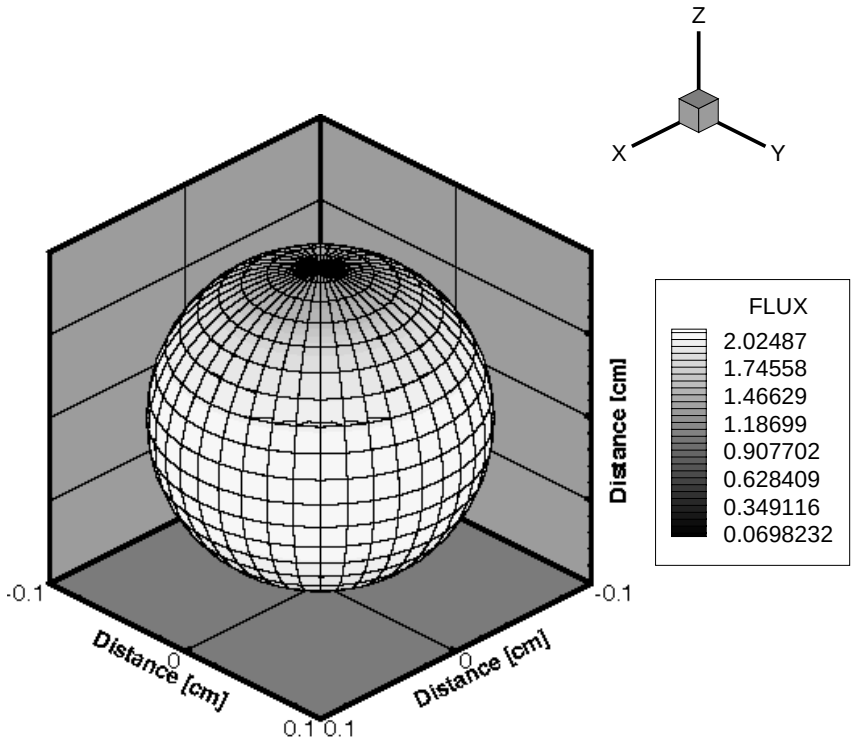

Figure 6.5: Two LEH Capsule at 59.19 picoseconds

basic features from the earlier time are featured in these two later figures. The LEH holes are the the coolest regions of the capsule and the warmest is along the equator.

Two additional scenarios were run using the same two holed LEH, with the only difference coming in the total surface area of the LEH. The first case was run with half the surface area of the NIF design and the second was run with twice the surface area. Table 6.3 compares the percent non-uniformity for each of the three cases.

As expected, the smaller the LEH, the more uniform the capsule illumination. The third column of Table 6.3 shows the percent increase in the rms non-uniformity over the previous surface area configuration. The TBIT method predicts that doubling the LEH surface area will approximately double the capsule non-uniformity. From the data calculated, the two LEH design is clearly unfavorable for successful implosions, as the best capsule illumination is over 10%, well above the 1% needed for successful implosion.

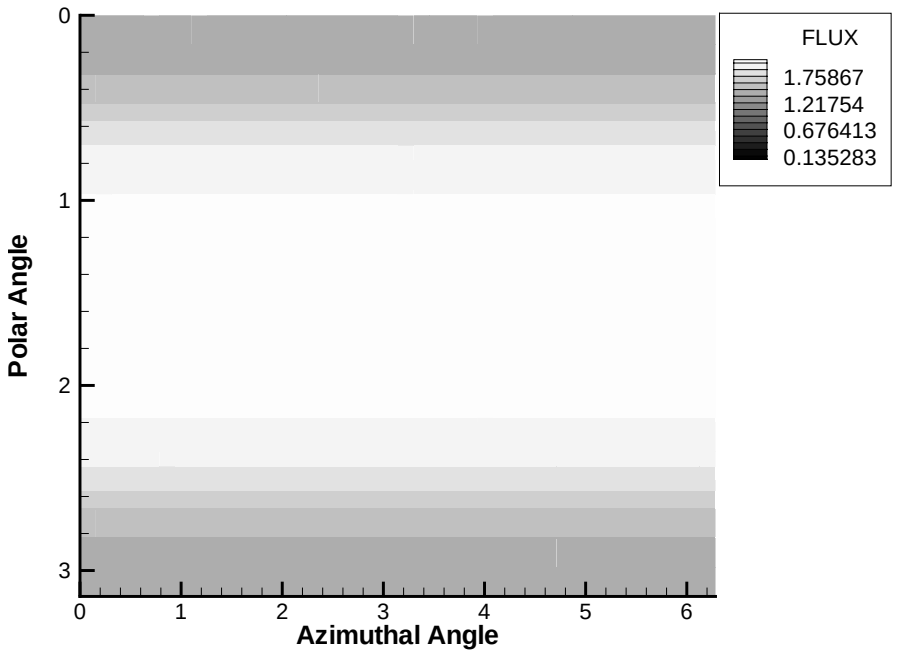

Figure 6.6: Two LEH Capsule at 59.19 picoseconds

Table 6.3: RMS Non-uniformity for Two-Hole Hohlraum

Total Hole Area (mm^2)	RMS Non-uniformity %	Percent Increase RMS Non-uniformity %
8.17	12.04	-
16.33	18.80	56.15
32.66	28.35	50.79

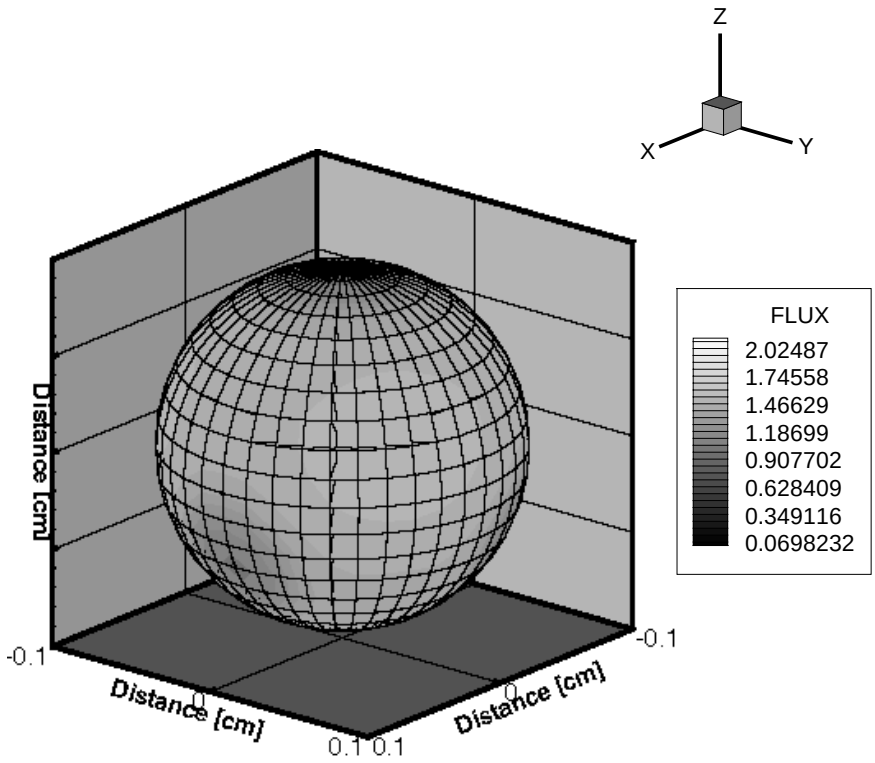

Figure 6.7: Four LEH Capsule at 27.32 picoseconds

6.1.2 Four LEH "Tetrahedral" Hohlraum

The proposed spherical NIF hohlraum was simulated, Table 6.2, and shown previously in Figure 6.1. Recall that the LEH holes that lay off the poles of the hohlraum are represented as "arcs" on the hohlraum instead of circular holes.

Figure 6.7 shows the capsule illumination at 27.32 picoseconds. At early times, the capsule illumination is fairly uniform except over the LEH. As expected, the portion of the capsule that has the most direct line of sight to the LEH is the coolest.

Figures 6.9 and 6.10 show the capsule illumination at 59.19 picoseconds. At this time, the hottest portion of the capsule are the three areas that are between the four LEH. At these locations, the capsule's surface has the greatest view of the hohlraum

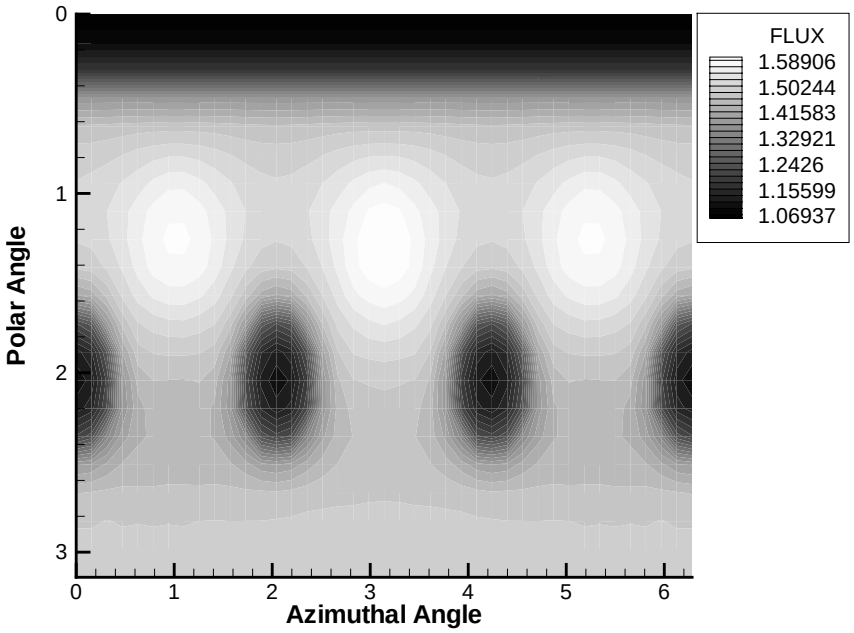

Figure 6.8: Four LEH Capsule at 27.32 picoseconds

without a LEH. As expected, the coolest regions are those that lay directly below the LEH. Schnittman ran a similar NIF tetrahedral capsule illumination using the *Buttercup* view-factor code. The calculated results showed a similar illumination pattern to that presented as the steady-state illumination patterns in Figures 6.9 and 6.10 [93].

As for the two-holed spherical hohlraum case, the tetrahedral hohlraum was run using identical conditions; however, the surface area of the LEH was changed. The smallest surface area is 50% that of the proposed NIF design, the middle value is the nominal case, and the largest is 200% of the NIF.

As expected, the smaller the LEH the more uniform the capsule illumination. The third column of Table 6.4 shows the percent increase in the rms non-uniformity over the previous surface area configuration. TBIT predicts that the NIF tetrahedral hohlraum lays within an optimal range of LEH area to total hohlraum surface area. A reduction of 50% for the surface area of the LEH decreases the non-uniformity by 13.72%. Whereas,

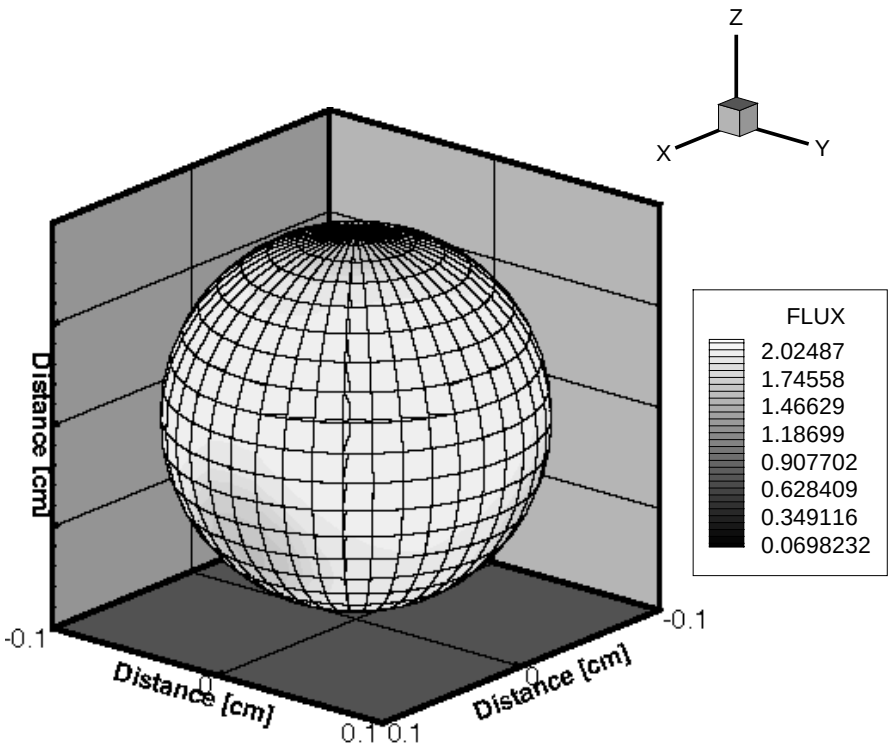

Figure 6.9: Four LEH Capsule at 59.19 picoseconds

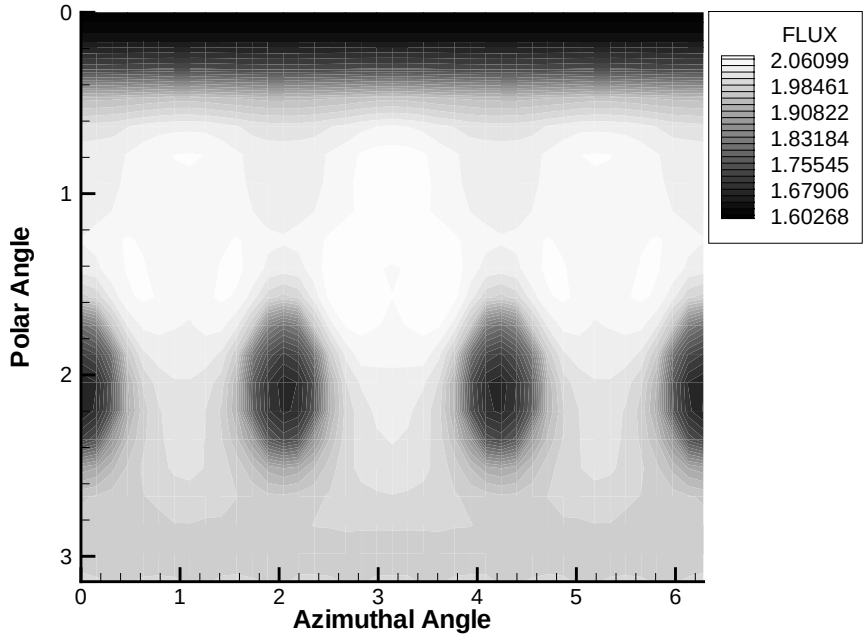

Figure 6.10: Four LEH Capsule at 59.19 picoseconds

Table 6.4: RMS Non-uniformity for Four-Hole Hohlraum

Total Hole Area (mm^2)	RMS Non-uniformity %	Percent Increase RMS Non-uniformity %
8.17	5.76	-
16.33	6.55	13.72
32.66	10.94	67.02

doubling the LEH area increases the non-uniformity by 67.02%.

Clearly, this capsule design is better than the two LEH presented earlier, as the illumination now varies over the capsule by a couple of a percent. The tetrahedral design has smaller radius LEH than the two holed design. The smaller LEH mean that any given point that lays with the "shadow" of the LEH can see more of the X-ray source on the hohlraum.

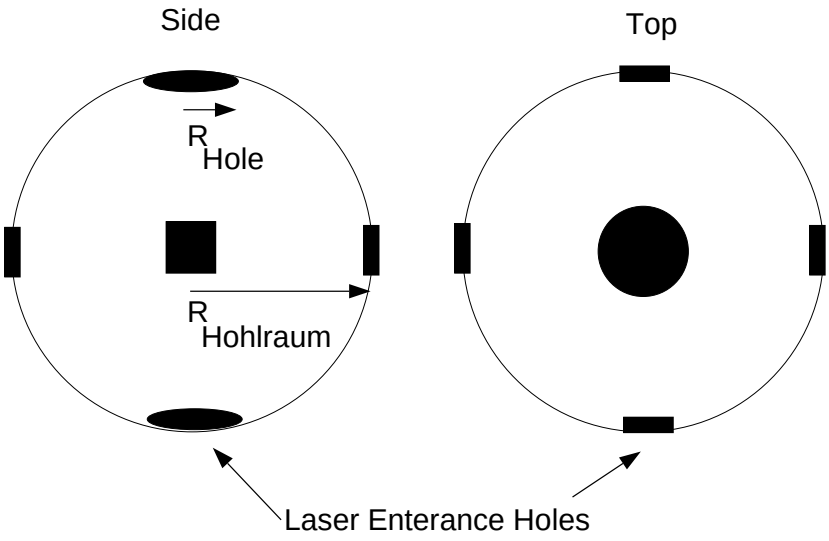

Figure 6.11: Six Laser Entrance Hole Spherical Hohlraum

6.1.3 Six Laser Entrance Holes

The final simulation is that of a six LEH hohlraum. The simulated six LEH hohlraum is shown in Figure 6.11. Again, as in the previous two cases the surface area is identical to the NIF design.

Figures 6.12and 6.13 show the capsule illumination at 27.32 picoseconds. As with the tetrahedral design, the illumination over the capsule is fairly uniform except over the LEH. Figure 6.14 shows that the "shadow" cast by the square panel LEH is oval on the capsule. This shows that the radiative transport within the hohlraum tends to soften any hard edges.

After 59.19 picoseconds, the capsule illumination has reached 95% the magnitude of the steady state illumination and the illumination pattern has stabilized. The coolest areas are the regions on the capsule directly facing the LEH. Like the previous cases, the hottest portion of the capsule is the portion that lays between the LEH. For the six LEH hohlraum, there are twelve hot spots on the capsule.

The six LEH design was run with the same geometric configuration but with 50% and

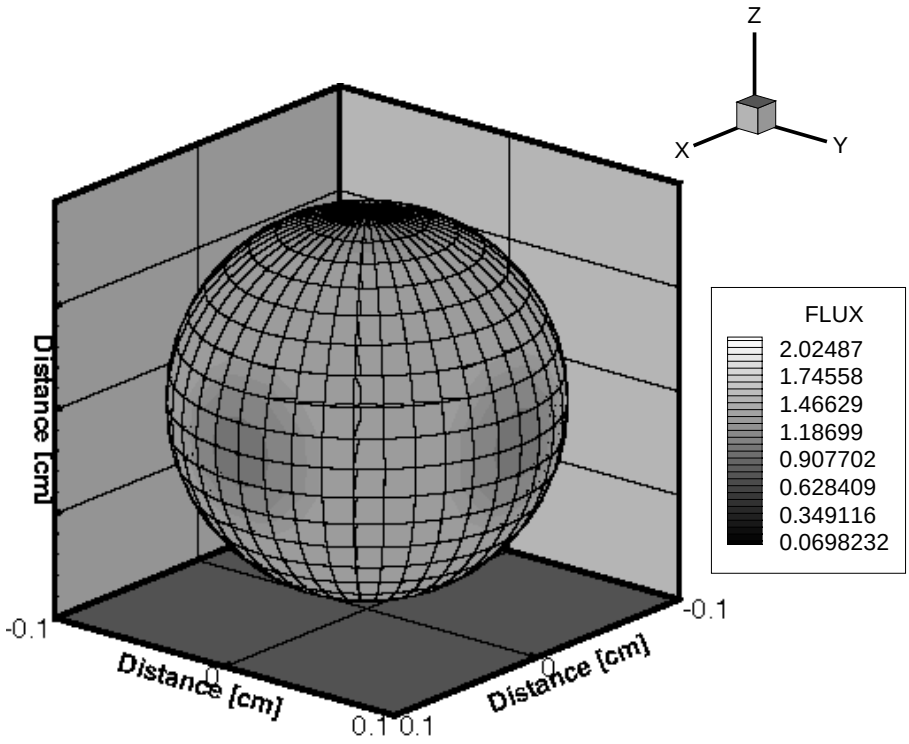

Figure 6.12: Six LEH Capsule at 27.32 picoseconds

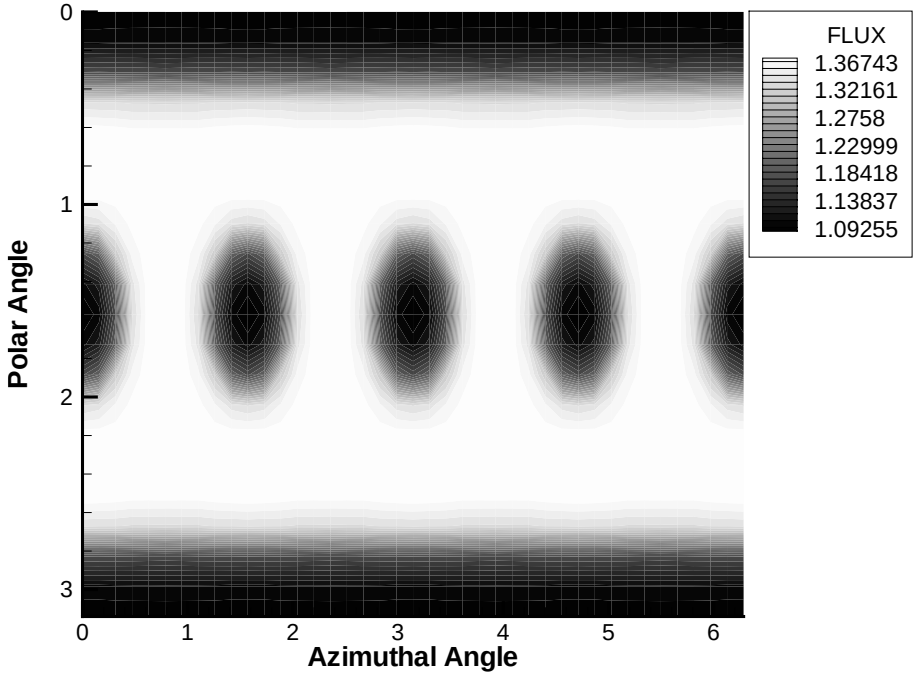

Figure 6.13: Six LEH Capsule at 27.32 picoseconds

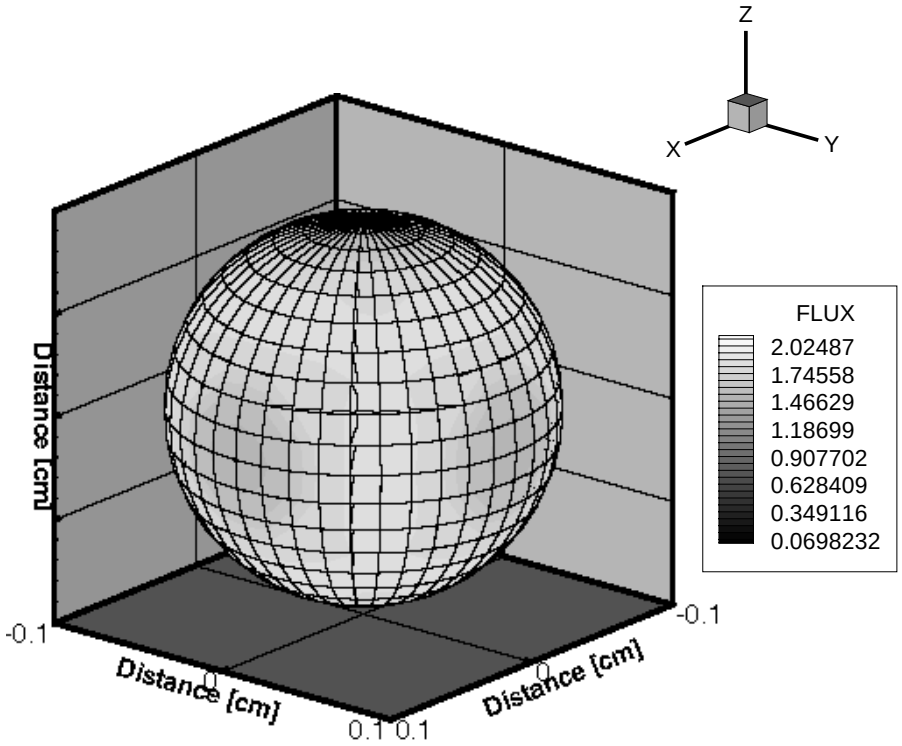

Figure 6.14: Six LEH Capsule at 59.19 picoseconds

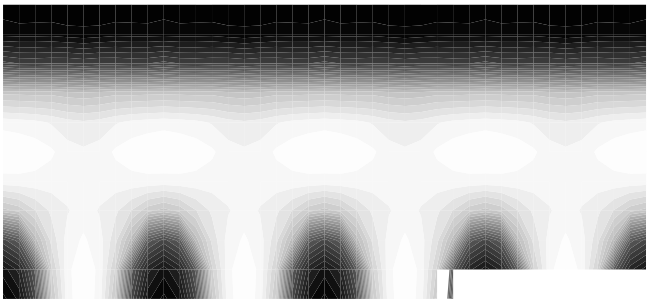

200% the surface area of the NIF design. As expected, the smaller the holes, the more uniform the capsule illumination. The non-uniformity for the six hole hohlraum is less than the previous two cases for all surface areas. This is expected as the greater number of holes for a given surface area should provide a better capsule illumination.

Table 6.5: RMS Non-uniformity for Six-Hole Hohlraum

Total Hole Area (mm^2)	RMS Non-uniformity %	Percent Increase RMS Non-uniformity %
8.17	4.46	-
16.33	5.79	29.82
32.66	9.43	62.87

As with the tetrahedral design, as the surface area of the LEH is halved, the non-uniformity of the capsule illumination only decreases by 29.82%. Whereas once the surface area is doubled, the non-uniformity increases by 62.87%.

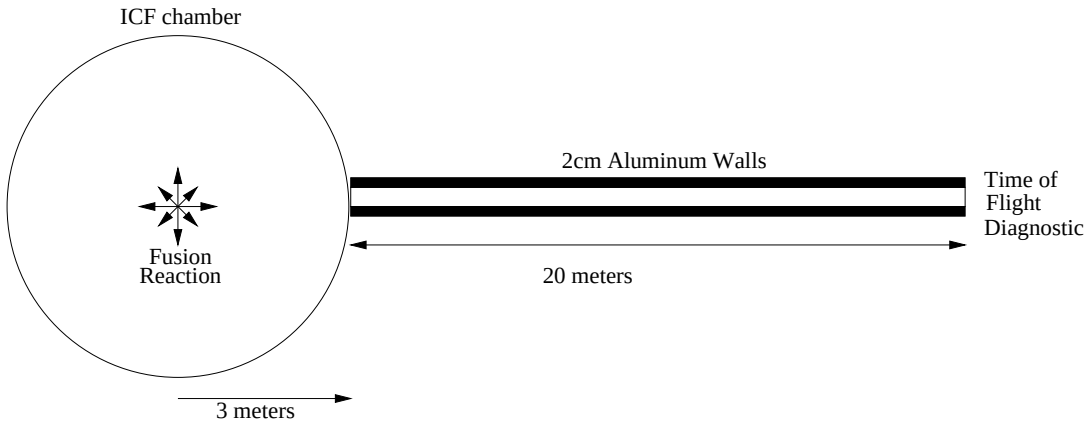

Figure 6.16: Neutron Time of Flight System - 1

6.2 2-D simulation of Neutron Time of Flight Diagnostic

A second application to which the TBIT method will be applied is the neutron time of flight diagnostics found on experimental ICF systems. Simply put, these diagnostic devices determine the energy spectrum of an ICF target by using neutron time-of-flight techniques. Hence, the energy of the neutrons can be easily determined knowing the length from the target and the time that it takes for neutrons to arrive at the target

Figure 6.16 shows the simple ICF time of flight diagnostic that was simulated. The fusion reaction occurs in a target chamber that has a 3 meter radius. The time of flight diagnostic tube is made out of aluminum with a thickness of 2 cm. The length of the tube is 20 meters in length. As the TBIT method can not model cylindrical geometries the time-of-flight tube is modeled using Cartesian coordinates. Thus, the tube is simulated as two parallel slabs of aluminum.

The neutrons entering into the tube, because of the radius of the ICF chamber and the diameter of the neutron diagnostic, have a spread of 19 degrees. This is shown in

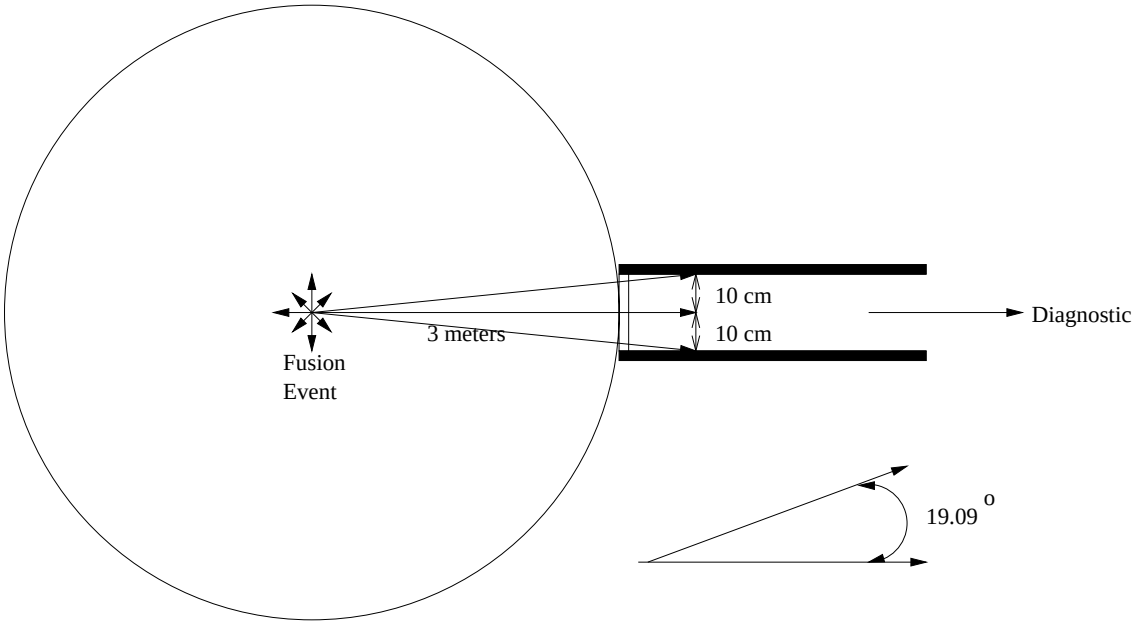

Figure 6.17: Neutron Time of Flight System - 2

Figure 6.17.

This means that neutrons entering the tube are not necessarily traveling directly down the tube. As a result, particles can travel down the tube in several different methods. These are shown in Figure 6.18. Neutrons that enter the tube very nearly radially outward can travel directly down the diagnostic tube without undergoing any collisions with the walls (case 1).

However, particles that enter the diagnostic tube in a 0.25 degree arc to either side of vertical will interact with the wall once before they reach the detector. These particles could then scatter in such a way that they are angled back down the tube and towards the detector (case 2). Particles that arrive at the detector after having scattered one or more times appear to arrive with a lower energy. These scattered neutrons have traveled a longer distance to the detector and even if they retain their initial velocity will arrive

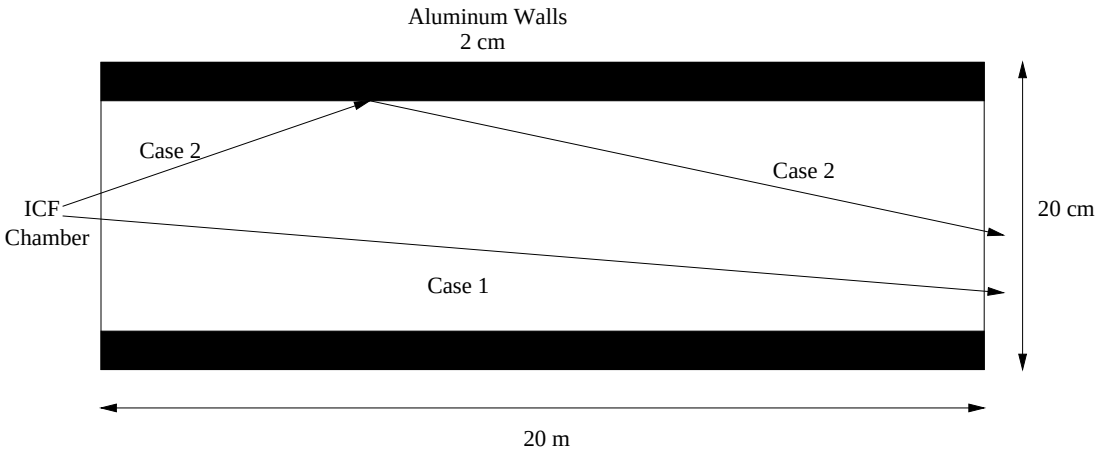

Figure 6.18: Neutron Time of Flight System - 3

later than a similar particle that travels directly down the tube.

Twenty-four energy groups were used to simulate the continuous energy spectrum of incoming neutrons that will impact the first wall and enter the diagnostic tube. These energy groups are shown in Table 6.6. All energy groups, except the first for which the particles have a velocity that corresponds to an energy of 14.1 MeV, have a velocity that corresponds to $E_{Midpoint}$ for that group.

All the incoming neutrons are assumed to have initial angles between -19.0 and 19.0 degrees. Time of flight calculations were then performed for each energy group and the two energy groups immediately below. Thus for the first calculation, the incoming source particles will have energies of 14.1 MeV and the code will then transport particles in this energy group and the resultant scattered particles from the 2nd and the 3rd energy group. Only two down-scattered energy groups are needed because the energy of a neutron scattering at a 90 degree angle off aluminum results in the neutron retaining 96% of its initial energy. Thus, two energy groups will cover all neutrons that have two large scattering events. In any case, most of the scattered particles that end up at the

diagnostic will be the result of small angle scattering events and thus possess nearly all of their original energy, but will travel a longer path length. The detector will tend to predict a spectrum slightly down-shifted in energy from the spectrum that enters in the diagnostic tube.

Five hundred spatial nodes were used along the length of the time of flight tube, or one node every 4 cm. Ten nodes were placed in the radial direction, or one node every 2 cm. The geometry was simulated using two-dimensional Cartesian coordinates. Ideally, the problem should be performed in cylindrical; however, as the method currently does not support cylindrical coordinates, Cartesian was used in substitution.

A source of uncollided neutrons was placed at the diagnostic entrance. The source has a pulse width of one dt, or the amount of time that it takes for particles to travel one dx. Downscattered neutrons are placed in the tube at the spatial and temporal position at which they are scattered from the higher energy group. The calculation was then allowed to proceed until there has been enough time for the particles in any given energy group to travel 30 meters, or 50% longer than the tube itself.

Figure 6.19 shows the neutron spectrum at the front of the tube (shown as the solid line) verses the spectrum that the diagnostic would see at the end of the 20 meter tube (data points) using the neutron energy groups provided in Table 6.6 [94]. There is very little difference between the two groups of data. This is because the energy groups are fairly far apart. As a result, any difference caused by small angle scattering resulting in slightly longer path length would not show up in these widely spaced energy groups.

Figure 6.20 shows a more detailed view of the energy spectrum that the detector would "see" resulting from a pulse of 14.1 MeV neutrons entering detector tube. The data is normalized to the flux value at the end of the tube for the "uncollided" direct flight 14.1 MeV neutrons. The figure shows that the vast majority of initial 14.1 MeV neutrons appear to the time of flight detector with energies above 13.9 MeV. This means,

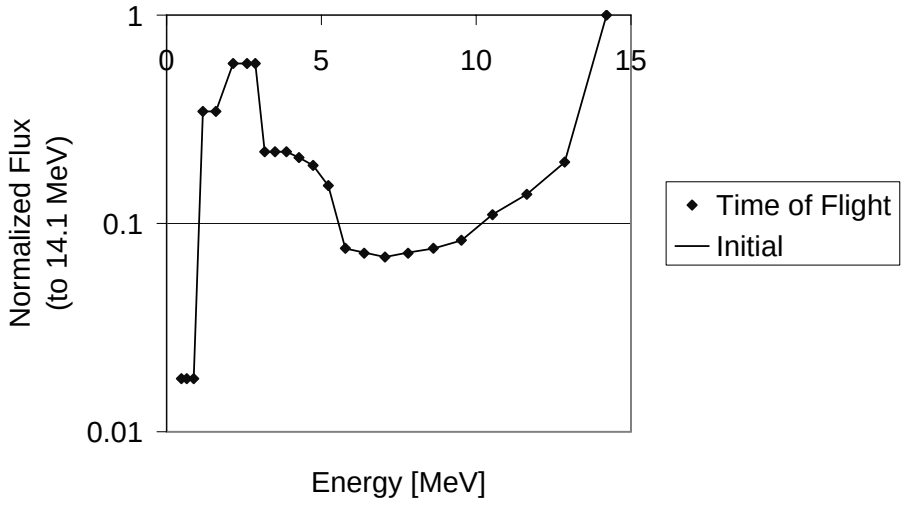

Figure 6.19: Spectrum at the Diagnostic vs Initial Spectrum

however, that if the detector can detect the differences of a fraction of an MeV, then there will be a slight drift towards lower energies.

The observations made for Figure 6.20 hold true for all the other energy groups. Figure 6.21, shows the observed energy spectrum for an initial particle flux of 1.5901 MeV (20th energy group). Like the previous case, a vast majority of particles lay within 95% of the energy of the initial particle flux. However, slight differences arise in the lower values of the graph. This is caused by the differences in the scattering cross section for the particular energy group. The higher the cross section, the more likely particles will be to scatter down the tube, once they interact with the aluminum tubing.

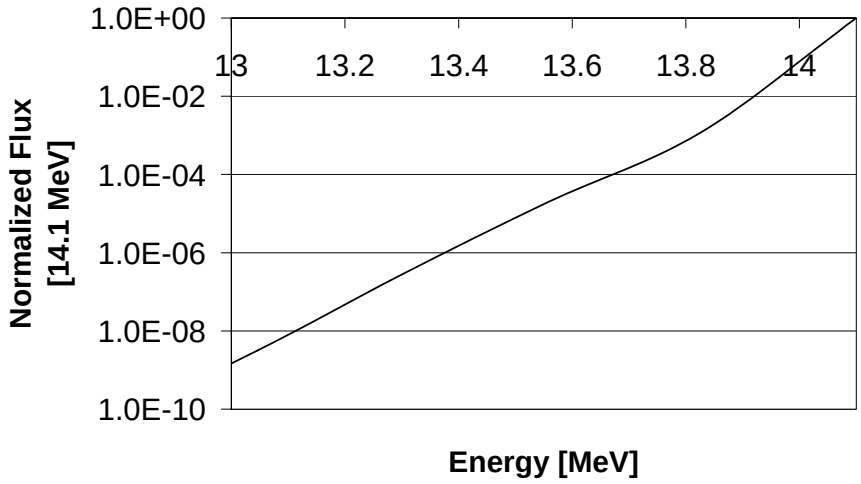

Figure 6.20: Spectrum seen by Diagnostic for 14.1 MeV Neutrons (Energy Group 1)

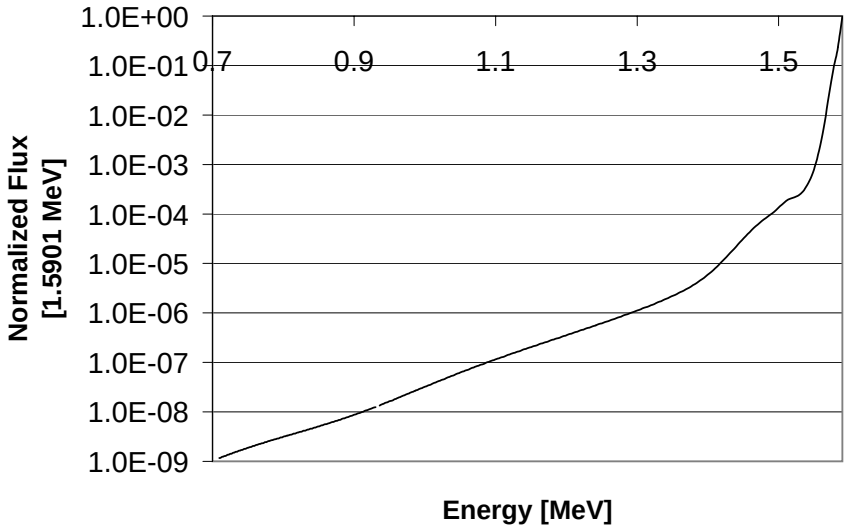

Figure 6.21: Spectrum seen by Diagnostic for 1.5901 MeV neutrons (Energy Group 20)

Table 6.6: Energy Groups (MeV) for Time of Flight Problem

$Group$	E_{Top}	E_{Low}	$E_{Midpoint}$
1	14.918	13.499	14.208
2	13.499	12.214	12.856
3	12.214	11.052	11.633
4	11.052	10.000	10.526
5	10.000	9.0484	9.5242
6	9.0484	8.1873	8.6187
7	8.1873	7.4082	7.7077
8	7.4082	6.7032	7.0557
9	6.7032	6.0653	6.3843
10	6.0653	5.4881	5.7767
11	5.4881	4.9659	5.2270
12	4.9659	4.4933	4.7296
13	4.4933	4.0657	4.2795
14	4.0657	3.6788	3.8722
15	3.6788	3.3287	3.5038
16	3.3287	3.0119	3.1703
17	3.0119	2.7253	2.8686
18	2.7253	2.4660	2.5956
19	2.4660	1.8268	2.1464
20	1.8268	1.3534	1.5901
21	1.3534	1.0026	1.1700
22	1.0026	0.74274	0.87267
23	0.74274	0.55023	0.64848

Chapter 7

Conclusion and Future Work

7.1 Conclusion

Radiation transport plays an important roll throughout the Inertial Confinement of Fusion process. The target must be illuminated with as symmetric a source as possible to ensure an isentropic compression. Once the fusion event begins, energy is taken away from the burn via radiation transport. This process represents a large percentage of the total energy loss.

Neutronic transport, similarly, is important to calculate accurately in ICF targets as it influences neutronic heating and the time-dependent neutron spectrum. Both radiative and neutronic transport are valuable as a diagnostic tool. As the ICF process is inherently time-dependent, a time-dependent transport method was deemed necessary.

Any time-dependent procedure must be benchmarked to ensure its results are accurate. The standard integral transport method was compared against a known infinite media benchmark. Four one-dimensional, finite media, time-dependent benchmarks were calculated: homogeneous Cartesian with uniform source, homogeneous Cartesian with localized source, homogeneous spherical with localized source, and heterogeneous Cartesian with localized source . The benchmarks were calculated by solving for the uncollided flux analytically and numerically solving for the collided flux.

The Time-Dependent Bubble Integral Transport (TBIT) method was introduced. The technique is able to follow the causality of particles exactly without the need to save the complete history of the problem like the "standard" integral method. TBIT was extended into multidimensional spherical and Cartesian geometries. The process was

then compared to the finite media time-dependent benchmarks presented in Chapter 3. In one-dimension, the TBIT method produced results that differed from the benchmarks at all temporal and spatial positions by no more than 1.6%.

The two-dimensional spherical TBIT technique was validated by posing the problem so that it was identical to the one-dimensional benchmark. This comparison showed that the two results differed by no more than 4.0%. Similarly, the three-dimensional spherical TBIT technique had errors of less than 6.5%. TBIT produced the highest errors in spherical geometry because of the added difficulty of calculating the streaming angles as the particles traverse the system. The TBIT method was shown to conserve particles to 1 part in every 100,000. This was performed by comparing the time-rate of change to the losses and gains at each spatial and temporal node.

A two-dimensional heterogeneous benchmark was calculated using the TBIT method. As discussed in Chapter 3, when producing benchmark quality results, an analytical solution for the uncollided flux is necessary. In two-dimensions, the analytical derivation becomes very unwieldy. Fortunately, the TBIT method produces results that are within a couple of percent of the "true" benchmark in Cartesian coordinates. Thus, a time-dependent benchmark was calculated using the TBIT method but using the identical Romberg convergence criteria presented in Chapter 3.

Two application driven results were calculated. A three-dimensional spherical capsule illumination was calculated for a two, four, and six hole spherical hohlraum. As the surface area of the laser entrance holes get larger, the capsule illumination becomes more non-uniform. The TBIT method predicted that the greater the number of LEH holes, for equal LEH surface areas, the more uniform the capsule illumination.

The second application was that of a neutron time of flight diagnostic typical to that found on ICF devices. The simulation showed that scattering effects from the wall will shift the "observed" spectrum seen by the detector only a small amount.

The TBIT technique was shown to be accurate and extendible into multi-dimensions. The method computes results much faster then the standard integral method, and does not suffer from the penalty of saving all of the accumulated information to calculate the next value.

7.2 Future Work

There are several areas that could be investigated further. First, every effort should be made to broaden the number and variety of time-dependent benchmarking tools that are available to the researcher. To this end, additional one-dimensional benchmarks could easily be created in a similar fashion to those presented in Chapter 3. Perhaps more important, would be the development of two and three dimensional time-dependent benchmarks. Extending the one-dimensional benchmarks into higher dimensions can only be done for spherical coordinates and, thus, the two and three dimensional Cartesian results for the TBIT method were not compared.

The functionality of the TBIT method could be expanded. Cylindrical geometries could be easily included in TBIT and thus all of the three major coordinate systems would be covered. This would allow capsule illumination simulations similar to the spherical hohlraum cases presented in Chapter 6 and to the Nova hohlraum simulation in Appendix F.

TBIT could be improved in how it handles vacuum boundary conditions. As mentioned earlier, the spatial directions are either distributed uniformly in the cosine of the angle or according to Gaussian quadrature rules. At vacuum boundaries, a minimum of half the angular directions are pointing in from the vacuum (Figure 7.1 case1). As there are no particles coming into the system from the vacuum boundary, all of these directions are essentially wasted when calculating the scalar flux. An alternative would be to redis-

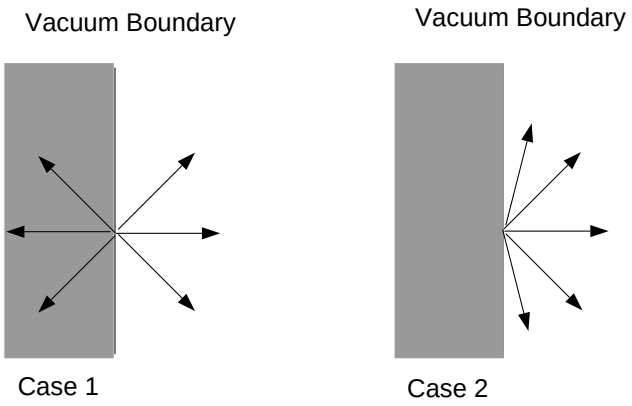

Figure 7.1: Angular Directions at Vacuum Boundaries

tribute the angular directions on the vacuum boundary such that every direction would now contribute to the scalar flux. A pictorial representation of this method is shown in Figure 7.1.

Currently, the TBIT technique is calculated on uniform meshes. This need not be the case. The calculation could proceed just as easily on non-uniform mesh spacing with the only modification resulting in the calculation of the time-step. The time-step would no longer be determined by the travel time across a single node, but, instead, be based on the time scale particles take to travel over a characteristic distance in the problem.

Similarly, the TBIT method could easily be extended into problems where the materials change after each time-step. With very little modification, the code could read in data at every time-step which would describe the material property changes within each node. With these two additions, the TBIT method could be integrated into a hydrodynamics code allowing a more accurate calculation of radiation transport than the diffusion based approximations currently used.

Finally, there are several areas of improvement in terms of computational efficiency. A graphical user interface could be created in order to set up complicated multi-dimensional

geometries with greater ease. The current configuration of text input becomes quite cumbersome for highly complicated geometries and mistakes are easily made.

All of the computer development has thus far been on Pentium-II class personal computers. The method could easily be extended onto parallel machines. The geometry of the problem would be spatially decomposed into smaller regions with each CPU calculating the time-dependent flux for the current time-step within the smaller spatial region. Information between the regions would be communicated through the boundary terms.

A final word must be said about benchmarking. The importance of highly accurate time-dependent benchmarking results can not be over-stated. The addition of multi-dimensional benchmark results that could be used to validate the multi-dimensional functionality of the TBIT method would only increase confidence in the algorithm.

References

[1] Krane K.S., *Introductory Nuclear Physics,* John Wiley and Sons, New York, 530 (1988).

[2] Duderstadt J.J. and Moses G.A., *Inertial Confinement Fusion,* John Wiley and Sons, New York, 8 (1982).

[3] Duderstadt J.J. and Moses G.A., *Inertial Confinement Fusion,* John Wiley and Sons, New York, 10 (1982).

[4] Nakao Y., Honda T., and et. al., "Calculational Method for Neutron Heating in Dense Plasma Systems (II)," *Journal of Nuclear Science and Technology*, **30**, 1207-1213 (1993).

[5] Johzaki T., Nakao Y, and et. al., "Neutron Heating Effects in Laser-Imploded DT Pellet," *Journal of Nuclear Science and Technology,* **32**, 81-83 (1995).

[6] Nuckolls J. and et. al., "Laser Interaction and Related Phenomena," *Nature,* **239**, 139 (1972).

[7] MacFarlane J. J., private communications.

[8] Winslow A., "Multifrequency-Grey Method for Radiation Diffusion with Compton Scattering," *Journal of Computational Physics,* **117**, 262-273 (1995).

[9] Duderstadt J.J. and Moses G. A., *Inertial Confinement Fusion,* John Wiley and Sons, New York, 125 (1982).

[10] Goel B. and Hobel W., "Plasma Physics and Controlled Nuclear Fusion Research 1984," *Proceedings of the 10th International Conference, London, 1984,* Vol 3, 345 (1985), IAEA, Vienna.

[11] Swift G. M. and et. al., "Modeling of the Neutronics of Inertial Confinement Fusion Pellets." *Transactions of the American Nuclear Society,* **33**, (1979).

[12] Seki Y. and Iida H., "Coupled 42-group Neutron and 21-Group Gamma-ray Cross Section Sets for Fusion Reactor Calculations," *JAERI-M* 8818, (1980).

[13] Nakao Y., Honda T., and et. al., "Calculational Method for Neutron Heating in Dense Plasma Systems (I)," *Journal of Nuclear Science and Technology*, **30**, 18-30 (1993).

[14] Shiba T., Nabeshima K., and et. al., *Nuclear Fusion,* **27**, 589 (1987).

[15] Martinez J.M., *Fusion Technology*, **17**, 476 (1990).

[16] Hill T. R. and Reed W. H., "TIMEX: A Time-Dependent Explicit Discrete Ordinates Program for the Solution of the Multigroup Transport Equations with Delayed Neutrons," LA6201-MS (1975).

[17] Nagel W., and Meszros P., "Time-Dependent Radiation Transport in a One-Dimensional Medium," *Journal of Quantitative Spectroscopy and Radiative Transfer,* **34**, 493-511 (1985).

[18] Ganapol B. D., "Solution of the One-Group Time-Dependent Neutron Transport Equation in an Infinite Medium by Polynomial Reconstruction," *Nuclear Science and Engineering*, **92**, 272-279 (1986).

[19] Syros C., "Solution of the Neutron Slowing Down Problem via a Multiple Collisional Approach," *Nuclear Science and Engineering,* **28**, 203 (1967).

[20] Stuart G. W. and Woodruff R. W., "Method of Successive Generations," *Nuclear Science and Engineering,* **3**, 339 (1958).

[21] Ganapol B. D., "Analytic Solution of the Monoenergetic Time-Dependent Albedo Problem," *Transactions of the American Nuclear Society,* **22**, 255 (1975).

[22] Windhofer P.F. and Pucker N., "Multiple-Collision Solutions for Time-Dependent Neutron Transport in Slabs of Finite Thickness," *Nuclear Science and Engineering,* **91**, 223-233 (1985).

[23] Ganapol B.D., "P_1 Approximation to the Time-Dependent Monoenergetic Neutron Transport Equation in Infinite Media," *Transport Theory and Statistical Physics,* **9**, 145 (1980).

[24] Ganapol B.D. and Grossman L. M., "The Collided Flux Method for Time-Dependent Neutron Transport," *Nuclear Science and Engineering*, **52**, 454-460 (1973).

[25] Ganapol B.D. and et. al., "Time-Dependent Neutron Transport in Spherical Geometry," *Transactions of the American Nuclear Society,* **32**, (1979).

[26] Ganapol B.D., "Time-Dependent Surface Angular Flux for a Semi-Infinite Medium with Specular Reflection," *Nuclear Science and Engineering,* **80**, 412 (1982).

[27] Ganapol B.D. and McKenty P.W., "The Generation of Time-Dependent Neutron Transport Solutions in Infinite Media," *Nuclear Science and Engineering,* **64**, 317 (1977).

[28] Tsuchihashi K, "LAMB-B: A FORTRAN Program Set for the Lattice Cell Analysis by Collision Probability Method," *JAERI-1259,* (1979).

[29] Tsuchihashi K. and Gotoh Y., "The Resonance Integral of Coated Particles," *Nuclear Science and Engineering,* **58**, 213-225 (1975).

[30] Lefvert T., "New Application of the Collision Probability Method in Neutron Transport Theory," *Prog. Nuc. Eng.,* **4**, 97 (1979).

[31] Kholin S. A., *USSR Computational Math and Mathematical Physics,* **4**, 213 (1964).

[32] Ganapol B. D., "Exact Time-Dependent Moments for the Monoenergetic Neutron Transport Equation with Isotropic Scattering," *Nuclear Science and Engineering*, **89**, 256-260 (1985).

[33] Zimmermann G. B., "Numerical Simulation of the High Density Approach to Laser Fusion," UCRL-74811, Lawrence Livermore National Laboratory, Livermore, California (1973).

[34] "LASNEX: A Laser Fusion Simulations Code," UCRL-50021-79, Laser Program Annual Report, Lawrence Livermore National Laboratory (1979).

[35] "LASNEX: A Laser Fusion Simulations Code," UCRL-50021-80, Laser Program Annual Report, Lawrence Livermore National Laboratory (1980).

[36] Morel J. E., Larsen E. W., and et. al., ' 'A Synthetic Acceleration Scheme for Radiative Diffusion Calculations," *Journal of Quantitative Spectroscopy and Radiative Transfer,* **34**, 243-261 (1985).

[37] Olson G. L., "Solution of the Radiation Diffusion Equation on an AMR Eulerian Mesh with Material Interfaces,"LA-UR-95-4174, (1996).

[38] Berger M.J. and Colella P., "Local Adaptive Mesh Refinement for Shock Hydrodynamics," *Journal of Computational Physics,* **82**, 64-84 (1989).

[39] Bell J. and et. al., "Three-Dimensional Adaptive Mesh Refinement for Hyperbolic Conservation Laws'," *SIAM Journal of Scientific Computing,* **15**, 127-138 (1994).

[40] Morel J.E. and et. al., "A Cell-Centered Lagrangian-Mesh Diffusion Differencing Scheme," *Journal of Computational Physics,* **103**, 286-299 (1992).

[41] Levermore C. D. and Pomraning G. C., "A Flux-Limited Diffusion Theory," *The Astrophysical Journal,* **248**, 321-334 (1981).

[42] Winsor N. K., "Velocity Space Methods for Fusion Reactor Plasmas," *Nuclear Science and Engineering,* **64**, 33 (1977),

[43] Duderstadt J.J. and Moses G. A., *Inertial Confinement Fusion,* John Wiley and Sons, New York, 130 (1982).

[44] Carlson B.G., "Solution of the Transport Equation by S_n Approximation," LA-1599, Los Alamos Scientific Laboratory (1953), Revised as LA-1891 (1955).

[45] Carlson B.G and K.D. Lathrop, *Transport Theory: The Method of Discrete Ordinates,* Gordon and Breach Science Publishers Ltd, New York, 165 (1968).

[46] Lewis E. E. and Miller W. F., *Computational Methods of Neutron Transport,* American Nuclear Society, La Grange Park, Illinois, 208-225 (1993).

[47] Bell G. I and Glasstone S., *Nuclear Reactor Theory,* Robert E. Krieger Publishing Company, Malabar, Florida (1985).

[48] Case K. M. and Zweifel P. F., *Linear Transport Theory,* Addison-Wesley Publishing Company, Reading, Massachusetts (1967).

[49] Verlarde G. and et. al., "Analysis of Laser-Fusion-Fission Systems: Development of Methods for Nuclear and Thermo-Hydrodynamic Calculations," *Atomkernenergie / Kerntechnik,* **35**, 40 (1980).

[50] Abdou M. A. and et. al., "MACK: A Program to Calculate Neutron Energy Release Parameters (Fluence-to-Kerma Factors) and Multigroup Neutron Reaction Cross Sections from Nuclear Data in ENDF Format," UWFDM-37, Nuclear Engineering and Engineering Physics Department, University of Wisconsin-Madison, (1973).

[51] Kornreich D. E and Ganapol B. D., "The Green's Function Method for Nuclear Engineering Applications," *Nuclear Science and Engineering,* **126**, 293-313 (1997).

[52] Siewert C. E. and P. Benoist, "The F_n Method in Neutron Transport Theory. Part I: Theory and Applications," *Nuclear Science and Engineering,* **69**, 156 (1979).

[53] Grandjean P. and Siewert C. E., "The F_n Method in Neutron Transport Theory. Part II: Applications and Numerical Results," *Nuclear Science and Engineering,* **69**, 161 (1979).

[54] Loyalka S. K., "Numerical Methods for Solving Integral Equations of Neutron Transport," *Nuclear Science and Engineering*, **56**, 317-318 (1975).

[55] Munier A., "Integral Form of the Time-Dependent Radiation Transfer Equation - I. Inhomogeneous Slab," *Journal of Quantitative Spectroscopy and Radiative Transfer,* **38**, 447-455 (1987).

[56] Henderson D. L. and Maynard C. W., "Time-Dependent Single-Collision Kernels for Integral Transport Theory," *Nuclear Science and Engineering*, **102**, 172-182 (1989).

[57] Olson K. R. and Henderson D. H., "Fuel Assembly Pulsing using Time-Dependent Integral Transport Methods," *Trans. Am. Nucl. Soc.*, **77**, 190 (1997).

[58] Olson K. R. and Henderson D. L., "Time-Dependent Neutral Particle Transport in Homogeneous Materials," *Transactions of the American Nuclear Society*, **76**, 211-214 (1997).

[59] S.K. Loyalka and R.W. Tsai, "A Numerical Method for Solving Integral Equations of Neutron Transport - II," *Nucl. Sci. Eng.*, **58**, 193 (1975).

[60] R.W. Tsai and S.K. Loyalka, "A Numerical Method for Solving Integral Equations of Neutron Transport: III," *Nucl. Sci. Eng.*, **61**, 536 (1976).

[61] G. Vainikko, *Multidimensional Weakly Singular Integral Equations*, Springer-Verlag, New York, (1993).

[62] P. Linz, *Analytical and Numerical Methods for Volterra Equations*, S.I.A.M., Philadelphia (1985).

[63] K.E. Atkinson, *An Introduction to Numerical Analysis*, 2nd Edition, John Wiley and Sons (1989).

[64] R.L. Burden and J.D. Faires, *Numerical Analysis*, 5th Edition, PWS Publishing Company, Boston (1993).

[65] P.M. Keller and J.C. Lee, "A Time-Dependent Collision Probability Method for One-Dimensional Space-Time Nuclear Reactor Kinetics," *Nucl. Sci. Eng.*, **129**, 124 (1998).

[66] Chenney W, and Kincaid D., *Numerical Mathematics and Computing,* Brooks / Cole Publishing Company, Pacific Grove, New York, 171-182 (1985).

[67] S. Wolfram, *Mathematica 3.0: A System for doing Mathematics by Computer.* Addison-Wesley, New-York (1996).

[68] S.A. Kholin, "Certain Exact Solutions of the Nonstationary Kinetic Equation Without Taking Retardation Into Account," *USSR Computational Mathematics and Mathematical Physics*, **4**, 213 (1964).

[69] V.C. Boffi, "Space-Time Flux Distributions in Neutron Transport Theory," *Nukleonik*, **8**, 448 (1966).

[70] C. Syros, "Time-Dependent Transport Solution in Plane Geometry," *Atomkernenergie*, **16**, 273 (1970).

[71] B.D. Ganapol, P.W. McKenty, and K.L. Peddicord, "The Generation of Time-Dependent Neutron Transport Solutions in Infinite Media," *Nucl. Sci. and Eng.*, **64**, 317 (1977).

[72] B.D. Ganapol and L.M. Grossman, "The Collided Flux Method for Time-Dependent Neutron Transport," *Nucl. Sci. Eng.*, **52**, 454 (1973).

[73] B.D. Ganapol, "Time-Dependent Moments of the Monoenergetic Transport Equation in Spherical and Cylindrical Geometry," *Nucl. Sci. Eng.*, **60**, 103 (1976).

[74] B.D. Ganapol, J.A. Royal and A.K. Henninger, "Time-Dependent Neutron Transport in Spherical Geometry," *Trans. Am. Nucl. Soc.*, **32**, 312 (1979).

[75] B.D. Ganapol, "Exact Time-Dependent Moments for the Monoenergetic Neutron Transport Equation with Isotropic Scattering," *Nucl. Sci. Eng.*, **89**, 256 (1985).

[76] B.D. Ganapol, "Reconstruction of the Time-Dependent Monoenergetic Neutron Flux from Moments," *J. Comp. Phys.*, **59**, 468 (1985).

[77] B.D. Ganapol, "Time-Dependent Surface Angular Flux for a Semi-Infinite Medium with Specular Reflection," *Nucl. Sci. Eng.*, **80**, 412, (1982).

[78] B.D. Ganapol and W.L. Filippone, "Time-Dependent Emergent Intensity from an Anisotropically-Scattering Semi-Infinite Atmosphere," *J. Quant. Spectrosc. Radiat. Transfer*, **27**, 15 (1982).

[79] B.D. Ganapol, "Solution of the One-Group Time-Dependent Neutron Transport Equation in an Infinite Medium by Polynomial Reconstruction," *Nucl. Sci. Eng.*, **92**, 272 (1986).

[80] B.D. Ganapol, "An Analytical Benchmark Solution to the Time-Dependent Multigroup Neutron Transport Equation," *Proc. Int. Topl. Mtg. Advances in Reactor Physics, Mathematics and Computation*, Paris, France, April 27-30, (1987).

[81] B.D. Ganapol, "Time-Dependent Continuous-Energy Neutron Transport in Spherical Geometry," *Trans. Am. Nucl. Soc.*, **34**, 283, (1980)

[82] J. Palmeri, "The One-Dimensional Monoenergetic Time-Dependent Transport Equation in Infinite Media (Revised)," *Trans. Theory Stat. Phys.*, **16**, 897 (1987).

[83] P.F. Windhofer and N. Pucker, "Multiple-Collision Solutions for Time-Dependent Neutron Transport in Slabs of Finite Thickness," *Nucl. Sci.Eng.*, **91**, 223 (1985).

[84] G. Bell and Glasstone, *Nuclear Reactor Theory*, Kreig Publishing Company, New York, (1979).

[85] Duderstadt J.J. and Moses G. A., *Inertial Confinement Fusion,* John Wiley and Sons, New York, 125 (1982).

[86] Press W. H., and et. al., Numerical Recipes in Fortran 77, Cambridge University Press, Cambridge, 134 (1992).

[87] Olson K. R. and Henderson D. H., "Radiation Transport in Hohlraums using Time-Dependent Integral Transport Methods," *13th Topical Meeting on the Technology of Fusion Energy*, June 7-11, Nashville TN (June 1998).

[88] R. Sanchez and B.D. Ganapol, "Benchmark Values for Monoenergetic Neutron Transport in One-Dimensional Cylindrical Geometry with Linearly Anisotropic Scattering," *Nucl. Sci. Eng.*, **84**, 61 (1985).

[89] B. Dahl, "Numerical Solutions of the Monoenergetic Neutron Transport Equations with Anisotropic Scattering," *Ph.D. Thesis*, Department of Reactor Technology, Chalmers University of Technology, Göteborg, Sweden (1985).

[90] Duderstadt J. J. and Hamilton L. J., *Nuclear Reactor Analysis,* John Wiley and Sons, New York, 606 (1977).

[91] Duderstadt J. J. and Hamilton L. J., *Nuclear Reactor Analysis,* John Wiley and Sons, New York, 312-313 (1977).

[92] Lindl J.D,. *Inertial Confinement Fusion* Springer-Verlag, New York, 11 (1998).

[93] Schnittman J.D. and Craxton R.S.,*Phys. Plasmas*, **3**, 3786-3797 (1998).

[94] Henderson D.L., *Time-Dependent Integral Transport Kernels, Leakage Rates and Collision Rates for Plane and Spherical Geometry*, Ph.D. Dissertation University of Wisconsin-Madison, 3 (1987).

[95] Bickley W. G. and Naylor J., *Phil. Mag.*, **20** , 343 (1935).

[96] Strikwerda J. C., *Finite Difference Schemes and Partial Differential Equations*, Chapman & Hall, New York, 63 (1989).

[97] Duderstadt J. J. and Hamilton L. J., *Nuclear Reactor Analysis,* John Wiley and Sons, New York, 606 (1977).

[98] Shestakov A. I., Kershaw D. S., and et. al., "Test Problems in Radiative Transfer Calculations," *Nuclear Science and Engineering,* **105**, 88-104 (1990).

[99] Badruzzaman A., "Finite-Moments Approaches to the Time-Dependent Boltzmann Equation," *Progress in Nuclear Energy,* **25**, 127-157 (1991).

[100] Brooks E. D. and Fleck J. A., *Journal of Computational Physics,* **67** 59-72 (1986).

[101] Drake D. J., "A View-Factor Method for Solving Time-Dependent Radiation Transport Problems Involving Fixed Surfaces with Intervening Participating Media," *Journal of Computational Physics,* **87**, 73-90 (1990).

Appendix A

Analytical Derivation of Heterogeneous Multigroup Kernels

A.1 Derivation of Heterogeneous Point Kernel

The monoenergetic neutral particle transport equation in a heterogeneous medium is:

$$\left(\frac{1}{v}\frac{\partial}{\partial t} + \hat{\Omega}\cdot\vec{\nabla} + \Sigma(\vec{r})\right)\psi(\vec{r},\hat{\Omega},t) = \frac{Q(\vec{r},t)}{4\pi}. \tag{A.1}$$

Taking the Laplace transform of the previous equation one arrives at:

$$\left(\hat{\Omega}\cdot\vec{\nabla} + \tilde{\Sigma}(\vec{r})\right)\tilde{\psi}(\vec{r},\hat{\Omega},s) \;\; = \frac{\tilde{Q}(\vec{r},s)}{4\pi}. \tag{A.2}$$

This last equation is the steady state transport equation with the macroscopic cross section replaced with $\tilde{\Sigma}(\vec{r}) = \Sigma(\vec{r}) + \dfrac{s}{v}$. Therefore if the heterogeneous steady-state point kernel is known, the time-dependent kernel is derived in a similar fashion to that presented in Henderson and Maynard [56]. The steady-state heterogeneous point kernel is [46]:

$$K_{pt}(\vec{r},\vec{r}^{\,\prime}) = \frac{\exp(-\tau(\vec{r},\vec{r}^{\,\prime}))}{4\pi R^2} \tag{A.3}$$

where:

$$\begin{aligned} R &= \left|\vec{r}-\vec{r}^{\,\prime}\right| \\ \tau(\vec{r},\vec{r}^{\,\prime}) &= \int_0^R \Sigma\left(\vec{r}-\omega\frac{\vec{r}-\vec{r}^{\,\prime}}{R}\right)d\omega \end{aligned}$$

The derivation of the heterogeneous point kernel then proceeds as follows:

$$K_{pt}(\vec{r},\vec{r}^{\,\prime},t) \;\; = \;\; \mathcal{L}^{-1}\left\{\frac{\exp\left(-\int_0^R\left[\Sigma(\vec{r}-\omega\frac{\vec{r}-\vec{r}^{\,\prime}}{R}) + \frac{s}{v}\right]d\omega\right)}{4\pi R^2}\right\}$$

$$
\begin{aligned}
&= \frac{\exp(-\tau(\vec{r},\vec{r}^{\,'}))}{4\pi R^2}\mathcal{L}^{-1}\left\{\exp\left(-\int_0^R \frac{s}{v}d\omega\right)\right\} \\
&= \frac{\exp(-\tau(\vec{r},\vec{r}^{\,'}))}{4\pi R^2}\mathcal{L}^{-1}\left\{\exp\left(-\frac{s}{v}R\right)\right\} \\
&= \frac{\exp(-\tau(\vec{r},\vec{r}^{\,'}))}{4\pi R^2}\delta\left(t-\frac{R}{v}\right) \\
&= \frac{\exp(-\tau(\vec{r},\vec{r}^{\,'}))}{4\pi\left|\vec{r}-\vec{r}^{\,\prime}\right|^2}\delta\left(t-\frac{\left|\vec{r}-\vec{r}^{\,'}\right|}{v}\right). \qquad \text{(A.4)}
\end{aligned}
$$

The time-dependent integral equation 2.35 is derived through the use of convolution integrals [56]. Therefore, the temporal dependence is expressed in terms of a time-shift $(t-t^{'})$ instead of absolute time t. The final form for the heterogeneous time-dependent point kernel is arrived by this replacement:

$$
K_{pt}(\vec{r},\vec{r}^{\,'};t,t') = \frac{\exp(-\tau(\vec{r},\vec{r}^{\,'}))}{4\pi\left|\vec{r}-\vec{r}^{\,\prime}\right|^2}\delta\left(t-t^{'}-\frac{\left|\vec{r}-\vec{r}^{\,'}\right|}{v}\right). \qquad \text{(A.5)}
$$

If the material is homogeneous, then the optical distance between any two points is $v\Sigma(t-t^{'})$ and one can show that the heterogeneous point kernel simplifies into the homogeneous case, as presented in Table 2.1.

A.2 Derivation of Heterogeneous Planar Kernels

The derivation of the heterogeneous planar kernel proceeds in similar fashion to that presented in Appendix A.1. The steady-state heterogeneous planar kernel is [46]:

$$
K_{pl}(x,x') = \frac{1}{2}E_1\left(\tau(x,x')\right). \qquad \text{(A.6)}
$$

The macroscopic cross section is replaced with the modified Laplace transformed cross section, $\tilde{\Sigma}(\vec{r}) = \Sigma(\vec{r}) + \frac{s}{v}$. The derivation proceeds as follows:

$$
K_l(x,x';t) = \mathcal{L}^{-1}\left\{\frac{1}{2}E_1\left[\int_0^{\left|x-x^{'}\right|} d\omega\Sigma\left(x-\omega\frac{x-x^{'}}{|x-x'|}\right)+\frac{s}{v}\right]\right\}
$$

$$
\begin{aligned}
&= \mathcal{L}^{-1}\left\{\frac{1}{2}E_1\left[\tau(x,x^{'})+\frac{s\left|x-x^{'}\right|}{v}\right]\right\} \\
&= \frac{1}{2}\int_1^{\infty}\frac{\exp\left(-\tau u\right)}{u}\mathcal{L}^{-1}\left\{\exp\left(\frac{-s\left|x-x^{'}\right|u}{v}\right)\right\}du \\
&= \frac{1}{2}\int_1^{\infty}\frac{\exp\left(-\tau u\right)}{u}\delta\left(t-\frac{\left|x-x^{'}\right|u}{v}\right)du \\
&= \frac{\exp\left(\frac{-\tau(x,x^{'})vt}{\left|x-x^{'}\right|}\right)}{2t}H\left(t-\frac{\left|x-x^{'}\right|}{v}\right). \qquad \text{(A.7)}
\end{aligned}
$$

As mentioned in Appendix A.1, the final form of the time-dependent kernels are arrived by replacing t with $t-t^{'}$ in equation A.7. The time-dependent heterogeneous slab kernel is:

$$K_{pl}(x,x^{'};t,t^{'})=\frac{\exp\left(\frac{-\tau(x,x^{'})v(t-t^{'})}{\left|x-x^{'}\right|}\right)}{2(t-t^{'})}H\left(t-t^{'}-\frac{\left|x-x^{'}\right|}{v}\right). \qquad \text{(A.8)}$$

If the material is homogeneous, then the optical distance between any two points is: $\Sigma\left|x-x^{'}\right|$. The planar kernel then becomes:

$$K_{pl}(x,x^{'},t)=\frac{\exp(-v\Sigma(t-t^{'}))}{2(t-t^{'})}H\left[t-t^{'}-\frac{|x-x^{'}|}{v}\right] \qquad \text{(A.9)}$$

As expected, the heterogeneous planar kernel simplifies into the homogeneous kernel as given in Table 2.1.

A.3 Derivation of Heterogeneous Line / 2-D Cartesian Kernel

The steady state heterogeneous line kernel is [46]:

$$K_l(r,r';\phi,\phi')=\frac{Ki_1\left(\tau(r,r';\phi,\phi')\right)}{2\pi\rho}, \qquad \text{(A.10)}$$

where:

$$\rho=\sqrt{r^2+r'^2-2rr'\cos(\phi-\phi')}, \qquad \text{(A.11)}$$

and $Ki_1(\tau)$ is the Bickley function defined as [95]:

$$Ki_1(x) = \int_0^{\pi/2} \exp\left(\frac{-x}{\sin\theta}\right) d\theta. \tag{A.12}$$

The macroscopic cross section is replaced with the modified Laplace transformed cross section $\tilde{\Sigma}(\vec{r}) = \Sigma(\vec{r}) + \frac{s}{v}$. The derivation for the time-dependent heterogeneous line kernel then proceeds:

$$\begin{aligned} K_l(r, r'; \phi, \phi'; t) &= \mathcal{L}^{-1}\left\{\frac{1}{2\phi\rho} Ki_1\left(\int_0^{\rho}\left[\Sigma\left(r - \omega\frac{r-r'}{\rho}\right) + \frac{s}{v}\right] d\omega\right)\right\} \\ &= \mathcal{L}^{-1}\left\{\frac{1}{2\phi\rho} Ki_1\left(\ \tau\left(r, r'\right) + \frac{s\rho}{v}\right)\right\} \\ &= \mathcal{L}^{-1}\left\{\frac{1}{2\phi\rho}\int_0^{\pi/2} \exp\left(\frac{-\tau\left(r, r'\right) + \frac{s\rho}{v}}{\sin\theta}\right) d\theta\right\} \\ &= \frac{\exp\left(\frac{-\tau(r,r')vt}{\rho}\right)}{2\pi t\sqrt{(vt)^2 - \rho^2}} H\left[t - \frac{\rho}{v}\right]. \end{aligned} \tag{A.13}$$

Replacing t with $t - t^{'}$ in A.13, the final form of the time-dependent heterogeneous line kernels is:

$$K_l(r, r'; \phi, \phi^{'}; t, t^{'}) = \frac{\exp\left(\frac{-\tau(r,r^{'},\phi,\phi^{'})v(t-t^{'})}{\rho}\right)}{2\pi(t-t^{'})\sqrt{\left[v(t-t^{'})\right]^2 - \rho^2}} H\left[t - t^{'} - \frac{\rho}{v}\right]. \tag{A.14}$$

Transforming equation A.14 into two-dimensional Cartesian coordinates one arrives at the following:

$$\begin{aligned} K_{2D,C}(x, x'; y, y^{'}; t, t^{'}) &= \frac{\exp\left(\frac{-\tau(x,x^{'};y,y^{'})v(t-t^{'})}{\sqrt{|x-x'|^2+|y-y'|^2}}\right)}{2\pi(t-t^{'})\sqrt{\left[v(t-t^{'})\right]^2 - |x-x'|^2 - |y-y'|^2}} \times \\ &\quad H\left[t - t^{'} - \frac{\sqrt{|x-x'|^2 + |y-y'|^2}}{v}\right]. \end{aligned} \tag{A.15}$$

Once again if the material is homogeneous, $\tau = \Sigma\sqrt{|x-x'|^2 + |y-y'|^2}$, the heterogeneous kernel simplifies into the homogeneous case, as presented in Table 2.1.

A.4 Derivation of Multigroup Kernels

The time dependent neutral particle equation for the g^{th} energy group in a heterogeneous medium with an arbitrary isotropic source is:

$$\left(\frac{1}{v_g}\frac{\partial}{\partial t} + \hat{\Omega}\cdot\vec{\nabla} + \Sigma_g\left(\vec{r}\right)\right)\psi_g\left(\vec{r},\hat{\Omega},t\right) = \frac{Q_g(\vec{r},t)}{4\pi}\,. \tag{A.16}$$

The resulting integral equation for the scalar flux in the g^{th} energy group is [56]:

$$\Phi_g(\vec{r},t) = \int_0^t dt' \int_{V'} K_g(\vec{r},\vec{r}\,';t,t')\,Q_g(\vec{r}\,',t')d\vec{r}\,'\,, \tag{A.17}$$

where: $K_g(\vec{r},\vec{r}\,';t,t')$ is the time-dependent kernel for the g^{th} energy group and $Q_g(\vec{r}\,',t')$ is the time-dependent source for the g^{th} energy group. The integration is carried out over the volume of interest, V', from $t=0$ until some later time t.

The heterogeneous kernels derived in Appendices A.1, A.2, and A.3 are used in multigroup transport. The only modification to these kernels is that now the optical depth is energy dependent. The multigroup source term must include an isotropic source and all the possible scattering events which result in a final energy within the g^{th} energy group. Table A.1 compares the homogeneous monoenergetic and the heterogeneous multigroup source terms.

Table A.1: Time-Dependent Source Term

Location	$Q_i(\vec{r}^{\,\prime}, t')$
Monoenergetic Homogeneous	$\Sigma_s \, \Phi(\vec{r}^{\,\prime}, t') + S(\vec{r}^{\,\prime}, t')$
Multigroup Heterogeneous	$\sum_{i=1}^{n} \left(\Sigma_{s_{i \rightarrow g}}(\vec{r}^{\,\prime}) \, \Phi_i(\vec{r}^{\,\prime}, t') \right) + S_g(\vec{r}^{\,\prime}, t')$

Appendix B

Analytical Derivation of Uncollided and Scattered Source for Benchmark Problems

Appendix B will give the analytical solutions for the integration of the kernel and the uncollided flux for the four benchmark problems presented in Chapter 3. Recall, that in general the time dependent integral equation takes the following form:

$$\Phi(\vec{r},t) = \int_0^t dt' \int_{V'} K(\vec{r},\vec{r}';t,t')\, Q(\vec{r}',t')\, d\vec{r}'\,, \tag{B.1}$$

where: $K(\vec{r},\vec{r}';t,t')$ is the time-dependent kernel and $Q(\vec{r}',t')$ is the time-dependent source. The source term $Q(\vec{r},t)$ includes contributions from both an isotropic scattering flux and an arbitrary isotropic source:

$$Q(\vec{r},t) = \Sigma_s\, \Phi(\vec{r},t) + S(\vec{r},t)\,. \tag{B.2}$$

Using the subtraction of the singularity method presented in Chapter 3, Equation B.1 takes the following form:

$$\begin{aligned}
\Phi^{n+1}(\vec{r},t) &= \int_0^t dt' \int_{V'} K(\vec{r},\vec{r}';t,t')[\Sigma_s\{\Phi^n(\vec{r}',t') - \Phi^n(\vec{r},t)\}]\, d\vec{r}' \\
&+ \int_0^t dt' \int_{V'} S(\vec{r}',t') K(\vec{r},\vec{r}';t,t')\, d\vec{r}' \\
&+ \Sigma_s \Phi(r,t) \int_0^t dt' \int_{V'} K(\vec{r},\vec{r}';t,t')\, d\vec{r}'\,.
\end{aligned} \tag{B.3}$$

The first term is calculated numerically using the procedures described in Chapter 3. The second term is simply the uncollided flux and the third is the integration of the kernel. In general neither of these terms can be analytically predetermined; however, for these simple benchmark cases a functional form can be found.

For each of the next four benchmark solutions analytical solutions for the second (uncollided flux) and third term (integration of the kernel) will be presented. The following benchmark cases will be presented:

- Appendix B.1: Homogeneous slab with uniform source
- Appendix B.2: Homogeneous slab with localized source
- Appendix B.3: Homogeneous sphere with localized source
- Appendix B.4: Heterogeneous slab with localized source

B.1 Analytical Expression for Uniform Source in Cartesian Coordinates

Section B.1 presents the uncollided flux and the integration of the kernel for a one-dimensional homogeneous slab with a uniform source. The geometry was already presented in Figure 3.3. The analytical solution for the uncollided flux is:

$$\begin{aligned}\int_0^t dt' \int_0^a S_o \frac{\exp(-\Sigma\, v[t-t'])}{2(t-t')} H\left(t-t'-\frac{|x-x'|}{v}\right) dx' = \\ +\frac{S_o}{\Sigma}\left(\left[1-e^{-\Sigma v t}\right]\right. \\ +\left[e^{-\Sigma v t}-e^{-\Sigma x}+\Sigma x\left\{E_1\left[\Sigma x\right]-E_1\left[\Sigma v t\right]\right\}\right] H\left[t-\frac{x}{v}\right] \\ +\left.\left[e^{-\Sigma v t}-e^{-\Sigma(a-x)}+\Sigma\left(a-x\right)\left\{E_1\left[\Sigma\left(a-x\right)\right]-E_1\left[\Sigma v t\right]\right\}\right] H\left[t-\frac{a-x}{v}\right]\right).\end{aligned} \tag{B.4}$$

Similarly, the analytical solution for the integration of the kernel for a one-dimensional homogeneous slab with a uniform source is identical to that presented in Equation B.5 with the arbitrary source term replaced with the scattered source $\Sigma_s \Phi^n\left(x,t\right)$.

B.2 Analytical Expression for Localized Source in Cartesian Coordinates

The analytical solution for the uncollided flux and the integration of the kernel in one-dimensional Cartesian coordinates for a homogeneous media with a localized source is

calculated. The geometry of the problem is shown in Figure 3.7. The slab has a width a with a localized source, confined from x_1 to x_2. The analytical solution for the uncollided flux with the following source distribution:

$$S\left(x',t'\right) = S_o H\left(x'-x_1\right) H\left(x_2-x'\right),$$

is:

$$\int_0^t dt' \int_0^a S_o\left(x',t'\right) \frac{\exp(-\Sigma\, v[t-t'])}{2(t-t')} H\left(t-t'-\frac{|x-x'|}{v}\right) dx' = \tag{B.5}$$

$$
\frac{S_o}{2\Sigma} * \begin{cases}
x \leq x_1 \\
\left[\left(e^{-\Sigma(x_1-x)} - e^{-\Sigma vt} - \Sigma\left(x_1-x\right)\left(E_1\left[\Sigma\left(x_1-x\right)\right] - E_1\left[\Sigma vt\right]\right)\right) H\left(t-\frac{x_1-x}{v}\right)\right. \\
\left. -\left(e^{-\Sigma(x_2-x)} - e^{-\Sigma vt} - \Sigma\left(x_2-x\right)\left(E_1\left[\Sigma\left(x_2-x\right)\right] - E_1\left[\Sigma vt\right]\right)\right) H\left(t-\frac{x_2-x}{v}\right)\right] \\
\\
x = x_1 \\
\left[\left(1-e^{-\Sigma vt}\right)H\left(t\right)\right. \\
\left. -\left(e^{-\Sigma(x_2-x)} - e^{-\Sigma vt} - \Sigma\left(x_2-x\right)\left(E_1\left[\Sigma\left(x_2-x\right)\right] - E_1\left[\Sigma vt\right]\right)\right) H\left(t-\frac{x_2-x}{v}\right)\right] \\
\\
x \leq x_2 \\
\left[2\left(1-e^{-\Sigma vt}\right)H\left(t\right)\right. \\
+\left(e^{-\Sigma(x-x_1)} - e^{-\Sigma vt} - \Sigma\left(x-x_1\right)\left(E_1\left[\Sigma\left(x-x_1\right)\right] - E_1\left[\Sigma vt\right]\right)\right) H\left(t-\frac{x-x_1}{v}\right) \\
\left. -\left(e^{-\Sigma(x_2-x)} - e^{-\Sigma vt} - \Sigma\left(x_2-x\right)\left(E_1\left[\Sigma\left(x_2-x\right)\right] - E_1\left[\Sigma vt\right]\right)\right) H\left(t-\frac{x_2-x}{v}\right)\right] \\
\\
x = x_2 \\
\left[\left(1-e^{-\Sigma vt}\right)H\left(t\right)\right. \\
\left. +\left(e^{-\Sigma(x-x_1)} - e^{-\Sigma vt} - \Sigma\left(x-x_1\right)\left(E_1\left[\Sigma\left(x-x_1\right)\right] - E_1\left[\Sigma vt\right]\right)\right) H\left(t-\frac{x-x_1}{v}\right)\right] \\
\\
x > x_2 \\
\left[\left(e^{-\Sigma(x-x_2)} - e^{-\Sigma vt} - \Sigma\left(x-x_2\right)\left(E_1\left[\Sigma\left(x-x_2\right)\right] - E_1\left[\Sigma vt\right]\right)\right) H\left(t-\frac{x-x_2}{v}\right)\right. \\
\left. -\left(e^{-\Sigma(x-x_1)} - e^{-\Sigma vt} - \Sigma\left(x-x_1\right)\left(E_1\left[\Sigma\left(x-x_1\right)\right] - E_1\left[\Sigma vt\right]\right)\right) H\left(t-\frac{x-x_1}{v}\right)\right].
\end{cases}
$$

Similarly, the analytical solution for the integration of the kernel for a one-dimensional homogeneous slab with a localized source is identical to that presented earlier in Equation B.5 with the source term replaced with the scattered source.

B.3 Analytical Expression for Localized Source in Spherical Coordinates

The analytical solution for the uncollided flux and the integration of the kernel in one-dimensional Spherical coordinates for a homogeneous sphere with a localized source is solved in Section B.3. The source is confined from r_1 to r_2 (where in this particular problem as shown in Figure 3.11 r_2 is equal to the outer radius a). The functional form of the source is:

$$S\left(r',t'\right) = S_o H\left(r'-r_1\right) H\left(r_2-r'\right),$$

The analytical solution for the uncollided flux is:

$$\int_0^t dt' \int_0^a S_o\left(r',t'\right) \frac{4\pi r'^2 \exp\left(-\Sigma\, v[t-t']\right)}{8\pi r r'(t-t')} H\left(t-t'-\frac{|r-r'|}{v}\right) dx' = \tag{B.6}$$

$$
+\frac{S_o}{2r} * \begin{cases}
0 \leq r \leq r_1 \\
\left[\frac{\left(r^2-r_1^2\right)}{2}\left[E_1\left[\Sigma\left(r_1-r\right)\right]-E_1\left[\Sigma vt\right]\right]-\frac{r}{\Sigma}\left[e^{-\Sigma(r_1-r)}-e^{-\Sigma vt}\right]\right. \\
\left.+\frac{1}{2\Sigma^2}\left[\left(1+\Sigma\left(r_1-r\right)\right)e^{-\Sigma(r_1-r)}-\left(1+\Sigma vt\right)E^{-\Sigma vt}\right]\right]H\left[t-\frac{(r_1-r)}{v}\right] \\
+\left[\frac{\left(r_2^2-r^2\right)}{2}\left[E_1\left[\Sigma\left(r_2-r\right)\right]-E_1\left[\Sigma vt\right]\right]-\frac{r}{\Sigma}\left[e^{-\Sigma(r_2-r)}-e^{-\Sigma vt}\right]\right. \\
\left.+\frac{1}{2\Sigma^2}\left[\left(1+\Sigma\left(r_2-r\right)\right)e^{-\Sigma(r_2-r)}-\left(1+\Sigma vt\right)E^{-\Sigma vt}\right]\right]H\left[t-\frac{(r_2-r)}{v}\right] \\
+\left[\frac{\left(r^2-r_2^2\right)}{2}\left[E_1\left[\Sigma\left(r+r_2\right)\right]-E_1\left[\Sigma vt\right]\right]-\frac{r}{\Sigma}\left[e^{-\Sigma(r+r_2)}-e^{-\Sigma vt}\right]\right. \\
\left.+\frac{1}{2\Sigma^2}\left[\left(1+\Sigma\left(r+r_2\right)\right)e^{-\Sigma(r+r_2)}-\left(1+\Sigma vt\right)e^{-\Sigma vt}\right]\right]H\left[t-\frac{(r+r_2)}{v}\right] \\
+\left[\frac{\left(r_1^2-r^2\right)}{2}\left[E_1\left[\Sigma\left(r+r_1\right)\right]-E_1\left[\Sigma vt\right]\right]+\frac{r}{\Sigma}\left[e^{-\Sigma(r+r_1)}-e^{-\Sigma vt}\right]\right. \\
\left.+\frac{1}{2\Sigma^2}\left[\left(1+\Sigma\left(r+r_1\right)\right)e^{-\Sigma(r+r_1)}-\left(1+\Sigma vt\right)e^{-\Sigma vt}\right]\right]H\left[t-\frac{(r+r_1)}{v}\right] \\
r_1 \leq r \leq r_2 \\
\left[\frac{\left(r_2^2-r^2\right)}{2}\left[E_1\left[\Sigma\left(r_2-r\right)\right]-E_1\left[\Sigma vt\right]\right]-\frac{r}{\Sigma}\left[e^{-\Sigma(r_2-r)}-e^{-\Sigma vt}\right]\right. \\
\left.+\frac{1}{2\Sigma^2}\left[\left(1+\Sigma\left(r_2-r\right)\right)e^{-\Sigma(r_2-r)}-\left(1+\Sigma vt\right)E^{-\Sigma vt}\right]\right]H\left[t-\frac{(r_2-r)}{v}\right] \\
+\left[\frac{\left(r^2-r_1^2\right)}{2}\left[E_1\left[\Sigma\left(r-r_1\right)\right]-E_1\left[\Sigma vt\right]\right]-\frac{r}{\Sigma}\left[e^{-\Sigma(r-r_1)}-e^{-\Sigma vt}\right]\right. \\
\left.+\frac{1}{2\Sigma^2}\left[\left(1+\Sigma\left(r-r_1\right)\right)e^{-\Sigma(r-r_1)}-\left(1+\Sigma vt\right)E^{-\Sigma vt}\right]\right]H\left[t-\frac{(r_1-r)}{v}\right] \\
+\frac{2r}{\Sigma}\left[1-e^{-\Sigma vt}\right] \\
+\left[\frac{\left(r^2-r_2^2\right)}{2}\left[E_1\left[\Sigma\left(r+r_2\right)\right]-E_1\left[\Sigma vt\right]\right]-\frac{r}{\Sigma}\left[e^{-\Sigma(r+r_2)}-e^{-\Sigma vt}\right]\right. \\
\left.+\frac{1}{2\Sigma^2}\left[\left(1+\Sigma\left(r+r_2\right)\right)e^{-\Sigma(r+r_2)}-\left(1+\Sigma vt\right)e^{-\Sigma vt}\right]\right]H\left[t-\frac{(r+r_2)}{v}\right] \\
+\left[\frac{\left(r_1^2-r^2\right)}{2}\left[E_1\left[\Sigma\left(r+r_1\right)\right]-E_1\left[\Sigma vt\right]\right]+\frac{r}{\Sigma}\left[e^{-\Sigma(r+r_1)}-e^{-\Sigma vt}\right]\right. \\
\left.+\frac{1}{2\Sigma^2}\left[\left(1+\Sigma\left(r+r_1\right)\right)e^{-\Sigma(r+r_1)}-\left(1+\Sigma vt\right)e^{-\Sigma vt}\right]\right]H\left[t-\frac{(r+r_1)}{v}\right].
\end{cases} \tag{B.7}
$$

Similarly, the analytical solution for the integration of the kernel for a one-dimensional homogeneous sphere with a localized source is:

$$
\Sigma_S \Phi^n\left(r,t\right)\int_0^t dt' \int_0^a \frac{4\pi r'^2 \exp\left(-\Sigma\, v[t-t']\right)}{8\pi r r'(t-t')} H\left(t-t'-\frac{|r-r'|}{v}\right) dx' = \tag{B.8}
$$

$$+\frac{\Sigma_s\Phi^n(r,t)}{2\Sigma} * \begin{cases} 2\left(1-e^{-\Sigma vt}\right)H(t) \\ \\ -\Big[E_2(\Sigma(a-r)) + \frac{\Sigma^2\left(a^2-r^2\right)}{2\Sigma r}E_1(\Sigma vt) - e^{-\Sigma vt} \\ +\frac{\Sigma(a-r)}{\Sigma r}E_2(\Sigma(a-r))\,\frac{1}{\Sigma r}E_3(\Sigma(a-r)) - \frac{(\Sigma vt)^2}{2\Sigma r}E_1(\Sigma vt) \\ -\frac{\Sigma vt}{\Sigma r}E_2(\Sigma vt) - \frac{1}{\Sigma r}E_3(\Sigma vt)\Big]H\left[t-\frac{a-r}{v}\right] \\ \\ -\Big[E_2(\Sigma(a+r)) - \frac{\Sigma^2\left(a^2-r^2\right)}{2\Sigma r}E_1(\Sigma vt) - e^{-\Sigma vt} \\ +\frac{\Sigma(a+r)}{\Sigma r}E_2(\Sigma(a+r)) \\ +\frac{1}{\Sigma r}E_3(\Sigma(a+r)) - \frac{(\Sigma vt)^2}{2\Sigma r}E_1(\Sigma vt) \\ -\frac{\Sigma vt}{\Sigma r}E_2(\Sigma vt) - \frac{1}{\Sigma r}E_3(\Sigma vt)\Big]H\left[t-\frac{a+r}{v}\right]. \end{cases}$$

B.4 Analytical Expression for Localized Source in Heterogeneous Cartesian Coordinates

As with the previous homogeneous cases, in order to calculate benchmark quality results for heterogeneous Cartesian geometries one uses the analytical results for the integration of the kernel and the uncollided flux. The integral equation for the time-dependent scalar flux in a homogeneous slab of width a with an uniformly distributed source is shown in Eqn. B.9.

$$\begin{aligned} \Phi^{n+1}(x,t) &= \int_0^t dt' \int_0^a K(x,x';t,t')\Sigma_s\{\Phi^n(x',t') - \Phi^n(x,t)\}\,dx' \\ &+ S_o\int_0^t dt' \int_0^a K(x,x';t,t')\,dx' \\ &+ \Sigma_s\Phi^n(x,t)\int_0^t dt' \int_0^a K(x,x';t,t')\,dx'. \end{aligned} \tag{B.9}$$

Where the heterogeneous planar kernel is:

$$K(x,x';t,t') = \frac{\exp\left(\frac{-\tau(x,x')vt}{|x-x'|}\right)}{2(t-t')}H\left(t-t'-\frac{|x-x'|}{v}\right). \tag{B.10}$$

The geometry of the problem used in this benchmark is presented in Figure 3.15. The slab has the same material on either side of the inner source material. The geometry, and hence the function form of the solution, is symmetric around the mid plan of the problem $x = \frac{a}{2}$. Therefore, the analytical solutions will take advantage of this and only present the analytical solution for the half space from $x \leq \frac{a}{2}$.

Although, this geometry is relatively simple. As will be shown the analytical solutions for the uncollided flux and the integration of the kernel, terms 2 and 3 in Equation B.9, are fairly unwieldy. This is due in most part to the changing functional form of the optical depth $\tau\left(x, x'\right)$ depending of whether the calculational point lays within the source region or outside.

The analytical solution for the uncollided flux with the following source distribution:

$$S\left(x', t'\right) = S_o H\left(x' - x_1\right) H\left(x_2 - x'\right),$$

$$\int_0^t dt' \int_0^a S_o\left(x', t'\right) \frac{\exp\left(\frac{-\tau(x,x')vt}{\left|x-x'\right|}\right)}{2\left(t-t'\right)} H\left(t - t' - \frac{\left|x - x'\right|}{v}\right) \tag{B.11}$$

$$
= \frac{S_o}{2} * \begin{cases}
x < x_2 \\
\frac{1}{\Sigma_1}\left\{2(\,1-e^{-\Sigma_1 vt}\,)H\left(t\right)\right. \\
+\left(e^{-\Sigma_1(x-x_1)}-e^{-\Sigma_1 vt}-\Sigma_1\left(x-x_1\right)\right. \\
\left(E_1\left[\Sigma_1\left(x-x_1\right)\right]-E_1\left[\Sigma_1 vt\right]\right)H\left(t-\frac{x-x_1}{v}\right) \\
-\left(e^{-\Sigma_1(x_2-x)}-e^{-\Sigma_1 vt}-\Sigma_1\left(x_2-x\right)\right. \\
\left.\left.\left(E_1\left[\Sigma_1\left(x_2-x\right)\right]-E_1\left[\Sigma_1 vt\right]\right)H\left(t-\frac{x_2-x}{v}\right)\right\}\right. \\
\\
x = x_2 \\
\frac{1}{\Sigma_1}\left\{(\,1-e^{-\Sigma_1 vt}\,)H\left(t\right)\right. \\
+\left(e^{-\Sigma_1(x-x_1)}-e^{-\Sigma_1 vt}-\Sigma_1\left(x-x_1\right)\right. \\
\left.\left.\left(E_1\left[\Sigma_1\left(x-x_1\right)\right]-E_1\left[\Sigma_1 vt\right]\right)H\left(t-\frac{x-x_1}{v}\right)\right\}\right. \\
\\
x > x_2 \\
\tau^* = (\Sigma_1-\Sigma_2)+\Sigma_2 x \\
\\
\frac{1}{\Sigma_2}\left\{e^{-\tau^*+\Sigma_1 x_2}-e^{-\tau^*-\Sigma(vt-x)}+e^{-\Sigma_1 vt}\left(\tau^*-\Sigma_1 v\right)Ei\left[-\tau^*+\Sigma_1 x\right]\right. \\
+e^{-\Sigma_1 vt}\left(\tau^*-\Sigma_1 x\right)Ei\left[\frac{vt[-\tau^*+\Sigma_1 x]}{x-x_2}\right] \\
\left.+\left(\tau^*-\Sigma_1 x_2\right)\left(Ei\left[-\tau^*+\Sigma_1 x_2\right]-Ei\left[\frac{vt[-\tau^*+\Sigma_1 x]}{x-x_2}\right]\right)\right\}H\left(t+\frac{x_2-x}{v}\right) \\
\frac{1}{\Sigma_2}\left\{e^{-\tau^*+\Sigma_1 x_1}-e^{-\tau^*-\Sigma(vt-x)}+e^{-\Sigma_1 vt}\left(\tau^*-\Sigma_1 v\right)Ei\left[-\tau^*+\Sigma_1 x\right]\right. \\
+e^{-\Sigma_1 vt}\left(\tau^*-\Sigma_1 x\right)Ei\left[\frac{vt[-\tau^*+\Sigma_1 x]}{x-x_1}\right] \\
\left.+\left(\tau^*-\Sigma_1 x_1\right)\left(Ei\left[-\tau^*+\Sigma_1 x_1\right]-Ei\left[\frac{vt[-\tau^*+\Sigma_1 x]}{x-x_1}\right]\right)\right\}H\left(t+\frac{x_1-x}{v}\right).
\end{cases}
$$

Similarly, the analytical solution for the integration of the kernel for a one-dimensional heterogeneous slab with a localized source from $x = x_1$ to $x = x_2$ is:

$$
\Sigma_{S,1}\phi^n\left(x,t\right)\int_0^t dt'\int_0^a \frac{\exp\left(\frac{-\tau(x,x')vt}{\left|x-x'\right|}\right)}{2\left(t-t'\right)}H\left(t-t'-\frac{\left|x-x'\right|}{v}\right) \tag{B.12}
$$

$$
= \frac{\Sigma_{S,1}\phi(x,t)}{2} * \begin{cases}
x < x_2 \qquad (x+vt) \le x_2 \qquad (x-vt) \ge x_1 \\
\\
\frac{1}{\Sigma_1}\left(1 - e^{-\Sigma_1 vt}\right) \\
\hline
x < x_2 \qquad (x+vt) > x_2 \qquad (x-vt) \ge x_1 \\
\tau^* = (\Sigma_1 - \Sigma_2) - \Sigma_1 x \qquad x_{high} = x + vt <> a \\
\\
\frac{1}{2\Sigma_1}\left\{2\left(1 - e^{-\Sigma_1 vt}\right)\right. \\
\left.\left(e^{-\Sigma_1(x_2-x)} - e^{-\Sigma_1 vt} + \Sigma(x_2 - x) - (Ei[\Sigma_1(x_2-x)] - Ei[-\Sigma_1 vt])\right\}\right. \\
\\
+\frac{1}{2\Sigma_2}\left\{e^{-\tau^*-\Sigma_2 x_2} - e^{-\Sigma_2 vt} - \left(e^{-\tau-\Sigma_2 x} + (\tau^* + \Sigma_2 x)\, Ei[-\tau^* - \Sigma_2 x]\right)\right. \\
+e^{-\Sigma_2 vt}(\tau^* + \Sigma_2 x)\, Ei\left[\frac{vt(\tau^*+\Sigma_2 x)}{x-x_2}\right] \\
\left.+ (\tau^* + \Sigma_2 x)\left(Ei[-\tau^* - \Sigma_2 x_2] - Ei\left[\frac{vt(\tau^*+\Sigma_2 x_2)}{x-x_2}\right]\right)\right\} \\
\\
-\frac{1}{2\Sigma_2}\left\{e^{-\tau^*-\Sigma_2 x_{high}} - e^{-\Sigma_2 vt}\left(e^{-\tau-\Sigma_2 x} + (\tau^* + \Sigma_2 x)\, Ei[-\tau^* - \Sigma_2 x]\right)\right. \\
+e^{-\Sigma_2 vt}(\tau^* + \Sigma_2 x)\, Ei\left[\frac{vt(\tau^*+\Sigma_2 x)}{x-x_{high}}\right] \\
\left.+ (\tau^* + \Sigma_2 x)\left(Ei[-\tau^* - \Sigma_2 x_{high}] - Ei\left[\frac{vt\left(\tau^*+\Sigma_2 x_{high}\right)}{x-x_{high}}\right]\right)\right\}
\end{cases}
$$

$$
= \frac{\Sigma_{S,1}\phi(x,t)}{2} * \left\{ \begin{array}{l}
x < x_2 \qquad (x+vt) > x_2 \qquad (x-vt) < x_1 \\
\tau^* = (\Sigma_1 - \Sigma_2) - \Sigma_1 x \qquad \tau^{**} = \Sigma_1 (x_2 - a + x) - \Sigma_2 x_2 \\
x_{high} = x + vt <> a \qquad x_{low} = (a-x) + vt <> a \\
\\
\frac{1}{2\Sigma_1} \left\{ 2\left(1 - e^{-\Sigma_1 vt}\right) \right. \\
- \left(e^{-\Sigma_1 (x_2 - x)} - e^{-\Sigma_1 vt} + \Sigma (x_2 - x) \right. \\
\left. (Ei[-\Sigma_1 (x_2 - x)] - Ei[-\Sigma_1 vt]) \right\} \\
- \left(e^{-\Sigma_1 (x_2 - (x-a))} - e^{-\Sigma_1 vt} + \Sigma (x_2 - (x-a)) \right. \\
\left. (Ei[-\Sigma_1 (x_2 - a + x)] - Ei[-\Sigma_1 vt]) \right\} \\
\\
+ \frac{1}{2\Sigma_2} \left\{ e^{-\tau^* - \Sigma_2 x_2} - e^{-\Sigma_2 vt} \left(e^{-\tau^* - \Sigma_2 x} + (\tau^* + \Sigma_2 x) Ei[-\tau^* - \Sigma_2 x] \right) \right. \\
+ e^{-\Sigma_2 vt} (\tau^* + \Sigma_2 x) Ei\left[\frac{vt(\tau^* + \Sigma_2 x)}{x - x_2} \right] \\
\left. + (\tau^* + \Sigma_2 x_2) \left(Ei[-\tau^* - \Sigma_2 x_2] - Ei\left[\frac{vt(\tau^* + \Sigma_2 x_2)}{x - x_2} \right] \right) \right\} \\
- \frac{1}{2\Sigma_2} \left\{ e^{-\tau^* - \Sigma_2 x_{high}} - e^{-\Sigma_2 vt} \left(e^{-\tau - \Sigma_2 x} + (\tau^* + \Sigma_2 x) Ei[-\tau^* - \Sigma_2 x] \right) \right. \\
+ e^{-\Sigma_2 vt} (\tau^* + \Sigma_2 x) Ei\left[\frac{vt(\tau^* + \Sigma_2 x)}{x - x_{high}} \right] \\
\left. + (\tau^* + \Sigma_2 x_{high}) \left(Ei[-\tau^* - \Sigma_2 x_{high}] - Ei\left[\frac{vt\left(\tau^* + \Sigma_2 x_{high}\right)}{x - x_{high}} \right] \right) \right\} \\
+ \frac{1}{2\Sigma_2} \left\{ e^{-\tau^{**} - \Sigma_2 x_2} - e^{-\Sigma_2 vt} \left(e^{-\tau^{**} - \Sigma_2 (a-x)} \right. \right. \\
\left. + (\tau^{**} + \Sigma_2 (a-x)) Ei[-\tau^{**} - \Sigma_2 (a-x)] \right) \\
+ e^{-\Sigma_2 vt} (\tau^{**} + \Sigma_2 (a-x)) Ei\left[\frac{vt(\tau^{**} + \Sigma_2 (a-x))}{a - x - x_2} \right] \\
\left. + (\tau^{**} + \Sigma_2 x_2) \left(Ei[-\tau^{**} - \Sigma_2 x_2] - Ei\left[\frac{vt(\tau^{**} + \Sigma_2 x_2)}{a - x - x_2} \right] \right) \right\} \\
- \frac{1}{2\Sigma_2} \left\{ e^{-\tau^{**} - \Sigma_2 x_{low}} - e^{-\Sigma_2 vt} \left(e^{-\tau - \Sigma_2 (a-x)} \right. \right. \\
\left. + (\tau^* + \Sigma_2 (a-x)) Ei[-\tau^{**} - \Sigma_2 (a-x)] \right) \\
+ e^{-\Sigma_2 vt} (\tau^{**} + \Sigma_2 (a-x)) Ei\left[\frac{vt(\tau^{**} + \Sigma_2 (a-x))}{a - x - x_{low}} \right] \\
\left. + (\tau^{**} + \Sigma_2 x_{low}) \left(Ei[-\tau^{**} - \Sigma_2 x_{low}] - Ei\left[\frac{vt(\tau^{**} + \Sigma_2 x_{low})}{a - x - x_{low}} \right] \right) \right\}
\end{array} \right.
$$

$$
= \frac{\phi(x,t)}{2} * \begin{cases}
x = x_2 \qquad (x - vt) \geq x_1 \\
\tau^* = (\Sigma_1 - \Sigma_2) - \Sigma_1 x \qquad \tau^{**} = \Sigma_1 (x_2 - a + x) - \Sigma_2 x_2 \\
x_{high} = x + vt <> a \qquad x_{low} = (a - x) + vt <> a \\
\\
\frac{\Sigma_{S,2}}{\Sigma_2} \left\{ \left(1 - e^{-\Sigma_2 vt}\right) \right. \\
- \left(e^{-\Sigma_2 \left(x - x_{high}\right)} - e^{-\Sigma_2 vt} + \Sigma_2 (x_{high} - x) \right. \\
\left. \left. (Ei\left[-\Sigma_2 (x_{high} - x)\right] - Ei\left[-\Sigma_2 vt\right]) \right) \right\} \\
+ \frac{\Sigma_{S,1}}{\Sigma_1} \left(1 - e^{-\Sigma_1 vt}\right) \\
\hline
x = x_2 \qquad (x - vt) < x_1 \\
\tau^* = (\Sigma_1 - \Sigma_2) - \Sigma_1 x \qquad \tau^{**} = \Sigma_1 (x_2 - a + x) - \Sigma_2 x_2 \\
x_{high} = x + vt <> a \qquad x_{low} = (a - x) + vt <> a \\
\\
\frac{\Sigma_{S,2}}{\Sigma_2} \left\{ \left(1 - e^{-\Sigma_2 vt}\right) \right. \\
- \left(e^{-\Sigma_2 \left(x - x_{high}\right)} - e^{-\Sigma_2 vt} + \Sigma_2 (x_{high} - x) \right. \\
\left. \left. (Ei\left[-\Sigma_2 (x_{high} - x)\right] - Ei\left[-\Sigma_2 vt\right]) \right) \right\} \\
\\
+ \frac{\Sigma_{S,1}}{\Sigma_1} \left\{ e^{-\tau^{**} - \Sigma_2 x_2} - e^{-\Sigma_2 vt} \left(e^{-\tau^{**} - \Sigma_2 (a - x)} + (\tau^{**} + \Sigma_2 (a - x)) \right. \right. \\
\left. Ei\left[-\tau^{**} - \Sigma_2 (a - x)\right] \right) \\
+ e^{-\Sigma_2 vt} (\tau^{**} + \Sigma_2 x_2) \, Ei\left[\frac{vt(\tau^{**} + \Sigma_2 (a - x))}{a - x - x_2} \right] \\
\left. + (\tau^{**} + \Sigma_2 x_2) \left(Ei\left[-\tau^{**} - \Sigma_2 (a - x)\right] - Ei\left[\frac{vt(\tau^{**} + \Sigma_2 x_2)}{a - x - x_2} \right] \right) \right\} \\
- \frac{\Sigma_{S,1}}{\Sigma_1} \left\{ e^{-\tau^{**} - \Sigma_2 x_{low}} - e^{-\Sigma_2 vt} \left(e^{-\tau - \Sigma_2 (a - x)} + (\tau^* + \Sigma_2 (a - x)) \right. \right. \\
\left. Ei\left[-\tau^{**} - \Sigma_2 (a - x)\right] \right) \\
+ e^{-\Sigma_2 vt} (\tau^{**} + \Sigma_2 (a - x)) \, Ei\left[\frac{vt(\tau^{**} + \Sigma_2 x_{low})}{a - x - x_{low}} \right] \\
\left. + (\tau^{**} + \Sigma_2 x_{low}) \left(Ei\left[-\tau^{**} - \Sigma_2 (a - x)\right] - Ei\left[\frac{vt(\tau^{**} + \Sigma_2 x_{low})}{a - x - x_{low}} \right] \right) \right\}
\end{cases}
$$

$$
= \frac{\phi(x,t)}{2} * \begin{cases}
x > x_2 \qquad (x - vt) \geq x_1 \\
\tau^* = (\Sigma_1 - \Sigma_2) - \Sigma_1 x \qquad \tau^{**} = \Sigma_1 (x_2 - a + x) - \Sigma_2 x_2 \\
x_{high} = x + vt <> a \qquad x_{low} = (a - x) + vt <> a \\
\\
\frac{\Sigma_{S,2}}{\Sigma_2} \left\{ \left(1 - e^{-\Sigma_2 vt}\right) \right. \\
- \left(e^{-\Sigma_2 \left(x_{high} - x\right)} - e^{-\Sigma_2 vt} + \Sigma_2 (x_{high} - x) \right. \\
\left. (Ei\left[-\Sigma_2 (x_{high} - x)\right] - Ei\left[-\Sigma_2 vt\right]) \right\} \\
\left. + \frac{\Sigma_{S,2}}{\Sigma_2} \left(1 - e^{-\Sigma_2 vt}\right) \right. \\
\hline
x > x_2 \qquad x_1 \leq (x - vt) < x_2 \\
\tau^* = (\Sigma_1 - \Sigma_2) - \Sigma_1 x \qquad \tau^{**} = \Sigma_1 (x_2 - a + x) - \Sigma_2 x_2 \\
x_{high} = x + vt <> a \qquad x_{low} = (a - x) + vt <> a \\
\\
\frac{\Sigma_{S,2}}{\Sigma_2} \left\{ 2 \left(1 - e^{-\Sigma_2 vt}\right) \right. \\
- \left(e^{-\Sigma_2 \left(x_{high} - x\right)} - e^{-\Sigma_2 vt} + \Sigma_2 (x_{high} - x) \right. \\
\left. (Ei\left[-\Sigma_2 (x_{high} - x)\right] - Ei\left[-\Sigma_2 vt\right]) \right) \\
- \left(e^{-\Sigma_2 (x - x_{low})} - e^{-\Sigma_2 vt} + \Sigma_2 (x - x_{low}) \right. \\
\left. (Ei\left[-\Sigma_2 (x - x_{low})\right] - Ei\left[-\Sigma_2 vt\right]) \right\} \\
\\
+ \frac{\Sigma_{S,1}}{\Sigma_1} \left\{ e^{-\tau^* + \Sigma_1 x_2} - e^{-\tau^* - \Sigma_1 vt} \left(e^{\Sigma_1 x} + e^{\tau^*} (\tau^* - \Sigma_1 x) Ei\left[-\tau^* + \Sigma_1 x\right] \right) \right. \\
+ e^{-\Sigma_1 vt} (\tau^* - \Sigma_1 x) Ei\left[\frac{vt(-\tau^* + \Sigma_1 x)}{x - x_2} \right] \\
\left. + (\tau^* - \Sigma_1 x_2) \left(Ei\left[-\tau^* + \Sigma_1 x_2\right] - Ei\left[\frac{vt(-\tau^* + \Sigma_1 x_2)}{x - x_2} \right] \right) \right\} \\
- \frac{\Sigma_{S,1}}{\Sigma_1} \left\{ e^{-\tau^* + \Sigma_1 x_{xlow}} - e^{-\tau^* - \Sigma_1 vt} \left(e^{\Sigma_1 x} + e^{\tau^*} (\tau^* - \Sigma_1 x) Ei\left[-\tau^* + \Sigma_1 x\right] \right) \right. \\
+ e^{-\Sigma_1 vt} (\tau^* - \Sigma_1 x) Ei\left[\frac{vt(-\tau^* + \Sigma_1 x)}{x - x_{low}} \right] \\
\left. + (\tau^* - \Sigma_1 x_{xlow}) \left(Ei\left[-\tau^* + \Sigma_1 x_{xlow}\right] - Ei\left[\frac{vt(-\tau^* + \Sigma_1 x_{low})}{x - x_{low}} \right] \right) \right\}
\end{cases}
$$

$$
\begin{aligned}
= \quad & \frac{\phi(x,t)}{2} * \Bigg\{ \\
& x > x_2 \qquad (x - vt) < x_1 \\
& \tau^* = (\Sigma_1 - \Sigma_2) - \Sigma_1 x \qquad \tau^{**} = \Sigma_1 (x_2 - a + x) - \Sigma_2 x_2 \\
& x_{high} = x + vt <> a \qquad x_{low} = (a - x) + vt <> a \\
& \\
& + \tfrac{\Sigma_{S,1}}{\Sigma_1} \Big\{ e^{-\tau^* + \Sigma_1 x_2} - e^{-\tau^* - \Sigma_1 vt} \left(e^{\Sigma_1 x} + e^{\tau^*} (\tau^* - \Sigma_1 x) Ei [-\tau^* + \Sigma_1 x] \right) \\
& + e^{-\Sigma_1 vt} (\tau^* - \Sigma_1 x) Ei \left[\tfrac{vt(-\tau^* + \Sigma_1 x)}{x - x_2} \right] \\
& + (\tau^* - \Sigma_1 x_2) \left(Ei [-\tau^* + \Sigma_1 x_2] - Ei \left[\tfrac{vt(-\tau^* + \Sigma_1 x_2)}{x - x_2} \right] \right) \Big\} \\
& - e^{-\tau^* + \Sigma_1 x_1} + e^{-\tau^* - \Sigma_1 vt} \left(e^{\Sigma_1 x} + e^{\tau^*} (\tau^* - \Sigma_1 x) Ei [-\tau^* + \Sigma_1 x] \right) \\
& - e^{-\Sigma_1 vt} (\tau^* - \Sigma_1 x) Ei \left[\tfrac{vt(-\tau^* + \Sigma_1 x)}{x - x_1} \right] \\
& - (\tau^* - \Sigma_1 x_1) \left(Ei [-\tau^* + \Sigma_1 x_1] - Ei \left[\tfrac{vt(-\tau^* + \Sigma_1 x_1)}{x - x_1} \right] \right) \Big\} \\
& \\
& \tfrac{\Sigma_{S,2}}{\Sigma_2} \Big\{ 2 \left(1 - e^{-\Sigma_2 vt} \right) \\
& - \Big(e^{-\Sigma_2 (x_{high} - x)} - e^{-\Sigma_2 vt} \\
& + \Sigma_2 (x_{high} - x) (Ei [-\Sigma_2 (x_{high} - x)] - Ei [-\Sigma_2 vt])) \\
& - \Big(e^{-\Sigma_2 (x - x_{low})} - e^{-\Sigma_2 vt} + \Sigma_2 (x - x_{low}) \\
& (Ei [-\Sigma_2 (x - x_{low})] - Ei [-\Sigma_2 vt])) \Big\} \\
& + \tfrac{\Sigma_{S,2}}{\Sigma_2} \Big\{ e^{-\tau^{**} + \Sigma_2 x_1} - e^{-\tau^{**} - \Sigma_2 vt} \left(e^{\Sigma_2 x} + e^{\tau^{**}} (\tau^{**} - \Sigma_2 x) Ei [-\tau^{**} + \Sigma_2 x] \right) \\
& + e^{-\Sigma_2 vt} (\tau^{**} - \Sigma_2 x) Ei \left[\tfrac{vt(-\tau^{**} + \Sigma_2 x)}{x - x_1} \right] \\
& + (\tau^{**} - \Sigma_2 x_1) \left(Ei [-\tau^{**} + \Sigma_2 x_1] - Ei \left[\tfrac{vt(-\tau^{**} + \Sigma_2 x_1)}{x - x_1} \right] \right) \Big\} \\
& + \tfrac{\Sigma_{S,2}}{\Sigma_2} \Big\{ e^{-\tau^{**} + \Sigma_2 x_{low}} - e^{-\tau^{**} - \Sigma_2 vt} \left(e^{\Sigma_2 x} + e^{\tau^{**}} (\tau^{**} - \Sigma_2 x) Ei [-\tau^{**} + \Sigma_2 x] \right) \\
& + e^{-\Sigma_2 vt} (\tau^{**} - \Sigma_2 x) Ei \left[\tfrac{vt(-\tau^{**} + \Sigma_2 x)}{x - x_{low}} \right] \\
& + (\tau^{**} - \Sigma_2 x_{low}) \left(Ei [-\tau^{**} + \Sigma_2 x_{low}] - Ei \left[\tfrac{vt(-\tau^{**} + \Sigma_2 x_{low})}{x - x_{low}} \right] \right) \Big\} . \Bigg\}
\end{aligned}
$$

Appendix C

Other Benchmark Quality Results

Although Chapter 3 and Appendix B go into great detail discussing the time-dependent benchmark methods and solutions, Appendix C endeavors to provide the researcher with a wider variety of benchmarks to use in validation.

C.1 Additional Data for Ganapol's Infinite media problem

In Section 3.3 the time-dependent integral method was compared to a semi-analytical benchmark problem published by B.D. Ganapol. In his paper, he only published specific values for the scalar flux at very specific temporal and spatial positions. Tables 3.4 and 3.6 show how the integral method compares with this benchmark.

The comparisons are very favorable with the two methods only differing in the fifth significant digit. The results in Tables C.1, C.2, and C.3 give the additional data for the points and times that were left out from Ganapol's original paper. The author hopes that the additional data will provide valuable information for future researchers.

C.2 Uniform Source of Thermal Neutrons in Carbon Slab

The time-dependent benchmark described in Section 3.3.2 was run using carbon instead of the unit material documented in Table 3.2. The geometry of the problem remains the same as shown in Figure 3.3; however, the slab is now 10 cm across instead of 10 mean free path lengths. The source strength remains 1.0 n/cm^3-s throughout the interior of the slab. The particles are thermal neutrons at 0.025 eV (2200 m/sec) instead of the unit velocity particles given in Chapter 3. The material properties of carbon at thermal

Table C.1: Additional Data for Ganapol's Infinite Media Problem

Time	1 [cm]	2 [cm]	3 [cm]	4 [cm]	5 [cm]
1	1.8394E-01	0.0000E+00	0.0000E+00	0.0000E+00	0.0000E+00
2	2.6256E-01	3.3834E-02	0.0000E+00	0.0000E+00	0.0000E+00
3	2.3942E-01	9.3835E-02	8.2978E-03	0.0000E+00	0.0000E+00
4	2.1736E-01	1.1360E-01	3.3287E-02	2.2895E-03	0.0000E+00
5	1.9957E-01	1.2105E-01	4.9595E-02	1.1823E-02	6.7379E-04
6	1.8523E-01	1.2322E-01	6.0604E-02	2.0710E-02	4.2106E-03
7	1.7347E-01	1.2293E-01	6.8028E-02	2.8447E-02	8.4157E-03
8	1.6364E-01	1.2143E-01	7.3032E-02	3.4901E-02	1.2790E-02
9	1.5528E-01	1.1935E-01	7.6384E-02	4.0186E-02	1.7004E-02
10	1.4806E-01	1.1699E-01	7.8590E-02	4.4479E-02	2.0905E-02
⋮	⋮	⋮	⋮	⋮	⋮
14	1.2673E-01	1.0737E-01	8.1292E-02	5.4845E-02	3.2828E-02
15	1.2269E-01	1.0514E-01	8.1159E-02	5.6305E-02	3.4985E-02
16	1.1901E-01	1.0300E-01	8.0859E-02	5.7469E-02	3.6876E-02
⋮	⋮	⋮	⋮	⋮	⋮
19	1.0968E-01	9.7166E-02	7.9349E-02	5.9663E-02	4.1241E-02
20	1.0702E-01	9.5402E-02	7.8724E-02	6.0078E-02	4.2344E-02
21	1.0455E-01	9.3719E-02	7.8066E-02	6.0376E-02	4.3305E-02

Table C.2: Additional Data for Ganapol's Infinite Media Problem - 2

Time	1 [cm]	2 [cm]	3 [cm]	4 [cm]	5 [cm]
24	9.8041E-02	8.9120E-02	7.5991E-02	6.0750E-02	4.5498E-02
25	9.6128E-02	8.7720E-02	7.5287E-02	6.0744E-02	4.6042E-02
26	9.4323E-02	8.6382E-02	7.4584E-02	6.0689E-02	4.6511E-02
⋮	⋮	⋮	⋮	⋮	⋮
29	8.9460E-02	8.2688E-02	7.2508E-02	6.0301E-02	4.7542E-02
30	8.7998E-02	8.1554E-02	7.1833E-02	6.0116E-02	4.7784E-02
31	8.6606E-02	8.0464E-02	7.1168E-02	5.9910E-02	4.7984E-02
⋮	⋮	⋮	⋮	⋮	⋮
34	8.2795E-02	7.7430E-02	6.9242E-02	5.9198E-02	4.8373E-02
35	8.1632E-02	7.6491E-02	6.8624E-02	5.8937E-02	4.8445E-02
36	8.0517E-02	7.5584E-02	6.8018E-02	5.8668E-02	4.8493E-02
⋮	⋮	⋮	⋮	⋮	⋮
39	7.7427E-02	7.3041E-02	6.6272E-02	5.7826E-02	4.8515E-02
40	7.6473E-02	7.2248E-02	6.5714E-02	5.7538E-02	4.8490E-02
41	7.5554E-02	7.1480E-02	6.5167E-02	5.7247E-02	4.8450E-02
⋮	⋮	⋮	⋮	⋮	⋮
44	7.2983E-02	6.9311E-02	6.3594E-02	5.6367E-02	4.8260E-02
45	7.2182E-02	6.8630E-02	6.3091E-02	5.6074E-02	4.8177E-02

Table C.3: Additional Data for Ganapol's Infinite Media Problem - 3

Time	10 [cm]	15 [cm]	20 [cm]	25 [cm]	30 [cm]
14	3.0305E-04	0.0000E+00	0.0000E+00	0.0000E+00	0.0000E+00
15	4.8585E-04	1.0197E-08	0.0000E+00	0.0000E+00	0.0000E+00
16	7.1607E-04	1.5374E-07	0.0000E+00	0.0000E+00	0.0000E+00
⋮	⋮	⋮	⋮	⋮	⋮
19	1.6652E-03	3.7778E-06	0.0000E+00	0.0000E+00	0.0000E+00
20	2.0542E-03	7.3483E-06	5.1529E-11	0.0000E+00	0.0000E+00
21	2.4718E-03	1.2927E-05	9.5159E-10	0.0000E+00	0.0000E+00
⋮	⋮	⋮	⋮	⋮	⋮
24	3.8509E-03	4.7200E-05	3.9693E-08	0.0000E+00	0.0000E+00
25	4.3391E-03	6.6215E-05	8.9812E-08	2.7776E-13	0.0000E+00
26	4.8355E-03	8.9794E-05	1.8188E-07	5.1332E-12	0.0000E+00
⋮	⋮	⋮	⋮	⋮	⋮
29	6.3463E-03	1.9136E-04	9.6593E-07	3.6602E-10	0.0000E+00
30	6.8493E-03	2.3629E-04	1.5136E-06	9.4930E-10	1.5596E-15
31	7.3489E-03	2.8702E-04	2.2788E-06	2.1781E-09	2.8663E-14
⋮	⋮	⋮	⋮	⋮	⋮
34	8.8138E-03	4.7417E-04	6.4353E-06	1.6015E-08	3.0620E-12
35	9.2873E-03	5.4807E-04	8.6471E-06	2.7650E-08	8.9947E-12
36	9.7521E-03	6.2755E-04	1.1382E-05	4.5651E-08	2.3115E-11

Table C.4: Material Properties for Thermal Neutrons in Carbon

Total cross section	.38532 cm^{-1}
Scattering cross section	.385 cm^{-1}
Isotropic source strength	1.0 n/cm^3-s

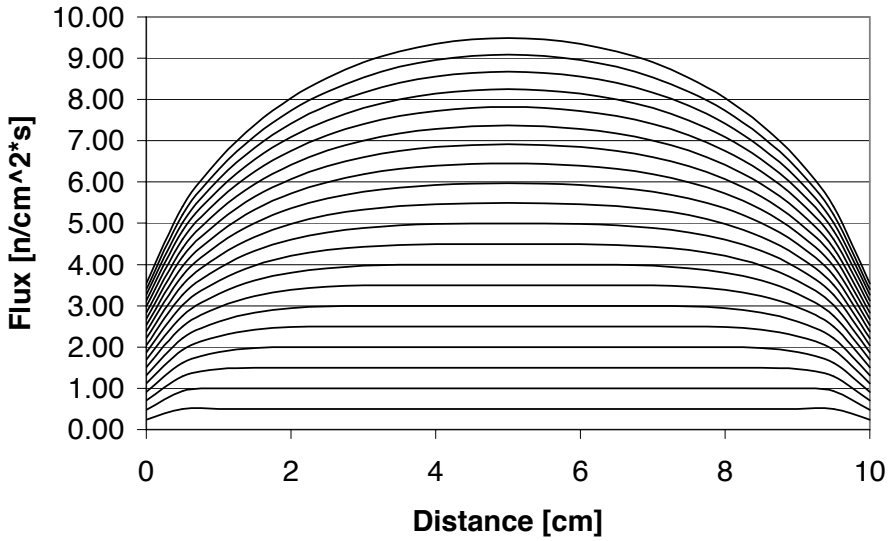

Figure C.1: Time-Dependent Flux for Thermal Neutrons with Uniform Source in Carbon

energies are given in Table C.4 [97].

The results shown in Table C.5 are qualitative values for the thermal neutron flux at discrete points in the slab after: 4.572 μs, 11.43 μs, 34.29 μs, and 45.73 μs respectively. At these particular times the particles have had enough time to travel roughly 1/10, 1/4, 1/2, 3/4 of the way, and finally completely across the slab.

Figure C.1 shows a graphical output for the scalar flux. As expected, the scalar flux increases in magnitude for each succeeding step during the early stages of the simulation. Each curve represents a time-step of 4.572 μ seconds. This is the amount of time that it takes for a thermal neutron to travel 1 cm.

Table C.5: Benchmark Solutions for Uniform Source in 10 cm Slab of Carbon

Distance cm	Time 4.572 μs	Time 11.43 μs	Time 22.86 μs	Time 34.29 μs	Time 45.73 μs
0.0	0.4773	1.1201	2.0444	2.8375	3.5379
0.5	0.9316	1.9278	3.2665	4.4025	5.4061
1.0	0.9998	2.2604	3.9108	5.3069	6.5424
1.5	0.9998	2.4200	4.3297	5.9503	7.3882
2.0	0.9998	2.4847	4.6048	6.4197	8.0348
2.5	0.9998	2.4990	4.7809	6.7619	8.5288
3.0	0.9998	2.4990	4.8886	7.0075	8.9000
3.5	0.9998	2.4990	4.9497	7.1780	9.1694
4.0	0.9998	2.4990	4.9806	7.2890	9.3518
4.5	0.9998	2.4990	4.9932	7.3515	9.4573
5.0	0.9998	2.4990	4.9960	7.3716	9.4918
5.5	0.9998	2.4990	4.9932	7.3515	9.4573
6.0	0.9998	2.4990	4.9806	7.2890	9.3518
6.5	0.9998	2.4990	4.9497	7.1780	9.1694
7.0	0.9998	2.4990	4.8886	7.0075	8.9000
7.5	0.9998	2.4990	4.7809	6.7619	8.5288
8.0	0.9998	2.4847	4.6048	6.4197	8.0348
8.5	0.9998	2.4200	4.3297	5.9503	7.3882
9.0	0.9998	2.2604	3.9108	5.3069	6.5424
9.5	0.9316	1.9278	3.2665	4.4025	5.4061
10.0	0.4773	1.1201	2.0444	2.8375	3.5379

C.3 Localized Source of Thermal Neutrons in Carbon Slab

The second time-dependent benchmark described in Section 3.3.3 was run using carbon instead of the unit material documented in Table 3.2. The geometry of the problem remains the same as shown in Figure 3.7; however, the slab is now 10 cm across instead of 10 mean free path lengths. The source region is confined to the inner 5 cm of the slab and possesses a source strength of 1.0 n/cm^3-s. The simulated particles are now thermal neutrons at 0.025 eV (2200 m/sec) instead of the unit velocity particles given in Chapter 4. The material properties of carbon at thermal energies are given in Table C.4.

The results shown in Table C.6 are qualitative values for the thermal neutron flux at discrete points in the slab after: 4.572 μs, 11.43 μs, 34.29 μs, and 45.73 μs respectively. At these particular times the particles have had enough time to travel roughly 1/10, 1/4, 1/2, 3/4, and finally completely across the slab.

Figure C.2 shows a graphical output for the scalar flux. The scalar flux increases in magnitude for each succeeding step during the early stages of the simulation. Each curve represents a time-step of 4.572 μ seconds. This is the amount of time that it takes for a thermal neutron to travel 1 cm. As with the unit material case, one can easily see that it takes a finite amount of time for particles to travel from the interior source region into the outer non-source region.

C.4 Localized Source of Thermal Neutrons in a Carbon Sphere

The third time-dependent benchmark described in Section 3.3.4 was run using carbon instead of the unit material documented in Table 3.2. The geometry of the problem remains the same as shown in Figure 3.11; however, the sphere is now 10 cm across with the source region confined to the outer 2 cm of the sphere. The source strength remains 1.0 n/cm^3-s. The simulated particles are now thermal neutrons at 0.025 eV (2200 m/sec)

Table C.6: Benchmark Solutions for Localized Source in 10 cm Slab of Carbon

Distance cm	Time 4.572 μs	Time 11.43 μs	Time 22.86 μs	Time 34.29 μs	Time 45.73 μs
0.0	0.0000	0.0000	0.1847	0.5468	0.9429
0.5	0.0000	0.0142	0.3633	0.9126	1.4869
1.0	0.0000	0.0773	0.6150	1.3304	2.0465
1.5	0.0000	0.2303	0.9860	1.8656	2.7100
2.0	0.0674	0.5413	1.5374	2.5771	3.5380
2.5	0.4999	1.2495	2.4980	3.6871	4.7517
3.0	0.9324	1.9577	3.4558	4.7773	5.9309
3.5	0.9998	2.2687	3.9948	5.4271	6.6526
4.0	0.9998	2.4217	4.3353	5.8513	7.1298
4.5	0.9998	2.4848	4.5261	6.0942	7.4051
5.0	0.9998	2.4990	4.5876	6.1735	7.4953
5.5	0.9998	2.4848	4.5261	6.0942	7.4051
6.0	0.9998	2.4217	4.3353	5.8513	7.1298
6.5	0.9998	2.2687	3.9948	5.4271	6.6526
7.0	0.9324	1.9577	3.4558	4.7773	5.9309
7.5	0.4999	1.2495	2.4980	3.6871	4.7517
8.0	0.0674	0.5413	1.5374	2.5771	3.5380
8.5	0.0000	0.2303	0.9860	1.8656	2.7100
9.0	0.0000	0.0773	0.6150	1.3304	2.0465
9.5	0.0000	0.0142	0.3633	0.9126	1.4869
10.0	0.0000	0.0000	0.1847	0.5468	0.9429

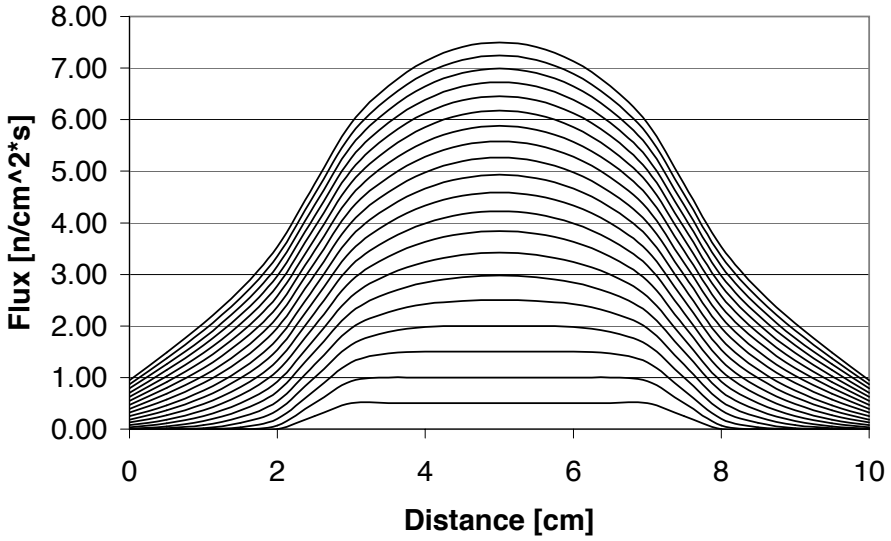

Figure C.2: Time-Dependent Flux for Thermal Neutrons with Localized Source in Carbon

instead of the unit velocity particles given in Chapter 3. The material properties of carbon at thermal energies are given in Table C.4.

The results shown in Table C.7 are qualitative values for the thermal neutron flux at discrete points in the sphere after: 4.572 μs, 11.43 μs, 34.29 μs, and 45.73 μs respectively. At these particular times the particles have had enough time to travel roughly 1/10, 1/4, 1/2, 3/4 of the way, and finally completely across the sphere.

Figure C.3 shows a graphical output for the scalar flux. The scalar flux increases in magnitude for each succeeding step as expected during the early stages of the simulation. Each curve represents a time-step of 4.572 μ seconds. This is the amount of time that it takes for a thermal neutron to travel 1 cm. As with the other localized cases, the thermal neutrons take a finite amount of time to travel from the outer regions of the sphere into the central non-source region

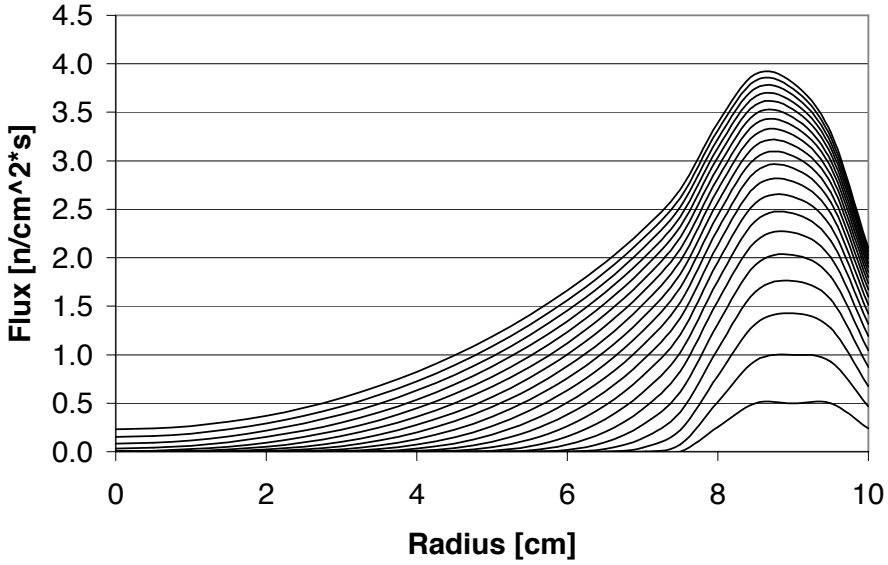

Figure C.3: Time-Dependent Flux for Thermal Neutrons with Localized Source in 10cm Sphere of Carbon

C.5 Localized Source of Thermal Neutrons in Heterogeneous slab

The final benchmark of Appendix C reproduces the heterogeneous benchmark in Section 3.3.5. The geometry of the problem remains the same as shown in Figure 3.15; however, the slab is now 10 cm across. The source region is confined to the inner 5 cm of the slab and possesses a source strength of 1.0 n/cm^3-s. The simulated particles are now thermal neutrons at 0.025 eV (2200 m/sec) instead of the unit velocity particles given in Chapter 3. The interior source region is 5 cm of water and the outer region is composed of natural uranium. The material properties of thermal neutrons in water and natural uranium are given in Table C.8 and Table C.9 [97].

The results shown in Table C.10 are qualitative values for the thermal neutron flux at discrete points in the slab after: 4.572 μs, 11.43 μs, 34.29 μs, and 45.73 μs respectively. At these particular times the particles have had enough time to travel roughly 1/10, 1/4, 1/2, 3/4 of the way, and finally completely across the slab.

Figure C.4 shows a graphical output for the scalar flux. The scalar flux increases in magnitude for each succeeding step as expected during the early stages of the simulation. Each curve represents a time-step of 4.572 μ seconds. This is the amount of time that it takes for a thermal neutron to travel 1 cm. As with the other localized cases, the thermal neutrons take a finite amount of time to travel from the outer regions of the sphere into the central non-source region.

The difference between the homogeneous localized carbon case and the heterogeneous water and uranium slab is evident in the non-source region. For this particular case, the natural uranium readily absorbs the thermal neutrons that travel from the inner water region. The high absorption cross section prevents thermal neutrons from building up to any large extent in the outer uranium region

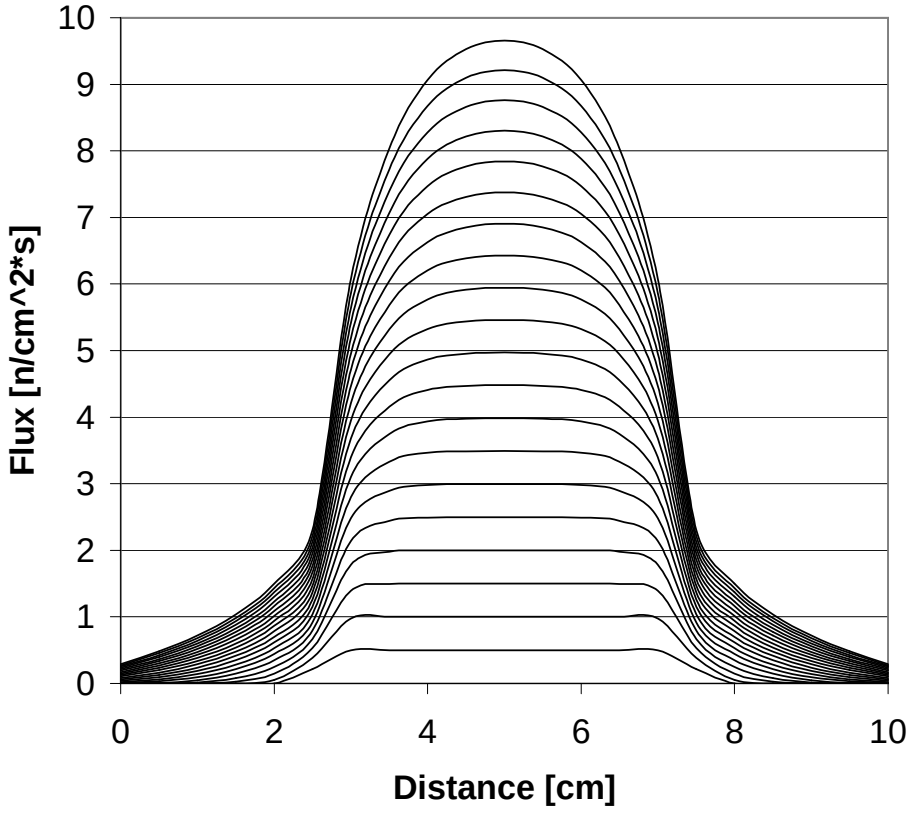

Figure C.4: Time-Dependent Flux for Thermal Neutrons in Heterogeneous Slab of Uranium and Water

Table C.7: Benchmark Solutions for 10 cm Sphere

Radius cm	Time 4.572 μs	Time 11.43 μs	Time 22.86 μs	Time 34.29 μs	Time 45.73 μs
0.0	0.0000	0.0000	0.0000	0.0000	0.2333
0.5	0.0000	0.0000	0.0000	0.0000	0.2400
1.0	0.0000	0.0000	0.0000	0.0058	0.2652
1.5	0.0000	0.0000	0.0000	0.0219	0.3087
2.0	0.0000	0.0000	0.0000	0.0507	0.3708
2.5	0.0000	0.0000	0.0000	0.0962	0.4525
3.0	0.0000	0.0000	0.0000	0.1613	0.5544
3.5	0.0000	0.0000	0.0064	0.2475	0.6773
4.0	0.0000	0.0000	0.0312	0.3582	0.8225
4.5	0.0000	0.0000	0.0840	0.4971	0.9915
5.0	0.0000	0.0000	0.1759	0.6677	1.1861
5.5	0.0000	0.0000	0.3153	0.8737	1.4084
6.0	0.0000	0.0193	0.5074	1.1198	1.6614
6.5	0.0000	0.0986	0.7623	1.4124	1.9508
7.0	0.0000	0.2767	1.0952	1.7641	2.2881
7.5	0.0733	0.6145	1.5400	2.2064	2.7048
8.0	0.5148	1.3179	2.2894	2.9310	3.3926
8.5	0.9376	1.9268	2.8883	3.4826	3.8966
9.0	0.9998	2.0295	2.9227	3.4476	3.8037
9.5	0.9270	1.8067	2.5719	3.0052	3.2930
10.0	0.4659	1.0459	1.5970	1.9013	2.1001

Table C.8: Material Properties for Thermal Neutrons in Water

Total Cross Section Σ	3.4522 cm^{-1}
Scattering cross section Σ_s	3.45 cm^{-1}

Table C.9: Material Properties for Thermal Neutrons in Natural Uranium

Total Cross Section Σ	0.542 cm^{-1}
Scattering cross section Σ_s	0.372 cm^{-1}

Table C.10: Benchmark Solutions for 10 cm Heterogeneous Slab of Water and Uranium

Distance cm	Time 4.572 μs	Time 11.43 μs	Time 22.86 μs	Time 34.29 μs	Time 45.73 μs
0.0	0.0000E+00	0.0000E+00	8.2388E-02	1.9278E-01	2.9115E-01
0.5	0.0000E+00	9.2952E-03	1.6483E-01	3.3455E-01	4.8462E-01
1.0	0.0000E+00	4.9935E-02	2.8722E-01	5.1560E-01	7.1673E-01
1.5	0.0000E+00	1.4784E-01	4.7876E-01	7.7483E-01	1.0353E+00
2.0	5.5604E-02	3.4752E-01	7.8523E-01	1.1644E+00	1.4984E+00
2.5	3.8215E-01	7.9512E-01	1.3656E+00	1.8605E+00	2.2982E+00
3.0	9.7250E-01	2.1430E+00	3.6781E+00	4.9545E+00	6.0742E+00
3.5	1.0002E+00	2.4432E+00	4.5581E+00	6.3973E+00	8.0426E+00
4.0	1.0002E+00	2.4918E+00	4.8673E+00	7.0539E+00	9.0642E+00
4.5	1.0002E+00	2.4960E+00	4.9547E+00	7.3110E+00	9.5279E+00
5.0	1.0002E+00	2.4961E+00	4.9709E+00	7.3755E+00	9.6580E+00
5.5	1.0002E+00	2.4960E+00	4.9547E+00	7.3110E+00	9.5279E+00
6.0	1.0002E+00	2.4918E+00	4.8673E+00	7.0539E+00	9.0642E+00
6.5	1.0002E+00	2.4432E+00	4.5581E+00	6.3973E+00	8.0426E+00
7.0	9.7250E-01	2.1430E+00	3.6781E+00	4.9545E+00	6.0742E+00
7.5	3.8215E-01	7.9512E-01	1.3656E+00	1.8605E+00	2.2982E+00
8.0	5.5604E-02	3.4752E-01	7.8523E-01	1.1644E+00	1.4984E+00
8.5	0.0000E+00	1.4784E-01	4.7876E-01	7.7483E-01	1.0353E+00
9.0	0.0000E+00	4.9935E-02	2.8722E-01	5.1560E-01	7.1673E-01
9.5	0.0000E+00	9.2952E-03	1.6483E-01	3.3455E-01	4.8462E-01
10.0	0.0000E+00	0.0000E+00	8.2388E-02	1.9278E-01	2.9115E-01

Appendix D

Additional Comments on Steady State results

Chapter 3 benchmarks the time-dependent methods against steady-state results produced using steady-state integral methods. These results were given without comment. In Appendix D, the methods and results will be discussed more in depth. For each of the four benchmark cases presented, the steady state results are produced using the same Romberg integration techniques as presented in Section 3.3. Convergence to a steady state result was found once the integration from the n to the $n+1$ level resulted in no less than four significant figures. Numerically the following integral is solved in each of the four benchmark cases:

$$\Phi^{n+1}(\vec{r}) = \int_0^a \left[\Sigma_s(\vec{r}')\,\Phi^n(\vec{r}') + S_o(\vec{r}')\right] K(\vec{r},\vec{r}')\,d\vec{r}'. \tag{D.1}$$

Similar to the time-dependent cases, the steady state kernels are singular when $\vec{r}'=\vec{r}$. Thus, the subtraction of the singularity method was used to numerically solve these problems. Applying the subtraction of the singularity method to Equation D.1 the following is obtained:

$$\begin{aligned}\Phi^{n+1}(\vec{r}) = & \\ &+\int_0^a \left[\Sigma_s(\vec{r}')\left(\Phi^n(\vec{r}') - \Phi^n(\vec{r})\right) + S_o(\vec{r}') - S_o(\vec{r})\right] K(\vec{r},\vec{r}')\,d\vec{r}' \\ &+\left(\Sigma_s(\vec{r})\,\Phi^n(\vec{r}) + S_o(\vec{r})\right)\int_0^a K(\vec{r},\vec{r}')\,d\vec{r}'.\end{aligned} \tag{D.2}$$

The first term in Eqn. D.2 is handled numerically. However, the singularity at $\vec{r}'=\vec{r}$ is now no longer a problem because the integrand is identical to zero. The second term is now calculated analytically and varies depending on the analytical form of the kernel.

Figure D.1: Steady-State solution for Homogeneous Slab with Uniform source

D.1 Steady-State Uniform Source in Homogeneous Slab

A steady-state solution for a uniform source in a homogeneous slab, as described in Section 3.3.2, was solved. The geometry of the problem is shown in Figure 3.3. Analytically integrating the one-dimensional homogeneous kernel in Equation D.2, one arrives at the following:

$$\int_0^a E_1\left(\Sigma\left|x-x'\right|\right)dx' = 2 - E_2\left[\Sigma x\right] - E_2\left[\Sigma\left(a-x\right)\right]. \tag{D.3}$$

The numerical values for this case are given in Table D.1 and shown in Figure D.1.

D.2 Steady-State Localized Source in Homogeneous Slab

The steady-state benchmark solution for a homogeneous slab with a localized source, as described in Section 3.3.3, was calculated. The geometry of the problem is shown in

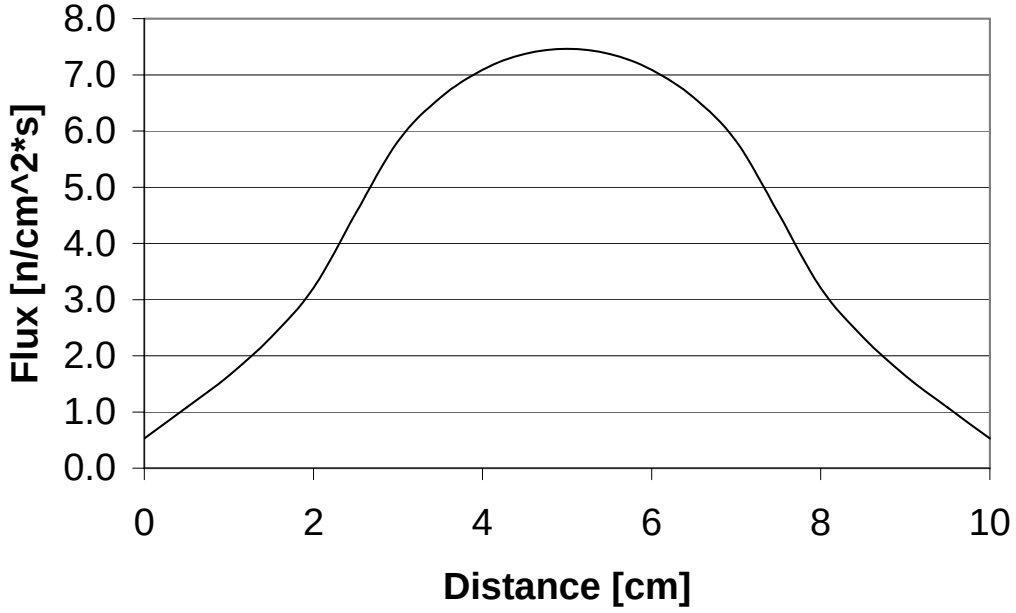

Figure D.2: Steady-State solution for Homogeneous Slab with Localized Source

Figure 3.7. Analytically integrating the one-dimensional homogeneous kernel one arrives at the previously derived Equation D.3. The numerical values for this case are given in Table D.1 and shown in Figure D.2.

D.3 Steady-State Localized Source in Homogeneous Sphere

The steady-state benchmark solution for a homogeneous sphere with a localized source distributed in the outer 2 mfp, as described in Section 3.3.4, was obtained. The geometry of the problem is shown in Figure 3.11. Analytically integrating the one-dimensional homogeneous spherical kernel in Equation D.2, one arrives at the following:

$$\int_0^a \frac{E_1\left[\Sigma\left|r-r'\right|\right]-E_1\left[\Sigma\left|r+r'\right|\right]}{8\pi r r'}dr' = \tag{D.4}$$
$$2\Sigma r+\Sigma a\left(E_2\left[\Sigma\left(a+r\right)\right]-E_2\left[\Sigma\left(a-r\right)\right]\right)+E_3\left[\Sigma\left(a+r\right)\right]-E_3\left[\Sigma\left(a-r\right)\right].$$

Figure D.3: Steady-State solution for Sphere with Localized Source

The numerical values for this case are given in Table D.1 and shown in Figure D.3.

D.4 Steady-State Localized Source in Heterogeneous Slab

The final steady-state benchmark was calculated for the heterogeneous slab, as described in Section 3.3.5 The geometry of the problem is shown in Figure 3.15. Analytically integrating the one-dimensional heterogeneous kernel in Equation D.6, one arrives at the following:

$$\int_0^a E_1\left[\tau\left(x,x'\right)\right]dx' = \tag{D.5}$$
$$\frac{1}{\Sigma_2}\left[e^{-\tau_1}\left(e^{\Sigma_2 x_1}-1\right)-\tau_1 E_i\left[-\tau_1\right]+\left(\tau_1-\Sigma_2 x_1\right)E_i\left[-\tau_1+\Sigma_2 x_1\right]\right]+$$
$$\frac{1}{\Sigma_1}\left[e^{-\tau_2}\left(e^{\Sigma_1 x}-e^{\Sigma_1 x_1}\right)+\left(\tau_2-\Sigma_1 x\right)E_i\left[-\tau_2+\Sigma_1 x\right]+\left(-\tau_2+\Sigma_1 x_1\right)E_i\left[-\tau_2+\Sigma_1 x_1\right]\right]+$$

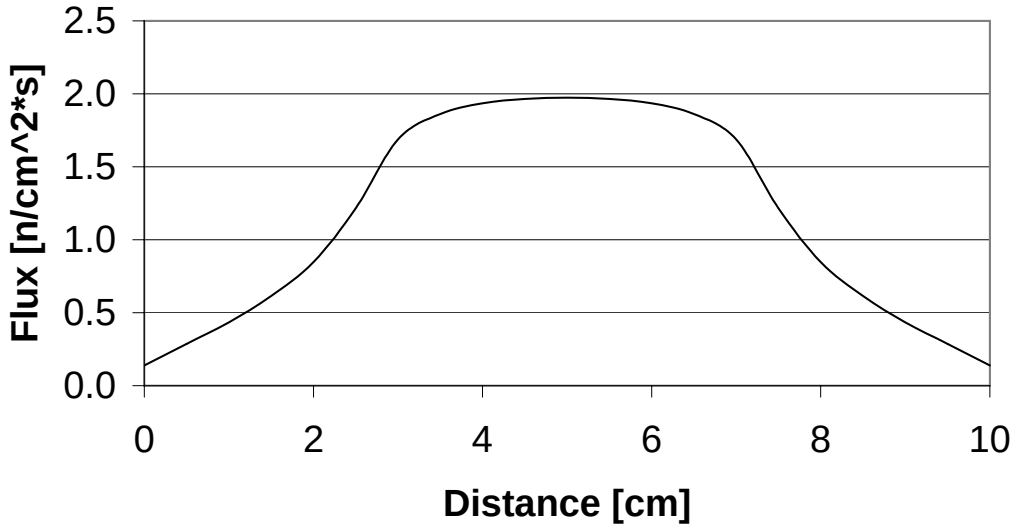

Figure D.4: Steady-State solution for Heterogeneous Slab with Localized source

$$\frac{1}{\Sigma_1}\left[e^{\tau_3-\Sigma_1 x}-e^{\tau_3-\Sigma_1 x_2}+\left(-\tau_3+\Sigma_1 x\right)E_i\left[\tau_3-\Sigma_1 x\right]+\left(\tau_3-\Sigma_1 x_2\right)E_i\left[\tau_3-\Sigma_1 x_2\right]\right]+$$
$$\frac{1}{\Sigma_2}\left[e^{-\tau_4}\left(e^{-\Sigma_2 x_2}-e^{-\Sigma_2 a}\right)-\left(\tau_4+\Sigma_2 a\right)E_i\left[-\tau_4-\Sigma_2 a\right]+\left(\tau_4+\Sigma_2 x_2\right)E_i\left[-\tau_4-\Sigma_2 x_2\right]\right],$$

where:

$$\begin{aligned}\tau_1 &= \Sigma_1\left(x-x_1\right)+\Sigma_2 x_1\\ \tau_2 &= \Sigma_1 x\\ \tau_3 &= \Sigma_1 x\\ \tau_4 &= \Sigma_1\left(x_2-x\right)+\Sigma_2 x_2.\end{aligned}$$

The numerical values for this case are given in Table D.1 and shown in Figure D.4.

Table D.1: Benchmark Solutions for Steady-State Cases

Distance mfp	Homogeneous Slab Uniform	Homogeneous Slab Localized	Homogeneous Sphere Localized	Heterogeneous Slab Localized
0.0	2.3865	0.5281	0.3428	0.1389
0.5	4.6020	1.0814	0.3467	0.2844
1.0	5.9124	1.6448	0.3588	0.4327
1.5	6.8572	2.3267	0.3795	0.6123
2.0	7.5562	3.2070	0.4096	0.8450
2.5	8.0742	4.5386	0.4505	1.2072
3.0	8.4535	5.8191	0.5039	1.6871
3.5	8.7230	6.5930	0.5723	1.8605
4.0	8.9028	7.0903	0.6586	1.9348
4.5	9.0057	7.3708	0.7669	1.9656
5.0	9.0392	7.4616	0.9025	1.9740
5.5	9.0057	7.3708	1.0721	1.9656
6.0	8.9028	7.0903	1.2851	1.9348
6.5	8.7230	6.5930	1.5549	1.8605
7.0	8.4535	5.8191	1.9023	1.6871
7.5	8.0742	4.5386	2.3695	1.2072
8.0	7.5562	3.2070	3.1654	0.8450
8.5	6.8572	2.3267	3.7351	0.6123
9.0	5.9124	1.6448	3.6202	0.4327
9.5	4.6020	1.0814	2.9950	0.2844
10.0	2.3865	0.5281	1.5366	0.1389

Appendix E

Description of Input File for TBIT

The input code for TBIT is a single file "tbit.in" which is placed in the directory where the executable tbit.exe is located. In Appendix E, a sample file will be provided and each input line will be discussed. In this section, lines that start with the word "Input" require that the user enter in data, while those that start with the word "Title" are just place holding lines that are used to describe the input that follows.

E.1 Geometry and Energy Group

The first four lines in Table E.1 are fairly self explanatory. The user must input the number of dimensions and the geometry type for the problem. Currently, TBIT only supports Cartesian and spherical geometries; however, the method is easily expanded into cylindrical coordinates. The input for lines 3 and 4 are not strictly needed. The reason for this is that the code determines whether or not the problem is homogeneous or heterogeneous based off the number of materials that are entered later in the data file.

Table E.1: Geometry and Energy Group input for TBIT

Line 1	Input: Number of Dimensions (1d, 2d, or 3d)
Line 2	Input: Geometry type (Cartesian or Spherical)
Line 3	Input: Material Type (Homogeneous or Heterogeneous)
Line 4	Input: Particle Type (Monoenergentic or Multigroup)

Table E.2: Number of Nodes in Each Spatial Direction input for TBIT

Line 5	Title: "Number of nodes in the x/r direction"
Line 6	Input: Number of nodes in the x/r direction
Line 7	Title: "Number of nodes in the y/theta direction"
Line 8	Input: Number of nodes in the y/theta direction
Line 9	Title: "Number of nodes in the z/phi direction"
Line 10	Input: Number of nodes in the z/phi direction

Similarly, whether or not the particles in the problem are monoenergetic or multigroup is determined based on the number of energy groups the user provides.

E.2 Number of Nodes in Each Spatial Direction

Lines 5-10 in Table E.2 are self explanatory, each input line determines the number of nodes for their respective spatial direction. Two items of interest should be mentioned, however. First the number of spatial nodes in the azimuthal spherical angle ϕ should be 1/2 the number in the polar angle θ. The polar angle only extends from 0 to π where as the polar angle extends from 0 to 2π; therefore, in order to keep the grid spacing uniform the number of nodes in the polar angle should be twice that of the azimuthal. The second item of interest, is that through benchmarking of the TBIT method it was found that the spatial step size should be less than or equal to the smallest mean free path length of any of the materials in the problem. Thus, the number of nodes in any given direction should be adjusted such that this constraint is met.

Table E.3: Energy Groups input for TBIT

Line 11	Title: "Number of Energy/Frequency Groups"
Line 12	Input: Number of Energy/Frequency Groups
Line 13	Title: "Energy of Groups (E(1), ...)"
Line 14+	Input: Number of Energy Groups

E.3 Energy Group Input

The user must enter in the number of energy or frequency groups. Then each energy/frequency group must be entered on a separate line. If there are two energy groups for neutrons one at 14.1 MeV and one at 5 MeV then the user would enter 14.1 on line 14 and 5.0 on line 15.

As line 14 in Table E.3, is the final line that is held in common for all possible geometries and energy groups, the following tables will have the line numbers omitted; however, the generalized lines are labeled alphabetically for each table for convenience when referring back to a particular line in their respective table.

E.4 Total Macroscopic Cross Section Input

The user must enter the number of materials for the problem on line b. For each material type, there must be a repeat of lines 'c' and 'd'. In addition for each energy group, the total macroscopic cross section $\Sigma(E)$ must be inputed on a new line for each energy group. Thus, if there are two materials with two energy groups the input must look like Table E.5.

Table E.4: Total Macroscopic Cross Section Input for TBIT

Line a	Title: "Number of Materials in Problem (Homogeneous = 1)"
Line b	Input: Number of materials in problem
Line c	Title: "Material 'n' Sigma Total"
Line d	Input: Sigma Total for each energy group
Line e	Input: "Material 'n' Sigma s"
Line f	Input: "Energy 1 (1→ 1, 1→ 2, 1→ 3 ....)
Line g	Input: Scattering Cross sections for Material n at Energy 1

Table E.5: Total Cross Section input for TBIT

Material '1' Sigma Total
$\Sigma_1(E_1)$
$\Sigma_1(E_2)$
Material '2' Sigma Total
$\Sigma_2(E_1)$
$\Sigma_2(E_2)$

Table E.6: Scattering Cross Section input for TBIT

Material '1' Sigma s
Energy 1 (1→ 1, 1→ 2, 1→ 3 ....)
$\sum_{s^1}^{E_1 \rightarrow E_1}$
$\sum_{s^1}^{E_1 \rightarrow E_2}$
Energy 2 (1→ 1, 1→ 2, 1→ 3 ....)
$\sum_{s^1}^{E_2 \rightarrow E_1}$
$\sum_{s^1}^{E_2 \rightarrow E_2}$
Material '2' Sigma s
Energy 1 (1→ 1, 1→ 2, 1→ 3 ....)
$\sum_{s^2}^{E_1 \rightarrow E_1}$
$\sum_{s^2}^{E_1 \rightarrow E_2}$
Energy 2 (1→ 1, 1→ 2, 1→ 3 ....)
$\sum_{s^2}^{E_2 \rightarrow E_1}$
$\sum_{s^2}^{E_2 \rightarrow E_2}$

E.5 Scattering Cross Section Input

In a similar fashion to the total macroscopic cross sections, the within group and down scattered cross sections must be entered for each material type and energy group. Each cross section must be entered on a new line. For example, if there are two material types and two energy groups lines 'e' and 'g' in Table E.6 would be the input. Although, one must input up-scattering cross sections they are not currently used in any calculations. Currently the TBIT method only supports down-scattered particles. Therefore, it is

Table E.7: Geometry and Material input for TBIT

Line a	Title: "Number of Regions"
Line b	Input: Number of Regions
Line c	Title: "Region 'n' (low,high,material)
Line d	Input: Node number for the lower boundary of the region
Line e	Input: Node number for the higher boundary of the region
Line f	Input: Material Number

recommended that one enter 0.0 for any scattering cross sections that result in higher energy groups.

As the geometry and material input for one, two and three dimensional systems differ. Each one will be described in its own section.

E.6 1-D geometry and material input

In one-dimensional coordinates, the input for the material/geometry is relatively easy to understand. The user enters the number of distinct material regions in the problem. If the sphere has an inner and an outer region then the input for line b would be two. Then for each region: the lower node number, the higher node number, and the material number is entered for each distinct region.

For example a one-dimensional spherical problem with 50 nodes and two materials (0 and 1) with material zero confined to the inner 25 nodes and material 1 confined to the outer 25 would have an input file as shown in Table E.8. A picture of the sample geometry is shown in Figure E.1.

Table E.8: Material/Geometry Sample Input for 1-D Spherical TBIT

“Number of Regions”
2
“Region ’1’ (low,high,material)
0
50
0
“Region ’2’ (low,high,material)
51
100
1

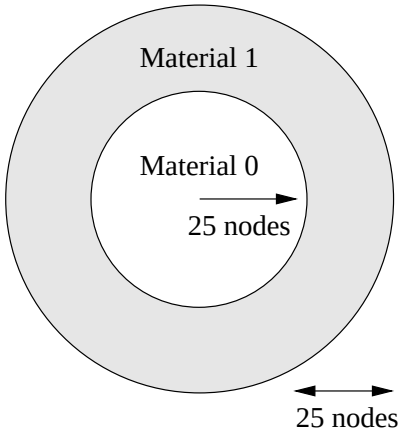

Figure E.1: Material/Geometry Sample Input for 1-D Spherical TBIT

Table E.9: Geometry and Material input for 2-D TBIT

Line a	Title: "Number of Regions"
Line b	Input: Number of Regions
Line c	Title: "Region 'n' (low,high,material,start row, end row)
Line d	Input: Node number for the lower 'x/r' boundary of the region
Line e	Input: Node number for the higher 'x/r' boundary of the region
Line f	Input: Material Number
Line g	Input: The starting row of this particular geometry slice in 'y/theta'
Line h	Input: The ending row of this particular geometry slice in 'y/theta'

E.7 2-D geometry and material input

In two-dimensions the definition of a region changes slightly from that presented in one-dimensional coordinates. A region in two-dimensions is when a geometry slice in the x/r direction changes from one row to another. This means that only when the geometry of the problem changes in y or theta is there a new region.

For example a two-dimensional Cartesian problem is shown in Figure E.2. The input file for this particular geometry would have an input similar to Table E.10.

E.8 3-D geometry and material input

In three-dimensional coordinates, a level is defined once the geometry in the x/y or r/theta direction changes with z/phi. Only when the geometry/material changes in z or phi is a new level defined. The definition of a region (as being in x/y or r/theta geometry) is unchanged.

Table E.10: Material/Geometry Sample Input for 2-D Cartesian TBIT

“Number of Regions”
2
“Region ’1’ (ylow,yhigh,xlow,xhigh,material)
0
50
0
50
0
51
100
1
“Region ’2’ (low,high,material)
51
100
0
50
1
51
100
0

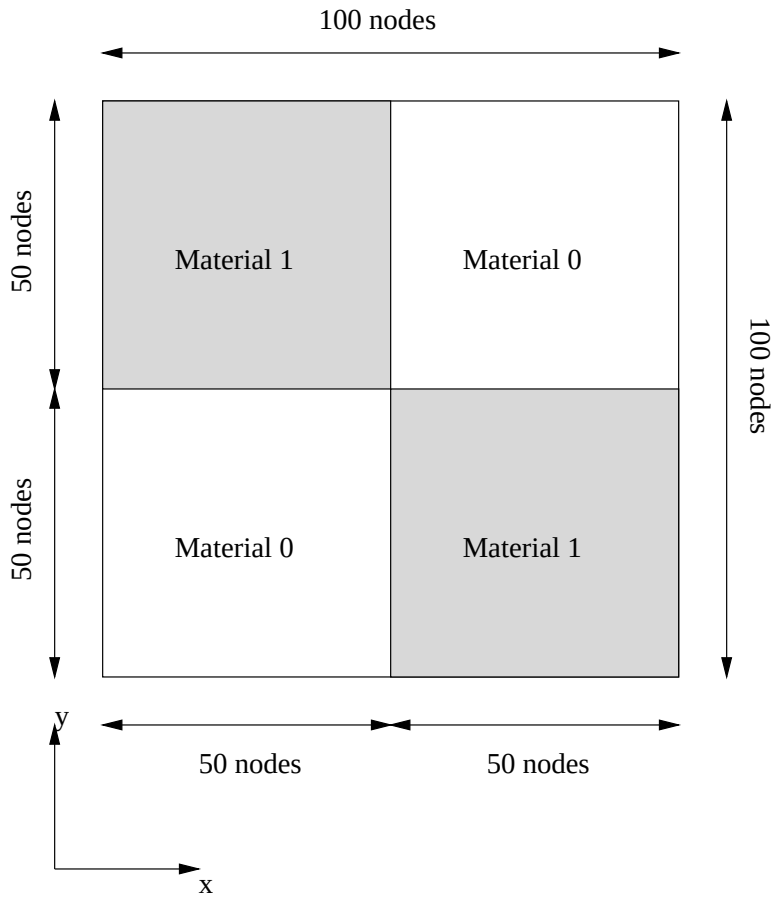

Figure E.2: Material/Geometry Sample Input for 2-D Cartesian TBIT

Table E.11: Geometry and Material input for 3-D TBIT

Line a	Title: “Number of Levels”
Line b	Input: Number of Levels
Line c	Input: “Level ’n’ (low,high)”
Line d	Input: Node number for the lower ’z/phi’ level
Line e	Input: Node number for the higher ’z/phi’ level
Line a	Title: “Number of Regions”
Line b	Input: Number of Regions
Line c	Title: “Region ’n’ (low,high,material,start row, end row)
Line d	Input: Node number for the lower ’x/r’ boundary of the region
Line e	Input: Node number for the higher ’x/r’ boundary of the region
Line f	Input: Material Number
Line g	Input: The starting row of this particular geometry slice in ’y/theta’
Line h	Input: The ending row of this particular geometry slice in ’y/theta’

For example a three-dimensional Cartesian problem is shown in Figure E.3. The input file for this particular geometry is shown in Table E.12.

E.9 Time-steps and Number of Radial and Angular Calculational Directions

The number of time-steps, as inputed in line 'b', is based off the highest energy group. Recall that the time step for the g^{th} energy group is defined as: $\Delta t = \frac{\Delta x}{v_g}$.

The input on line 'c' defines the number of polar angular directions to use when calculating the integrated scalar flux. Likewise, line 'f' defines the number of azimuthal directions; however, this is only included in three-dimensional geometries. The azimuthal and polar angles are distributed uniformly in Cosine of the angle and not over the angle itself. In principle the greater the number of directions the higher the accuracy; however, this increases the computational time.

There are two comments to be made at this point. First, as mentioned earlier for the 3-D spherical geometry, the azimuthal angle ranges from 0 to π or one-half that of the polar angle. Therefore the number of nodes should be one-half those inputed in line 'd'. Finally, the number of directions in the polar angle should be roughly equal to the number of theta directions in spherical coordinates.

The number nodes in the radial direction is inputed on line 'g'. This is the number of nodes that are distributed over one Δx when the integration is taking place along a specific angular direction. The number of nodes in the radial direction should be greater than 4. Any number of nodes less than four and the TBIT method is forced to use a Newton-Cotes type rule to integrate along the radial direction. This means that the calculational point at $(\vec{r}, t)$ is included in the calculation. As mentioned in Chapter 4, the particle flux at a particular point and time can not contribute to its own scattered flux. Therefore, one should use open or semi-open type rules that do not include the origin of

Table E.12: Material/Geometry Sample Input for 3-D Cartesian TBIT

Column A	Column B
“Number of Layers”	
2	
“Level1”	“Level 2”
0	51
50	100
“Number of Regions”	“Number of Regions”
2	2
“Region ’1’ (ylow,yhigh,xlow,xhigh,material)	“Region ’1’ (ylow,yhigh,xlow,xhigh,material)
0	0
50	50
0	0
50	50
0	1
51	51
100	100
1	0
“Region ’2’ (ylow,yhigh,xlow,xhigh,material)	“Region ’2’ (ylow,yhigh,xlow,xhigh,material)
51	51
100	100
0	0
50	50
1	0
51	51
100	100
0	1

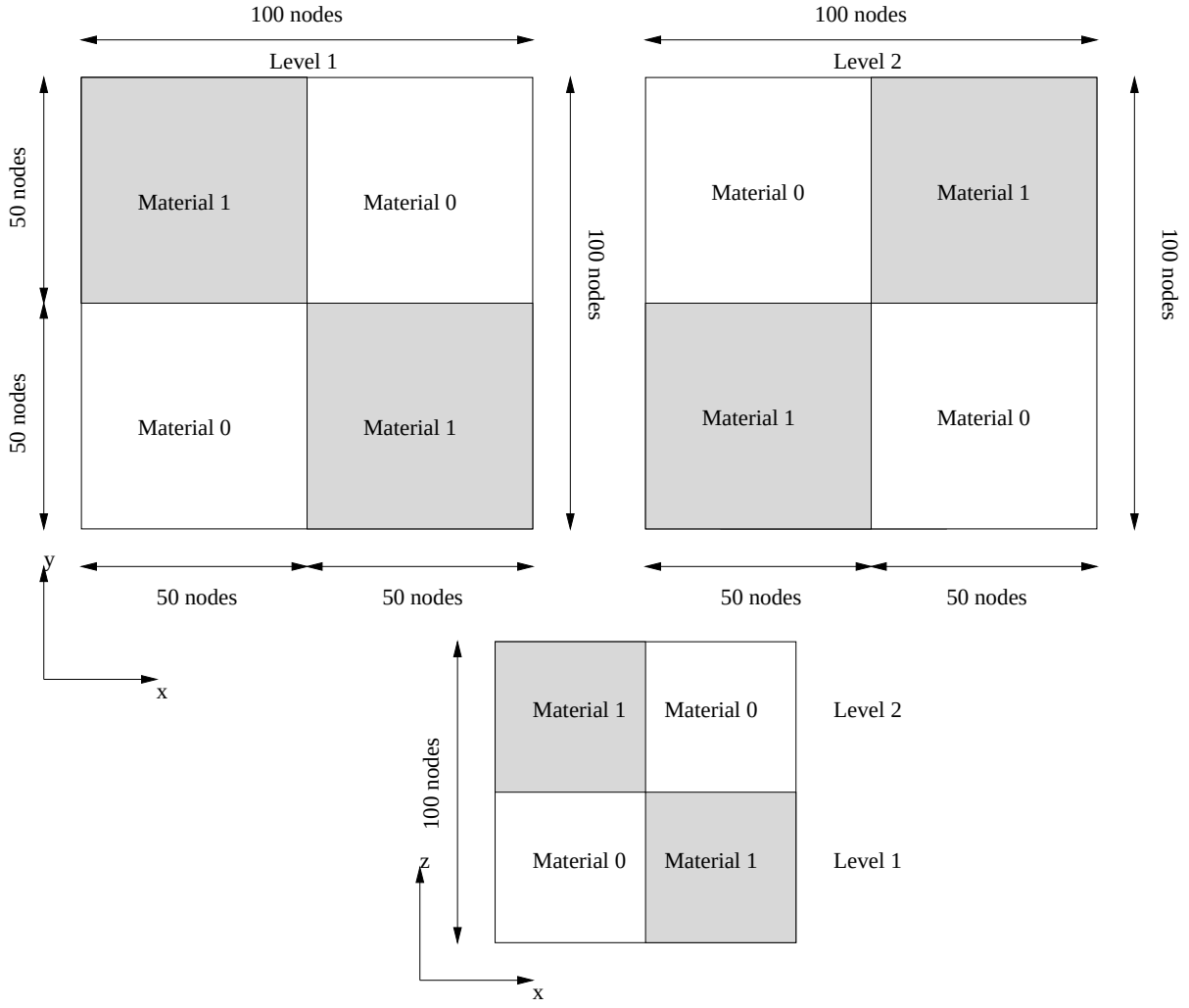

Figure E.3: Material/Geometry Sample Input for 3-D Cartesian TBIT

Table E.13: Geometry and Energy Group input for TBIT

Line a	Title: "Time Steps"
Line b	Input: Number of time-steps
Line c	Title: "Angular Directions"
Line d	Input: Number directions in the polar angle
Line e	Title: *3-D only* "Phi Angular Directions"
Line f	Input: *3-D only* Number directions in the azimuthal angle
Line g	Title: "Nodes in the radial direction"
Line h	Input: Number of nodes in the radial direction

the "bubble". The smallest number of nodes that one can use while still using an open rule is 5 and therefore the smallest number of nodes in the radial direction should be greater than 4.

E.10 Output Variables

Several output variables need to be read into the input file before the TBIT code is run. The input on line 'b' determines the number of time-steps that need to be calculated before additional output is written. The input on line 'd' determines the the number spatial steps in the 'x/r' direction before additional data is written to the output file. The input on line 'f' and 'h' determines the number of spatial steps in the 'y/theta' and 'z/phi'; however, unlike the input for line 'd' these are only included for problems of two and three dimensions respectfully.

Table E.14: Geometry and Energy Group input for TBIT

Line a	Title: "Output time-steps"
Line b	Input: Number of time-steps before one outputs to file
Line c	Title: "Output 'x/r'-Spatial Steps"
Line d	Input: Number of 'x/r'-spatial steps between output
Line e	Title: *2-D or 3-D only* "Output 'y/theta'-Spatial Steps"
Line f	Input: *2-D or 3-D only* Number of 'y/theta'-spatial steps between output
Line g	Title: *3-D only* "Output 'z/phi'-Spatial Steps"
Line h	Input: *3-D only* Number of 'z/phi'-spatial steps between output

E.11 End of Input File

The input file ends with several variables that still need to be determined. Line 'b' inputs the maximum percent error between iterations for the scattered source. Corresponding values for the percent error should be 10^{-6} or less; however, the lower the iteration error the greater the amount of time that the code must spend in calculating the scattered source. Typically, for every order of magnitude of the percent error, the TBIT method requires that number of iterations in calculating the scattered flux.

The input on line 'd' determines whether or not a balance calculation for each spatial mesh will be calculated. An input of 1 results in a balance calculation and 0 is a negative result. Only, the one-dimensional Cartesian coordinates have the balance calculations subroutines included.

The final line of input on line 'f' determines whether or not the highest energy group defaults to a velocity of 1 cm/s. This input was included to help compare the TBIT

Table E.15: Geometry and Energy Group input for TBIT

Line a	Title: "Error"
Line b	Input: Maximum percent error between iterations on each time-step
Line c	Title: "Balance Calculations"
Line d	Input: '1' to perform a balance calculation for each unit cell zero for a negative result
Line e	Title: "Unit Velocity"
Line f	Input: '1' to default maximum particle velocity to $1cm/s$ '0' for negative result

method to the time-dependent benchmarks as described in Chapter 3.

Appendix F

Hohlraum Illumination using "Standard" Integral Methods

The general form for time-dependent integral transport equation using the standard integral method is:

$$\Phi(\vec{r},t) = \int_0^t dt' \int_{V'} K(\vec{r},\vec{r}';t,t')\, Q(\vec{r}',t')\, d\vec{r}'\,, \tag{F.1}$$

where: $K(\vec{r},\vec{r}';t,t')$ is the time-dependent kernel for the geometry of interest and $Q(\vec{r}',t')$ is the time-dependent source. The integration is carried out over the volume of interest V' from time zero until the time of interest t. The source term includes contributions from both an isotropic scattering flux and an arbitrary isotropic source:

$$Q(\vec{r},t) = \Sigma_s\, \Phi(\vec{r},t) + S(\vec{r},t)\,. \tag{F.2}$$

The time-dependent heterogeneous kernel in three-dimensional Cartesian coordinates was derived in Appendix A. For three-dimensional radiation transport within a hohlraum, the kernel takes the following form:

$$K(\vec{r},\vec{r}';t,t') = \frac{exp(-\tau\,(\vec{r},\vec{r}'))}{4\pi|\vec{r}-\vec{r}'|c[t-t']}\delta\left(t-t'-\frac{|\vec{r}-\vec{r}'|}{c}\right), \tag{F.3}$$

where: $|\vec{r}-\vec{r}'|$ is the distance between the point at which one is calculating the scalar flux at and the test point where one is integrating to. In Cartesian coordinates, this distance is just:

$$|\vec{r}-\vec{r}'| = \sqrt{(x-x')^2+(y-y')^2+(z-z')^2}. \tag{F.4}$$

In principle, any type of three-dimensional, monoenergetic, neutral particle, time-dependent problem could be determined by solving Equation. F.1. However, several assumptions will be made which will simplify Eqn. F.1 at the cost of limiting the resulting equation to the specific problem of solving hohlraum type calculations.

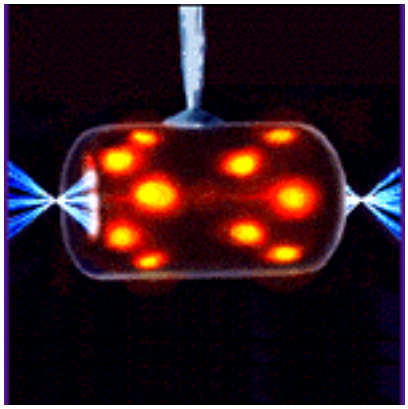

Figure F.1: Nova Capsule Illumination

F.1 Geometry of Problem

Only a single type of geometry will be examined, that of a NOVA target, as shown in Figure F.1. The physical dimensions of the NOVA hohlraum, laser entrance hole, and capsule are provided in Figure F.2.

Table F.1 shows the number and dimension of the nodes for the three regions in the NOVA target: capsule, cylinder (part of the hohlraum), and left and right rings (part of the hohlraum).

The values were chosen to meet two different types of criteria. The spacing between each of the nodes has to be fairly uniform. This is done to ensure that the communication time between the nodes of the three geometry types is approximately equal. In addition, the number of nodes are chosen such that the grid spacing is relatively fine. When the grid spacing is refined, the calculated accuracy should increase. However, the computational time increases as the cubed number of nodes in the z-direction on the hohlraum.

As a compromising balance between the two contradictory goals of fast run time and

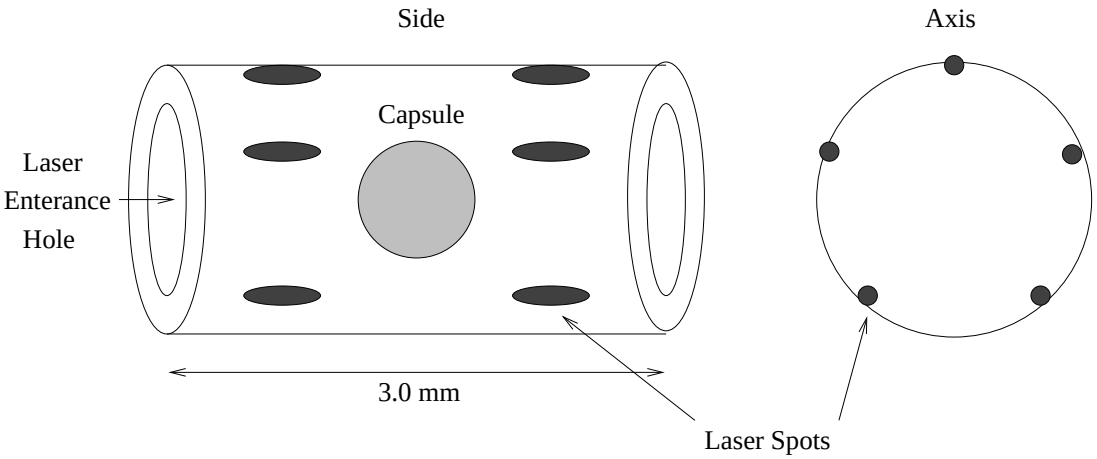

Figure F.2: Geometry and Dimensions for Nova Target

Table F.1: Number and Dimension of Nodes

Location	**Number of Nodes**	**Dimensions [cm]**
Z-Hohlraum (dz_h)	32	0.0766
Theta-Hohlraum ($d\theta_h$)	65	0.0773
Radius-Rings (dr_r)	3	0.0667
Theta-Rings ($d\theta_r$)	65	0.0773
Polar-Angle Capsule ($d\theta_c$)	22	0.0771
Azimuthal-Angle Capsule ($d\phi_c$)	11	0.0771

accurate results, the number of nodes in the z direction of the hohlraum was chosen such that the communication time between adjacent the nodes is approximately 0.25 picoseconds. This decision then fixed the grid spacing on the other two surfaces, as shown in Table F.1.

F.2 Simplifying Assumptions

The full fledged integral transport equation, Equation F.1, with the three dimensional time-dependent kernel, Equation F.3, can be quite challenging to solve. However, with several assumptions Equation F.1 can be reduced into a much simpler form. These simplifying assumptions are:

1. The capsule is assumed to be totally black. Any X-rays incident on the capsule will be absorbed and not remitted.

2. The filler gas within the hohlraum has zero opacity. Therefore, X-rays traveling within the hohlraum will not scatter or be absorbed. Furthermore, only the X-ray flux incident on the surfaces of capsule and the hohlraum will be calculated.

3. The albedo of the hohlraum is set to a constant 0.8 throughout the simulation,independent of position, time and incident X-ray flux. X-rays on the hohlraum's surface are emitted isotropicically and remitted instantaneously.

4. The geometry of the hohlraum and capsule remains fixed throughout the simulation. No provisions will be made for the deformation of the capsule or the hohlraum.

With these simplifying assumptions the time-dependent integral transport equation for this system is:

$$\Phi(\vec{r},t) = \int_0^t dt' \int_S \frac{Q\left(\vec{r}',t'\right)}{4\pi|\vec{r}-\vec{r}'|^2} H\left(t - t' - \frac{|\vec{r}-\vec{r}'|}{v}\right) dS' \,. \tag{F.5}$$

The integration is carried out over the surface of the hohlraum, although the calculational node for the scalar flux can occur on the surface of the capsule, because only the inside of the hohlraum is a source for X-rays. The capsule was assumed to be completely black and there is not any filler gas to scatter X-ray's within the hohlraum. Therefore, the only location which is a source for X-rays, be that an isotropic source from the lasers or remitted, is the surface of the hohlraum itself.

Although the simplifying assumptions reduced the previous full fledge integral equation, numerically solving Equation F.5 still poses some difficulties. The Heaviside function, within the time-dependent kernel, provides causality information for a particle's motion. A finite amount of time must pass before a particle can affect the flux at a location other than where it was born or scattered. From a computational standpoint, only points for which there has been enough time for the X-rays to travel to the calculation node need be included in the calculation.

A second difficulty arises from the fact that not every point within this hohlraum can "see" every other point. The capsule is assumed to absorb any and all X-rays that intersect with it. A 'view-factor' calculation must be performed to determine whether or not X-rays produced at the i^{th} node can see the surface of interest.

F.3 View-Factor

For the X-rays to affect the flux at any given point on the hohlraum or the capsule, there must be a direct line of sight from the place where the X-ray was born to the calculational point. View-factors from the node of interest, on the capsule or on the hohlraum, are only from the node of interest to all the nodes on the hohlraum. This is because the capsule is assumed to be completely black and the filler gas is assumed to not scatter any of the X-rays, Assumption 2. If the calculation node can see the test node, then the

code assumes that the calculation node can see the complete incremental area for which the node represents.

Therefore, two types of view-factor calculations must be performed. The first calculation is whether or not the calculational point on the hohlraum can see the test point, regardless of the capsule. The second calculation is whether or not the capsule intersects with the line of sight.

A unit vector is drawn from the center of the capsule to the calculation node. Similarly, a unit vector is drawn from the calculation node to the test node on the surface of the hohlraum. The angle between these two vectors is just:

$$\theta = \cos^{-1}\left(\vec{r_1} \cdot \vec{r_2}\right). \tag{F.6}$$

If the angle between the two vectors is greater than $\frac{\pi}{2}$ then the calculation node on the capsule can not see the test node on the hohlraum.

A similar calculation is performed to determine whether or not the two nodes are blocked by the capsule. A unit vector is drawn from the calculation node to the center of the sphere. A second unit vector is drawn from the calculation node to the test node, both of which reside on the hohlraum. The angle between the two unit vectors is:

$$\theta = \cos^{-1}\left(\vec{r_1} \cdot \vec{r_2}\right). \tag{F.7}$$

The distance of closest approach for the $\vec{r}$ is just:

$$\|\vec{k}\| = \|\vec{s}\| \cdot \sin\left(\theta\right). \tag{F.8}$$

If the distance of closest approach is greater than the radius of the capsule then the calculation node can see the test node. If the distance of closest approach is less than the radius of the capsule, then the line of sight between the calculation node and the test node passes through the capsule and the two nodes can not communicate with each other directly.

Table F.2: Incremental Areas

Location on Hohlraum	dA_i
Cylinder	$R_h d\theta_h dz_h$
Ring	$r_i d\theta_r dr_r$

F.4 Numerical Evaluation

Once the view-factor calculations are complete, the calculation can then continue and either include or exclude the source contribution that the test node makes. If the test node is not in the line of sight, then the code increments to the next test node and the view factor for this 'new' location is determined and the process described in the previous section is repeated.

If however the test node can influence the X-ray flux at the calculation node, then the area around the test node can influence the flux as described in Equation F.5. The X-ray flux at a specific point is just:

$$\Phi_c(x,y,z;t) = \sum_{t=1}^{ViewableNodes} \frac{S_i\left(t - \frac{Dis_{t\to c}}{v}\right)\exp^{-\Sigma Dis_{t\to c}}}{4\pi Dis_{t\to c}^2} H\left(t - \frac{Dis_{t\to c}}{v}\right) dA_i, \qquad \text{(F.9)}$$

where: $Dis_{t\to c}$ is the distance between the test node and the calculation node, $S_i\left(t - \frac{Dis_{t\to c}}{v}\right)$ is the source strength at the ith test point at an earlier time corresponding to the flight time over the distance between the two nodes, and dA_i is the differential area which surrounds the test node. This differential area varies depending on whether the test node in on the cylindrical portion of the hohlraum or on one of the two 'rings' which bound the laser entrance hole.

After summing over the visible test points is completed and the calculation node lays on the hohlraum, the computer code then sets the remitted source at 80% of the incoming flux. The code assumes that the remitted x-rays are isotropic and that they are remitted

within one time-step, 0.25 picoseconds. The capsule is assumed to be completely black and therefore will not remit any incident x-rays. The net current across the calculated node 'c' is:

$$J_c = \hat{n} \cdot \vec{J} = \int d\Omega \hat{n} \cdot \hat{\Omega}\, \psi\left(\vec{r}, \hat{\Omega}, t\right). \tag{F.10}$$

The remitted isotropic source at the calculated node is then:

$$S_c = \alpha_c \sum_{t=1}^{n} \frac{S_t \cos\theta_{t\to c} \exp(-\Sigma Dis_{t\to c})\, dA_t}{\left(Dis_{t\to c}\right)^2} \tag{F.11}$$

where: α_c is the albedo at the calculated node, $\cos\theta_{t\to c}$ is the angle between the unit outward normal and the unit vector between the calculated node and the test node, and $Dis_{t\to c}$ is the distance between the calculated node and the test node.

The remitted source is a summation of the incident fluxes from the visible nodes. Once the X-ray flux and the isotropic remitted source strength are calculated for the current node, the code then increments to the next calculational node and the process of finding the view-factors for this new node begins again.

F.5 Numerical Results

Two different scenarios with simulated NOVA hohlraums will be investigated. A NOVA hohlraum is shown in Figure F.1. As already mentioned, the dimensions from the NOVA hohlraum will be used in the numerical simulation. Further investigation of Figure F.1 shows that there are five lasers which enter into the laser entrance hole and illuminate the hohlraum. In each of the simulations, the spacing of the X-ray sources on the hohlraum will be modeled after the NOVA experiment, Figure F.1. For each case the calculation was allowed to run for 25 picoseconds, at which time the capsule illumination was plotted.

Two different scenarios were investigated. The first case simulated the nominal illumination of the NOVA capsule. The left side of Figure F.3 is the graphical representation of the source distribution for the uniform illumination case.

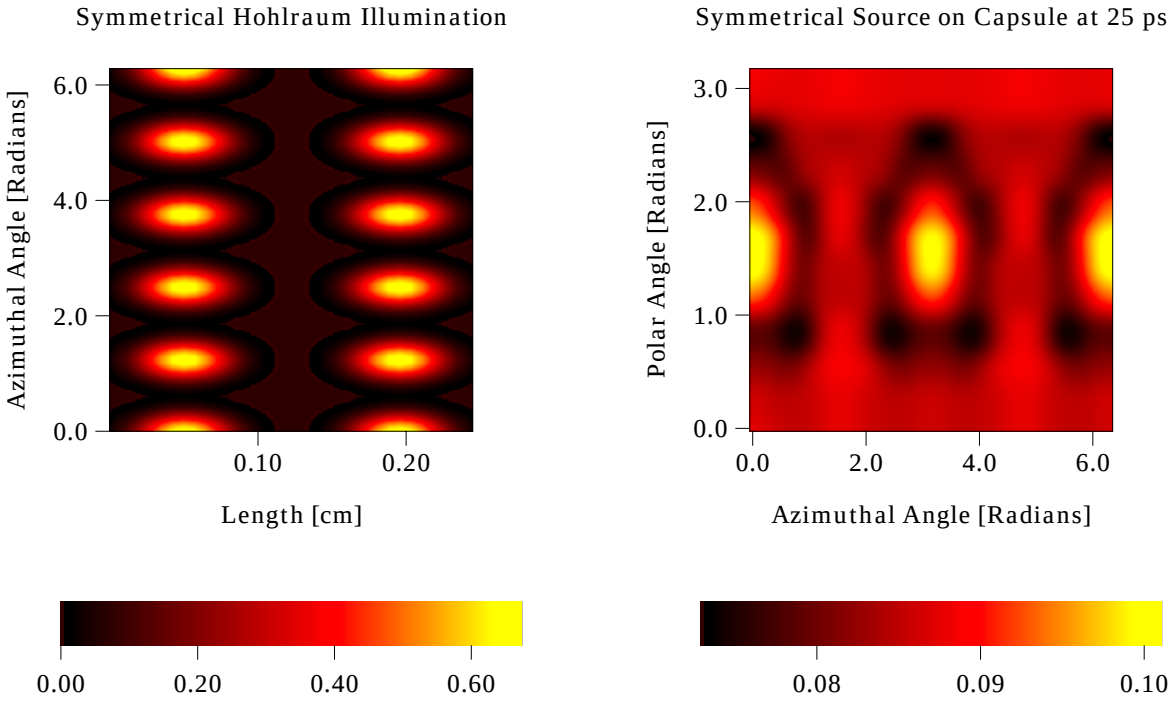

Figure F.3: Nominal Capsule Illumination

The capsule is symmetrically illuminated by five X-ray sources on either side of the hohlraum. The right side of Figure F.3 is a two dimensional representation of the capsule illumination. As shown in the figure, integral transport predicts that the capsule illumination varies by no more than 20% for any given point. As expected, the hottest portion of the capsule is the area that faces all five sources. The coolest portion of the capsule is the region on either side, which only has a partial line of sight to any given source. These regions are evident from the five cool regions, which lay in a ring just outside the central hot spot.

The second case simulated a non-uniform illumination of the NOVA capsule. As shown on the left side of Figure F.4, the right side of the capsule is illuminated by five sources whereas the left is illuminated only by four.

As shown in Figure F.4, the region of the capsule that has the most direct line of

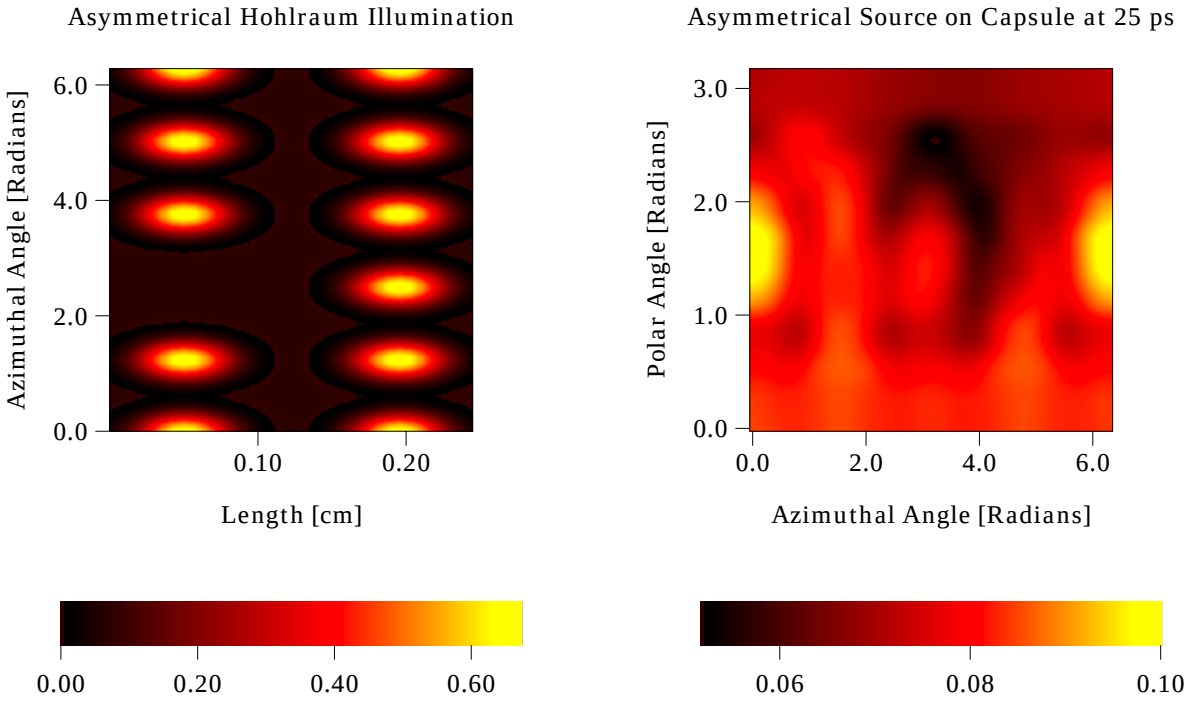

Figure F.4: Non-Uniform Capsule Illumination

sight to the source that is turned off, is the coolest. The asymmetry in the illumination affects not only the portions of the capsule nearest to it, but the illumination over the entire capsule. The capsule illumination for this asymmetrical case varies approximately by a factor of two.